NASA TECHNICAL NOTE
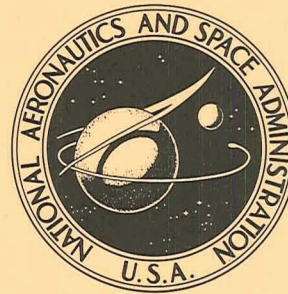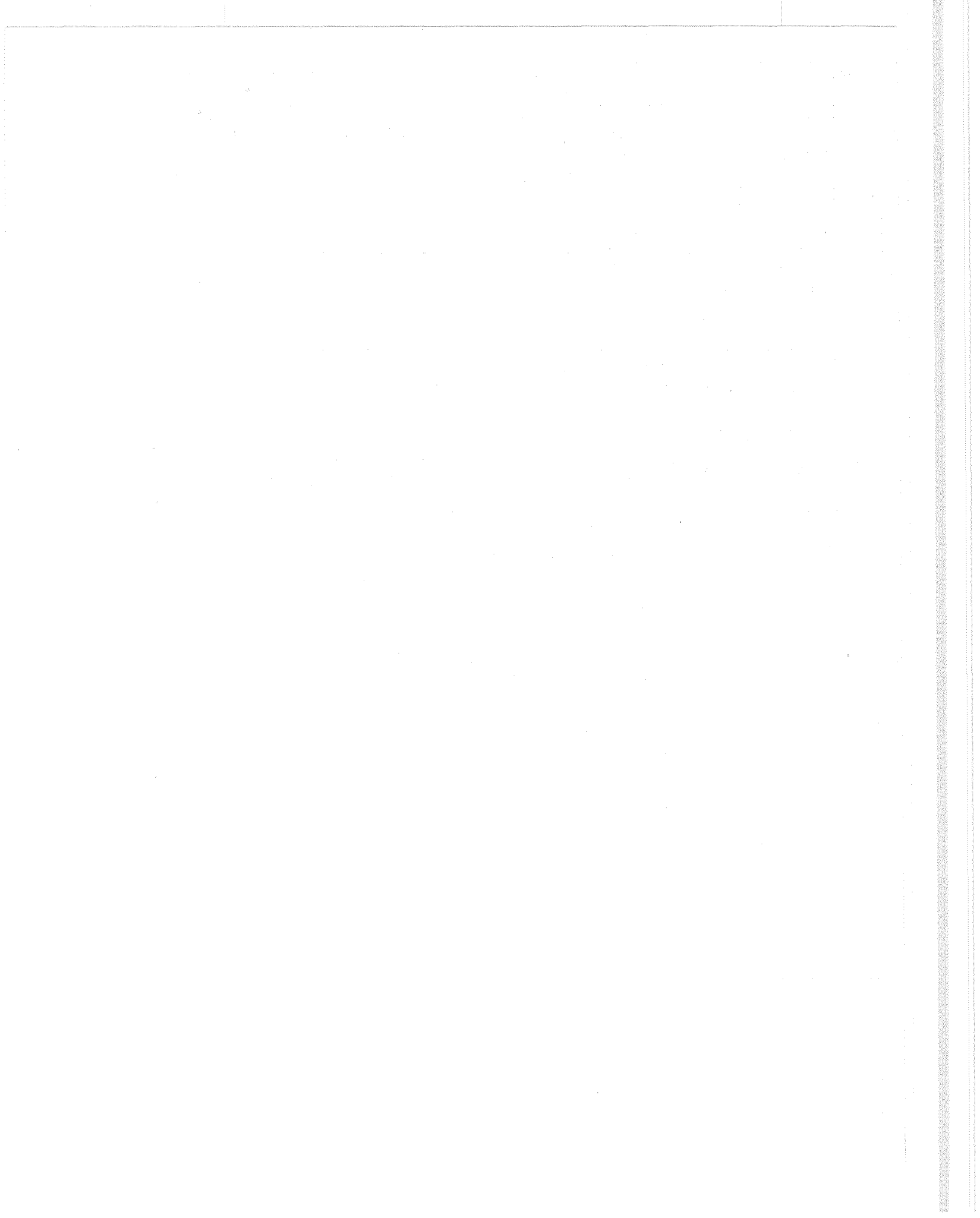
NASA TN D-7139

NASA TN D-7139

L42P

ANALYTICAL AND EXPERIMENTAL STUDIES OF SHOCK INTERFERENCE HEATING IN HYPERSONIC FLOWS

by J. Wayne Keyes and Frank D. Hains

Langley Research Center
Hampton, Va. 23365

NATIONAL AERONAUTICS AND SPACE ADMINISTRATION • WASHINGTON, D. C. • MAY 1973

1. Report No. NASA TN D-7139	2. Government Accession No.	3. Recipient's Catalog No.
4. Title and Subtitle ANALYTICAL AND EXPERIMENTAL STUDIES OF SHOCK INTERFERENCE HEATING IN HYPERSONIC FLOWS		5. Report Date May 1973
		6. Performing Organization Code
7. Author(s) J. Wayne Keyes and Frank D. Hains		8. Performing Organization Report No. L-8423
9. Performing Organization Name and Address NASA Langley Research Center Hampton, Va. 23365		10. Work Unit No. 501-06-08-01
		11. Contract or Grant No.
12. Sponsoring Agency Name and Address National Aeronautics and Space Administration Washington, D.C. 20546		13. Type of Report and Period Covered
		14. Sponsoring Agency Code

15. Supplementary Notes

The experimental data were obtained jointly with Bell Aerospace Co. under Contract NAS 1-9606. The second author was formerly with Bell Aerospace Co., Div. of Textron, Inc., Buffalo, New York, and is presently with Science Applications, Inc., Arlington, Virginia.

16. Abstract

The paper presents an analytical and experimental study of the aerodynamic heating resulting from six types of shock interference patterns encountered in high-speed flow. Center-line measurements of pressure and heat-transfer distributions on basic bodies were obtained in four wind tunnels for Mach numbers from 6 to 20, specific heat ratios from 1.27 to 1.67, and free-stream Reynolds numbers from 3×10^6 to 25.6×10^6 per meter. Peak heating and peak pressures up to 17 and 7.5 times stagnation values, respectively, were measured. In general, results obtained from semiempirical methods developed for each of the six types of interference agreed with the experimental peaks.

17. Key Words (Suggested by Author(s)) Shock interference heating and pressures Shock—boundary-layer interaction Shear layer attachment Jet impingement Shock interactions	18. Distribution Statement Unclassified – Unlimited

19. Security Classif. (of this report) Unclassified	20. Security Classif. (of this page) Unclassified	21. No. of Pages 139	22. Price* $3.00

CONTENTS

ANALYTICAL AND EXPERIMENTAL STUDIES OF SHOCK
INTERFERENCE HEATING IN HYPERSONIC FLOWS

By J. Wayne Keyes and Frank D. Hains[*]
Langley Research Center

SUMMARY

This paper presents an analytical and experimental study of shock interference heating in hypersonic flows. The study included measurements of heat-transfer and pressure amplification from interference effects, and the development of flow models and methods of predicting the peak values suitable for engineering purposes. Theoretical parametric studies were also conducted to determine the effect of flow and geometric variables on interference heating. The experimental investigation was conducted in four facilities which encompassed a Mach number range from 6 to 20, specific heat ratios of 1.27, 1.40, and 1.67 and free-stream Reynolds number from 3×10^6 to 25.6×10^6 per meter. Six interference flow patterns defined in previous investigations were generated by the interaction between a plane shock and the bow shock created by a 0.025-meter- and a 0.051-meter-diameter hemisphere, a cylindrical fin, and a 30° wedge.

In most cases, calculations based on the flow models and methods developed in the present investigation gave reasonable estimates of the measured peak pressure and heat transfer when real-gas effects were negligible. Flow-visualization data are currently necessary to utilize the methods since measured shock lengths and angles are required. Pressure and heat-transfer peaks as high as 7.5 and 17 times stagnation values were recorded on the 0.051-meter-diameter hemisphere at Mach 6. Values up to 11.5 and 15 times undisturbed wedge pressure and laminar heating, respectively, were also measured at Mach 6. Results of the parametric study indicated that shock interference heating is strongly affected by Mach number, specific heat ratio, impinging shock strength, and model geometry. Because of real-gas effects, interference heating on the actual flight vehicle may be higher than that measured on a wind-tunnel model.

INTRODUCTION

Shock interference heating is a problem in the design of the thermal protection system and structural components of high-speed vehicles such as the space shuttle and the

---

[*]Formerly with Bell Aerospace Co., Div. of Textron, Inc., Buffalo, New York, and presently with Science Applications, Inc., Arlington, Virginia.

hypersonic cruise aircraft. (See refs. 1 to 5.) Extremely high pressure and heating can occur in small areas on the vehicle's surface because of interfering flow fields which also may be unsteady. These interfering flow fields or shock interference patterns are sensitive to Mach number, free-stream flow conditions, and angle-of-attack changes as the vehicle moves along its flight path.

Some previous investigations of shock interference flows are reported in references 6 to 31 (see table I) and references 32 to 34. Few of these references present a conclusive understanding of the overall shock interference problem. Edney (ref. 6) made a detailed study of the entire spectrum of interference flow patterns. Edney defined six types of shock interference patterns and showed that as a result of the shape and type of pattern, the local pressure and heating peaks were caused by either shock—boundary-layer interaction, free shear layer attachment, or supersonic jet impingement. Other mechanisms resulting from shock interaction which cause less severe heating and pressure effects are (1) the jet grazing the surface and (2) an expansion fan interacting with the surface boundary layer.

The present paper presents the results of a comprehensive analytical and experimental study of shock interference heating. The purposes of this study were

(1) To determine the effects of Mach number, specific heat ratio, impinging shock strength, and geometry on the pressure and heat-transfer amplification for each type of interference pattern

(2) To develop semiempirical methods using the flow models of reference 6 to calculate both the inviscid and viscous interactions as well as the peak pressure and heat transfer for each type (computer programs generated from these methods are presented in ref. 35).

The experimental study was conducted over a wide range of free-stream Mach numbers (Mach 6 to 20), specific heat ratios (1.27, 1.40, and 1.67), unit Reynolds numbers (3×10^6 to 25.6×10^6 per meter), and impinging shock strength (shock generator angles up to 30°). Center-line pressure and heat-transfer distributions and flow-visualization data were obtained on several basic shapes.

Because of the large quantity of information gathered, the results are presented in two parts. The first part includes a discussion of the flow models and methods of prediction, a comparison of experimental and calculated results, and the results of a parametric study made by use of the prediction methods. The second part covers the experimental phase of the study. Included also is an appendix on interference heating for a typical space shuttle configuration. Some results from the present study are available in references 36 to 39.

TABLE I.- SUMMARY OF SHOCK INTERFERENCE INVESTIGATIONS

Reference number	Author and date	M_∞	$N_{Re,\infty}/m$	Fin diameter, d, m	Shock generator angle, θ_i, deg	Fin sweep, λ, deg	Measurements		Visualization		$\dfrac{Q_{max}}{Q_{ref}}$	Remarks (a)
							p	Q	Schlieren	Oil		
6	Edney (1968)	4.6	4.06×10^6 to 47.29×10^6		0 to 15		x	x	x		10	Axisymmetric blunt bodies and fins. Novel techniques to measure p_{pk} and Q_{pk}.
		7	1.10×10^6 to 7.68×10^6		0 to 5							
7	Newlander (1961)	2.65	4.33×10^6 to 14.96×10^6	0.071	16.25	0		x		x	1.8	Wedge and fin mounted on flat plate. Partially immersed in boundary layer.
		3.51									2.0	
		4.44									3.1	
8	Carter and Carr (1961)	2.0		0.019	*	0			x			*Not applicable. Shock generated by hemisphere/cylinder forebody.
		2.53 to 5.5	52.36×10^6 to 98.42×10^6	0.019	*	0		x			0.1 to 0.5 (M_∞ = 3) 1.5 to 2 (M_∞ = 4)	Free flight to 3.2 km altitude.
9	Beckwith (1964)	4.15	56.69×10^6 to 141.73×10^6	0.028	0	20	x	x	x		2.5	
10	Jones (1964)	6.0	2.36×10^6 to 28.74×10^6	0.027	0	60	*x	x	x		1 to 3	*Only at $N_{Re,\infty}/m = 28.74 \times 10^6$. Model yawed up to 30°.
11	Siler and Deskins (1964)	19.0	0.94×10^6	0.051	0 to 40	0 to 60	x	x	x		2.5 to 5	
12	Bushnell (1965)	8.0	3.03×10^6 to 3.43×10^6	0.025	12	45 and 60	x	x	x		3 to 5	
13	Francis (1965)	9.0	0.57×10^6 to 3.78×10^6	0.025	*6.34 ±20	0 ±20		x	x		1 to 4	*Cone and wedge with one cylindrical and one wedge fin, both fixed.
14	Gulbran et al. (1965)											
15	Knox (1965)											
16	Popinski (1965)											
17	Ray and Palko (1965)	6, *8, 10	1.89×10^6 to 11.81×10^6	0.051	0 to 60	0 to 60	x	x	x	x	2.5 to 5	*Data not presented for M_∞ = 8.
18	Gulbran et al. (1967)											
19	Heirs and Loubsky (1967)	14	0.31×10^6	0.025	0 to 15	0, 22.5, 45		x	x	x	10	Luminous photographs supplement schlieren photographs.
20	Uselton (1967)											
21	Bushnell (1968)	8	1.65×10^6 to 16.50×10^6		12	0, 76		x	x		2	
22	Watts (1968)*											*Data generally not available.
23	Young, Kaufman, and Korkegi (1968)	3, 5	1.77×10^6 to 4.65×10^6	0.019	0	0	x		x	x		
24	Jones and Hunt (1969)	8						x	x		15.5	Apollo antenna.
25	Mashburn (1969)	4.8		0.005 to 0.038	0	0	x		x			
26	Spurlin (1969)											
27	Martindale (1970)											
28	Teterin (1967)	5		0.041	10	0		x	x		5	
29	Holden (1972)	6.5 to 13	32.80×10^6 to 328.00×10^6		0 to 20		x	x	x		50	
30	Kaufman, Korkegi, and Morton (1972)	2.5, 3.0 4.0	31.50×10^6 18.50×10^6	0.010, 0.019, 0.025	0	0	x	x	x			
31	Haslett et al. (1972)	8	1.18×10^6 to 11.80×10^6		1.5 to 15		x	+x	*x		1.15	*Shadowgraphs also. +Thermocouple and phase-change coating data.

^{a}Items marked with asterisks and crosses apply to items so marked in other columns.

<center>SYMBOLS</center>

A   constant in equation (2) and figure 6

c   specific heat of model material

c_p specific heat at constant pressure

d   diameter

h   heat-transfer coefficient

k   thermal conductivity of model material

L   model length

L_{SH} shock displacement length (see figs. 5 and 7)

ℓ distance (see fig. 44)

ℓ_{SL} shear layer length (eqs. (3) and (4), fig. 5)

M   Mach number

N   exponent in equations (1) and (2) and figure 6

N_{Pr} Prandtl number

N_{Re} Reynolds number

p   pressure

p_{cyl} stagnation line pressure on cylindrical leading-edge fin

p_{stag} stagnation pressure on hemisphere or free-stream pitot pressure

p_{wedge} wedge pressure

Q   heat-transfer rate

4

Q_{cyl}	laminar stagnation-line heat-transfer rate on cylindrical leading-edge fin
Q_{stag}	laminar stagnation-point heat-transfer rate on hemisphere
Q_{wedge}	heat-transfer rate on wedge
R_b	hemisphere radius
$R_{b,j}$	sphere radius of jet body (fig. 10)
R_c	radius of jet bow shock (fig. 10)
s	surface coordinate
T	temperature
T_m	phase-change-coating melt temperature
u	velocity
$\bar{w}$	jet width at impingement (see figs. 7 and 10)
$X = \dfrac{x}{L}$	
X_i	impingement location on wedge from leading edge (fig. 3, fig. 4, fig. 11, and fig. 12)
x	axial coordinate
x_i, y_i	coordinates of shock intersection location relative to stagnation point on hemisphere
α	angle of attack
α_j	inclination of jet relative to surface (fig. 10)
β	shock angle

$\bar{\beta}$ heat-transfer parameter in figure 44

β_i impinging shock angle

γ specific heat ratio

$\delta_{j,s}$ jet bow shock standoff distance (fig. 10)

δ_{SL} shear layer thickness at wall in equations (2), (3), and (4)

θ body angle for hemisphere

θ_b local body slope

θ_i shock generator angle

$\bar{\theta}_5$ shear layer angle relative to surface (fig. 5)

λ fin sweep angle

μ viscosity

ρ density

Subscripts:

aw   adiabatic wall

cyl   cylindrical leading edge

init   initial

j   jet

L   laminar value

max   maximum value

pitot   pitot value

pk   peak value

ref   reference value

SH   shock

SL   shear layer

stag   hemisphere stagnation point

T   turbulent value

t   total value

u   undisturbed value

w   wall value

wedge   wedge value

∞ free-stream value

Special notation:

1, 2, . . ., 8   regions of flow pattern

BS, IP, IS, ⎫   bow shock, impingement point, imping shock, shear layer,
SL, TS   ⎭   transmitted shock (see fig. 1)

I, II, . . ., VI   types of interference patterns

ANALYSIS AND COMPARISONS WITH DATA

TYPES OF SHOCK INTERFERENCE PATTERNS

In evaluating the effects of shock interference heating, it is necessary to determine the type of interference pattern that will exist when two shocks of different strengths intersect. The pattern that will occur depends on body geometry, the strength of the impinging shock, and its position relative to the body. (See ref. 6.) The six possible

shock interference flow patterns defined by Edney are shown in figure 1. For the sake of simplicity an example of how the interference patterns can change on a hemisphere from one type to another with impinging shock location is presented in figure 2.

The interference patterns can be further grouped according to the mechanism that caused the pressure and heat-transfer change at the surface. Types I, II, and V are associated with a shock—boundary-layer interaction and type III is characterized by an attaching free shear layer. Type IV is characterized by an impinging or grazing super-sonic jet and type VI by an expansion-fan—boundary-layer interaction.

FLOW MODELS AND METHODS OF PREDICTION

The six flow models are similar to those discussed in reference 6; therefore, only the model highlights and modifications are discussed in the following section. In general, the methods of predicting the peak pressure and heating are semiempirical and are pri-marily for engineering design calculations. The methods are based upon local two-dimensional flow models with the exception of types III and V where a tangent-cone approximation is used for three-dimensional bodies. Computer programs generated from these methods are described in reference 35.

Type I Interference

A type I interference pattern occurs when two weak shocks of opposite families intersect as shown in figure 3. These weak shocks can be attached shocks generated by wedges and cones or parts of detached shocks located well downstream of the sonic point. (See fig. 2.) The actual rise in pressure and heating at the surface is caused by the inter-action of the transmitted impinging shock and the wall boundary layer. The flow field associated with type I is supersonic throughout.

The flow conditions in regions 2 and 3 are calculated from the Rankine-Hugoniot shock relation of reference 40 once the flow conditions in region 1 and the strengths of the bow and impinging shocks are specified. Unless the strengths of the two shocks are equal, a shear layer will be produced at point A and between regions 4 and 5 where the static pressures must be equal and the flow directions parallel. An iterative procedure is utilized to obtain the strength of the transmitted shocks and the orientation of the shear layer relative to the free-stream direction which satisfy these conditions. From the strength of the transmitted impinging shock and the local surface inclination at impinge-ment, flow conditions in region 6 are calculated by using the Rankine-Hugoniot shock relations. When the regular oblique shock reflection at the surface is no longer possible, a Mach reflection (refs. 41 and 42) will occur as shown in the insert of figure 3 with the pressure rise from region 2 to region 6 at the wall approximated by the normal shock relations.

When the pressure rise is known, the heat transfer can be obtained from shock—boundary-layer interaction studies. Calculations based on methods developed in several of these studies, for example, references 43 to 45, were compared with experimental data in reference 46. It was found that these methods gave good heating estimates for weak shocks at low supersonic Mach numbers. For a strong shock—boundary-layer interaction and a higher Mach number, the agreement was not as good. A promising method based on the Lax-Wendroff difference technique for the solution of the time-dependent Navier-Stokes equations has been presented by MacCormack (ref. 47). However, any of these detailed methods require considerable computer time and are not suitable for rapid engineering calculations. In the present study, the following correlations and constants developed by Markarian (ref. 48) were used for predicting the peak heating. The correlations are of the form

$$\frac{Q_{pk}}{Q_u} = \left(\frac{p_{pk}}{p_u}\right)^N \tag{1}$$

where $N = 1.29$ for laminar interactions and 0.85 for turbulent interactions and p_{pk}/p_u is the inviscid pressure ratio p_6/p_2 across the interaction. Calculation of the peak heating requires a knowledge of the reference or undisturbed heating Q_u upstream of the interaction. In the present study, reference values Q_{wedge} are obtained from expressions in reference 49 for laminar and turbulent boundary layers on plane surfaces by using the measured location of the impingement point. Also, the reference pressure p_{wedge} is the undisturbed value ahead of the interaction on the wedge.

Type II Interference

A type II interference pattern occurs when two shocks of opposite families intersect as shown in figure 4. Both shocks are weak as in type I, but are of such strength that in order to turn the flow, a Mach reflection must exist in the center of the flow field with an embedded subsonic region located between the intersection points (A and B) and the accompanying shear layers. (See also ref. 42, p. 557.) On a blunt body, type II interference occurs when the impinging shock intersects the bow shock nearer to the sonic point than type I, as shown in figure 2. A detailed analysis of the complete flow field is difficult because the extent of the subsonic region (region 5) is unknown and depends on the size and shape of the body (ref. 6). The conditions in the supersonic regions (4 and 6) can be calculated, since the influence of the impinging shock on these regions is small compared with the influence of the bow shock (ref. 6). The inviscid pressure ratio p_6/p_2 across the reflected shock at the shock—boundary-layer interaction can be calculated from these conditions.

If the free-stream conditions in region 1 and either the body angle or shock angle are known, the triple shock at point A is solved by using an iterative procedure similar to type I with the exception that strong shock relations are used between regions 1 and 5. A Mach reflection with a nearly normal leg at the wall apparently forms when the regular shock reflection between regions 4 and 6 is no longer possible. (See sketch in fig. 4.) The heat-transfer rise is determined by using equation (1) and p_6/p_2. The reference or undisturbed pressure and heating upstream of X_i are also calculated in exactly the same manner as for type I.

Type III Interference

A type III shock interference pattern occurs when a weak impinging shock intersects a strong detached bow shock as shown in figure 5. The shear layer emanating from the shock intersection (point A) attaches to the surface with subsonic flow above the layer turning upward and subsonic flow below the layer passing through an oblique shock in order to turn parallel with the surface. Whether the shear layer attaches to the surface depends on the Mach number in region 4 M_4, and the angle between the shear layer and the surface $\bar{\theta}_5$. If M_4 is sufficiently high and $\bar{\theta}_5$ does not exceed the maximum turning angle for M_4, then the layer will be attached. If, however, the maximum angle is exceeded, the shear layer will detach and a type IV pattern will be formed. If it is assumed that the shear layer attaches at point C and the oblique shock does exist, then another triple shock will occur at point B. (See fig. 5.) On a blunt body the shock intersection occurs near or above the lower sonic point as shown in figure 2.

The conditions in regions 2 and 4 are obtained by solving the triple shock at point A by using an iterative procedure. Required are the impinging shock strengths and the free-stream flow conditions. The iteration also requires the use of the strong shock relations between regions 1 and 2. Results from this exact analysis are used in an approximate analytic technique to determine the peak pressure and heat transfer at shear layer attachment. The strength of shock BC is determined by assuming the angle between the shear layer and the local body slope $\bar{\theta}_5$ is known. The peak wall pressure in region 5 is calculated by using the flow conditions in region 4 and the Rankine-Hugoniot shock relations for attachment on a two-dimensional body. For attachment on a three-dimensional body, tangent-cone approximations (ref. 35) are used by assuming that shock BC is conical. In the present study the tangent-cone method is used since the model configuration consisted of a plane shock impinging with the bow shock of a hemisphere.

Peak heating caused by an attaching free shear layer is analogous to a reattaching separated boundary layer. (See ref. 6.) In the present study, correlations proposed by Bushnell and Weinstein (ref. 50) for reattachment heating on two-dimensional ramps are

used. The peak heating at attachment is

$$Q_{pk} = A\rho_{w,5}u_5 c_p\left(T_{aw} - T_w\right)\left(\frac{\mu_w \sin \bar{\theta}_5}{\rho_{w,5}u_5 \delta_{SL}}\right)^N \qquad (2)$$

where the shear layer thickness at attachment δ_{SL} is given by

$$\delta_{SL} = 5\left(\frac{\ell_{SL}\mu_4}{\rho_4 u_4}\right)^{0.5} \qquad \text{(Laminar)} \qquad (3)$$

$$\delta_{SL} = 0.123\,\ell_{SL} \qquad \text{(Turbulent)} \qquad (4)$$

The shear layer length ℓ_{SL} (AC in fig. 5) is calculated by use of the measured shock displacement length L_{SH} and the geometry of the shock shear layer triangle ABC. Shear layer transition data presented in reference 39 are useful in determining the state of the shear layer at attachment since it has been shown in references 6 and 38 that the heating for turbulent attachment is higher than that for laminar attachment for the same pressure rise. The constants A and N in equation (2) as obtained from data in reference 50 for a laminar shear layer are 0.19 and 0.5 and for a turbulent shear layer, 0.021 and 0.2.

A comparison which was made in reference 38 of peak heating for free shear layer attachment (data from present study) and reattaching separated boundary-layer curves (from ref. 50) is reproduced in figure 6 with some modifications. The flagged data based on the calculated laminar shear layer thickness are corrected for the difference in constants (five in eq. (3) and four in ref. 38). Corrections to the helium data (solid symbols) using revised calculated shear layer lengths are also included. Since the shear layer in the Mach 6 data at the lower Reynolds numbers $\left(\text{based on } \delta_{SL}\right)$ may be transitional, both the laminar and turbulent values are shown. It can be seen in figure 6 that more realistic values of A are 0.40 for laminar and 0.06 for turbulent free shear layer attachments. For a transitional shear layer attachment, both the laminar and turbulent values of δ_{SL} are used with the turbulent constant to calculate the peak heating. Possible reasons for this difference in the values of A are that the correlations in reference 50 for reattaching separated boundary layers are for two-dimensional ramps and the attaching free shear layers in reference 38 are three-dimensional in nature. Also, the shear layer angles relative to the surface are higher for the attaching shear layer than the reattaching boundary layers.

In the present study the reference heating Q_{stag} used for type III interference is the laminar stagnation-point value on a hemisphere (ref. 51) obtained from

$$Q_{stag} = 0.76(N_{Pr})^{-0.6} c_p (\rho_w \mu_w)^{0.1} (\rho_{stag} \mu_{stag})^{0.4} (T_{stag} - T_w) \left[\left(\frac{du_w}{ds} \right)_{stag} \right]^{0.5} \tag{5}$$

where the velocity gradient (from ref. 52) is

$$\left(\frac{du_w}{ds} \right)_{stag} = \frac{u_\infty}{R_b} \left\{ \frac{\gamma - 1}{\gamma} \left[1 + \frac{2}{(\gamma - 1)M_\infty^2} \right] \left(1 - \frac{1}{\gamma M_\infty^2} \right) \right\}^{0.5} \tag{6}$$

and the subscript stag refers to values at the edge of the boundary layer. The refer-
ence pressure p_{stag} is the stagnation pressure on a hemisphere.

<div align="center">Type IV Interference</div>

When a weak impinging shock intersects the nearly normal part of the bow shock,
a type IV interference occurs. This interference results in a complex flow pattern with
a supersonic jet embedded in the subsonic flow region between the bow shock and the
surface. (See figs. 2 and 7.) Up to region 6 the flow model is the same as type III;
therefore, type IV interference can be considered a special case of type III interference
with a detached shear layer $\left(\bar{\theta}_5 > \theta_4, \text{ fig. 5} \right)$. From figure 7, it can be seen that the jet
consists of triangular regions, the actual number of regions being dependent upon the
standoff distance of the entire configuration. Upon impingement on the wall, a jet bow
shock is produced that creates a small stagnation region with high pressure and heating.
As stated in reference 6, the peak heating is dependent upon the peak pressure, the jet
width, the jet angle of incidence with the surface, and the state of the jet (laminar or
turbulent), where all these quantities are interrelated.

Flow conditions and the geometry of this complex jet pattern shown in figure 7 are
calculated by assuming zero shear layer thickness and neglecting jet mixing with the
slower moving flow in regions 2 and 5. Conditions in regions 2, 3, and 4 and the shear
layer deflection angle are obtained in the same way as those for type III. Orientation of
the continuation of the bow shock between regions 3 and 5 and the shock between regions 4
and 6 are determined from the triple-point solution at point B. It is assumed that a
shear layer emanates from point B to form the lower jet boundary between regions 5
and 6 $\left(p_5 = p_6 \right)$. The location of point C is determined from the geometry of the triangle
enclosing region 4 by using the shock displacement distance L_{SH} (which is obtained
empirically). The pressure differential between regions 2 and 5 $\left(p_5 > p_2 \right)$ causes the jet
to turn upward.

Since the flow in the jet passes through a series of expansions and weak compres-
sion waves, the conditions in regions 6 and 8 $\left(p_6 = p_5 = p_8, \text{ etc.} \right)$ and all subsequent

12

even-numbered regions in the jet are the same. Likewise the conditions in all odd-numbered regions are the same. The total pressure in the jet is assumed to be constant. The incremental increases in the flow deflection angle between regions such as θ_7 to θ_6 are constant. Based on this reasoning, an expansion fan centered at E and intersecting the lower jet boundary at F complete the jet geometry through region 8. Good agreement between measured and calculated flow patterns was realized in reference 6 by using these assumptions.

It has been shown in reference 6 that two possible shock configurations can occur at the intersection of the bow and impinging shocks depending on their relative strengths. Figure 8(a) shows sketches of the jet configuration for a downward sloping shear layer with the jet bow shock located in region 8 whereas figure 8(b) shows the configuration for an upward sloping shear layer. Only the downward sloping shear layer was seen in the present study. In some configurations the jet was turned sufficiently to graze or move parallel to the wall without impinging as observed in schlieren photographs. In this case (denoted type IVa) even though impingement does not occur, regions of high heating are produced because of the interaction of the jet flow with the boundary layer.

A typical example of how the calculated total pressure varies in a type IV pattern as a function of free-stream pitot pressure is presented in figure 9. The jet total pressure, the total pressure in region 4, and the wall stagnation pressures of the jet in regions 7 and 8 remain relatively high compared with the free-stream pitot pressure. The wall stagnation pressure is obtained from normal-shock relations by using conditions in region 7 or 8. Also an approximate 10-percent difference in wall stagnation pressure occurred with a small shift in jet bow shock location from region 7 to region 8.

In order to calculate the peak heating at jet impingement, the jet stagnation velocity gradient along the wall must be determined. Several methods have been suggested for calculating the velocity gradient and the peak heating. (See refs. 6 and 36.) A method discussed in reference 6 for impingement on a sphere suggests that the peak heating is analogous to that on a blunt body (diameter equal to the jet width) submerged in a supersonic flow field (jet flow). An expression based on this analogy is

$$\frac{Q_{pk}}{Q_{stag}} = 1.03\left(\frac{R_b}{\overline{w}} \frac{p_{pk}}{p_{stag}}\right)^{0.5} \tag{7}$$

where p_{pk} and Q_{pk} are stagnation values on a cylinder of diameter $\overline{w}$ (jet width) and where p_{stag} and Q_{stag} are the stagnation values on a sphere of radius R_b. This expression was obtained by using equations in reference 53 and assuming the jet to be laminar with nearly normal impingement. The constant in expression (7) is a function of the heating parameter in reference 53. (Value shown is for ratio of a wall temperature

to total temperature of 0.5 and a Prandtl number of 0.7.) Good agreement between experimental and calculated values was obtained in reference 6 for a Mach number of 4.6 and $R_b/\bar{w} \approx 17.5$ by use of this method.

A more detailed method for finding the stagnation point velocity gradient is presented in reference 36, where the Belotserkovskii strip integral method (based on refs. 54 to 56) is used. The velocity gradient is found to be a function of jet Mach number, specific heat ratio, and jet shock standoff distance. However, it was shown in reference 57 that results obtained by use of this method are in error for the low jet Mach numbers $\left(M_j < 2.5\right)$ which were encountered in the present study.

The velocity gradient used in the present investigation is obtained from an analogy similar to that of reference 6. Even though in reality the jet is impinging on a plane surface when compared with the jet size $\left(R_b/\bar{w} \gg 1\right)$, the stagnation velocity gradient can be approximated by the gradient on a small sphere "jet body" immersed in a supersonic flow field of height equal to the jet width. The flow model of the jet impingement region is shown in figure 10. Flow conditions upstream of the jet bow shock (for example, in region 7 or 8) are known from the previous flow analysis once the jet bow shock location is specified. Inclination of the jet α_j is assumed to be normal to the wall on the basis of experimental data. The jet bow shock is assumed to be a circular arc of radius R_c. (See ref. 36.) The orientation of the sonic line relative to the wall and the jet boundary as shown in figure 10 is based on information in references 57 and 58 for $M_j < 2.8$ at $\gamma = 1.4$. Equation (6) is used to calculate the velocity gradient for a specified jet velocity u_j and Mach number M_j depending on the region containing the bow shock. The jet-body radius in this case $R_{b,j}$ is computed by using a value of $\delta_{j,s}/\bar{w}$; the calculated width $\bar{w}$ for a given region, and correlations of $\delta_{j,s}/R_{b,j}$ as a function of inverse jet normal shock density ratios obtained from reference 59. An approximate value of $\delta_{j,s}/\bar{w} = 0.45$ was used for calculated jet Mach numbers from 1.2 to 2.5 at $\gamma = 1.4$. This value of $\delta_{j,s}/\bar{w}$ seems to be realistic when compared with calculated values given in reference 56 to normal impingement and jet Mach numbers from 3 to 5. Also, the present schlieren data and data from reference 6 verify this value (0.45) for $\delta_{j,s}/\bar{w}$. Therefore, the velocity gradient at the jet stagnation point is calculated once the necessary quantities are known for the given region that includes the jet bow shock.

A sample calculation of the velocity gradient for the jet bow shock located in region 8 for $M_\infty = 6$ and $\gamma = 1.4$ follows. The calculated jet width, jet velocity, and Mach number ahead of the jet bow shock in region 8 are 0.701 mm, 562.02 m/sec, and 1.53, respectively. The jet bow shock standoff distance $\delta_{j,s}$ is

$$\delta_{j,s} = \left(\frac{\delta_{j,s}}{\bar{w}}\right)\bar{w} = 0.315 \text{ mm}$$

where $\dfrac{\delta_{j,s}}{\overline{w}} = 0.45$. A value of $\dfrac{\delta_{j,s}}{R_{b,j}} = 0.54$ is found in figure 17 of reference 59 by using the inverse normal shock density ratio for $M_j = 1.53$. Then the radius of the jet body is

$$R_{b,j} = \frac{\delta_{j,s}}{\delta_{j,s}/R_{b,j}} = 0.584 \text{ mm}$$

Finally, the velocity gradient is obtained from equation (6) modified for jet nomenclature

$$\left(\frac{du_w}{ds}\right)_{stag} = \frac{u_j}{R_{b,j}} \left\{ \frac{\gamma - 1}{\gamma}\left[1 + \frac{2}{(\gamma - 1)M_j^{\,2}}\right]\left(1 - \frac{1}{\gamma M_j^{\,2}}\right)\right\}^{0.5} = 7.631 \times 10^5 \text{ per second}$$

The peak heating rate for a given region is calculated by using equation (5) and the calculated flow condition and velocity gradient for that region. In the present study, equations (5) and (6) are also used to calculate the reference stagnation heating on the hemispheric model. The reference pressure is the hemisphere stagnation pressure. It was stated in reference 6 that the peak heating is directly proportional to the square root of the jet width $\overline{w}$ which, in turn, is dependent on the measured displaced shock length L_{SH} (fig. 7) as a scale length. A simplified method that would give this length as a function of free-stream conditions and body geometry would relieve the present method from its dependence on experimental measurements of L_{SH} and $\delta_{j,s}/\overline{w}$. Other phenomena that may influence the peak heating, but are not considered in the present study, are the type and growth of the shear layers bounding the jet and jet turbulence. (See ref. 6.)

Type V Interference

Type V interference involves the intersection of two oblique shocks of the same family which occurs just above the upper sonic point as illustrated in figures 2 and 11. Type V is analogous to type II with the exception that a thin jet appears at the shock intersection at point A instead of a shear layer and the impinging shock directly influences the flow upstream of the model. The actual increase in pressure and heat transfer on the surface is a result of the shock from point B interacting with the boundary layer. The small jet from point A and the shear layer emanating from the triple point at B (fig. 11) converge as the subsonic flow in region 4 accelerates to sonic velocity. Both the jet and shear layer intermix and may graze the surface and thus cause some increase in heating. (See ref. 6.) Flow conditions and the pressure and heat-transfer rise across

the shock—boundary-layer interaction in the supersonic regions near the body are calculated by use of the same procedure as discussed for type II and equation (1) for plane surfaces.

In the present investigation the type V interference pattern was observed on a swept cylindrical leading-edge fin. The pressure rise across the shock—boundary-layer interaction was calculated by using the tangent-cone approximation discussed for type III and the heating rise was calculated by use of equation (1). The undisturbed or reference values used in this case were the laminar stagnation-line pressure and heat transfer on a cylinder. (See ref. 60.)

Type VI Interference

The supersonic flow pattern for type VI interference shown in figure 12 consists of the intersection of two weak shocks of the same family and results in a weak bow shock. A shear layer and an expansion fan (that interacts with the boundary layer) are also formed at the intersection (point A). The interaction at the surface results in a local decrease in pressure and heating. (See ref. 61.)

The flow conditions in region 3 are determined by using the oblique shock relations and the specified free-stream conditions and flow angle in a manner similar to that for type I. Once θ_b is specified, the flow in region 4 is calculated. An iterative scheme is used to determine the location of the coalesced bow shock that separates regions 1 and 2 to satisfy continuity of the pressures and flow direction across the shear layer between regions 2 and 5. The flow from region 4 must pass through the expansion fan to turn parallel to the shear layer. The relations for a Prandtl-Meyer expansion from reference 40 are used in this iteration to go from region 4 to region 5. In order to turn parallel with the surface, the flow passes through a series of weak reflected expansion waves in going from region 5 to region 6. The total reduction in pressure from region 4 to region 6 is twice the decrease across the first expansion fan for low Mach numbers and small turning angles (ref. 42, p. 451).

The heat-transfer relation (eq. (1)) is used to calculate the reduction in heating by using p_6/p_4. This procedure is justified since it has been shown in reference 61 that this equation gives a good prediction of the heating reduction for turbulent interactions. A comparison of type VI laminar data from the present investigation with the correlation in reference 38 indicates that the same justification may be used for laminar interactions. The reference values in the present study are the undisturbed values ahead of the interaction on a wedge.

COMPARISON OF CALCULATED AND EXPERIMENTAL RESULTS

In this section typical examples of experimental center-line pressure and heat-transfer distributions, primarily peak values, are compared with calculated levels for the six types of interference patterns. Flow-visualization photographs are presented to indicate the type of interference and details of the flow field. Experimental models used in this investigation included hemispheres, a cylindrical leading-edge fin, and a 30° wedge. Surface static pressures were measured by using conventional electrical strain-gage transducers and heat-transfer coefficients were obtained by use of the phase-change coating technique. In the interest of clarity, details concerning the models, test conditions, and experimental techniques are discussed in the experimental study along with tabulations and plots of experimental data not shown in the analysis. In general, the discussion presented in this section also covers the experimental results. The pressure and heat-transfer data are presented in nondimensional form, stagnation-point values $\left(p_{stag} \text{ and } Q_{stag}\right)$ being used for the hemisphere data. Stagnation-line pressure and heat-transfer values $\left(p_{cyl} \text{ and } Q_{cyl}\right)$ are used for the fin data. The reference pressure for the wedge p_{wedge} is the calculated wedge value without interference. Reference heating for the wedge Q_{wedge} is arbitrarily chosen as the local laminar value at the midpoint of the wedge (X = 0.5) with the exception of type VI where the reference value is taken as the maximum measured wedge value ahead of the interaction.

Type I Interference

Type I interferences on the 30° wedge at $\alpha = 0^O$ (wedge center line parallel with flow) for $\theta_i = 10^O$ and $\theta_i = 15^O$ are shown in figures 13 and 14, respectively. Measured peak pressure for both shock generator angles θ_i is approximately 10 to 15 percent higher than the calculated value. This difference is probably due to the extensive separation of the laminar boundary layer on the wedge (caused by the shock—boundary-layer interaction) and the resulting complex shock system which allows a greater pressure recovery than the nonseparated case). Differences between the measured and calculated peak heating levels are probably also influenced by the separated flow.

Type II Interference

An example of a type II interference pattern on the 30° wedge at $\alpha = 25^O$ and $\theta_i = 15^O$ is presented in figure 15. The reflected shock that occurs at the upper triple point in the bow shock interacts with the wedge boundary layer and causes the increase in pressure and heat transfer. A region of transonic flow exists behind the reflected shock between the surface and the shear layer. (See, for example, refs. 32 and 33.) Calculated peak pressure levels shown in figure 15 are obtained by assuming (1) a Mach

reflection with a normal shock loss at the wall (upper line) and (2) the pressure rise for an attached shock corresponding to the upstream Mach number M_2. A pressure spike was not measured, evidently because of the finite pressure tap spacing since the measured value should have occurred between the two calculated levels. The peak heat-transfer level was underpredicted.

Type III Interference

Examples of type III interference on a 0.051-meter-diameter hemisphere at Mach 6 with $\theta_i = 14.8^\circ$ are shown in figures 16 and 17. The basic difference between these two examples is that the shear layer attaches at a lower point in figure 17 than in figure 16. The measured pressure peaks are underpredicted approximately 15 percent probably because of viscous effects (shear layer deflection and growth and three-dimensional flow). As expected, heating peaks, in general, are underpredicted approximately 50 to 65 percent by use of the constants of reference 50. Better agreement is obtained by using the constants from the correlation of reference 38 (based upon the present data) and the calculated laminar and turbulent shear layer thicknesses. The maximum heating amplification measured in this study for a type III interference (14 times stagnation heating) is shown in figure 16(c).

Typical results of tests conducted in the other three facilities with a 0.025-meter-diameter hemisphere are presented in figures 18 to 20. The type of interference was determined from the location of the shock intersection and the shape of the peaks. In general, the agreement between measured and calculated pressure and heat-transfer peaks was not as good as that for the Mach 6 results, probably because of errors incurred in measuring parameters from photographs and the finite pressure tap spacing (10°) on the model. Viscous effects, in addition to these reasons, may explain the poor agreement in the nitrogen tests. (See fig. 18.) Flow condensation due to a low stagnation temperature may have influenced the pressure measurements in the CF_4 facility. A good indication of how the surface flow is affected by an attaching shear layer can be seen in figure 20(c).

Type IV Interference

Since the type IV interference results in the most severe heating (ref. 6), an extensive investigation was conducted by using the 0.051-meter-diameter hemisphere, the 30° wedge, and the fin model in the Mach 6 air tunnel. Additional tests were conducted with the 0.025-meter-diameter hemisphere in the other facilities.

Typical examples of type IV interference on the 0.051-meter-diameter hemisphere at Mach 6 for $\theta_i = 5^\circ$, 10°, and 15° are shown in figures 21 to 23. Jet impingement

18

occurs between 20° and 30° below the axis of the hemisphere with nearly normal impinge-ment. In general, calculations based on conditions in regions 7 and 8 and the measured value at $\dfrac{\delta_{j,s}}{\overline{w}} = 0.45$ bracket the measured peak pressure and heat transfer. Compar-isons of the measured and calculated (no interference) pressures and heat-transfer dis-tributions on the hemisphere indicate the strong influence of the jet flow along the surface.

Results in helium at Mach 20.2 and nitrogen at Mach 19.8 obtained on the 0.025-meter-diameter hemisphere are presented in figures 24 and 25. Agreement between the measured and calculated peak values was not as good as the Mach 6 results, large differences occurring in the nitrogen tests. Better agreement would probably result if the proper values of $\delta_{j,s}/\overline{w}$ were known for each gas. Oblique jet impingement and shear layer growth could also explain the lower measured peak values. However, the predicted values provide conservative estimates.

Comparisons of measured and calculated values on the 30° wedge at $\alpha = 50.3^O$ and at Mach 6 are presented in figure 26. Good agreement exists between the pressure results whereas the heating peak is underpredicted. The high measured heating peak may be the result of turbulent jet impingement. (See ref. 6.)

An example of a type IVa interference (grazing jet) on the unswept cylindrical fin at Mach 6 is shown in figure 27. The plane of symmetry of the fin and the leading edge of the shock generator are perpendicular. In this case the supersonic jet curls upward because of the higher pressure differential across the jet than that encountered on the hemisphere or wedge. The peaks and dips observed in the pressure and heat transfer are the result of shocks and expansions in the grazing jet interacting with the fin boundary layer. Agreement between the data and the calculated stagnation line values on the lower part of the fin is only fair, probably because of the curved bow shock.

Type V Interference

A type V interference pattern occurred on the cylindrical fin when it was swept back 25° (center line at 65° to free-stream flow) as shown in figure 28. Good agreement between measured and calculated heating peaks was obtained for all type V tests. Since the fin bow shock was detached, the predicted heating value was calculated by use of the measured bow shock angle β_3 below the shock intersection and the maximum angle θ_6 for a regular shock reflection at the wall. The secondary heating peak occurring near $X = 0.6$ is a result of the thinning of the boundary layer by the grazing jet and shear layer.

Type VI Interference

An example of type VI interference on the upper surface of the 30° wedge is shown in figure 29. The theoretical pressure reduction from the expansion-fan impingement agrees well with the experimental level. Although equation (1) was developed for shock—boundary-layer interactions, the use of the laminar form and the calculated pressure reduction gives a good indication of the amount of local heat-transfer reduction. The reason for the first dip in the heating distribution is unknown. Unlike the other wedge data, the reference heating is taken as the maximum measured value ahead of the interaction.

Summary of Comparisons of Calculated and Experimental Data

In summary, for most cases calculations made for the different types of interference were in fair to good agreement with measured peak values for gases where real-gas effects are negligible and good flow-visualization photographs were available. (See table II.)

Empirical Inputs for Methods of Prediction

The main problem that exists in using these local two-dimensional methods is their dependency on measurements (see table III) from flow-visualization photographs or other empirical sources. These inputs along with the specified upstream flow conditions, surface geometry, and pressure and heat-transfer distributions without interference can be used to calculate interference heating on complex configurations. Other problem areas include the effects of (1) shear layer growth, (2) oblique jet impingement, (3) jet bow shock standoff distance, (4) gas chemistry, and (5) three-dimensional flow on interference heating.

TABLE II.- SUMMARY OF COMPARISONS OF CALCULATED

AND EXPERIMENTAL DATA

Type of interference	Test conditions	Pressure amplification		Heat-transfer amplification	
		Calculated	Experimental	Calculated	Experimental
I (with separation)	$M_\infty = 6.0$; $\gamma = 1.40$; $\theta_i = 10^\circ$; 30° wedge	5.6	6.5	Laminar, 8.5 Turbulent, 13.5	14.8
I (with separation)	$M_\infty = 6.0$; $\gamma = 1.40$; $\theta_i = 15^\circ$; 30° wedge	10.2	11.7	Laminar, 18.8	11.5
II	$M_\infty = 6.0$; $\gamma = 1.40$; $\theta_i = 15^\circ$; 30° wedge	[a]1.5	1.5	Laminar, [a]2.4	3.3
III	$M_\infty = 6.0$; $\gamma = 1.40$; $\theta_i = 15^\circ$; 0.051-m-diameter hemisphere	3.5	4.2	Turbulent, 13.4	13.9
III	$M_\infty = 20.2$; $\gamma = 1.67$; $\theta_i = 10^\circ$; 0.025-m-diameter hemisphere	6.3	7.2	Laminar, 7.4	8.2
III	$M_\infty = 19.9$; $\gamma = 1.40$; $\theta_i = 15^\circ$; 0.025-m-diameter hemisphere	8.3	4.5	Laminar, 10.2	5.9
IV	$M_\infty = 6.0$; $\gamma = 1.40$; $\theta_i = 14.8^\circ$; 0.051-m-diameter hemisphere	[b]8.4 [b]8.3	7.5 6.5	[b]14.4 [b]16.2	14.2 16.8
IV	$M_\infty = 20.2$; $\gamma = 1.67$; $\theta_i = 5^\circ$; 0.025-m-diameter hemisphere	[b]9.9	5.4	[b]16.5	5.7
IV	$M_\infty = 19.8$; $\gamma = 1.40$; $\theta_i = 10^\circ$; 0.025-m-diameter hemisphere	[b]36.9	4.3	[b]62.5	6.4
IV	$M_\infty = 6.0$; $\gamma = 1.40$; $\theta_i = 15^\circ$; 30° wedge	[b]8.5	7.5	[b]14.0	19.4
V	$M_\infty = 6.0$; $\gamma = 1.40$; $\theta_i = 20^\circ$; cylindrical fin	4.6	2.5	Turbulent, 3.9	3.6
VI	$M_\infty = 6.0$; $\gamma = 1.40$; $\theta_i = 5^\circ$; 30° wedge	21-percent reduction	20-percent reduction	22-percent reduction	14-percent reduction

[a]Regular shock reflection.
[b]Jet bow shock in region 8, figure 7.

TABLE III.- EMPIRICAL INPUTS FOR VARIOUS TYPES OF INTERFERENCE

Type of interference	Empirical input
I	(1) Impinging and bow shock angles at intersection (2) Impingement location on surface (sphere, wedge, fin, etc.)
II	(1) Impinging and bow shock angles at intersection (2) Impingement location on surface (sphere, wedge, fin, etc.)
III	(1) Impinging and bow shock angles at intersection (2) Shock displacement length or shear layer length for computing thickness of shear layer at surface (3) Shear layer angle relative to local body slope
IV	(1) Impinging and bow shock angles at intersection (2) Shock displacement length or shear layer length for computing jet coordinates and width (3) Ratio of jet bow shock standoff distance to jet width
V	(1) Impinging and bow shock angles at intersection (2) Impingement location on surface (sphere, wedge, fin, etc.)
VI	(1) Impinging and bow shock angles at intersection (2) Impingement location on surface (sphere, wedge, fin, etc.)

PARAMETRIC STUDY USING COMPUTATIONAL METHODS

Calculations were carried out for each type of shock interference at a variety of flow conditions to determine the dependence of peak pressure and heating on the specific heat ratio γ, free-stream Mach number M_∞, and impinging shock strength (shock generator angle θ_i). Body angle θ_b, shear layer angle $\bar{\theta}_s$, and shock displacement length L_{SH} were also varied to determine their effect on the peaks for some types of interference. The free-stream total conditions and wall temperature remained fixed for all types. These calculations were made by assuming impingement on a wedge at $X_i = 0.305$ meter for types I, II, V, and VI and on a 0.305-meter-diameter sphere for types III and IV. The heating results were calculated by use of a recovery factor of $(N_{Pr})^{0.5}$ for laminar and $(N_{Pr})^{0.33}$ for turbulent $(N_{Pr} = 0.72)$. Also these calculations are based on ideal gas relations and do not account for real-gas effects.

Type I Interference

The results of a parameter variation study for type I interference are presented in figures 30 and 31 for laminar and turbulent boundary layers with a fixed impingement location and body angle. Figure 30 presents the variation of pressure and heat-transfer amplification with shock generator angle for several free-stream Mach numbers and specific heat ratios. Both the pressure and heat-transfer amplification increase with increasing impinging shock strength and free-stream Mach number until the transition from a regular reflection to a Mach reflection takes place. Beyond this point the amplification remains constant until the beginning of a type II interference. For a given Mach number and θ_i, the amplification decreases with increasing γ. The high heat-transfer amplification for the laminar case (fig. 30(b)) is the result of the low heating rates ahead of the shock—boundary-layer interaction Q_2 for $X_i = 0.305$ meter. Figure 31 shows that the amplification decreases with increasing body angle for the case of a regular shock reflection and for a fixed M_∞, γ, and θ_i. The reason for this decrease is that the reflected shock becomes weaker with increasing θ_b and thus results in a lower pressure rise from region 2 to region 6.

Type II Interference

The variation of the pressure and heat-transfer (laminar and turbulent) amplification with body angle is shown in figure 32 for a type II interference at several values of M_∞ and γ for a regular shock reflection. Calculations of the flow near the wedge are independent of θ_i. The amplification decreases with increasing body angles and specific heat ratio for the same reason as type I. For a given θ_b, the amplification also increases with Mach number.

Type III Interference

Pressure and laminar and turbulent heat-transfer amplification as a function of shock generator angle are shown in figure 33 for attaching shear layers. The shock displacement length L_{SH} and shear layer angle $\bar{\theta}_5$ are fixed. Heat-transfer peak calculations are based on constants from reference 38 as discussed previously. The maximum amplification occurs between $\theta_i = 10^\circ$ to $\theta_i = 20^\circ$ depending on the Mach number and γ. The pressure amplification increases and the heat-transfer amplification decreases with increasing Mach number for a given θ_i and γ. Actually, the heating amplification will follow the same trend as the pressure. (See ref. 6.) This reverse trend for the heating in the present study is the result of using constant total pressure and temperature for M_∞ and γ instead of varying these conditions for each M_∞ and γ. For a given θ_i and M_∞, the amplifications decrease with increasing γ. The variation of the stagnation reference values with M_∞ and γ is shown in figure 34.

The effects of variations in shear layer angle and shock displacement length (shear layer thickness) on the pressure and heat-transfer amplifications for $M_\infty = 10$ and $\gamma = 1.4$ are shown in figures 35 and 36, respectively.

Type IV Interference

The variation of the pressure and heating amplification with the shock generator angle for an impinging laminar jet is presented in figure 37 for a constant shock displacement length. These calculations are made by assuming the jet bow shock in region 8, $\dfrac{\delta_{j,s}}{w} = 0.45$, and jet impingement normal to the wall. Both the pressure and heat-transfer amplifications increase with increasing Mach number for a given θ_i, a maximum occurring between $\theta_i = 10^O$ and $\theta_i = 20^O$, whereas the amplification decreases with increasing γ for a given M_∞ and θ_i. The large increases in pressure and heating amplification at different γ values are primarily due to the decrease in reference values shown in figure 34. The reduction in heating due to increasing the shock displacement length (or jet scale length) is shown in figure 38.

Type V Interference

The pressure and heat-transfer amplification as a function of θ_i is presented in figure 39 for a regular shock reflection at the wall. Both the pressures and heating amplification increase with increasing θ_i and M_∞. At a constant M_∞ and θ_i, the amplification decreases with an increase in γ. The effect of increasing body angle on the amplification is shown in figure 40.

Type VI Interference

Pressure and heat-transfer reduction rates as a function of θ_i for an expansion-fan—boundary-layer interaction (laminar and turbulent) are shown in figure 41. The largest reduction occurs between $\theta_i = 7^O$ and $\theta_i = 9^O$. For a given θ_i the amount of reduction becomes larger with increasing Mach number, whereas for a given M_∞ and θ_i the reduction is lower for an increase in γ.

EXPERIMENTAL STUDY

OBJECTIVE

The objective of the experimental phase of the study was to determine the type of interference pattern generated for a given shock configuration and to investigate the effects of Mach number, unit Reynolds number, specific heat ratio, and strength of the impinging shock on the center-line peak pressure and heat transfer on basic shapes.

APPARATUS AND TEST CONDITIONS

Test Facilities

A brief outline of the tunnels used in this study is presented in table IV:

TABLE IV.- TEST FACILITIES

Facility	Test gas	γ	M_∞	$\left(p_{t,\infty}\right)_{max}$, N/cm^2	$\left(T_{t,\infty}\right)_{max}$, K	Facility description in reference
Langley 20-inch Mach 6 tunnel	Air	1.40	6	362	561	62
Langley 22-inch helium tunnel	Helium	1.67	20	2069	533	63
Langley hypersonic nitrogen tunnel	Nitrogen	1.40	19	6895	2222	64 and 65
Pilot CF$_4$ facility at the Langley Research Center	Tetrafluoromethane $\left(CF_4\right)$	*1.27	*8.9	2000	500	66

*M_∞ and γ are effective values calculated by using the method of reference 66. At $T_{t,\infty} = 291$ K some flow condensation was present.

Models

The experimental setup shown in figure 42(a) was designed to use interchangeable models and was employed in the Mach 6 air, Mach 20 helium, and Mach 19 nitrogen tests. A slightly different arrangement was used for the pressure test in the smaller scale CF$_4$ facility. (See fig. 42(b).)

The interchangeable models included a 0.025-meter-diameter hemisphere, a 0.051-meter-diameter hemisphere, a 0.025-meter-diameter cylindrical leading-edge fin, and a 30° included angle wedge. Both pressure and heat-transfer models were constructed for each configuration. Pressure models were constructed of stainless steel and the heat-transfer models were constructed of silica base epoxy material. Solid stainless-steel (type 347) heat-transfer models were also used to measure peak heating in some facilities. Sketches of the models showing the center-line pressure tap locations are in figure 43.

The thermophysical properties (specific heat, thermal conductivity, and density) were measured on samples of material for each heat-transfer model. The value of $\sqrt{\rho c k}$ used was approximately $1.80 \frac{kW\text{-sec}^{1/2}}{m^2}$ for the epoxy models and $7.26 \frac{kW\text{-sec}^{1/2}}{m^2}$ for the stainless-steel models.

Test Parameters

A summary of the models used, type of test, nominal flow conditions, and types of interference patterns studied is presented in table V.

TABLE V.- SUMMARY OF TEST PARAMETERS

Test	Model	Type of test	Shock generator angles and plate size	M_∞	γ	$p_{t,\infty}$, N/cm^2	$T_{t,\infty}$, K	$N_{Re,\infty}/m$	Types of interference
6344	0.051-m-diameter hemisphere	Pressure and schlieren	5° (5°) 30° 0.152 m × 0.254 m	6	1.40	83 290	478	7.9×10^6 25.6×10^6	III and IV
6352	0.051-m-diameter hemisphere	Heat transfer	5° (5°) 25° 0.152 m × 0.254 m	6	1.40	83 290	478	7.9×10^6 25.6×10^6	III and IV
6358	Fin 30° wedge	Pressure and schlieren	5° (5°) 25° 0.152 m × 0.254 m	6	1.40	83, 290 290	478	7.9×10^6 25.6×10^6 25.6×10^6	IV, V I, II, VI
6363	0.051-m-diameter hemisphere, fin, 30° wedge	Heat transfer	5° (5°) 25° 0.152 m × 0.254 m	6	1.40	290 83, 290 290	478	25.6×10^6 7.9×10^6 25.6×10^6	III, IV IV, V I, II, VI
357	0.025-m-diameter hemisphere	Pressure and schlieren	5° (5°) 15° 0.152 m × 0.254 m	20	1.67	690	433	9.8×10^6	III and IV
373	0.025-m-diameter hemisphere	Heat transfer	5° (5°) 15° 0.152 m × 0.254 m	20	1.67	690	433	9.8×10^6	III and IV
16	0.025-m-diameter hemisphere	Pressure, heat transfer, and electronic beam	5° (5°) 15° 0.152 m × 0.254 m	19	1.40	4137 to 4482	1644	3.0×10^6	III and IV
63	0.025-m-diameter hemisphere	Pressure, shadowgraph, and oil flow	5° (5°) 15° 0.051 m × 0.089 m	8.9	1.27	896 to 1034	292	5.6×10^6	III and IV

EXPERIMENTAL TECHNIQUES AND DATA ACCURACY

The method of testing used in all facilities was to measure the center-line pressure distribution on the model and at the same time photograph the shock patterns by use of schlieren, shadowgraph, or electron-beam techniques. The hemispheric model position relative to the impinging shock was varied vertically while the shock generator angle remained fixed. The hemisphere was moved in small increments to measure as close as possible the peak pressure and to form various shock interference patterns. The fin model was mounted vertically and positioned so that impingement occurred at approximately the same location on the model for both the unswept (0°) and swept (25°) cases. Various types of interference flows were studied with the 30° wedge by varying the wedge angle of attack. Conditions for the heat-transfer runs were selected after evaluating the pressure and flow-visualization data.

Pressure Tests

Conventional wind-tunnel pressure-measuring techniques were used for all tests. Electrical strain-gage pressure transducers were used for model static, tunnel free-stream pitot, and tunnel stagnation pressure measurements.

All pressure transducers were calibrated to an accuracy of 0.25 percent of full scale. Based on this calibration accuracy and the repeatability of data, the pressure ratios measured in air and helium have a maximum deviation of ±0.08. The maximum deviations in the nitrogen and CF_4 tests are somewhat greater. The reason for this deviation is that the models were instrumented primarily to measure the peak value and not the lower pressures on the undisturbed regions of the model.

Heat-Transfer Tests

The heat-transfer tests were conducted by using the phase-change coating technique and methods described in reference 67. Because of the highly nonuniform heat-transfer distribution on the models, some models were tested with two or more temperature coatings. In some cases, peak heating was so high that the coating needed was near T_{aw}; thus, short melt times and the possibility of large errors were indicated. To measure these peaks, the stainless-steel model with its large value of $\sqrt{\rho c k}$ was used. This procedure permitted the use of a lower melt temperature coating and resulted in longer melt times.

Heat-transfer data are subject to numerous and often large sources of error. Errors in measuring the thermophysical properties of the model material, the melt temperatures and times, the initial model wall temperature, and the initial time at exposure to the free stream can affect the accuracy of the heat-transfer data. A very important

source of error in most heat-transfer tests is in determining the adiabatic wall temperature distribution. For the present test, T_{aw} was assumed to be equal to the freestream total temperature, since it is very difficult to determine the adiabatic wall temperature in such complex flow patterns as occur in shock interference regions. An analysis of these combined errors indicates that the peak heating ratios measured at Mach 6 in air may have a maximum error of about 29 percent (25 percent at Mach 20 in helium). The errors in the heat-transfer data in other areas will be less. Inaccuracies due to errors in T_{aw}, T_m, and T_{init} would be less in the nitrogen tests since $T_{t,\infty}$ was higher.

A semi-infinite slab solution of the general heat conduction equation is used to reduce the heating data. (See ref. 67.) In order for this assumption to be valid, the radius of curvature must be much greater than the depth of heat penetration (ref. 67). As stated in reference 68, the heat-penetration depth for the semi-infinite slab is approximately independent of the aerodynamic heat-transfer coefficient and depends only on the thermal diffusivity of the wall material and the thermal diffusion time. The minimum distance from peak heating for which the semi-infinite slab solution is valid can also be determined by using the melt time. (See ref. 68.) The expression for this distance is shown in figure 44 for Mach 6 test conditions. For example, for a heating amplification of 10 at a melt temperature of 394 K, the minimum distance over the body diameter is 0.0084. Although this method does not account for lateral conduction errors, this figure does indicate where these errors can occur.

Flow Visualization

Schlieren, shadowgraph, or electron-beam photographs were taken in all tests. For the Mach 6 air and the Mach 20 helium tests, details of the interference region were observed by using the schlieren technique. The electron-beam flow-visualization technique described in reference 69 was used in the Mach 19 nitrogen tunnel. Shadowgraphs using nonparallel light were obtained in the CF_4 tests. Oil-flow patterns were also made in this facility with the use of a mixture of titanium dioxide and silicon oil.

The best flow-visualization photographs were obtained in the Mach 6 air facility. Details observed in the Mach 6 photographs were used to determine the type of interference from photographs taken in the lower density facilities.

PRESENTATION OF EXPERIMENTAL RESULTS

Pressure and heat-transfer data not included in the analysis are presented as data plots (see table VI) or in tabular form. Tabulations of the test flow conditions, reference pressures, and lengths measured from flow-visualization photographs for all pressure

tests are given in table VII. These lengths include the shock displacement length L_{SH} and the coordinates x_i, y_i of the intersection of the impinging shock and the heimsphere bow shock. All lengths have been nondimensionalized with respect to the hemisphere nose radius R_b. Wall temperatures $\left(T_w = T_m\right)$, reference heat-transfer rates, and model material are presented in table VIII for all heat-transfer tests. Peak heating values measured in the Mach 19 nitrogen tunnel (test 16) are also presented in table VIII(d). Pressure data not plotted are given in table IX in nondimensional form. The reference pressure for the hemisphere tests is the stagnation pressure on the nose or the free-stream pitot pressure p_{stag}. On the fin the calculated stagnation-line value on the cylindrical leading edge p_{cyl} is used. The wedge reference pressure p_{wedge} is the calculated value on the wedge without interference with the exception of the $\alpha = 50^{\circ}$ case where the measured free-stream pitot pressure is used. The reference heating for the hemisphere Q_{stag} is calculated by using equations (5) and (6). (See ref. 51.) Stagnation-line values Q_{cyl} obtained from an expression in reference 60 are used for the cylindrical fin. The reference heating for the wedge Q_{wedge} was calculated by using an expression in reference 49 and was arbitrarily chosen as the value at the midpoint of the wedge (X = 0.5). Tables VII to IX are presented before the figures.

The plotted data (figs. 45 to 79) are grouped by configuration, Mach number, specific heat ratio, and type of interference as outlined in table VI.

Calculated peak pressure and heat-transfer levels obtained from the analytical methods are shown in the figures for comparative purposes. The dashed curves shown on the hemisphere figures (figs. 45 to 57, 69 to 79) are the pressure (modified Newtonian) and laminar heat-transfer distributions without interference and the solid curves are data fairings. Undisturbed pressure and heat-transfer levels (dashed lines in figs. 58 to 67) for the cylindrical fin were calculated by use of the stagnation-line expressions in reference 60 by assuming that the bow shock is parallel with the leading edge. The pressure calculation shown in figure 68(a) are the total and static pressures behind a normal shock.

TABLE VI.- INDEX TO PRESSURE AND HEAT-TRANSFER FIGURES

Figure	Model	M_∞	γ	Test gas	θ_i, deg	Type of interference
45	0.051-m-diameter hemisphere	5.94	1.40	Air	0	No interference
46	↓	↓	↓	↓	10	III
47					15	↓
48					20	
49					25	↓
50					5	IV
51					10	
52					15	
53					15	
54					20	
55		↓			25	
56		6.00			10	
57	↓	6.00			20	↓
58	Cylindrical fin	5.94			10	IVa
59		↓			15	
60		20			20	
61		6.00			10	
62		6.00			15	↓
63		5.94			10	V
64		5.94			15	
65		5.94			20	
66		6.00			10	
67	↓	↓			15	↓
68	30° wedge	↓	↓	↓	0	No interference
69	0.025-m-diameter hemisphere	20.20	1.67	Helium	0	No interference
70		↓	↓	↓	5	III
71					10	
72					15	
73		↓	↓	↓	15	↓
74		19.70	1.40	Nitrogen	0	No interference
75		20.60	↓	↓	10	III
76		20.20	↓	↓	15	IV
77		8.90	1.27	CF_4	0	No interference
78	↓	↓	↓	↓	10	III
79	↓	↓	↓	↓	15	III

CONCLUDING REMARKS

An extensive analytical and experimental study of shock-interference heating has been conducted on simple shapes. This study covered a wide range of free-stream Mach numbers, specific heating ratios, Reynolds numbers, and location and strength of the impinging shock.

In most cases, calculations based on semiempirical methods developed in the present paper gave reasonable estimates of the measured peak pressures and heating for the six types of interferences (for test gases where real-gas effects are negligible). Correlations of pressure and heat transfer based on previous studies gave fair estimates of the heating levels for shock—boundary-layer interactions (types I, II, and V interferences). Correlations of the present data indicate that heating levels for attaching shear layers (type III interference) are from 50 to 65 percent higher than the peak heating for reattaching separated boundary layers. Calculations for peak heating due to an impinging supersonic jet (type IV interference) were made by assuming that the flow is analogous to the stagnation heating on a small sphere submerged in the jet flow.

The highest experimental pressure and heating amplification were obtained in the Mach 6 air investigations (along with good-quality flow-visualization photographs). Amplification factors up to 11.7 and 14.8 times the undisturbed wedge pressure and laminar heating, respectively, were measured for shock—boundary-layer interactions. Peak heating 13.9 times the laminar stagnation point value was measured on a 0.051-meter-diameter hemisphere for the shear layer attachment. Peak pressures 7.5 times the free-stream pitot pressure and peak heating 16.8 times the stagnation point heating were measured on the hemisphere for the supersonic jet impingement. Pressure and heating reductions of approximately 20 and 14 percent of the wedge values ahead of the disturbance occurred for the expansion-fan—boundary-layer interaction (type VI interference). Results of the investigation conducted in the other facilities were affected by the limitations of the flow-visualization techniques and the smaller model size.

The theoretical parametric study showed that shock interference heating is strongly influenced by free-stream Mach number, specific heat ratio, impinging shock strength, and model geometry. In general, pressure and heat-transfer amplification for shock—boundary-layer interactions increase with increasing Mach number and shock strength and decrease with increasing specific heat ratio. For a fixed Mach number, specific heat ratio, and shock strength, the amplification decreases with increasing body angle. Pressure amplification for shear layer attachment increases with increasing Mach number whereas the heating decreases. This condition is primarily a result of the magnitude of the actual peaks and the reference values used. Both the pressure and heat-transfer amplification increase with increasing Mach number and decrease with

31

increasing specific heat ratio for jet impingement. These results indicate that because of real-gas effects, interference heating on the actual flight vehicle may be considerably higher than that measured in a wind tunnel.

The present methods of predicting peak heating are dependent on length scale measurements from flow-visualization data. Semiempirical methods are needed to relax this requirement. Other problem areas that require considerable investigations are the effects of shear layer growth, oblique jet impingement, and jet bow shock standoff distance as well as gas chemistry and three-dimensional flow on shock interference heating.

Langley Research Center,
National Aeronautics and Space Administration,
Hampton, Va., January 22, 1973.

APPENDIX

INTERFERENCE HEATING ON A TYPICAL SPACE

SHUTTLE CONFIGURATION

A limited analysis of heating along a typical space shuttle ascent trajectory indicates that interference heating can occur in several locations on a mated shuttle configuration as illustrated in figure 80. Depending on the relative positions of the bodies, the free-stream conditions, and the angle of attack, one or more of the six types of interference may appear on the nose of the orbiter, between the fuel tank and the orbiter, and between the fuel tank and the rocket motors. Heating due to interfering shocks may also appear on the leading edge of wings and control surfaces depending on the amount of sweep. An example of how the type of interference pattern and its location can vary on the nose sections of a mated configuration is illustrated in figure 81 for a typical shuttle ascent trajectory. Initially, there will be little or no shock interference between the bodies. As the vehicle accelerates, type V or type VI interference appears on the upper surface of the orbiter. With further increase in Mach number, the shock interaction moves downward on the nose of the orbiter and types IV and III interferences will develop. Here the largest heating will develop as shown in the present study. A further increase in Mach number leads to a type II and finally a type I pattern. The reflected shocks can reflect back and forth several times in the region between the bodies to produce hot spots over an extended region on both surfaces. Some areas of interference heating can be eliminated by the proper spacing and placement of components and by sweeping back wings and control surfaces.

REFERENCES

1. Anon.: Space Transportation System Technology Symposium, I - Aerothermodynamics and Configurations. NASA TM X-52876, 1970.

2. Anon.: Investigation of Shock Wave Impingement and Interaction During Space Shuttle Flight Maneuvers. LMSC/HREC D16772, Tech. Brief, Lockheed Missiles & Space Co., Feb. 8, 1971.

3. Anon.: NASA Space Shuttle Technology Conference. Vol. I - Aerothermodynamics, Configurations, and Flight Mechanics. NASA TM X-2272, 1971.

4. Korkegi, Robert H.: Survey of Viscous Interactions Associated With High Mach Number Flight. AIAA J., vol. 9, no. 5, May 1971, pp. 771-784.

5. Ryan, B. M.: Summary of the Aerothermodynamic Interference Literature. Tech. Note 4061-160, Naval Weapons Center (China Lake, Calif.), Apr. 1969.

6. Edney, Barry: Anomalous Heat Transfer and Pressure Distributions on Blunt Bodies at Hypersonic Speeds in the Presence of an Impinging Shock. FFA Rep. 115, Aeronaut. Res. Inst. of Sweden, 1968.

7. Newlander, Robert A.: Effect of Shock Impingement on the Distributions of Heat-Transfer Coefficients on a Right Circular Cylinder at Mach Numbers of 2.65, 3.51, and 4.44. NASA TN D-642, 1961.

8. Carter, Howard S.; and Carr, Robert E.: Free-Flight Investigation of Heat Transfer to an Unswept Cylinder Subjected to an Incident Shock and Flow Interference From an Upstream Body at Mach Numbers up to 5.50. NASA TN D-988, 1961.

9. Beckwith, Ivan E.: Experimental Investigation of Heat Transfer and Pressures on a Swept Cylinder in the Vicinity of Its Intersection With a Wedge and Flat Plate at Mach Number 4.15 and High Reynolds Numbers. NASA TN D-2020, 1964.

10. Jones, Robert A.: Heat-Transfer and Pressure Investigation of a Fin-Plate Interference Model at a Mach Number of 6. NASA TN D-2028, 1964.

11. Siler, L. G.; and Deskins, H. E.: Effect of Shock Impingement on Heat-Transfer and Pressure Distributions on a Cylindrical-Leading-Edge Model at Mach Number 19. AEDC-TDR-64-228, U.S. Air Force, Nov. 1964.

12. Bushnell, Dennis M.: Interference Heating on a Swept Cylinder in Region of Intersection With a Wedge at Mach Number 8. NASA TN D-3094, 1965.

13. Francis, W. Leon: Experimental Heat-Transfer Study of Shock Impingement on Fins in Hypersonic Flow. J. Spacecraft Rockets, vol. 2, no. 4, July-Aug. 1965, pp. 630-632.

14. Gulbran, C. E.; Redeker, E.; Miller, D. S.; and Strack, S. L.: Heating in Regions of Interfering Flow Fields — Part I. Two- and Three-Dimensional Interactions at Mach 8. AFFDL-TR-65-49, Pt. I, U.S. Air Force, July 23, 1965.

15. Knox, E. C.: Measurements of Shock-Impingement Effects on the Heat-Transfer and Pressure Distributions on a Hemicylinder Model at Mach Number 19. AEDC-TR-65-245, U.S. Air Force, Nov. 1965.

16. Popinski, Z.: Shock Wave-Boundary Layer Interaction. Proceedings of the Third International Heat Transfer Conference — Vol. II, Amer. Inst. Chem. Eng., Aug. 1966, pp. 262-273.

17. Ray, A. D.; and Palko, R. L.: An Investigation of the Effects of Shock Impingement on a Blunt Leading Edge. AEDC-TR-65-153, U.S. Air Force, July 1965.

18. Gulbran, C. E.; Redeker, E.; Miller, D. S.; and Strack, S. L.: Heating in Regions of Interfering Flow Fields. Part II: Leading Edge Shock Impingement. AFFDL-TR-65-49, Pt. II, U.S. Air Force, Jan. 1967.

19. Hiers, Robert S.; and Loubsky, William J.: Effects of Shock-Wave Impingement on the Heat Transfer on a Cylindrical Leading Edge. NASA TN D-3859, 1967.

20. Uselton, James C.: Fin Shock/Boundary-Layer Interaction Tests on a Flat Plate With Blunted Fins at M = 3 and 5. AEDC-TR-67-113, U.S. Air Force, June 1967. (Available from DDC as AD 815 760.)

21. Bushnell, Dennis M.: Effects of Shock Impingement and Other Factors on Leading-Edge Heat Transfer. NASA TN D-4543, 1968.

22. Watts, Joe D.: Flight Experience With Shock Impingement and Interference Heating on the X-15-2 Research Airplane. NASA TM X-1669, 1968.

23. Young, Frank L.; Kaufman, Louis G., II; and Korkegi, Robert H.: Experimental Investigation of Interactions Between Blunt Fin Shock Waves and Adjacent Boundary Layers at Mach Numbers 3 and 5. ARL 68-0214, U. S. Air Force, Dec. 1968. (Available from DDC as AD 684 537.)

24. Jones, Robert A.; and Hunt, James L.: Measurements of Mutual Interference Heating for a Probe Antenna Mounted on an Apollo Reentry Configuration. NASA TM X-1787, 1969.

25. Mashburn, J. H.: Turbulent Boundary Layer Separation Ahead of Cylindrical Protuberances in Supersonic Flow. ARL-TR-69-17, The University of Texas at Austin, Aug. 1969. (Available from DDC as AD 690 947.)

26. Spurlin, C. J.: Heat-Transfer Tests of a Multipurpose Entry Vehicle at Mach Number 10. AEDC-TR-69-206, U.S. Air Force, Nov. 1969. (Available from DDC as AD 861 055.)

27. Martindale, W. R.: Interference Heating Measurements on a Hypersonic Cruise Vehicle Wing Using the Phase-Change Paint Technique. AEDC-TR-70-78, U.S. Air Force, Apr. 1970. (Available from DDC as AD 867 803.)

28. Teterin, M. P.: Investigation of a Supersonic Gas Flow and Heat Transfer in the Region of an Incident Shock Wave on a Cylinder. NASA TT F-11,795, 1968.

29. Holden, M. S.: Shock Wave-Turbulent Boundary Layer Interaction in Hypersonic Flow. AIAA Paper No. 72-74, Jan. 1972.

30. Kaufman, Louis G., II; Korkegi, Robert H.; and Morton, Leo C.: Shock Impingement Caused by Boundary Layer Separation Ahead of Blunt Fins. RM-536, Grumman Aerospace Corp., Feb. 1972. (Available from DDC as AD 737 507.)

31. Haslett, Robert A.; Kaufman, Louis G., II; Romanowski, Richard F.; and Urkowitz, Michael: Interference Heating Due to Shock Impingement. AFFDL-TR-72-66, U.S. Air Force, July 1972.

32. Keyes, J. Wayne: Pressures and Heat Transfer on a 75° Swept Delta Wing With Trailing-Edge Flap at Mach 6 and Angles of Attack to 90°. NASA TN D-5418, 1969.

33. Keyes, J. Wayne; and Ashby, George C., Jr.: Calculated and Experimental Hinge Moments on a Trailing-Edge Flap of a 75° Swept Delta Wing at Mach 6. NASA TN D-4268, 1967.

34. Whitehead, Allen H., Jr.; and Keyes, J. Wayne: Flow Phenomena and Separation Over Delta Wings With Trailing-Edge Flaps at Mach 6. AIAA J., vol. 6, no. 12, Dec. 1968, pp. 2380-2387.

35. Morris, Dana J.; and Keyes, J. Wayne: Computer Programs for Predicting Supersonic and Hypersonic Interference Flow Fields and Heating. NASA TM X-2725, 1973.

36. Edney, B. E.; Bramlette, T. T.; Ives, J.; Hains, F. D.; and Keyes, J. W.: Theoretical & Experimental Studies of Shock Interference Heating. Rep. No. 9500-920-195, Bell Aerospace Co., Oct. 1970.

37. Hains, F. D.; and Keyes, J. Wayne: Shock Interference Heating in Hypersonic Flows. AIAA J., vol. 10, no. 11, Nov. 1972, pp. 1441-1447.

38. Keyes, J. Wayne; and Morris, Dana J.: Correlations of Peak Heating in Shock Interference Regions at Hypersonic Speeds. J. Spacecraft & Rockets, vol. 9, no. 8, Aug. 1972, pp. 621-623.

39. Birch, Stanley F.; and Keyes, J. Wayne: Transition in Compressible Free Shear Layers. J. Spacecraft & Rockets, vol. 9, no. 8, Aug. 1972, pp. 623-624.

40. Ames Research Staff: Equations, Tables, and Charts for Compressible Flow. NACA Rep. 1135, 1953. (Supersedes NACA TN 1428.)

41. Liepman, H. W.; and Roshko, A.: Elements of Gasdynamics. John Wiley & Sons, Inc., c.1957.

42. Shapiro, Ascher H.: The Dynamics and Thermodynamics of Compressible Fluid Flow. Vol. II, Ronald Press Co., c.1954.

43. Reyhner, T. A.; and Flügge-Lotz, I.: The Interaction of a Shock Wave With a Laminar Boundary Layer. Int. J. Non-Linear Mech., vol. 3, no. 2, June 1968, pp. 173-199.

44. Lees, Lester; and Reeves, Barry L.: Supersonic Separated and Reattaching Laminar Flows: I. General Theory and Application to Adiabatic Boundary-Layer/Shock-Wave Interactions. AIAA J., vol. 2, no. 11, Nov. 1964, pp. 1907-1920.

45. Nielsen, Jack N.; Lynes, Larry L.; and Goodwin, Frederick K.: Calculation of Laminar Separation With Free Interaction by the Method of Integral Relations. AFFDL TR 65-107, U.S. Air Force.
Part I – Two-Dimensional Supersonic Adiabatic Flow, Oct. 1965. (Available from DDC as AD 626 160.)
Part II – Two-Dimensional Supersonic Nonadiabatic Flow and Axisymmetric Supersonic Adiabatic and Nonadiabatic Flows, Jan. 1966. (Available from DDC as AD 630 765.)

46. Murphy, John D.: A Critical Evaluation of Analytic Methods for Predicting Laminar-Boundary-Layer Shock-Wave Interaction. NASA SP-228, 1970, pp. 515-539.

47. MacCormack, Robert W.: Numerical Solution of the Interaction of a Shock Wave With a Laminar Boundary Layer. Proceedings of the Second International Conference on Numerical Methods in Fluid Dynamics. Vol. 8 of Lecture Notes in Physics, Maurice Holt, ed., Springer-Verlag, 1971, pp. 151-163.

48. Markarian, C. Franklyn: Heat Transfer in Shock Wave-Boundary Layer Interaction Regions. NWC TP 4485, AD 849 532, U.S. Navy, Nov. 1968.

49. Eckert, E. R. G.: Engineering Relations for Friction and Heat Transfer to Surfaces in High Velocity Flow. J. Aeronaut. Sci. (Readers' Forum), vol. 22, no. 8, Aug. 1955, pp. 585-587.

50. Bushnell, Dennis M.; and Weinstein, Leonard M.: Correlation of Peak Heating for Reattachment of Separated Flows. J. Spacecraft & Rockets, vol. 5, no. 9, Sept. 1968, pp. 1111-1112.

51. Fay, J. A.; and Riddell, F. R.: Theory of Stagnation Point Heat Transfer in Dissociated Air. J. Aeronaut. Sci., vol. 25, no. 2, Feb. 1958, pp. 73-85, 121.

52. Lees, Lester: Laminar Heat Transfer Over Blunt-Nosed Bodies at Hypersonic Flight Speeds. Jet Propulsion, vol. 26, no. 4, Apr. 1956, pp. 259-269, 274.

53. Reshotko, Eli; and Cohen, Clarence B.: Heat Transfer at the Forward Stagnation Point of Blunt Bodies. NACA TN 3513, 1955.

54. Xerikos, J.; and Anderson, W. A.: A Critical Study of the Direct Blunt Body Integral Method. Rep. SM-42603, Missiles & Space Syst. Div., Douglas Aircraft Co., Inc., Dec. 28, 1962.

55. Traugott, Stephen C.: An Approximate Solution of the Direct Supersonic Blunt-Body Problem for Arbitrary Axisymmetric Shapes. J. Aerosp. Sci., vol. 27, no. 5, May 1960, pp. 361-370.

56. Bukovshin, V. G.; and Shestova, N. P.: Incidence of Plane Supersonic Jet on a Plane at an Arbitrary Angle. Fluid Dynamics, vol. 2, no. 4, July-Aug., 1967, pp. 97-100.

57. Gummer, J. H.; and Hunt, B. L.: The Impingement of a Uniform, Axisymmetric, Supersonic Jet on a Perpendicular Flat Plate. Aeronaut. Quart., vol. XXII, pt. 4, Nov. 1971, pp. 403-420.

58. Hayes, Wallace D.; and Probstein, Ronald F.: Hypersonic Flow Theory. Vol. I — Inviscid Flows. Second ed., Academic Press, 1966.

59. Van Dyke, Milton D.; and Gordon, Helen D.: Supersonic Flow Past a Family of Blunt Axisymmetric Bodies. NASA TR R-1, 1959.

60. Beckwith, Ivan E.; and Gallagher, James J.: Local Heat Transfer and Recovery Temperatures on a Yawed Cylinder at a Mach Number of 4.15 and High Reynolds Number. NASA TR R-104, 1961. (Supersedes NASA MEMO 2-27-59L.)

61. Back, L. H.; and Cuffel, R. F.: Changes in Heat Transfer From Turbulent Boundary Layers Interacting With Shock Waves and Expansion Waves. AIAA J., vol. 8, no. 10, Oct. 1970, pp. 1871-1873.

62. Goldberg, Theodore J.; and Hefner, Jerry N. (With appendix by James C. Emery): Starting Phenomena for Hypersonic Inlets With Thick Turbulent Boundary Layers at Mach 6. NASA TN D-6280, 1971.

63. Arrington, James P.; Joiner, Roy C., Jr.; and Henderson, Arthur, Jr.: Longitudinal Characteristics of Several Configurations at Hypersonic Mach Numbers in Conical and Contoured Nozzles. NASA TN D-2489, 1964.

64. Clark, Frank L.; Ellison, James C.; and Johnson, Charles B.:   Recent Work in Flow Evaluation and Techniques of Operations for the Langley Hypersonic Nitrogen Facility.   NASA paper presented at Fifth Hypervelocity Techniques Symposium (Denver, Colo.), Mar. 28-30, 1967.

65. Beckwith, Ivan E.; Harvey, William D.; and Clark, Frank L. (With appendix A by Ivan E. Beckwith, William D. Harvey, and Christine M. Darden and appendix B by William D. Harvey, Lemuel E. Forrest, and Frank L. Clark):   Comparisons of Turbulent-Boundary-Layer Measurements at Mach Number 19.5 With Theory and an Assessment of Probe Errors.   NASA TN D-6192, 1971.

66. Jones, Robert A.; and Hunt, James L. (With Appendix A by James L. Hunt, Kathryn A. Smith, and Robert B. Reynolds and Appendix B by James L. Hunt and Lillian R. Boney):   Use of Tetrafluoromethane To Simulate Real-Gas Effects on the Hypersonic Aerodynamics of Blunt Vehicles.   NASA TR R-312, 1969.

67. Jones, Robert A.; and Hunt, James L.:   Use of Fusible Temperature Indicators for Obtaining Quantitative Aerodynamic Heat-Transfer Data.   NASA TR R-230, 1966.

68. Hunt, James L.; and Jones, Robert A.:   Effects of Several Ramp-Fairing, Umbilical, and Pad Configurations on Aerodynamic Heating to Apollo Command Module at Mach 8.   NASA TM X-1640, 1968.

69. Hillard, Marvin E., Jr.; Harvey, William D.; and Emory, M. Lawrence: Measurements of Shock Wave Location in Hypersonic Nitrogen Flow.   Spacecraft & Rockets, vol. 8, no. 9, Sept. 1971, pp. 1004-1006.

TABLE VII.- PRESSURE TEST CONDITIONS, REFERENCE PRESSURE,
AND FLOW-VISUALIZATION DATA

(a) Test 6344, 0.051-m-diameter hemisphere, Mach 6 air.
Values of p_{stag} are the measured free-stream pitot pressure.

Run	Θ_i, deg	$p_{t,\infty}$, N/cm²	$T_{t,\infty}$, K	p_{stag}, N/cm²	Type	x_i/R_b	y_i/R_b	L_{SH}/R_b
2b	14.8	85	472	2.57	IV	0.268	-0.395	0.268
4a	14.8	291	474	8.67	IV	.252	-.427	.284
4b	14.8	84	456	*2.56	IV	.253	-.389	.262
5a	14.8	294	477	8.73	III	.233	-.548	.456
5b	14.8	83	452	2.56	IV	.248	-.513	.408
7a	14.8	292	476	8.78	III	.209	-.650	.612
7b	14.8	82	479	2.58	III	.214	-.621	.563
9a	14.8	294	474	8.75	IV	.253	-.330	.204
9b	14.8	85	478	2.56	IV	.257	-.340	.204
11a	9.8	286	477	8.60	IV	.223	-.252	.175
12a	9.8	293	475	8.74	IV	.224	-.369	.321
12b	9.8	79	472	2.42	IV	.218	-.340	.266
13a	9.8	286	472	8.62	III	.224	-.447	.466
13b	9.8	85	468	2.61	IV	.228	-.417	.389
16a	9.8	297	479	8.84	III	.194	-.561	.710
16b	9.8	87	472	2.65	III	.204	-.515	.602
17a	4.8	291	475	8.68	IV	.204	-.199	.179
17b	4.8	81	480	2.55	IV	.200	-.141	.088
18a	4.8	293	467	8.74	IV	.214	-.146	.079
18b	4.8	83	473	2.60	IV	.233	-.253	.292
20a	4.8	291	475	8.74	III	.165	-.389	.574
20b	4.8	81	481	2.56	III	.175	-.340	.397
21a	4.8	293	476	8.72	IV	.185	-.243	.243
21b	4.8	78	473	2.47	IV	.194	-.175	.146
22a	19.8	295	471	8.83	IV	.282	-.417	.252
22b	19.8	85	486	2.71	IV	.301	-.418	.243
24a	19.8	293	476	8.64	IV	.292	-.544	.350
24b	19.8	85	469	2.57	IV	.286	-.524	.359
25a	19.8	293	479	8.83	IV	.272	-.593	.438
25b	19.8	84	469	2.57	IV	.292	-.602	.457
26a	19.8	296	475	8.83	III	.262	-.680	.564
26b	19.8	85	475	2.61	III	.252	-.690	.568
27b	0	83	475	2.53	**	----	-----	----
28a	24.8	291	476	8.75	IV	.301	-.534	.320
28b	24.8	85	474	2.64	IV	.330	-.544	.340
29a	24.8	298	480	8.87	IV	.311	-.632	.418
29b	24.8	84	477	2.58	IV	.291	-.640	.437
30a	24.8	295	477	8.78	IV	.301	-.690	.506
30b	24.8	85	476	2.60	IV	.301	-.710	.524
31a	24.8	295	472	8.83	III	.272	-.777	.612
31b	24.8	83	477	2.55	III	.262	-.786	.641
33a	29.7	293	473	*8.76	IV	.330	-.826	.622
33b	29.7	83	472	2.53	IV	.310	-.836	.660
34a	29.7	293	474	8.77	IV	.379	-.564	.321
34b	29.7	83	475	2.51	IV	.388	-.551	.340
36a	29.7	295	472	8.81	IV	.388	-.551	.330
36b	29.7	84	472	2.56	IV	.388	-.551	.330

*Estimated.
**No interference.

TABLE VII.- PRESSURE TEST CONDITIONS, REFERENCE PRESSURE, AND FLOW-VISUALIZATION DATA – Continued

(b) Test 6358, fin model, Mach 6 air

Run	Θ_i, deg	λ, deg	$p_{t,\infty}$, N/cm^2	$T_{t,\infty}$, K	p_{cyl}, N/cm^2	Type
1a	15.0	24.8	292	481	*7.15	V
1b	15.0	24.8	80	477	*2.05	V
2a	15.0	24.8	291	486	*7.12	V
2b	15.0	24.8	83	468	*2.12	V
3a	10.0	24.7	292	477	*7.15	V
3b	10.0	24.7	85	472	*2.17	V
4a	5.0	24.7	291	479	*7.15	V
4b	5.0	24.7	84	472	*2.16	V
5a	15.0	24.7	292	482	*7.16	V
5b	15.0	24.7	81	465	*2.08	V
6a	20.0	24.7	294	489	*7.21	V
6b	20.0	24.7	84	467	*2.15	V
7a	19.9	24.8	293	473	*7.17	V
7b	19.9	24.8	83	469	*2.13	V
8a	24.9	24.8	294	488	*7.19	V
8b	24.9	24.8	83	469	*2.12	V
9a	0	24.8	292	483	*7.15	**
9b	0	24.8	83	474	*2.14	**
10a	0	0	292	488	8.72	**
10b	0	0	84	472	2.60	**
11a	24.9	0	292	486	8.73	IVa
11b	24.9	0	86	470	2.68	IVa
12a	19.9	0	290	488	8.69	IVa
12b	19.9	0	86	468	2.68	IVa
13a	14.9	0	291	487	8.72	IVa
13b	14.9	0	85	472	2.65	IVa
14a	14.9	0	292	485	8.78	IVa
14b	14.9	0	83	471	2.62	IVa
15a	10.0	0	288	484	8.72	IVa
15b	10.0	0	83	469	2.57	IVa
16a	5.0	0	290	487	8.68	IVa
16b	5.0	0	81	473	2.51	IVa
17a	10.0	30.0	292	387	*6.52	V
17b	10.0	30.0	82	466	*1.84	V
18a	5.0	30.0	292	487	*6.52	V
18b	5.0	30.0	83	467	*1.86	V

*The values of p_{cyl} are the calculated stagnation line pressure on an infinite cylinder without interference. In all other runs, p_{cyl} is the measured freestream pitot pressure.

**No interference.

TABLE VII.- PRESSURE TEST CONDITIONS, REFERENCE PRESSURE,

AND FLOW-VISUALIZATION DATA – Continued

(c) Test 6358, 30° wedge, Mach 6 air

Run	θ_i, deg	θ_b, deg	α, deg	$p_{t,\infty,2}$, N/cm²	$T_{t,\infty}$, K	p_{wedge}, N/cm²	Type
19	5.0	-15.0	0	290	491	*1.11	I
20	5.0	-15.0	0	292	488	*1.12	I
21	10.0	-15.0	0	290	488	*1.12	I
22	15.0	-15.0	0	291	493	*1.12	I
23	0.0	-15.0	0	292	501	*1.12	**
25	5.0	-64.1	49.1	294	494	8.74	III
26	10.0	-65.3	50.3	297	491	8.89	III
27	10.0	-65.3	50.3	293	494	8.75	III
28	15.0	-65.3	50.3	292	492	8.73	IV
29	0.0	-65.6	50.6	291	492	8.76	**
30	5.0	-39.8	24.8	295	493	*5.46	II
31	10.0	-39.8	24.8	294	492	*5.44	II
32	10.0	-39.5	24.5	296	486	*5.40	II
33	10.0	-39.5	24.5	295	492	*5.38	II
34	0.0	-39.6	24.6	292	491	*5.23	**
35	10.0	-39.5	24.5	294	492	*5.36	II
36	10.0	-39.5	24.5	293	489	*5.34	II
37	15.0	-39.5	24.5	294	492	*5.36	II
38	5.1	39.6	-24.6	296	492	***6.93	VI

*Calculated wedge pressure without interference.
**No interference.
***Calculated wedge pressure including pressure rise across impinging shock. All other values of p_{wedge} are measured free-stream pitot pressure. Shear layer did not attach to wedge in runs 25, 26, or 27.

(d) Test 357, 0.025-m-diameter hemisphere, Mach 20 helium. Values of p_{stag} are measured free-stream pitot pressure.

Run	θ_i, deg	$p_{t,\infty,2}$, N/cm²	$T_{t,\infty}$, K	$p_{stag,2}$, N/cm²	Type	x_i/R_b	y_i/R_b	L_{SH}/R_b
2	0	701	434	1.92	**	0.16	----	---
3	14.9	699	434	1.91	IV	.38	-0.23	0.43
4	14.9	699	434	1.91	IV	.37	-.14	.16
5	14.9	698	436	1.90	III	.23	-.25	.23
6	14.9	701	439	1.92	III	.22	-.36	.41
7	9.7	701	452	1.92	IV	.32	-.18	.18
8	9.7	699	442	1.91	IV	.29	-.12	.11
9	9.7	698	453	1.90	IV	.26	-.31	.25
10	9.7	699	444	1.91	III	.26	-.48	.49
11	4.5	701	444	1.92	*	---	----	---
12	4.5	700	442	1.92	IV	.25	0	.10
13	4.5	702	447	1.92	IV	.29	-.19	.33
14	4.5	698	443	1.91	III	.23	-.30	.30
15	14.7	698	453	1.91	IV	.32	-.38	.27
16	14.7	699	443	1.91	IV	.33	-.32	.22
17	14.7	702	447	1.92	IV	.34	-.25	.22
18	9.6	701	445	1.92	III	.31	-.37	.37
19	9.6	699	447	1.91	IV	.29	-.30	.26
20	9.6	701	451	1.92	IV	.26	-.20	.27
21	9.6	697	440	1.90	IV	.29	-.37	.30

*Poor schlieren photograph.
**No interference.

TABLE VII.- PRESSURE TEST CONDITIONS, REFERENCE PRESSURE,

AND FLOW-VISUALIZATION DATA – Concluded

(e) Test 16, 0.025-m-diameter hemisphere, Mach 19 nitrogen.
Values of p_{stag} are measured free-stream pitot pressure.

Run	Θ_i, deg	$p_{t,\infty}$, N/cm^2	$T_{t,\infty}$, K	p_{stag}, N/cm^2	Type	x_i/R_b	y_i/R_b	L_{SH}/R_b
1	15.0	4357	1622	0.444	IV	0.29	-0.18	0.116
2	15.0	4411	1644	.450	III	.20	-.65	.449
3	10.0	4360	1633	.487	IV	.20	-.16	.086
4	10.0	4422	1689	.448	III-IV	.20	-.39	.185
5	10.0	4400	1678	.419	III	.13	-.68	.415
6	10.0	4306	1644	.445	IV	.20	-.31	.133
7	10.0	4473	1678	.466	IV	.20	-.20	.085
9	0	4471	1678	.519	**	.12	----	----

**No interference.

(f) Test 63, 0.025-m-diameter hemisphere, Mach 8.9 CF$_4$. Values of
p_{stag} are measured free-stream pitot pressure.

Run	Θ_i, deg	$p_{t,\infty}$, N/cm^2	$T_{t,\infty}$, K	p_{stag}, N/cm^2	Type
1	14.9	981	292	0.953	IV
2	14.9	950	291	.924	IV
3	14.9	912	289	.879	IV
4	14.9	972	289	.952	III
5	14.9	993	293	.973	III
6	14.9	974	292	.960	III
7	14.9	930	289	.919	III
8	14.9	965	292	.948	III
9	10.0	964	291	.951	IV
10	10.0	961	291	.951	IV
11	10.0	969	290	.963	III
12	10.0	909	289	.889	III
13	10.0	981	293	.960	IV
14	10.0	986	291	.973	IV
15	10.0	952	288	.946	III
16	5.0	1024	296	1.005	IV
17	5.0	987	291	.971	IV
18	5.0	983	294	.961	IV
19	5.0	970	291	.956	III
20	0	969	293	.949	**

**No interference.

43

TABLE VIII.- HEAT-TRANSFER TEST CONDITIONS, WALL TEMPERATURES, REFERENCE HEAT-TRANSFER RATES, AND MODEL MATERIAL

(a) Tests 6352 and 6363, 0.051-m-diameter hemisphere, Mach 6 air. Reference heating rate Q_{stag} is the calculated stagnation point value on the hemisphere.

Run	Θ_i, deg	$p_{t,\infty}$, N/cm^2	$T_{t,\infty}$, K	T_w, K	Q_{stag}, W/cm^2	Type	Model material
			Test 6352				
1	14.8	277	478	422	*3.08	IV	Steel
2	14.8	290	471	422	2.76	IV	Epoxy
3	14.8	283	489	394	5.25	IV	Epoxy
8	14.8	85	484	436	*1.50	IV	Epoxy
9	14.8	86	473	394	2.43	IV	Epoxy
10	0	85	473	325	*4.55	**	Epoxy
12	14.8	84	476	436	*1.24	III	Epoxy
13	14.8	85	474	394	2.46	III	Epoxy
14	9.9	83	468	436	*.96	IV	Epoxy
15	9.9	86	472	394	2.41	IV	Epoxy
16	9.9	83	474	422	*1.58	III	Epoxy
17	9.9	82	472	394	2.36	III	Epoxy
18	19.7	81	477	422	1.59	IV	Epoxy
19	19.7	84	473	394	2.42	IV	Epoxy
20	19.7	79	473	436	*1.11	IV	Epoxy
21	19.7	81	477	422	*1.63	III	Epoxy
22	19.7	83	476	394	2.49	III	Epoxy
23	24.6	83	474	436	*1.16	IV	Epoxy
24	24.6	84	476	394	2.49	IV	Epoxy
25	24.6	84	473	422	*1.55	III	Epoxy
26	24.6	83	476	394	2.47	III	Epoxy
27	14.8	84	493	450	*1.33	IV	Epoxy
28	14.8	83	478	394	2.51	IV	Epoxy
29	14.8	85	493	450	1.33	IV	Epoxy
30	9.9	81	474	436	1.15	III	Epoxy
31	9.9	290	492	408	*4.69	IV	Steel
32	9.9	277	486	394	5.02	IV	Epoxy
33	9.9	291	487	422	3.67	IV	Epoxy
			Test 6363				
36	14.8	289	486	408	*4.37	III	Steel
37	14.8	292	488	436	2.94	III	Epoxy
39	14.8	290	486	408	4.41	III	Epoxy
40	14.8	290	489	436	*3.00	III	Epoxy
41	19.8	288	486	422	*3.70	IV	Steel
42	19.8	287	488	422	3.70	IV	Epoxy
43	24.8	290	494	422	*4.07	IV	Steel
44	24.8	287	487	422	3.63	IV	Epoxy
46	5.0	288	488	436	*2.95	IV	Epoxy
48	5.0	82	476	422	*1.62	IV	Epoxy

*Reference value for the calculated peak as well as the experimental data.
**No interference.

TABLE VIII.- HEAT-TRANSFER TEST CONDITIONS, WALL TEMPERATURES, REFERENCE HEAT-TRANSFER RATES, AND MODEL MATERIAL — Continued

(b) Test 6363, fin model, Mach 6 air. Q_{cyl} is the calculated stagnation line value on an infinite cylinder without interference.

Run	Θ_i, deg	λ, deg	$p_{t,\infty}$, N/cm²	$T_{t,\infty}$, K	T_w, K	Q_{cyl}, W/cm²	Type	Model material
3	15.0	25.0	80	481	394	*2.72	V	Epoxy
6	9.9	25.0	81	488	394	*2.97	V	Epoxy
9	9.9	25.0	290	488	436	*3.10	V	Epoxy
10	14.9	24.9	292	485	436	*2.94	V	Epoxy
13	19.8	24.9	291	488	436	*3.10	V	Epoxy
14	19.8	24.9	81	473	422	*1.61	V	Epoxy
18	19.9	0	83	471	394	*2.85	IVa	Epoxy
19	19.9	0	292	489	422	*4.39	IVa	Epoxy
20	14.9	0	289	491	422	*4.87	IVa	Epoxy
22	14.9	0	83	476	394	*2.58	IVa	Epoxy
23	9.9	0	293	486	422	*4.56	IVa	Epoxy
24	9.9	0	86	471	394	*2.83	IVa	Epoxy

*Reference value for the calculated peak as well as the experimental data.

(c) Test 6363, 30° wedge, Mach 6 air. Q_{wedge} is the calculated heating at the midpoint of the wedge without interference for all runs except runs 63 and 64. For runs 63 and 64, Q_{wedge} is based on the maximum heating ahead of the expansion-fan—boundary-layer interaction.

Run	Θ_i, deg	Θ_b, deg	α, deg	$p_{t,\infty}$, N/cm²	$T_{t,\infty}$, K	T_w, K	Q_{wedge}, W/cm²	Type	Model material
26	9.9	-15.0	0	289	489	394	0.96	I	Epoxy
27	9.9	-15.0	0	294	484	422	*.64	I	Epoxy
28	9.9	-15.0	0	288	488	367	1.25	I	Epoxy
33	14.8	-65.0	50.0	292	484	436	*1.28	IV	Epoxy
34	14.8	-65.0	50.0	292	484	450	.92	IV	Epoxy
52	15.0	-15.0	0	278	486	436	*.51	I	Epoxy
53	15.0	-15.0	0	291	490	367	1.26	I	Epoxy
55	0	-64.8	49.8	294	488	394	2.50	**	Epoxy
60	15.0	-40.3	25.3	291	489	394	*1.61	II	Epoxy
63	5.0	40.5	25.5	290	488	367	10.44	VI	Epoxy
64	5.0	40.5	25.5	290	488	422	*5.67	VI	Epoxy

*Reference value for the calculated peak as well as the experimental data.
**No interference.

TABLE VIII.- HEAT-TRANSFER TEST CONDITIONS, WALL TEMPERATURES, REFERENCE
HEAT-TRANSFER RATES, AND MODEL MATERIAL — Concluded

(d) Test 373, 0.025-m-diameter hemisphere, Mach 20 helium. Reference heating rate Q_{stag} is the calculated stagnation point value on the hemisphere.

Run	Θ_i, deg	$p_{t,\infty}$, N/cm^2	$T_{t,\infty}$, K	T_w, K	Q_{stag}, W/cm^2	Type	Model material
2	15.1	705	432	394	*4.55	III	Steel
3	15.1	703	432	394	4.47	III	Epoxy
5	15.1	705	434	394	*4.82	III	Steel
6	15.1	708	432	381	6.25	III	Epoxy
8	10.1	706	434	367	*8.19	III	Steel
9	10.1	707	434	381	6.51	III	Epoxy
11	10.1	705	431	381	6.09	III	Epoxy
12	10.1	705	435	367	8.33	III	Epoxy
19	5.1	704	428	381	*5.68	IV	Steel
20	5.1	704	429	381	5.82	IV	Epoxy
22	5.1	705	438	367	*8.60	III	Steel
23	5.1	707	434	367	8.21	III	Epoxy
24	5.1	703	429	381	5.81	III	Epoxy
25	0	706	436	381	6.70	**	Epoxy
26	10.1	707	436	381	*6.25	III	Steel

*Reference value for calculated peak as well as the experimental data.
**No interference.

(e) Test 16, 0.025-m-diameter hemisphere, Mach 19 nitrogen. Q_{stag} is the calculated stagnation point value on the hemisphere.

Run	Θ_i, deg	$p_{t,\infty}$, N/cm^2	$T_{t,\infty}$, K	T_w, K	Q_{stag}, W/cm^2	Type	Model material
13	15.0	4309	1633	506	24.58	III	Steel
14	15.0	4368	1600	547	23.13	IV	Steel
19	10.0	4296	1628	436	25.96	III	Steel
20	10.0	4226	1600	533	22.95	IV	Steel

TABLE IX.- ADDITIONAL PRESSURE DATA

(a) Test 6344, 0.051-m-diameter hemisphere, Mach 6 air.
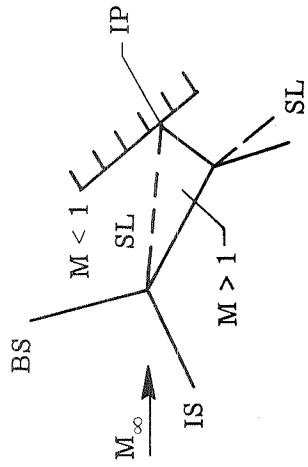
Values of p_{stag} are listed in table VII(a).

Θ, deg	p/p_{stag}							
	Run 2b	Run 4b	Run 9a	Run 12a	Run 13a	Run 16a	Run 16b	Run 18a
-80.5	0.548	0.568	0.570	0.342	0.326	0.330	0.316	0.175
-70.7	.857	.879	.885	.559	.549	.618	.526	.299
-60.5	1.329	1.342	1.344	.908	.873	1.264	1.049	.508
-55.5	1.556	1.587	1.565	1.078	.969	1.560	1.619	.627
-50.3	1.823	1.849	1.816	1.216	1.248	1.758	1.897	.760
-45.4	2.038	2.075	2.028	1.602	2.356	1.459	1.977	.923
-40.3	2.251	2.310	2.257	1.515	3.118	1.000	1.399	1.245
-35.3	2.451	2.502	2.455	2.188	1.751	1.009	.982	1.722
-30.3	2.664	2.380	2.613	3.800	.955	.997	.992	1.525
-25.3	4.522	5.702	3.147	1.067	.956	.992	.980	.979
-20.1	.594	.574	1.981	.966	.993	.996	.980	1.011
-15.3	1.011	1.030	.458	.976	1.007	1.002	.995	1.011
-10.0	.934	.929	1.193	.989	1.006	1.009	.994	1.007
-4.9	.968	.996	.901	.994	1.015	.010	1.007	1.014
0	.973	.980	.944	.986	1.003	1.006	1.004	1.010
5.0	.943	.958	.945	.967	.984	.992	.984	.995
10.1	.911	.919	.898	.937	.951	.961	.956	.966
15.0	.856	.869	.854	.890	.905	.915	.909	.920
20.0	.791	.809	.799	.837	.848	.856	.845	.862
25.2	.720	.738	.724	.772	.781	.787	.784	.793
45.2	.434	.451	.430	.462	.466	.469	.469	.473
65.3	.183	.206	.191	.196	.199	.197	.207	.201
85.4	.059	.061	.064	.066	.067	.063	.073	.064

Θ, deg	p/p_{stag}							
	Run 18b	Run 20a	Run 20b	Run 21a	Run 21b	Run 22b	Run 24a	Run 25a
-80.5	0.179	0.174	0.171	0.180	0.185	0.784	0.779	0.765
-70.7	.294	.310	.292	.302	.305	1.151	1.147	1.121
-60.5	.506	.564	.504	.512	.510	1.659	1.660	1.695
-55.5	.621	.727	.627	.634	.625	1.877	1.883	2.066
-50.3	.755	.936	.792	.769	.753	2.130	2.170	1.964
-45.4	.878	1.123	1.064	.900	.882	2.346	2.578	3.395
-40.3	1.029	1.199	1.446	1.056	1.034	2.544	2.489	6.996
-35.3	1.176	1.059	1.591	1.190	1.153	2.731	5.934	1.645
-30.3	1.349	1.003	1.159	1.661	1.286	2.894	1.529	.938
-25.3	2.663	.997	1.020	2.215	1.444	4.720	.676	.954
-20.1	1.066	.996	1.003	1.006	2.508	2.227	.959	.967
-15.3	.976	.995	1.008	.977	1.091	.375	.953	.976
-10.0	.977	1.006	1.001	.997	.979	.554	.959	.981
-4.9	1.013	1.010	1.011	1.008	.997	1.272	.962	.974
0	1.001	1.016	1.015	1.002	1.003	.843	.958	.963
5.0	.989	1.004	.997	.988	.994	.949	.930	.938
10.1	.964	.977	.977	.962	.967	.866	.886	.906
15.0	.925	.929	.922	.913	.908	.818	.836	.857
20.0	.858	.869	.858	.856	.842	.762	.781	.801
25.2	.790	.798	.798	.786	.781	.696	.714	.737
45.2	.478	.477	.476	.469	.475	.425	.433	.446
65.3	.213	.198	.204	.196	.206	.208	.191	.194
85.4	.070	.063	.068	.063	.069	.076	.065	.064

TABLE IX.- ADDITIONAL PRESSURE DATA — Continued

(a) Concluded

Θ, deg	p/p_{stag}							
	Run 25b	Run 26a	Run 28b	Run 29a	Run 30a	Run 30b	Run 31a	Run 33a
-80.5	0.757	0.768	0.954	0.938	0.927	0.913	0.911	1.032
-70.7	1.112	1.119	1.324	1.304	1.332	1.319	1.224	1.427
-60.5	1.642	1.672	1.854	1.816	1.787	1.736	2.552	2.705
-55.5	2.034	2.912	2.058	2.014	2.093	2.224	4.082	3.620
-50.3	1.964	4.890	2.307	2.304	3.442	3.861	3.707	5.312
-45.4	3.341	2.801	2.479	2.885	5.311	5.428	1.596	1.639
-40.3	6.299	1.087	2.638	4.918	1.967	1.949	.946	.938
-35.3	2.029	.965	4.567	3.823	.880	.891	.947	.964
-30.3	.883	.959	4.842	.605	.936	.923	.950	.974
-25.3	.962	.978	.680	1.045	.951	.955	.980	.986
-20.1	.953	.995	.483	.896	.950	.915	.981	.992
-15.3	.973	.999	1.015	.958	.966	.958	.992	.995
-10.0	.975	1.001	.863	.959	.967	.953	.982	.993
-4.9	.977	1.000	.918	.966	.964	.970	.988	.981
0	.964	.989	.945	.954	.950	.955	.974	.971
5.0	.938	.970	.922	.924	.927	.940	.956	.944
10.1	.918	.938	.889	.884	.895	.915	.926	.910
15.0	.861	.884	.822	.828	.845	.858	.874	.862
20.0	.799	.825	.760	.773	.790	.792	.815	.802
25.2	.739	.756	.703	.706	.725	.732	.746	.737
45.2	.448	.454	.427	.426	.438	.443	.448	.444
65.3	.208	.195	.216	.196	.196	.221	.199	.190
85.4	.073	.063	.084	.066	.065	.076	.066	.064

Θ, deg	p/p_{stag}				
	Run 33b	Run 34a	Run 34b	Run 36a	Run 36b
-80.5	0.997	1.059	1.053	1.057	1.044
-70.7	1.388	1.400	1.396	1.400	1.387
-60.5	2.685	1.865	1.877	1.862	1.870
-55.5	3.812	2.047	2.084	2.042	2.077
-50.3	4.297	2.276	2.324	2.270	2.313
-45.4	1.973	2.463	2.487	2.450	2.446
-40.3	.991	2.658	2.684	2.644	2.661
-35.3	.924	2.756	2.800	2.746	2.759
-30.3	.950	5.098	5.178	5.027	5.096
-25.3	.981	3.025	2.652	3.208	3.054
-20.1	.980	.621	.582	.652	.621
-15.3	.985	.385	.461	.378	.438
-10.0	.978	.477	.593	.441	.540
-4.9	.962	1.322	1.156	1.275	1.096
0	.963	.815	.901	.860	.971
5.0	.945	.733	.823	.710	.800
10.1	.907	.911	.838	.904	.828
15.0	.867	.715	.758	.726	.762
20.0	.795	.679	.705	.667	.696
25.2	.739	.671	.661	.664	.654
45.2	.447	.394	.401	.394	.403
65.3	.196	.175	.184	.175	.187
85.4	.070	.064	.073	.064	.074

TABLE IX.- ADDITIONAL PRESSURE DATA — Continued

(b) Test 6358, fin model, Mach 6 air. Values of p_{cyl} are listed in table VII(b).

X	p/p_{cyl}							
	Run 1a	Run 1b	Run 4a	Run 4b	Run 5a	Run 5b	Run 6a	Run 6b
0.063	2.337	2.283	1.670	1.600	2.350	2.283	2.291	2.243
.094	2.261	2.205	1.635	1.558	2.279	2.215	2.213	2.171
.125	2.211	2.166	1.614	1.531	2.227	2.180	2.152	2.117
.156	2.184	2.140	1.598	1.512	2.196	2.147	2.128	2.080
.187	2.163	2.120	1.582	1.500	2.169	2.128	2.778	2.356
.219	2.150	2.110	1.569	1.488	2.156	2.122	1.746	2.314
.250	2.135	2.094	1.555	1.489	2.140	2.102	.954	1.185
.282	2.125	2.085	1.555	1.490	2.131	2.124	.683	.726
.313	2.097	2.079	1.644	1.504	2.099	2.053	.665	.677
.345	2.164	2.091	1.288	1.582	2.687	2.149	.793	.678
.375	2.515	2.738	1.020	1.218	2.012	2.487	1.013	.883
.407	1.415	1.892	.968	.980	1.098	1.399	1.155	1.080
.438	.871	1.013	1.044	.933	.803	.845	1.122	1.151
.470	.653	.797	1.043	.997	.642	.652	1.035	1.013
.500	.616	.667	1.012	1.043	.605	.644	1.021	1.022
.531	.735	.662	1.021	1.006	.850	.718	1.009	.975
.563	.981	.812	1.022	.988	1.036	.933	1.012	.996
.595	1.084	1.004	1.027	.990	1.136	1.060	1.013	.991
.625	1.176	1.089	1.025	.996	1.106	1.141	1.013	.986
.688	1.006	.996	1.013	.995	1.027	.987	1.005	.989
.750	1.008	.997	1.005	.977	1.007	.986	.995	.975
.813	1.007	.996	1.009	.979	1.003	.991	.998	.980
.876	.998	.981	1.009	.976	.996	.978	.998	.978
.938	.993	.976	1.007	.978	.993	.972	.995	.977

X	p/p_{cyl}							
	Run 8a	Run 8b	Run 9a	Run 9b	Run 10a	Run 10b	Run 11a	Run 11b
0.063	2.007	1.980	1.109	1.102	1.008	0.991	2.570	2.513
.094	1.939	1.920	1.092	1.090	1.019	.999	2.531	2.472
.125	1.881	1.867	1.082	1.086	1.018	1.005	2.490	2.449
.156	1.853	1.830	1.072	1.063	1.017	1.009	2.481	2.450
.187	1.838	1.814	1.064	1.048	1.015	1.009	2.494	2.468
.219	1.848	1.834	1.064	1.056	1.013	1.006	2.519	2.497
.250	1.861	1.842	1.060	1.048	1.012	.992	2.541	2.513
.282	2.381	1.987	1.066	1.067	1.017	.995	2.509	2.494
.313	1.970	2.281	1.046	1.017	1.012	.992	2.338	2.380
.345	1.113	1.268	1.037	.993	1.016	1.023	1.951	2.006
.375	.951	.925	1.045	1.015	1.012	1.009	1.492	1.580
.407	.780	.885	1.043	1.029	1.006	.993	1.019	1.035
.438	.708	.721	1.048	1.022	1.007	.995	.940	.905
.470	.760	.658	1.032	.979	1.013	.993	1.152	1.034
.500	.963	.870	1.048	1.057	1.014	1.008	1.133	1.145
.531	1.023	.978	1.031	1.009	1.014	.994	1.014	.997
.563	1.110	1.048	1.045	1.031	1.014	1.009	1.076	1.042
.595	1.085	1.102	1.044	1.029	1.016	1.000	1.049	1.030
.625	1.037	1.021	1.042	1.024	1.017	1.004	1.046	1.031
.688	1.042	1.009	1.039	1.028	1.014	1.003	1.039	1.025
.750	1.014	.983	1.035	1.011	1.017	1.002	1.020	1.009
.813	1.012	.988	1.036	1.010	1.017	1.018	1.008	1.007
.876	1.001	.982	1.034	1.010	1.009	.998	.999	.987
.938	1.000	.978	1.030	1.012	1.006	1.001	.982	.979

TABLE IX.- ADDITIONAL PRESSURE DATA — Continued

(b) Concluded

X	p/p_{cyl}							
	Run 13a	Run 13b	Run 16a	Run 16b	Run 17a	Run 17b	Run 18a	Run 18b
0.063	2.644	2.584	1.640	1.584	2.105	2.098	1.689	1.669
.094	2.654	2.585	1.650	1.583	2.039	2.035	1.644	1.624
.125	2.637	2.575	1.644	1.576	1.987	1.991	1.603	.592
.156	2.640	2.576	1.639	1.578	1.960	1.973	1.580	1.580
.187	2.630	2.576	1.629	1.584	1.941	1.955	1.561	1.577
.219	2.619	2.580	1.610	1.577	1.920	1.925	1.543	1.556
.250	2.606	2.561	1.591	1.575	1.912	1.918	1.694	1.565
.282	2.547	2.537	1.520	1.558	2.186	1.909	1.167	1.724
.313	2.351	2.386	1.259	1.521	1.113	1.979	.978	1.225
.345	1.805	1.980	1.048	1.149	.908	.997	.958	.899
.375	1.188	1.349	1.044	1.026	.736	.883	1.015	.919
.407	.956	.903	1.040	1.026	.863	.787	1.054	1.031
.438	1.154	1.054	1.029	1.014	1.003	.869	1.054	1.059
.470	1.024	1.005	1.013	.986	1.058	.964	1.033	.987
.500	1.068	1.048	1.008	1.012	1.037	1.080	1.037	1.045
.531	1.044	1.007	1.000	.978	1.011	1.017	1.027	1.006
.563	1.048	1.041	1.005	1.009	1.043	1.065	1.038	1.071
.595	1.041	1.033	1.000	.990	1.037	1.055	1.032	1.044
.625	1.034	1.026	1.004	.987	1.033	1.053	1.025	1.045
.688	1.014	1.013	1.004	1.003	1.030	1.073	1.016	1.046
.750	1.008	.992	1.006	.994	1.014	1.028	1.017	1.027
.813	1.010	1.008	1.005	.996	1.007	1.020	1.024	1.028
.876	1.006	.995	1.002	.983	1.007	1.011	1.019	1.022
.938	.994	.986	.996	.987	1.013	.022	1.022	1.030

TABLE IX.- ADDITIONAL PRESSURE DATA – Continued

(c) Test 6358, 30° wedge model, Mach 6 air. Values of p_{wedge} are listed in table VII(c).

X	p/p_{wedge}							
	Run 19	Run 20	Run 23	Run 25	Run 26	Run 27	Run 30	Run 31
0.216	1.181	1.096	1.083	1.000	1.019	1.006	1.405	1.394
.260	1.371	1.091	1.059	1.005	1.023	1.014	1.480	1.395
.303	1.441	1.101	1.066	.996	1.013	1.006	1.434	1.402
.347	1.452	1.090	1.068	.996	1.004	1.001	1.430	1.412
.389	1.764	1.103	1.067	.993	1.004	1.001	1.436	1.417
.433	2.632	1.082	1.093	.982	1.000	.994	1.428	1.424
.476	2.854	1.158	1.121	.984	1.988	.996	1.429	1.425
.519	2.845	1.242	1.059	.986	.991	.993	1.433	1.419
.563	2.847	1.320	1.058	.983	.988	.983	1.441	1.424
.606	2.835	1.365	1.042	.989	.993	.989	1.449	1.429
.649	2.887	1.430	1.045	.981	.980	.985	1.438	1.433
.692	2.849	2.198	1.059	.983	.984	.985	1.441	1.428
.735	2.936	2.765	1.054	.981	.976	.976	1.426	1.417
.780	2.954	2.873	1.038	.984	.985	.984	1.440	1.403
.822	2.954	2.905	1.064	.982	.981	.989	1.432	1.391
.865	2.953	2.891	1.067	.979	.973	1.046	1.412	1.367

X	p/p_{wedge}				
	Run 32	Run 33	Run 34	Run 35	Run 36
0.216	1.534	1.480	1.114	1.417	1.464
.260	1.526	1.475	1.107	1.420	1.465
.303	1.525	1.478	1.109	1.429	1.470
.347	1.530	1.485	1.117	1.445	1.479
.389	1.530	1.487	1.123	1.450	1.483
.433	1.528	1.493	1.132	1.470	1.500
.476	1.522	1.483	1.108	1.458	1.479
.519	1.516	1.475	1.084	1.449	1.462
.563	1.531	1.484	1.087	1.472	1.477
.606	1.531	1.484	1.069	1.474	1.487
.649	1.533	1.488	1.057	1.482	1.484
.692	1.529	1.486	1.038	1.475	1.480
.735	1.520	1.472	1.015	1.465	1.471
.780	1.512	1.460	.997	1.465	1.462
.822	1.505	1.449	.988	1.457	1.454
.865	1.489	1.424	.970	1.438	1.429

TABLE IX.- ADDITIONAL PRESSURE DATA — Continued

(d) Test 357, 0.025-m-diameter hemisphere, Mach 20 helium. Values of p_{stag} are listed in table VII(d).

Θ, deg	p/p_{stag}							
	Run 3	Run 4	Run 7	Run 8	Run 9	Run 11	Run 12	Run 15
-90	0.421	0.418	0.269	0.265	0.283	0.036	0.119	0.424
-80	.665	.665	.464	.457	.484	.053	.206	.639
-70	1.070	1.076	.812	.798	.833	.049	.415	1.040
-60	1.554	1.560	1.252	1.233	1.268	.076	.703	1.549
-50	2.145	2.128	1.816	1.799	1.885	.198	1.134	2.223
-40	2.740	2.710	2.339	2.323	2.509	.673	1.666	2.913
-30	3.189	3.180	2.801	2.729	3.351	1.711	2.134	4.872
-20	3.442	3.454	3.326	3.124	4.141	2.768	2.557	2.941
-10	3.666	3.426	3.657	3.264	.719	3.640	2.784	.596
0	.654	1.873	.553	1.790	.895	3.835	2.396	1.014
10	.725	.471	.954	.591	.819	3.310	.667	.842
20	.803	.653	.772	.801	.737	1.962	.793	.732
30	.604	.603	.614	.621	.622	.621	.615	.597

Θ, deg	p/p_{stag}				
	Run 16	Run 17	Run 19	Run 20	Run 21
-90	0.431	0.423	0.281	0.275	0.283
-80	.647	.636	.449	.443	.451
-70	1.080	1.065	.819	.797	.820
-60	1.590	1.557	1.273	1.261	1.256
-50	2.207	2.136	1.839	1.798	1.874
-40	2.793	2.712	2.419	2.306	2.354
-30	3.235	3.151	3.216	2.771	5.417
-20	6.002	3.426	5.624	3.253	1.237
-10	.730	3.675	.658	3.799	.930
0	.903	.568	.853	.571	.973
10	.901	.769	.805	.931	.893
20	.762	.803	.729	.773	.797
30	.613	.592	.613	.614	.660

TABLE IX.- ADDITIONAL PRESSURE DATA — Concluded

(e) Test 16, 0.025-m-diameter hemisphere, Mach 19 nitrogen.

Values of p_{stag} are listed in table VII(e).

Θ, deg	p/p_{stag}		
	Run 4	Run 6	Run 7
-90	0.322	0.219	0.217
-80	.446	.318	.362
-70	.863	.775	.817
-60	1.271	1.142	1.223
-50	1.857	1.628	1.727
-40	2.824	2.350	2.397
-30	3.725	2.948	2.872
-20	2.628	3.703	3.534
-10	.883	1.542	3.285
0	1.084	.890	1.418
10	.979	.837	.685
20	.678	1.547	.548
30	.636	.546	.554

(f) Test 63, 0.025-m-diameter hemisphere, Mach 8.9 CF_4.

Values of p_{stag} are listed in table VII(f).

Θ, deg	p/p_{stag}							
	Run 1	Run 2	Run 3	Run 5	Run 6	Run 7	Run 9	Run 10
-80	0.044	0.054	0.101	0.175	0.457	0.327	0.045	0.152
-70	.238	.266	.439	.635	.999	.760	.194	.460
-60	.770	.778	1.128	1.386	2.078	1.425	.586	.856
-50	1.722	1.683	1.936	2.052	1.581	2.031	1.181	1.273
-40	2.499	2.451	2.475	2.548	.991	2.615	1.660	1.702
-30	2.841	2.830	2.973	3.806	.952	3.686	1.999	1.842
-20	2.919	2.837	2.214	.941	.937	.920	2.103	2.095
-10	2.325	2.277	1.223	.886	1.945	.948	1.935	1.079
0	.786	.871	.796	.955	.967	.971	1.394	.896
10	.675	.649	.822	.926	.939	.923	.939	.948
20	.679	.658	.778	.823	.842	.831	.825	.859
30	.596	.615	.603	.649	.673	.687	.664	.696

Θ, deg	p/p_{stag}							
	Run 12	Run 13	Run 14	Run 15	Run 16	Run 17	Run 18	Run 19
-80	0.294	0.186	0.170	0.293	0.133	0.080	0.098	0.107
-70	.522	.492	.481	.521	.274	.201	.239	.244
-60	.872	.860	.859	.847	.466	.403	.446	.420
-50	1.507	1.257	1.248	1.412	.695	.668	.671	.588
-40	1.164	1.698	1.675	1.702	.991	.955	.858	.726
-30	.997	2.623	1.990	1.009	1.250	1.228	.932	.781
-20	.933	.917	1.536	.927	1.364	1.102	.880	.807
-10	.959	.955	.914	.955	1.342	.953	.935	.916
0	.963	.949	.996	.953	1.199	.961	.962	.962
10	.940	.916	.917	.925	.932	.928	.938	.943
20	.851	.825	.831	.838	.821	.832	.842	.846
30	.702	.666	.676	.684	.674	.666	.693	.701

Figure 1.- Six types of shock interference patterns.
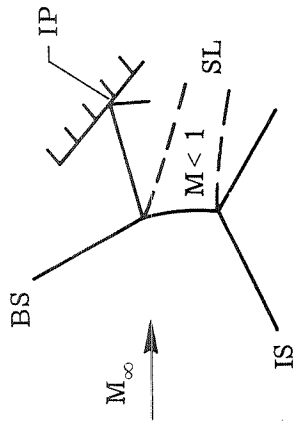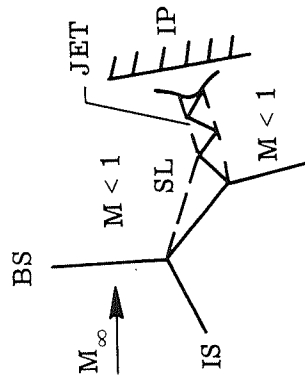
(a) Type I.

(b) Type II.

(c) Type III.

(d) Type IV.

(e) Type V.

(f) Type VI.

Type VI
expansion wave
impingement

Bow shock

Type V shock
impingement

Sonic point

M_∞

Type IV
supersonic jet
impingement

Sonic point

Type III shear
layer attachment

Impinging
shock

Type II shock
impingement

Type I shock
impingement
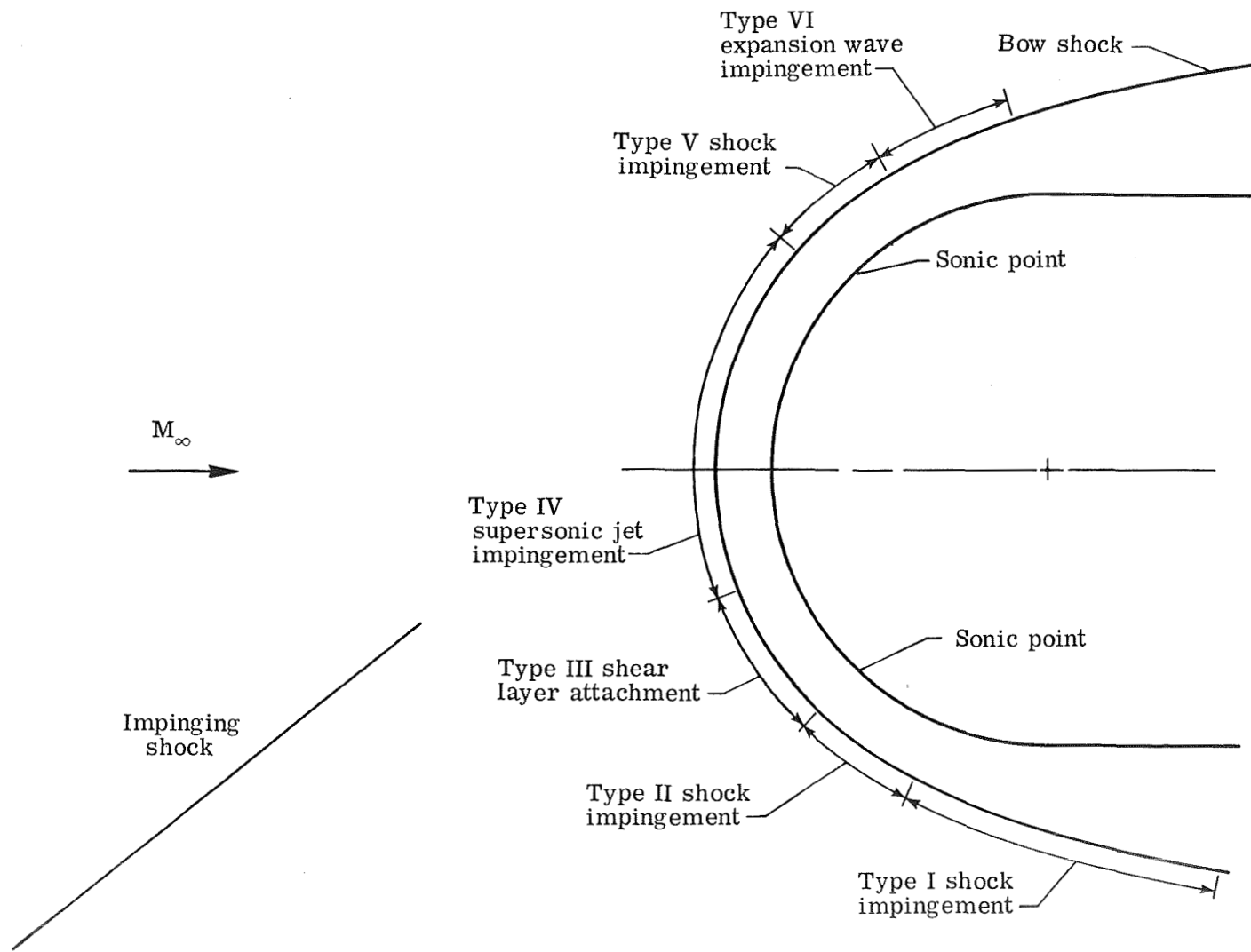
Figure 2.- Location of the types of interference on a hemisphere.
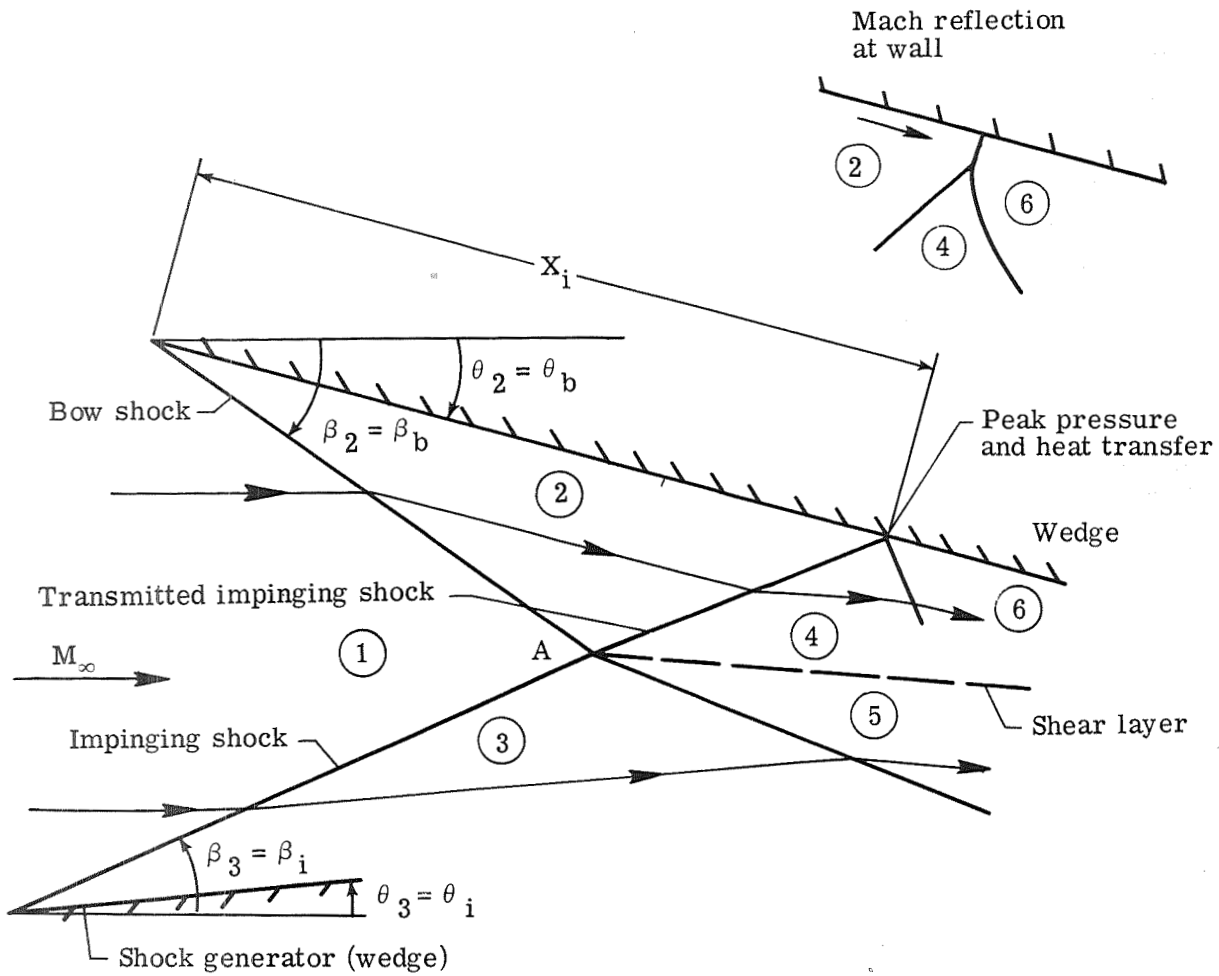
Figure 3.- Type I shock interference pattern.
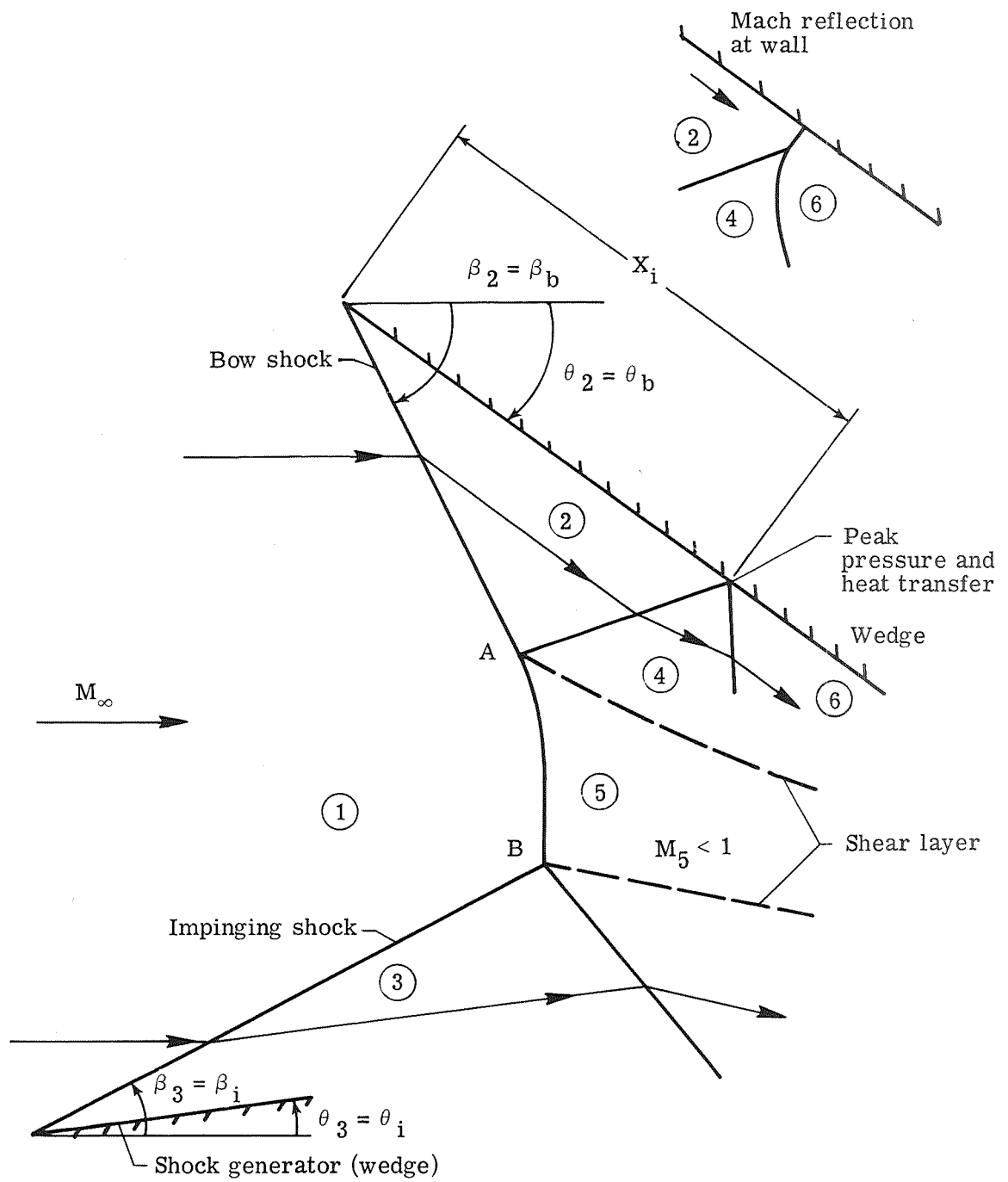
Figure 4.- Type II shock interference pattern.
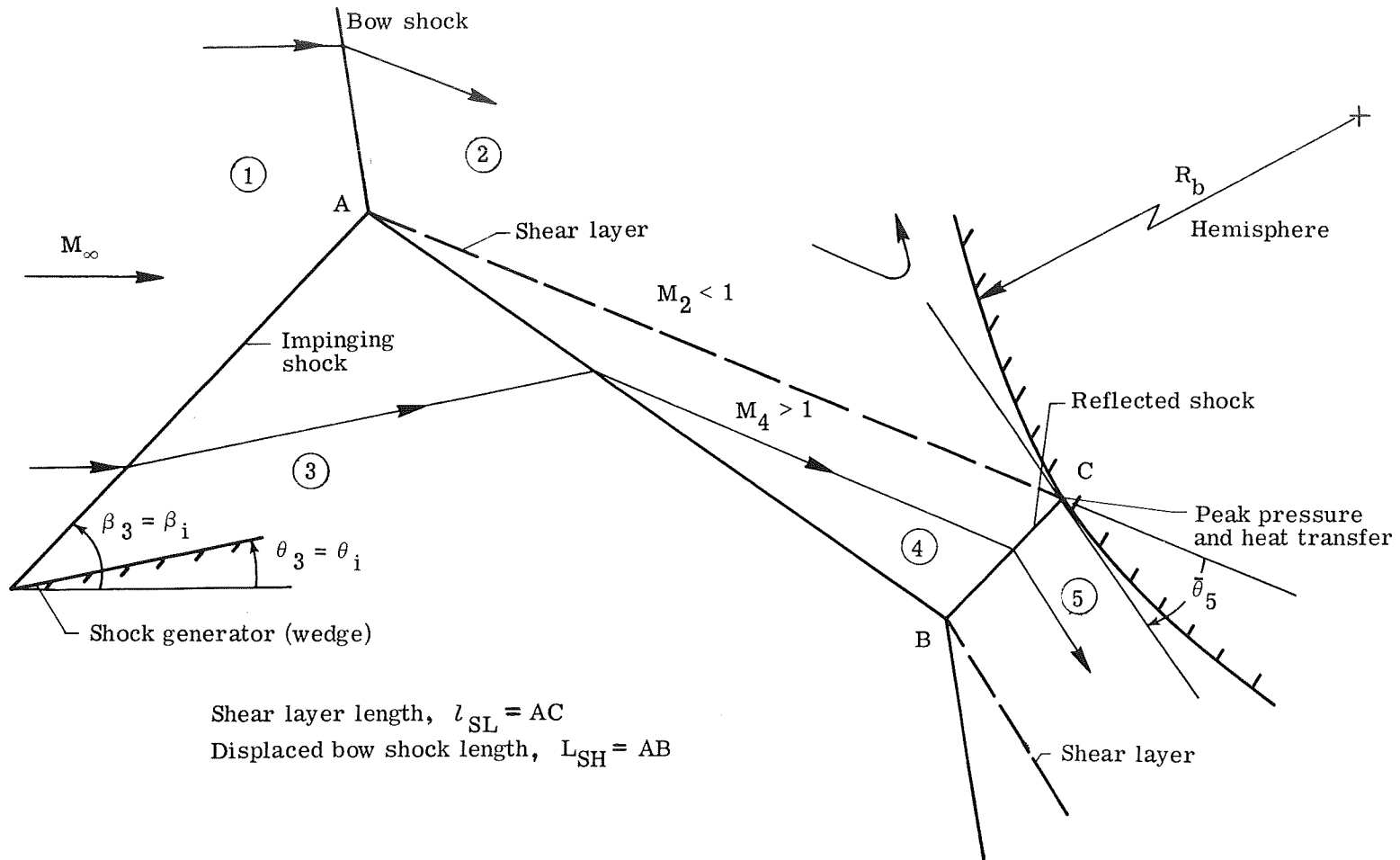
Figure 5.- Type III shock interference pattern.
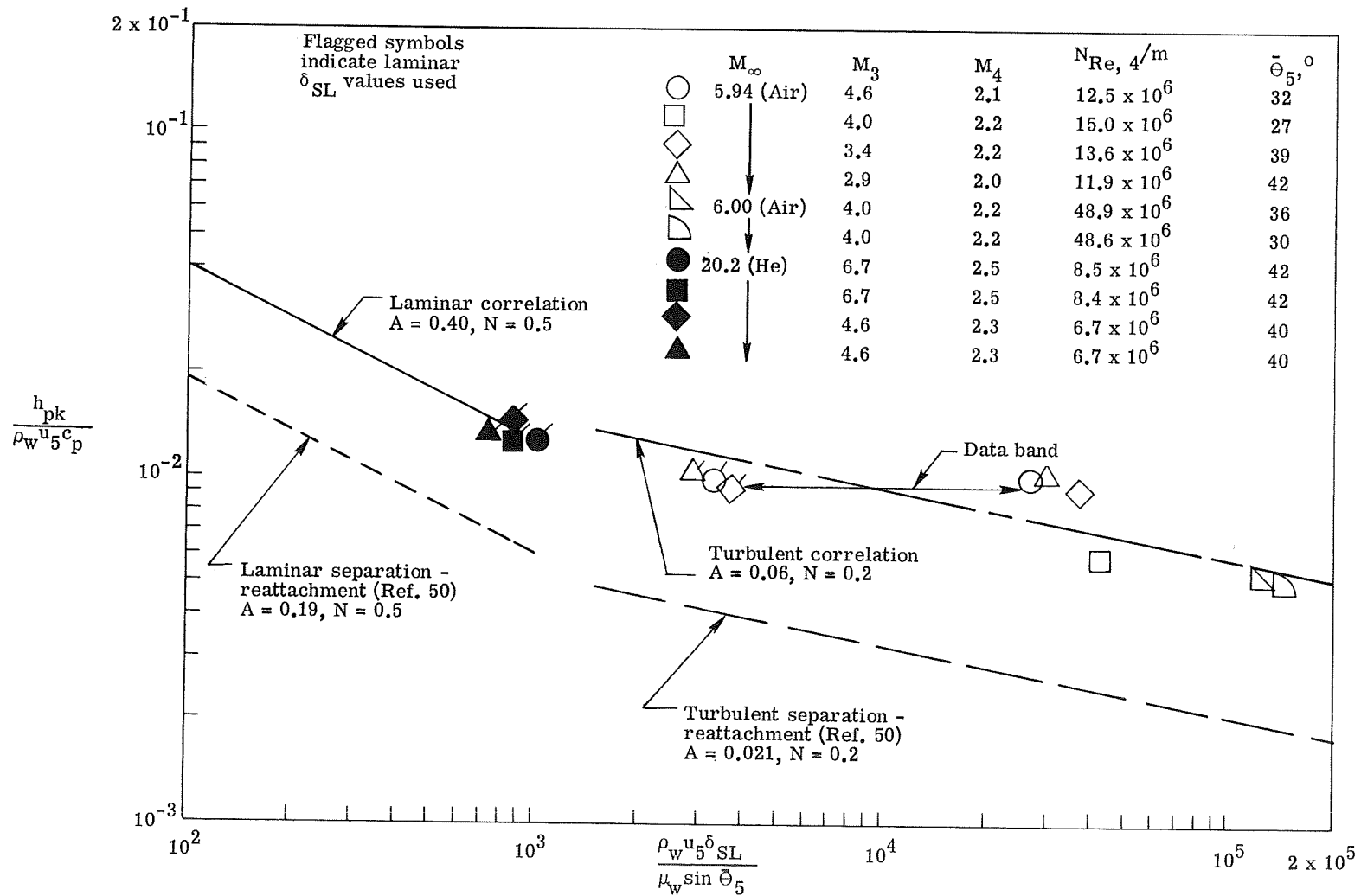
Figure 6.- Heat-transfer correlations for laminar and turbulent free shear layer attachment (ref. 38). $T_w/T_{t,\infty} \approx 0.9$.
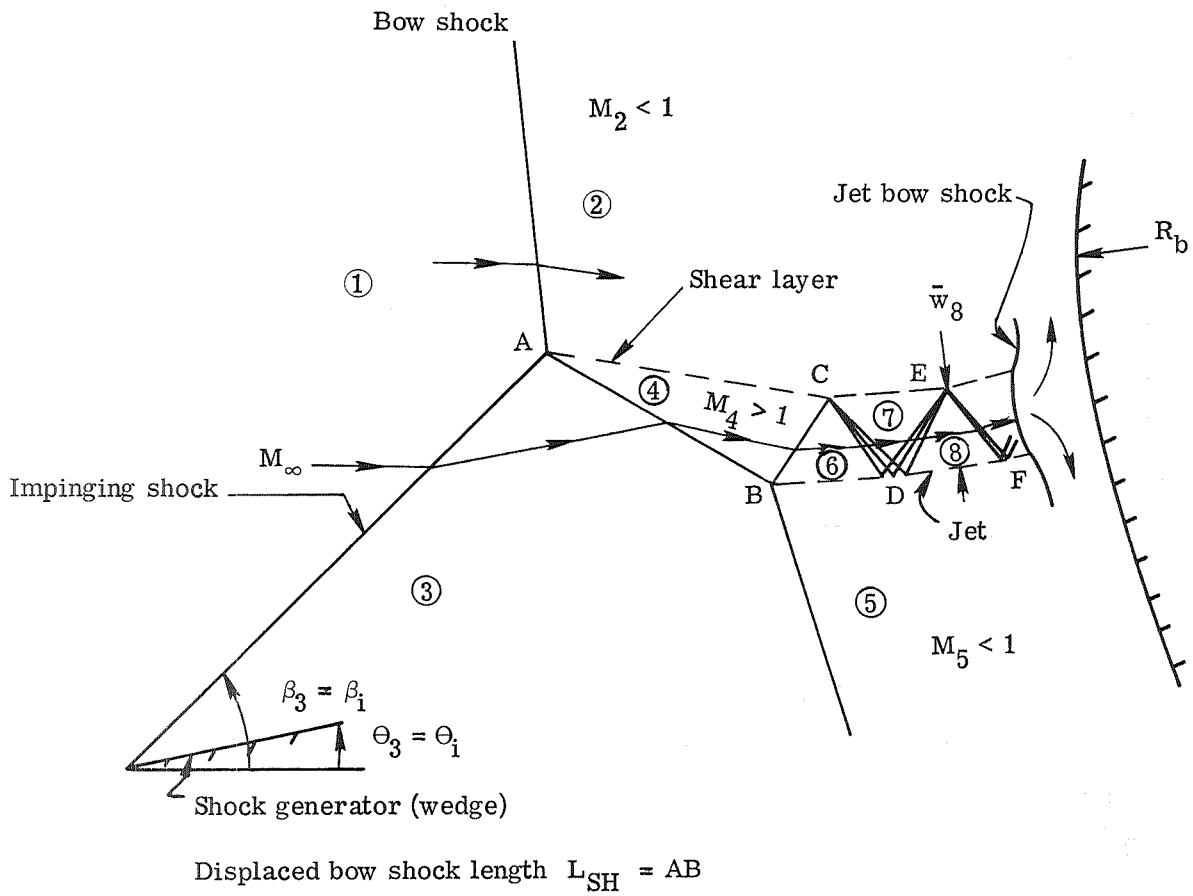
Figure 7.- Type IV shock interference pattern.
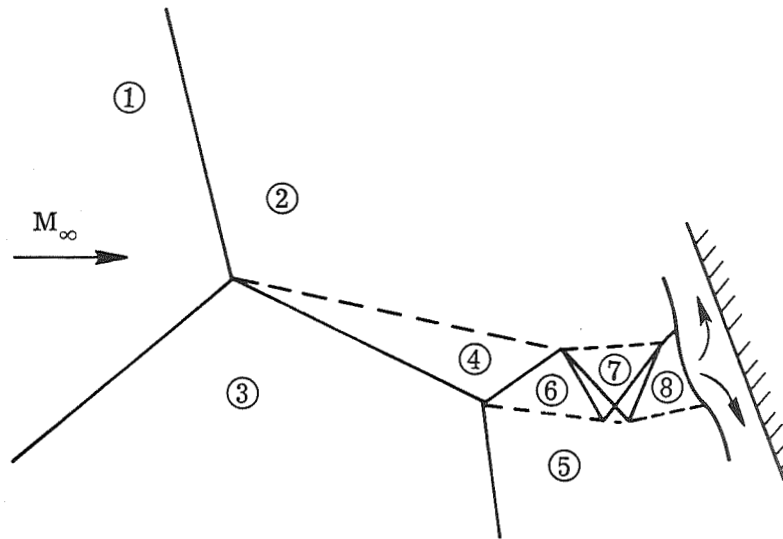
(a) Downward sloping shear layer.
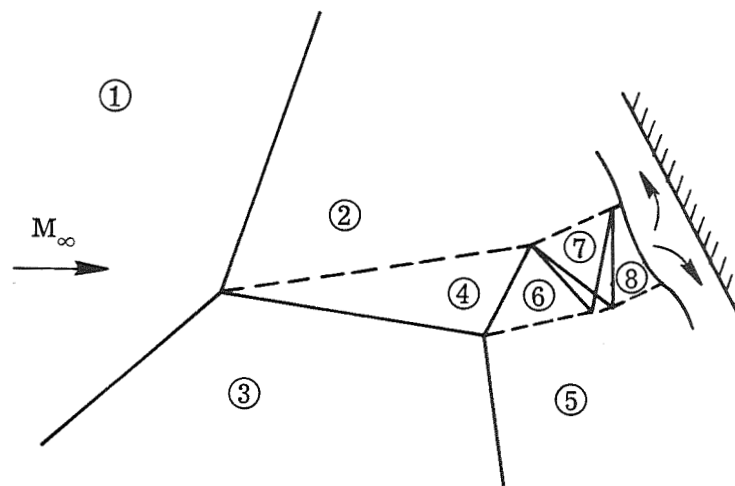
(b) Upward sloping shear layer.

Figure 8.- Jet configuration for downward and upward sloping shear layers with jet bow shock in region 8.
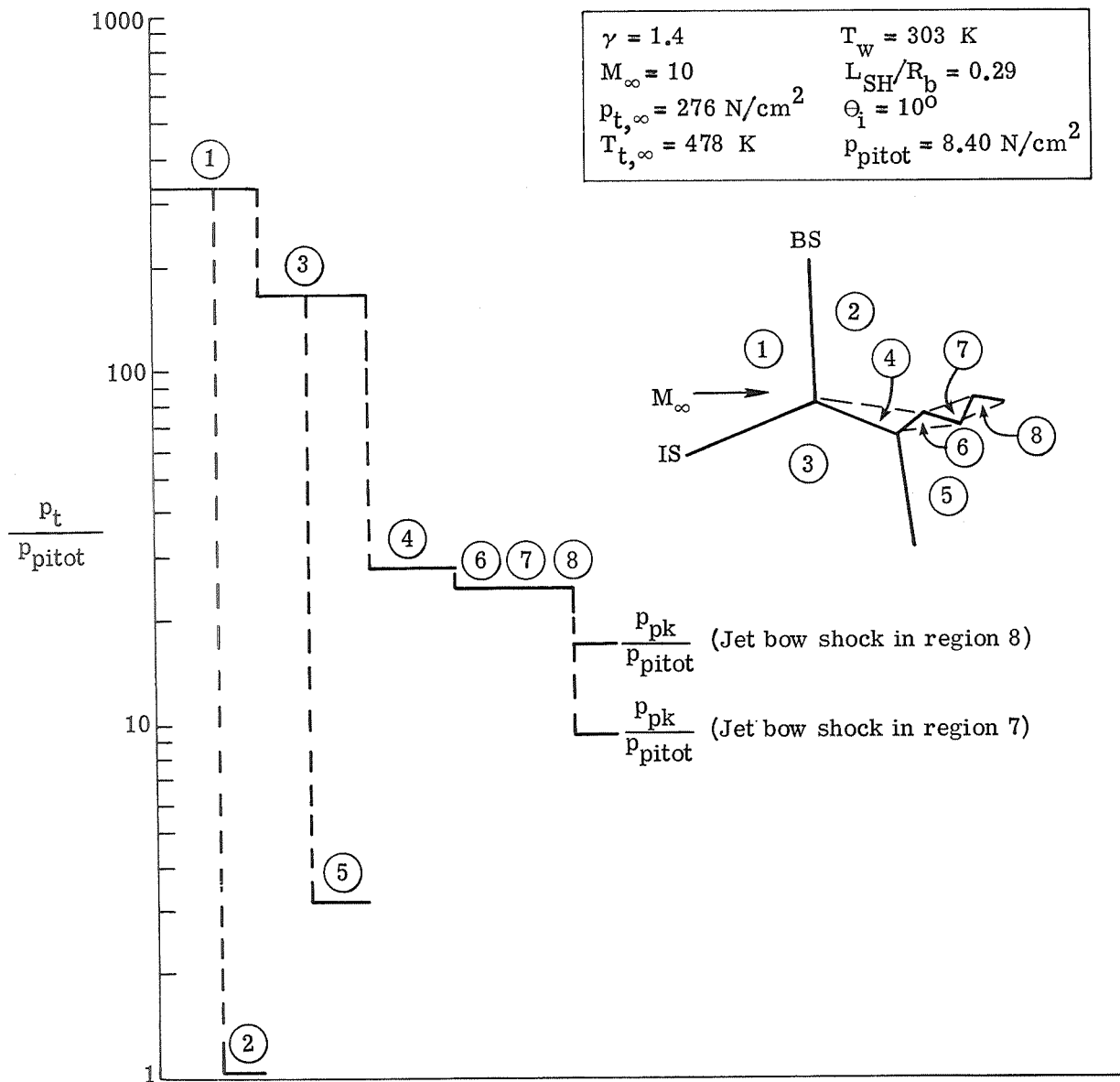
Figure 9.- Total-pressure distribution for type IV interference.

The chart axis label reads $\dfrac{p_t}{p_{pitot}}$ with values 1, 10, 100, 1000.

The box contains:

$\gamma = 1.4$ $T_w = 303 \text{ K}$

$M_\infty = 10$ $L_{SH}/R_b = 0.29$

$p_{t,\infty} = 276 \text{ N/cm}^2$ $\theta_i = 10^0$

$T_{t,\infty} = 478 \text{ K}$ $p_{pitot} = 8.40 \text{ N/cm}^2$

$\dfrac{p_{pk}}{p_{pitot}}$ (Jet bow shock in region 8)

$\dfrac{p_{pk}}{p_{pitot}}$ (Jet bow shock in region 7)
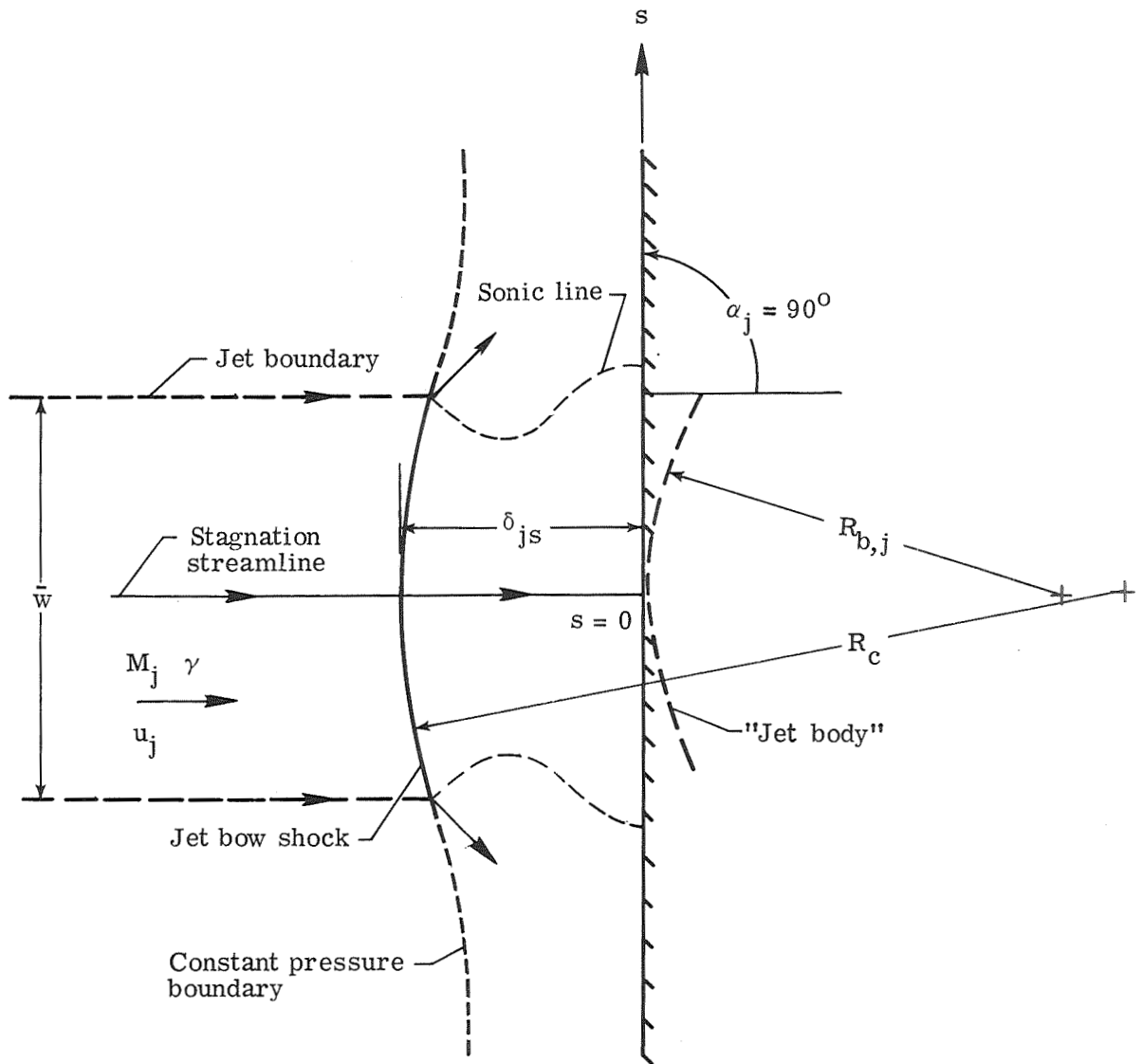
Figure 10.- Normal jet impingement model for $M_j < 2.8$ (ref. 57).
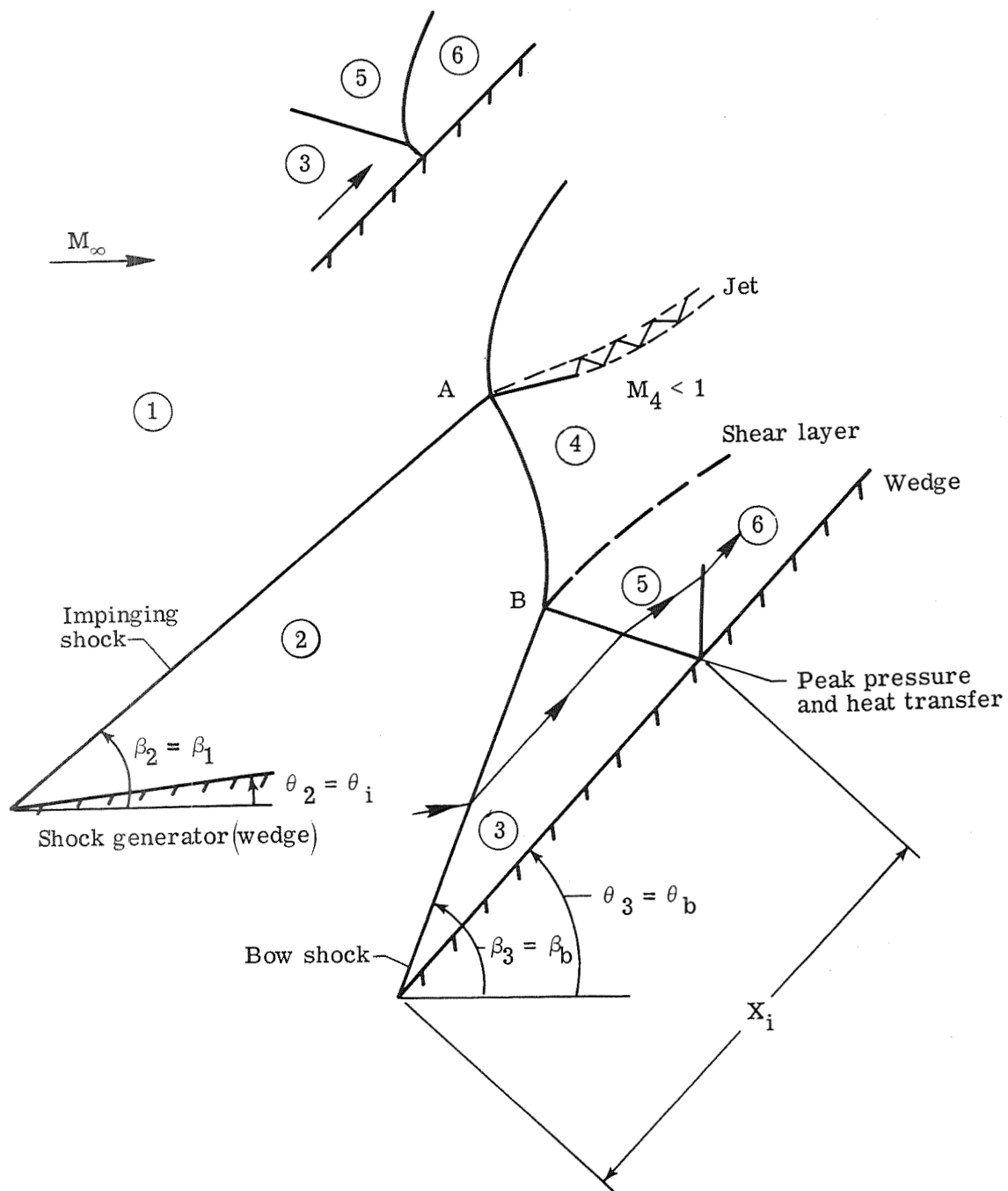
Figure 11.- Type V shock interference pattern.
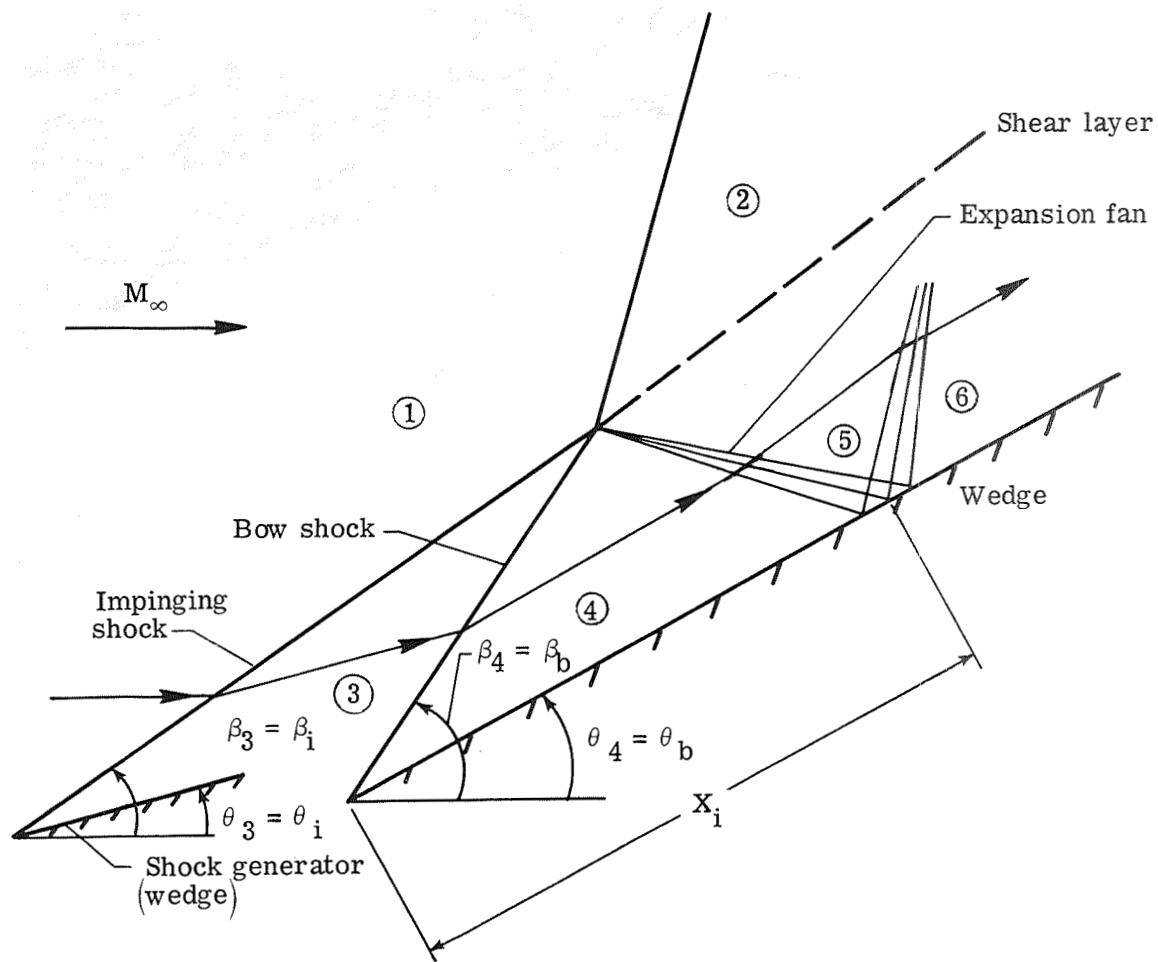
Figure 12.- Type VI shock interference pattern.
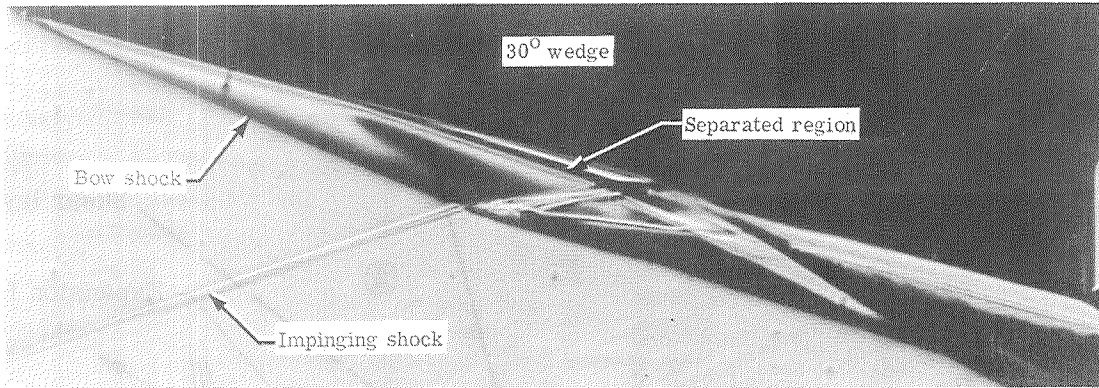
(a) Schlieren photograph.

L-73-232

Test run	$P_{t,\infty}$, N/cm^2	$T_{t,\infty}$, K	P_{wedge}, N/cm^2	θ_i, deg	θ_b, deg
6358 - 21	290	488	1.12	10.0	-15.0

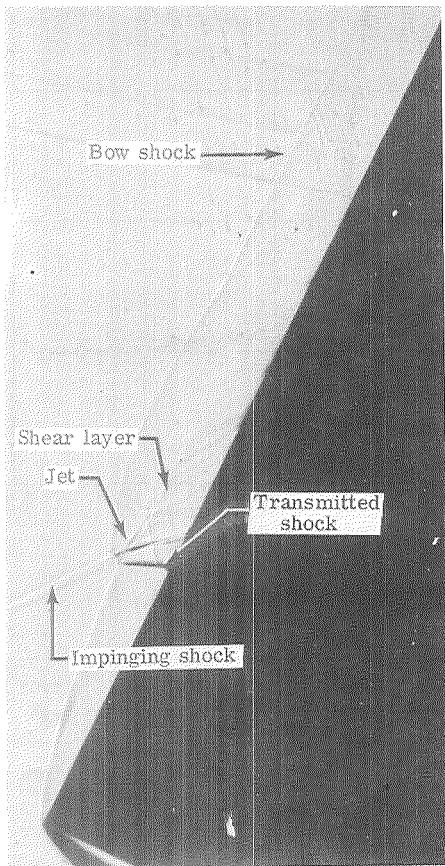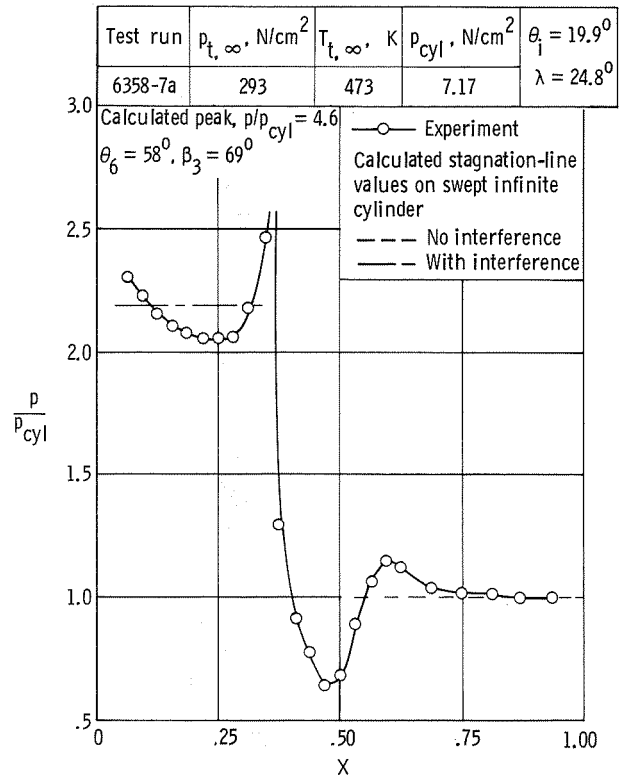| Test run	$P_{t,\infty}$, N/cm^2	$T_{t,\infty}$, K	T_w, K	Q_{wedge}, W/cm^2	$\theta_i = 9.9^0$
6363-26 ◯	289	489	394	0.96	$\theta_b = -15.0^0$
6363-27 □	294	484	422	0.64	
6363-28 ◇	288	488	367	1.25	
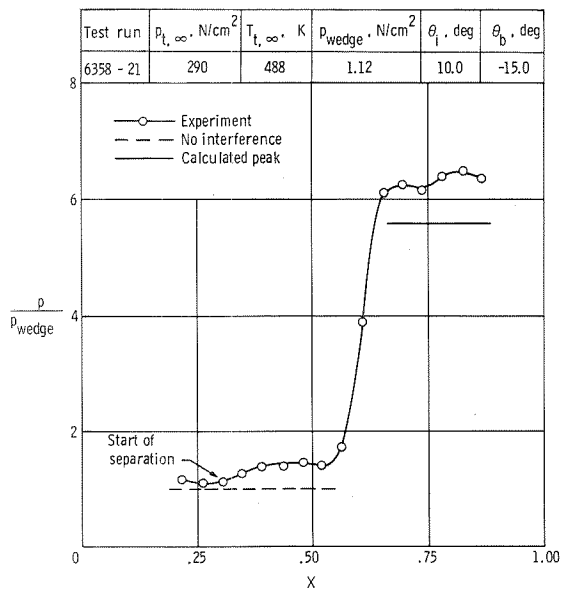
(b) Pressure distribution.
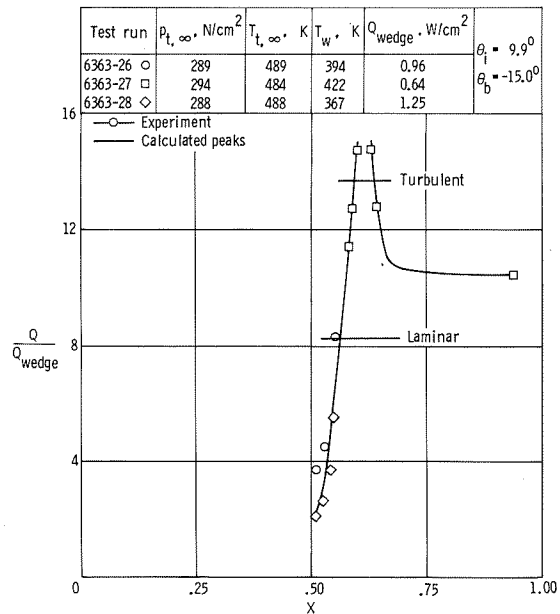
(c) Heat-transfer distribution.

Figure 13.- Type I interference on a 30^0 wedge at Mach 6.00 in air. $\theta_i = 9.9^0$; $N_{Re,\infty}/m \approx 25.8 \times 10^6$; $\gamma = 1.4$.
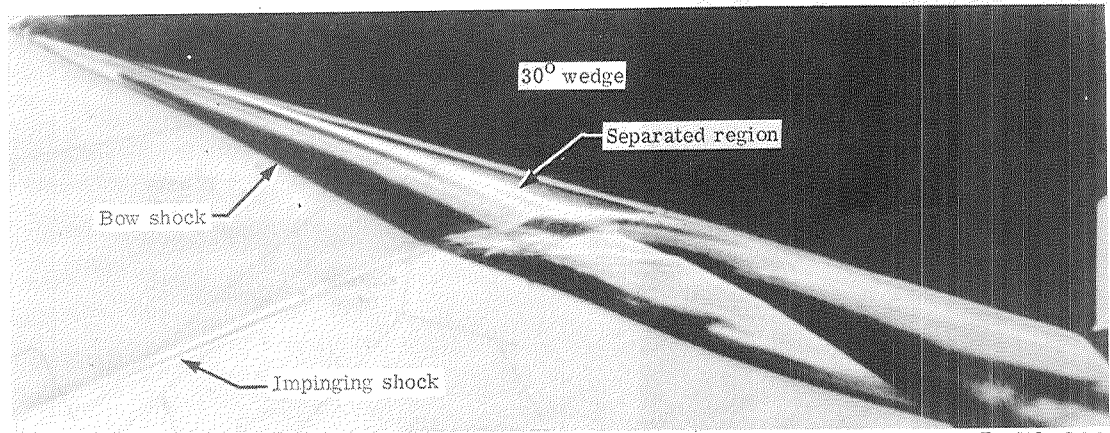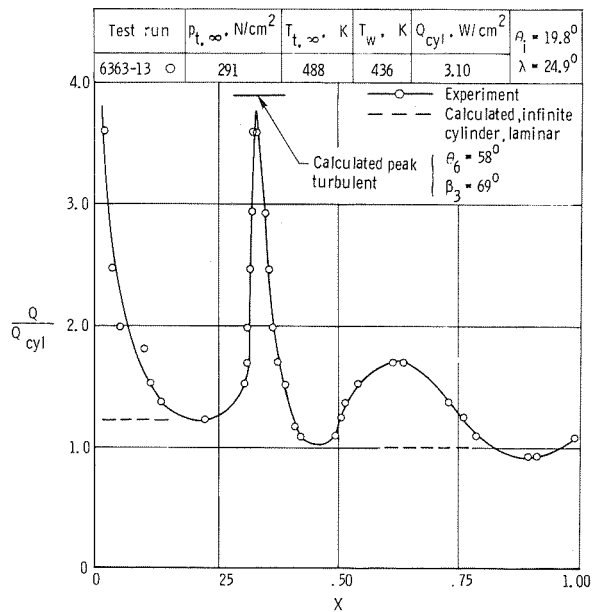
(a) Schlieren photograph.
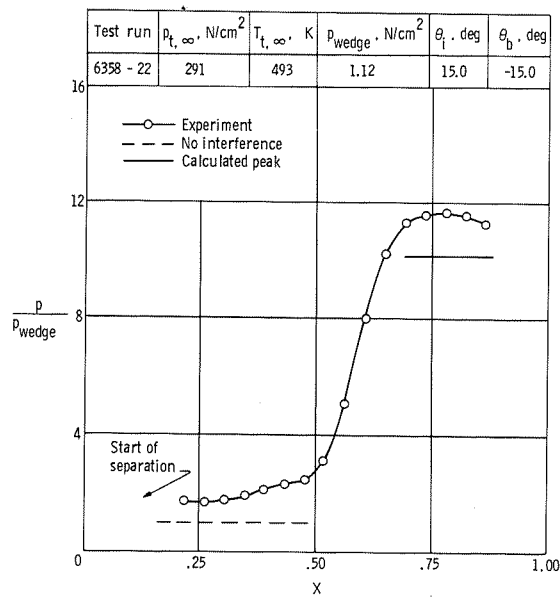
(b) Pressure distribution.
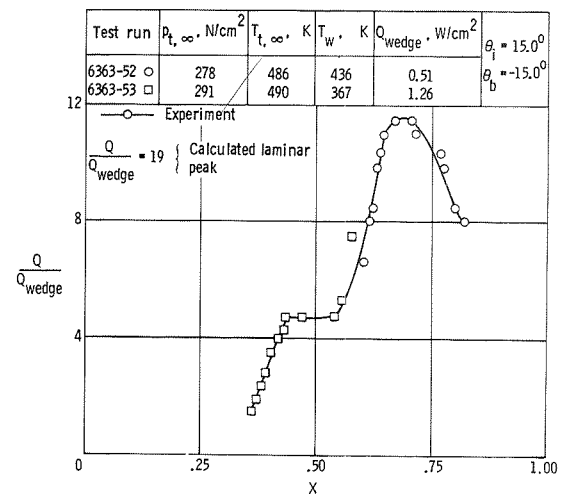
(c) Heat-transfer distribution.

Figure 14.- Type I interference on a 30° wedge at Mach 6.00 in air. $\theta_i = 15^O$; $N_{Re,\infty}/m \approx 25.3 \times 10^6$; $\gamma = 1.4$.
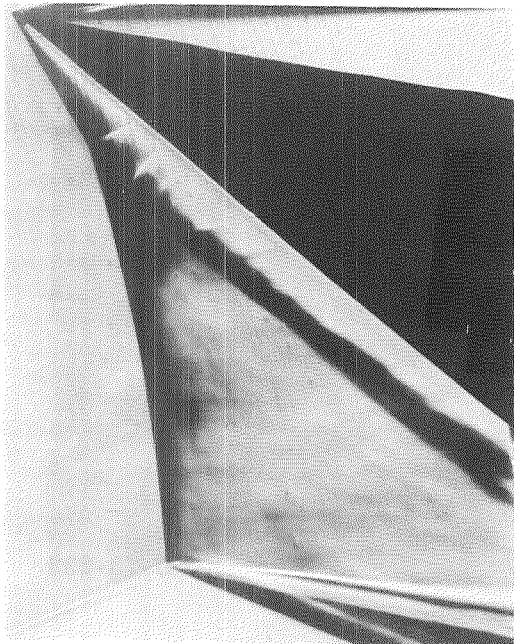
L-73-234

(a) Schlieren photograph.
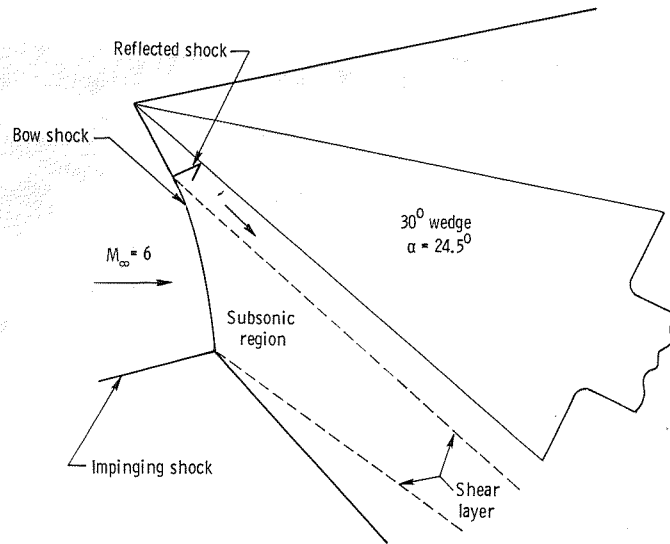
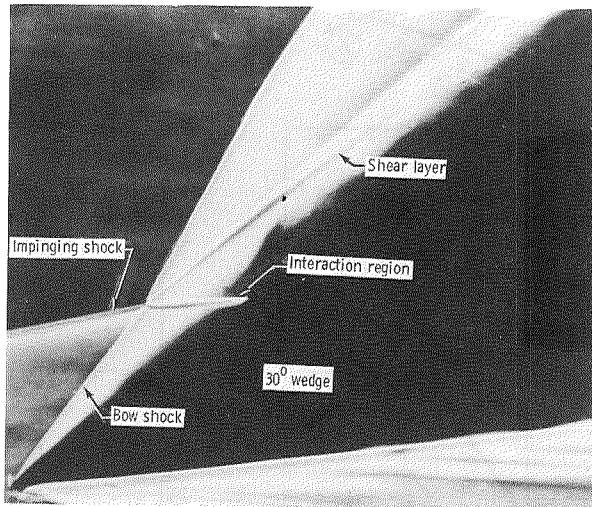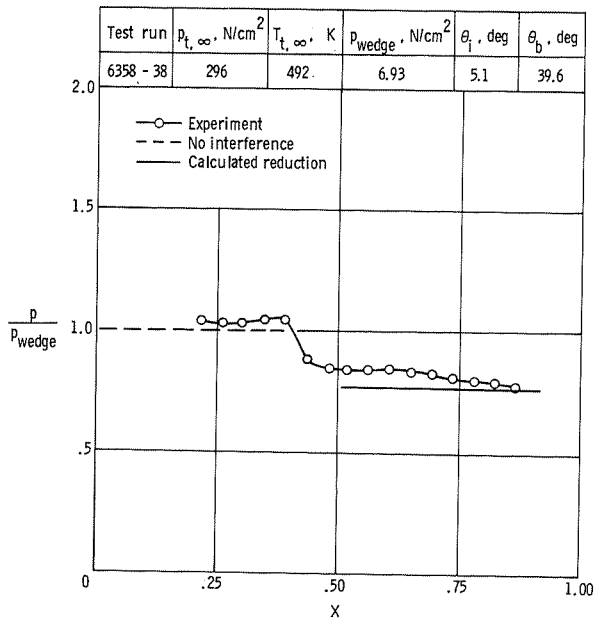(b) Sketch of shock pattern.
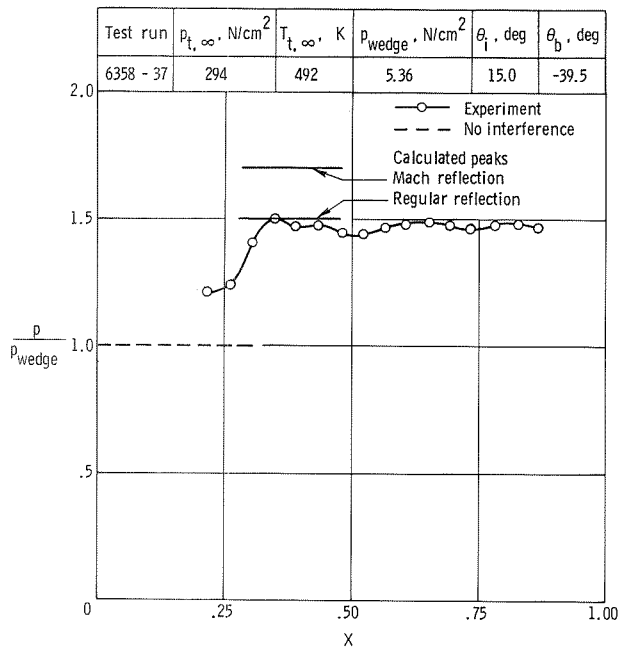
(c) Pressure distribution.
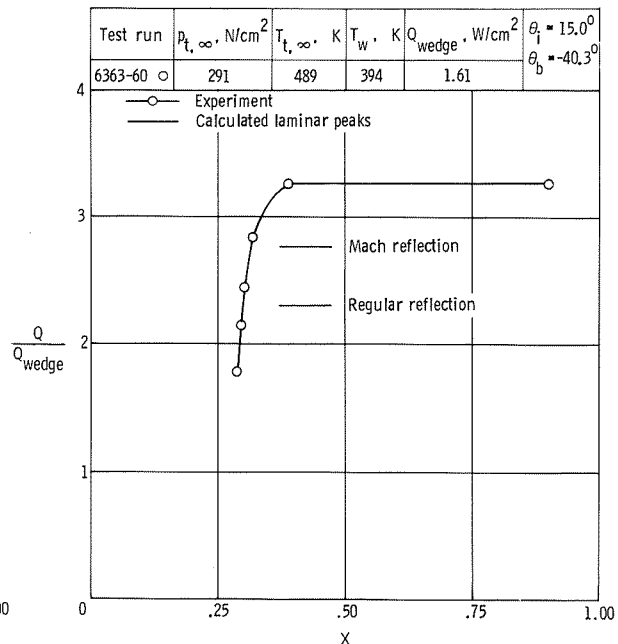
(d) Heat-transfer distribution.

Figure 15.- Type II interference on a 30° wedge at Mach 6.00 in air.
$\theta_i = 15^O$; $N_{Re,\infty}/m \approx 25.7 \times 10^6$; $\gamma = 1.4$.
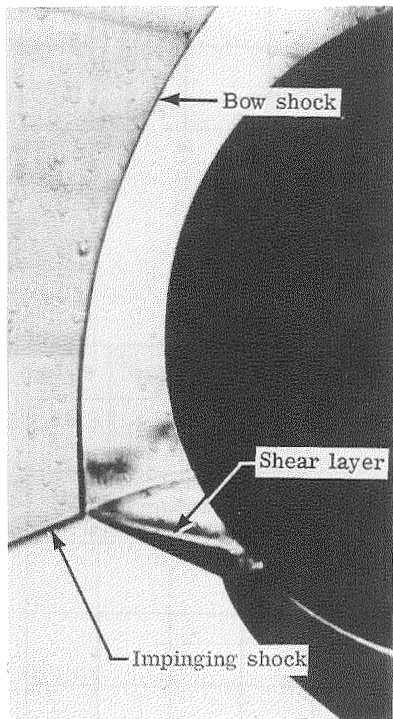
Test run	$p_{t,\infty}$, N/cm²	$T_{t,\infty}$, K	p_{stag}, N/cm²	θ_i, deg	$\bar{\theta}_5$, deg
6344 - 5a	294	477	8.73	14.8	36.0

Experiment
No interference
Calculated peak

(b) Pressure distribution.

Test run		$p_{t,\infty}$, N/cm²	$T_{t,\infty}$, K	T_w, K	Q_{stag}, W/cm²	θ_i, deg
6363 - 36	○	289	486	408	4.37	14.8
6363 - 37	□	292	488	436	2.94	14.8

Ref. 38 $\left\{ \begin{array}{l} \delta_{SL,L}, \; \dfrac{Q_{pk}}{Q_{stag}} = 23.5 \\ \delta_{SL,T} \end{array} \right.$

Experiment
No interference
Calculated turbulent peaks

Ref. 50 $\{ \delta_{SL,T}$
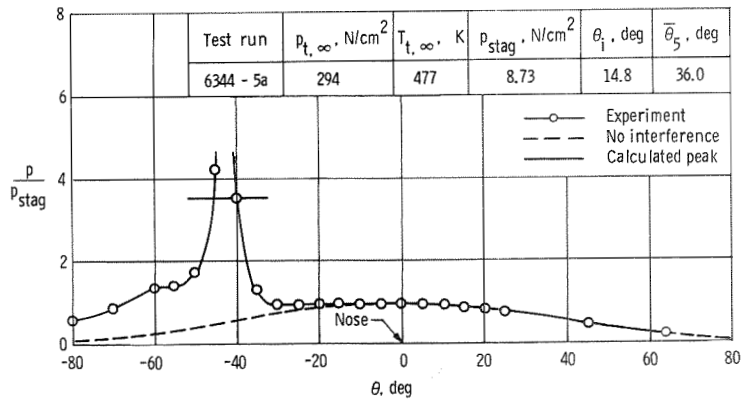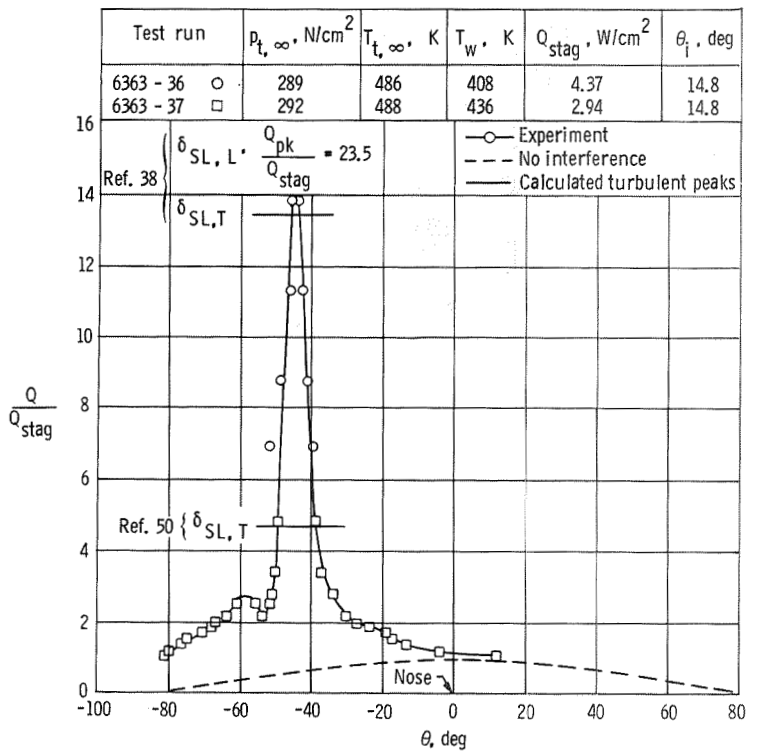
(c) Heat-transfer distribution.

Figure 16.- Type III interference on a 0.051-m-diameter hemisphere at Mach 6.00 in air. $\theta_i = 14.8°$; $N_{Re,\infty}/m = 25.9 \times 10^6$; $\gamma = 1.4$.

Test run	$p_{t,\infty}$, N/cm²	$T_{t,\infty}$, K	p_{stag}, N/cm²	θ_i, deg	$\bar{\theta}_5$, deg
6344 - 7a	292	476	8.78	14.8	30.0

(b) Pressure distribution.

Test run		$p_{t,\infty}$, N/cm²	$T_{t,\infty}$, K	T_w, K	Q_{stag}, W/cm²	θ_i, deg
6363 - 40	○	290	489	436	3.00	14.8
6363 - 39	□	290	486	408	4.41	14.8

(c) Heat-transfer distribution.

Figure 17.- Type III interference on a 0.051-m-diameter hemisphere at Mach 6.00 in air. $\theta_i = 14.8°$; $N_{Re,\infty}/m \approx 25.8 \times 10^6$; $\gamma = 1.4$.
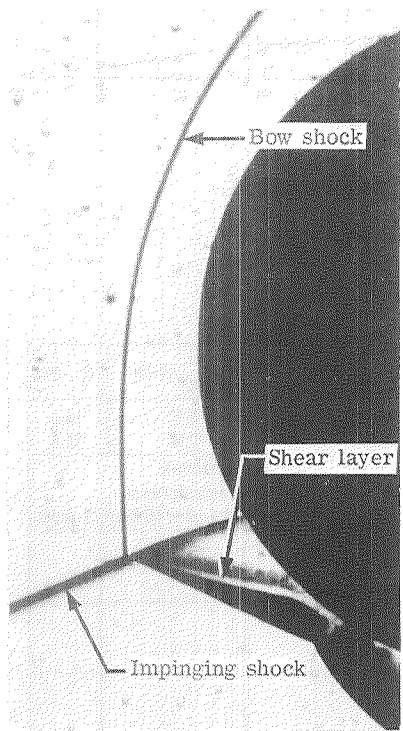
L-73-236
(a) Schlieren photograph.

L-73-237

(a) Schlieren photograph.

Test run	$p_{t,\infty}$, N/cm^2	$T_{t,\infty}$, K	p_{stag}, N/cm^2	θ_i, deg	$\overline{\theta}_5$, deg
357 - 18	701	445	1.92	9.6	41.5

(b) Pressure distribution.

Test run		$p_{t,\infty}$, N/cm^2	$T_{t,\infty}$, K	T_w, K	Q_{stag}, W/cm^2	θ_i, deg
373 - 26	○	707	436	381	6.25	10.1
373 - 11	□	705	431	381	6.51	10.1
373 - 12	◇	705	435	367	8.33	10.1
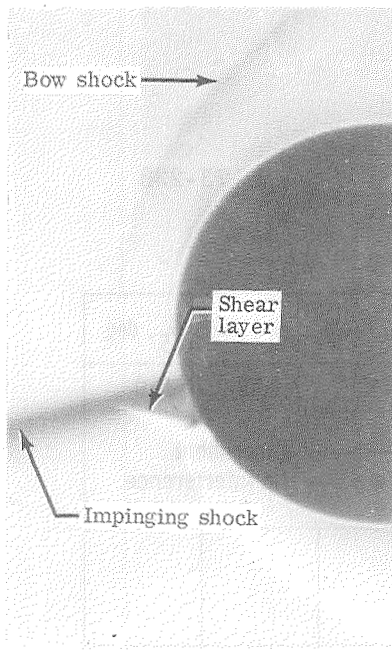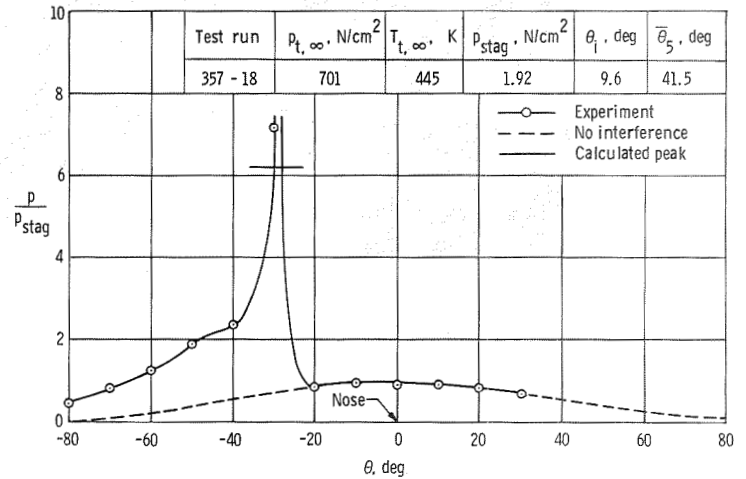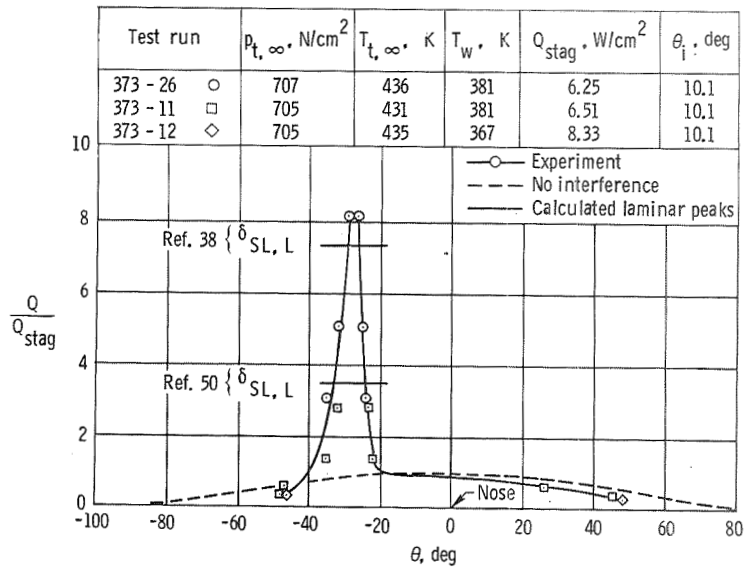
(c) Heat-transfer distribution.

Figure 18.- Type III interference on a 0.025-m-diameter hemisphere at Mach 20.2 in helium. $\theta_i \approx 10^O$; $N_{Re,\infty}/m \approx 9.8 \times 10^6$; $\gamma = 1.67$.
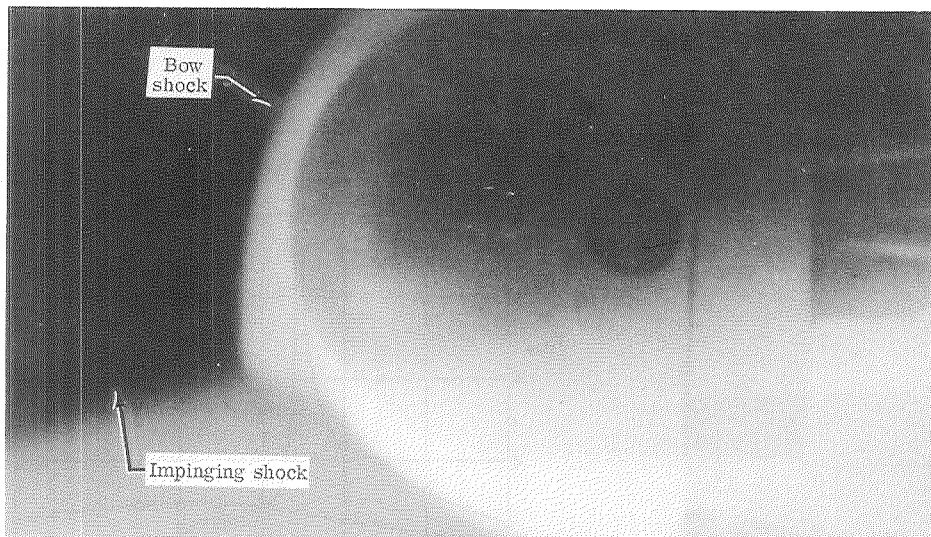
L-73-238

(a) Electron beam photograph.

Test run	$p_{t,\infty}$, N/cm^2	$T_{t,\infty}$, K	p_{stag}, N/cm^2	θ_i, deg	$\bar{\theta}_5$, deg
16 - 2	4411	1644	0.450	15.0	40.0
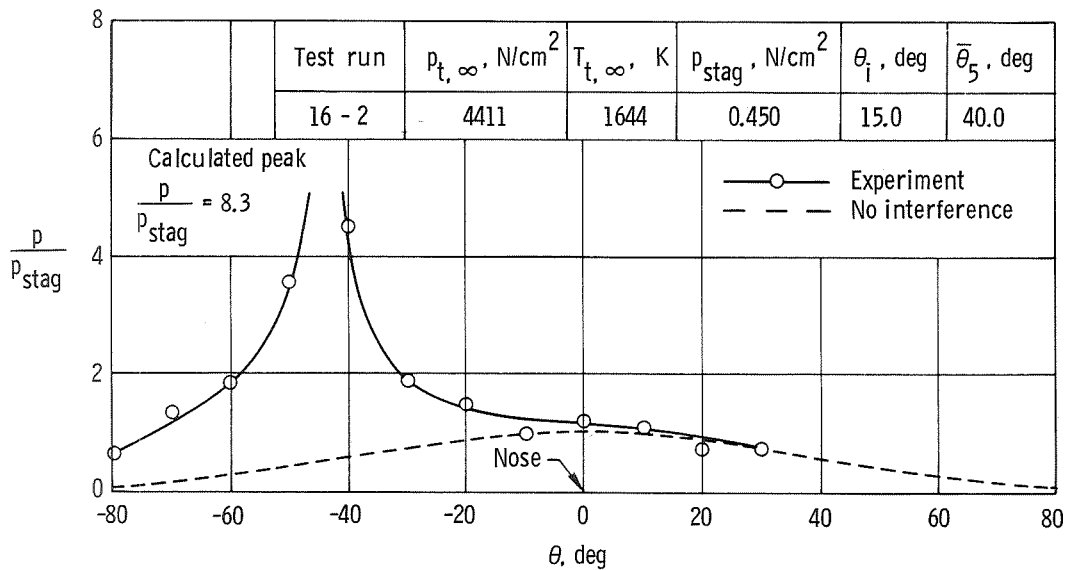
(b) Pressure distribution.

	Experiment	Calculated (laminar)
$\dfrac{Q_{pk}}{Q_{stag}}$	5.90	4.4 (Ref. 50) 10.2 (Ref. 38)

(c) Peak heat transfer (Run 16-13).

Figure 19.- Type III interference on a 0.025-m-diameter hemisphere at Mach 19.9 in nitrogen. $\theta_i = 15^O$; $N_{Re,\infty}/m \approx 2.8 \times 10^6$; $\gamma = 1.4$.

72

(a) Shadowgraph.

L-73-239

Test run	$p_{t,\infty}$, N/cm^2	$T_{t,\infty}$, K	p_{stag}, N/cm^2	θ_i, deg	$\overline{\theta}_5$, deg
63 - 4	972	289	0.952	14.9	20.0
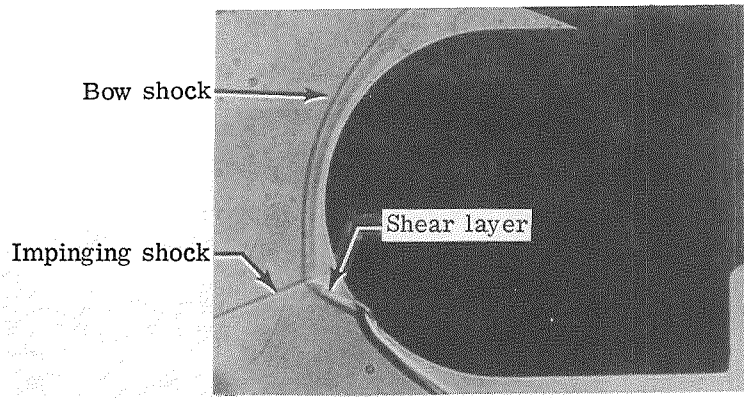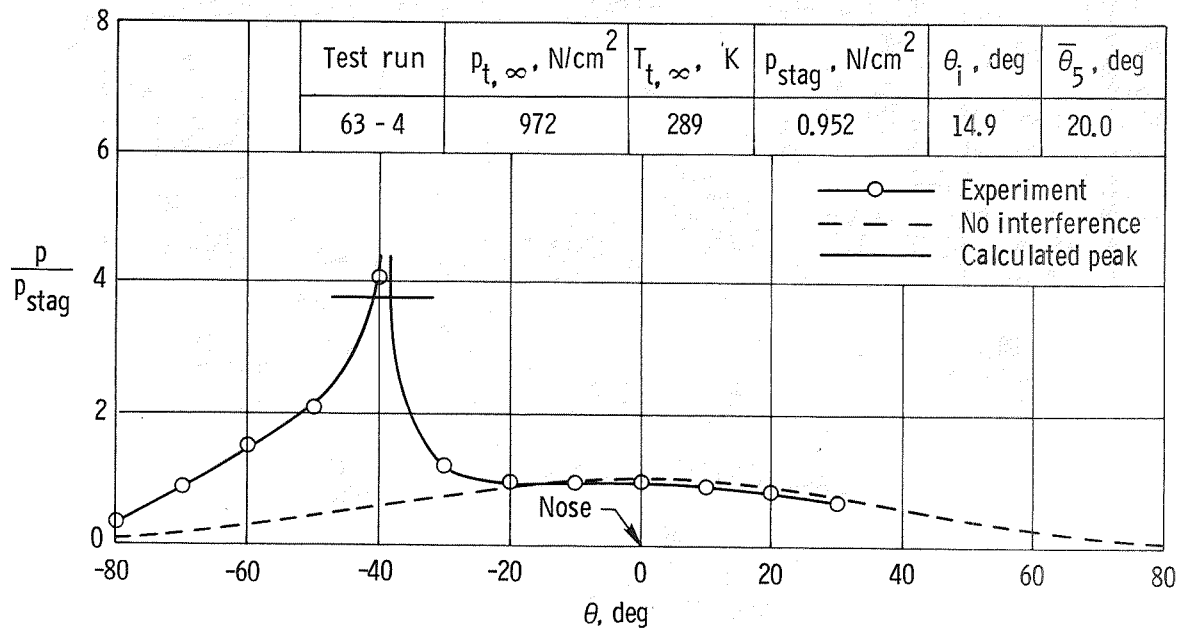
(b) Pressure distribution.

Figure 20.- Type III interference on a 0.025-m-diameter hemisphere at Mach 8.9 in CF$_4$. $N_{Re,\infty}/m \approx 5.6 \times 10^6$; $\gamma = 1.27$.

Stagnation region

Shear layer attachment
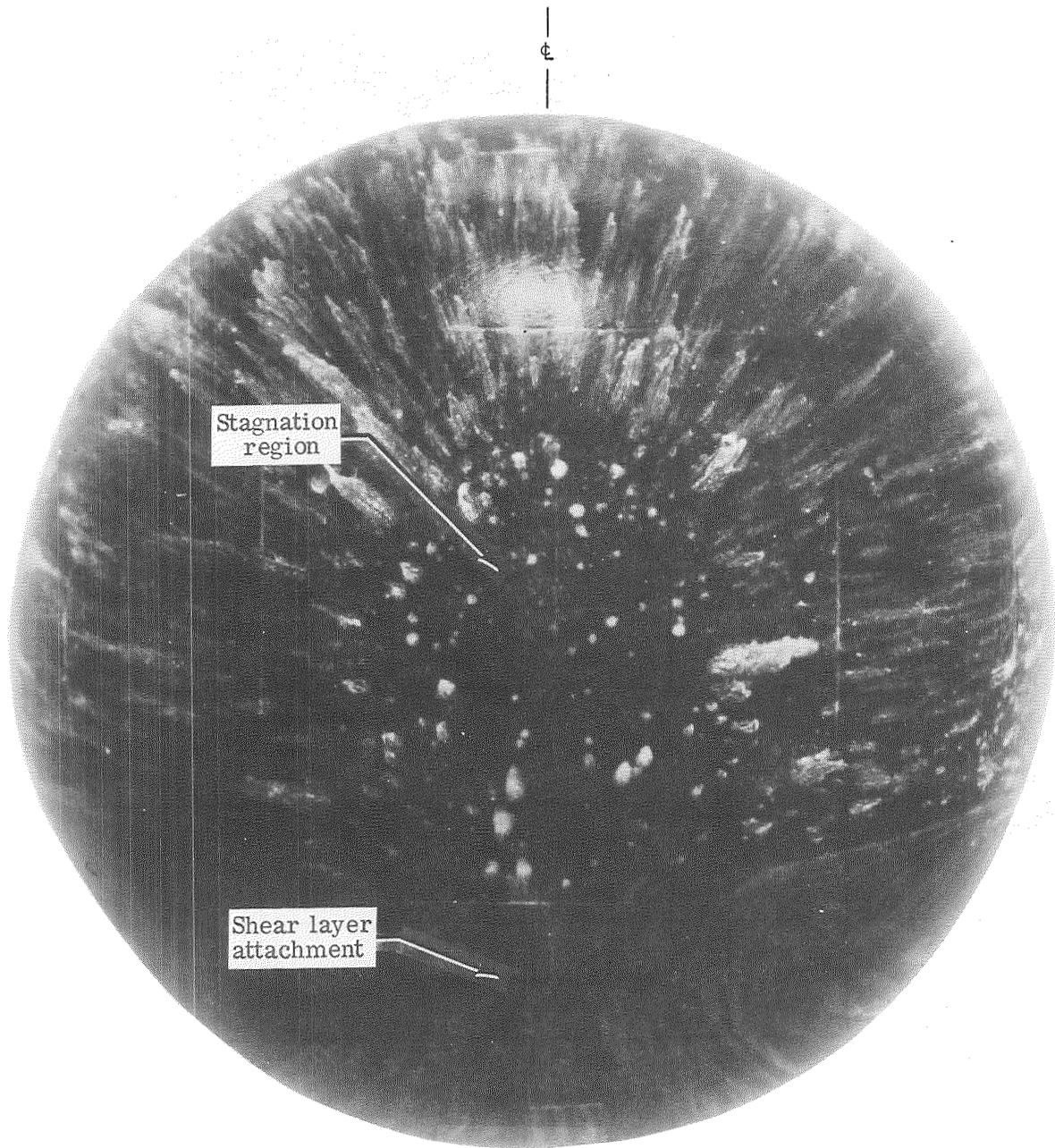
L-73-240

(c) Oil flow distribution.

Figure 20.- Concluded.
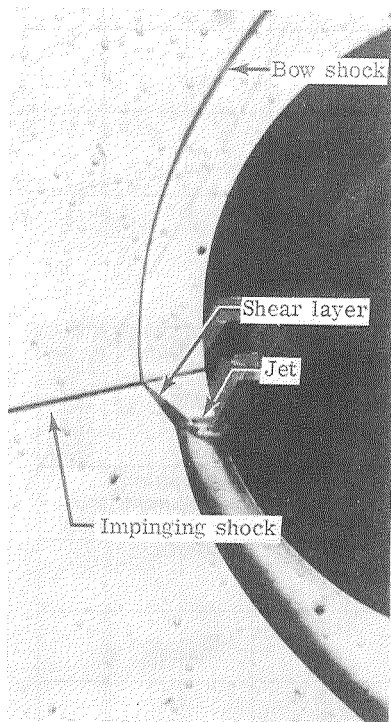
74

L-73-241

(a) Schlieren photograph.

Test run	$p_{t,\infty}$, N/cm^2	$T_{t,\infty}$, K	p_{stag}, N/cm^2	θ_i, deg
6344 - 17a	291	475	8.68	4.8

(b) Pressure distribution.

Test run	$p_{t,\infty}$, N/cm^2	$T_{t,\infty}$, K	T_w, K	Q_{stag}, W/cm^2	θ_i, deg
6363 - 46 ○	288	488	436	2.95	5.0
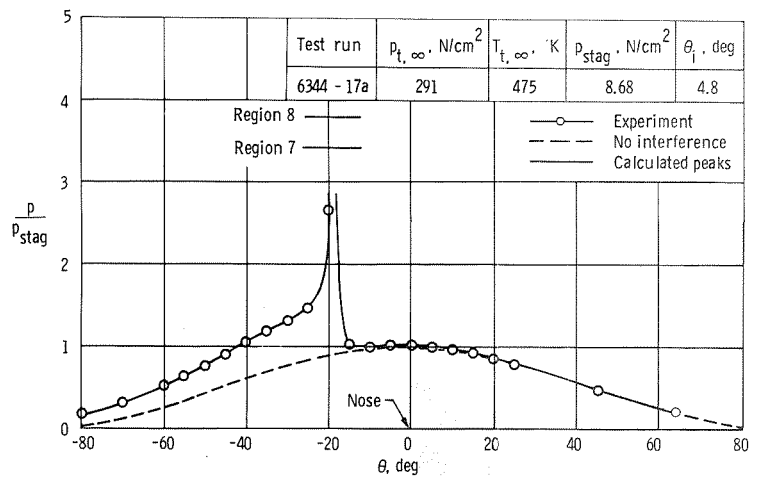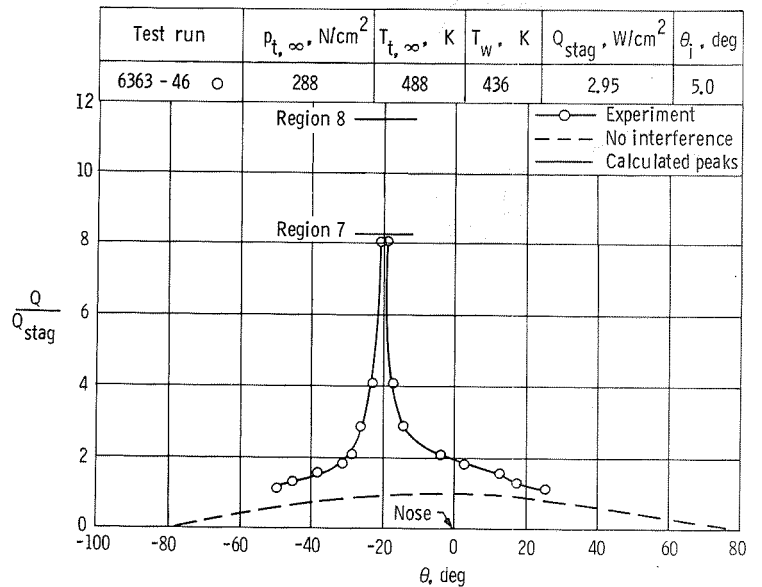
(c) Heat-transfer distribution.

Figure 21.- Type IV interference on a 0.051-m-diameter hemisphere at Mach 6.00 in air. $\theta_i \approx 5^O$; $N_{Re,\infty}/m \approx 25.6 \times 10^6$; $\gamma = 1.4$.

75
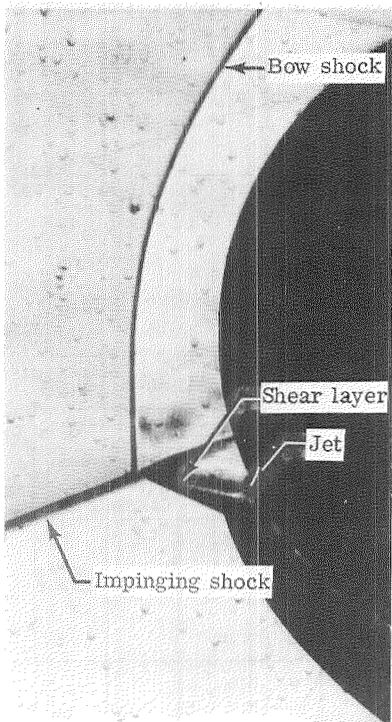
L-73-242

(a) Schlieren photograph.
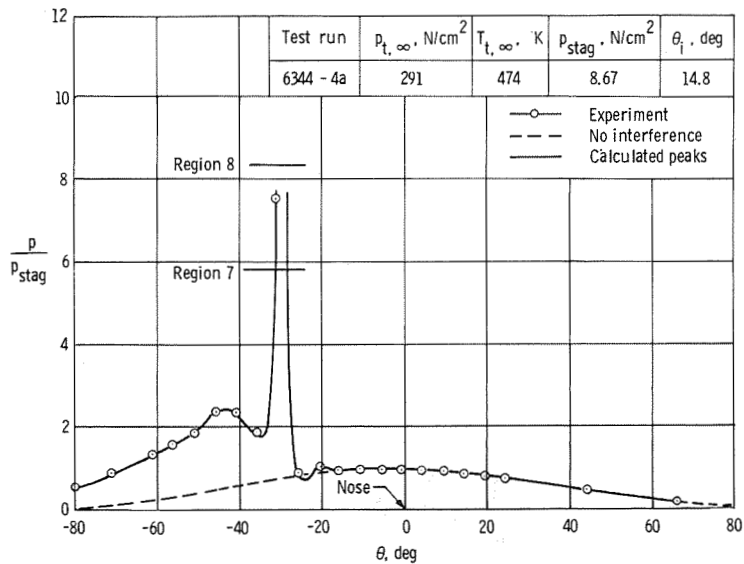
(b) Pressure distribution.
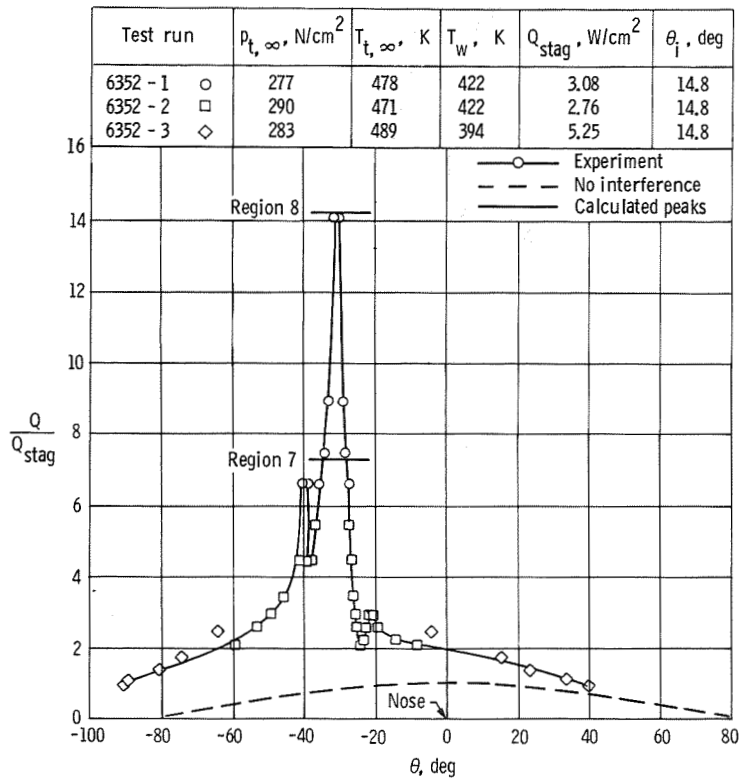
(c) Heat-transfer distribution.

Figure 22.- Type IV interference on a 0.051-m-diameter hemisphere at Mach 6.00 in air. $\theta_i = 14.8^O$; $N_{Re,\infty}/m \approx 25.7 \times 10^6$; $\gamma = 1.4$.
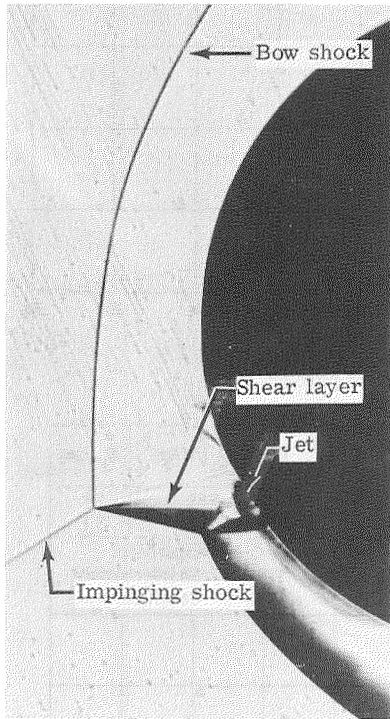
L-73-243

(a) Schlieren photograph.

Test run	$p_{t,\infty}$, N/cm^2	$T_{t,\infty}$, K	p_{stag}, N/cm^2	θ_i, deg
6344 - 28a	291	476	8.75	24.8

(b) Pressure distribution.

Test run		$p_{t,\infty}$, N/cm^2	$T_{t,\infty}$, K	T_w, K	Q_{stag}, W/cm^2	θ_i, deg
6363 - 43	O	290	494	422	4.07	24.8
6363 - 44	□	287	487	422	3.63	24.8
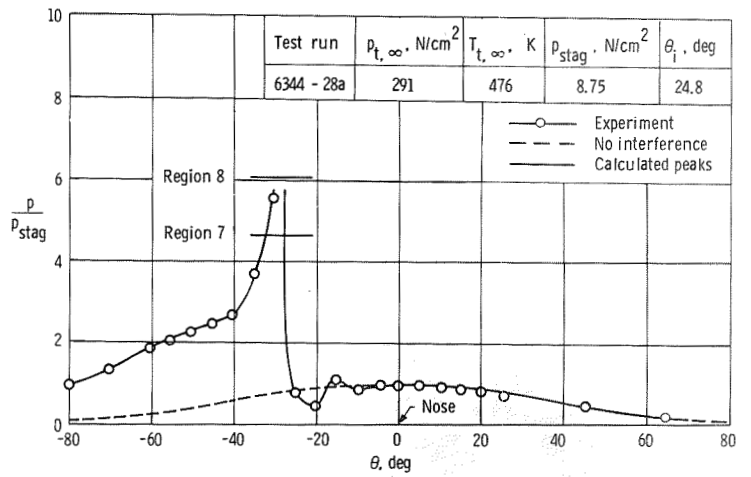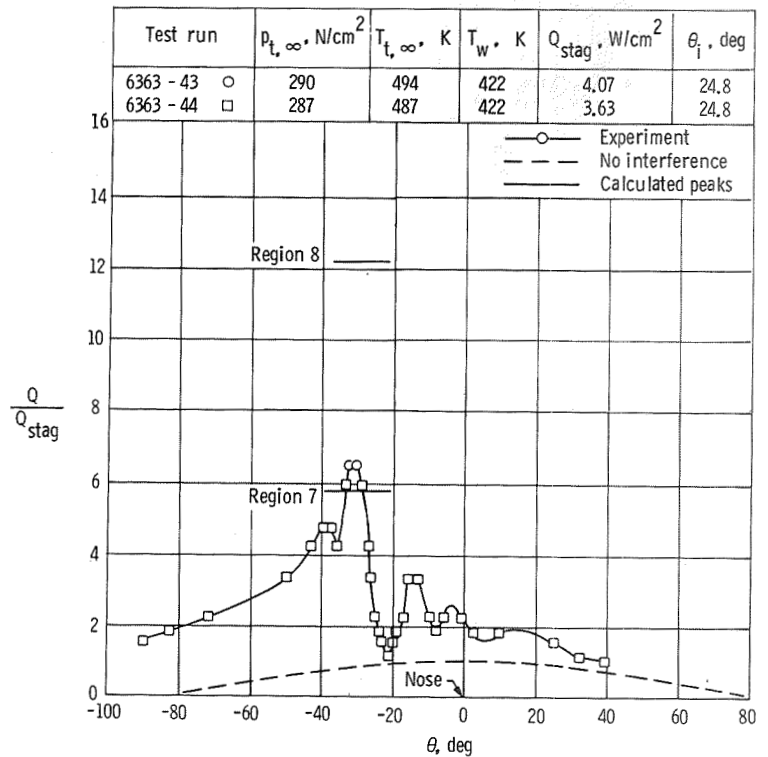
(c) Heat-transfer distribution.

Figure 23.- Type IV interference on a 0.051-m-diameter hemisphere at Mach 6.00 in air.
$\theta_i = 24.8^O$; $N_{Re,\infty}/m \approx 25.4 \times 10^6$; $\gamma = 1.4$.
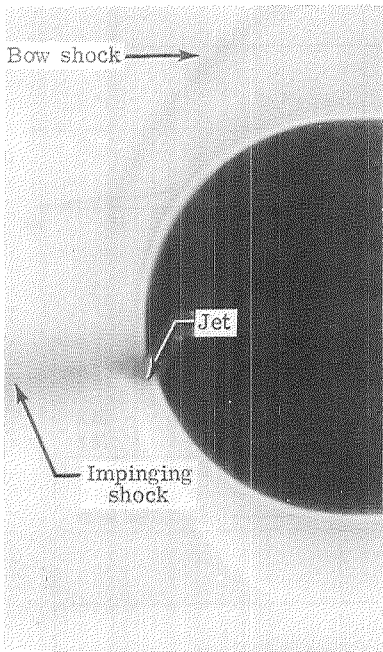
77

(a) Schlieren photograph.
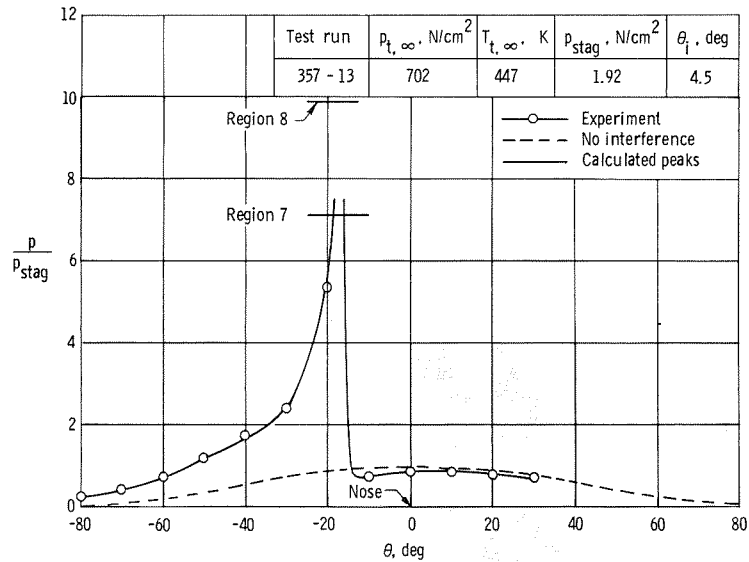
L-73-244

(b) Pressure distribution.
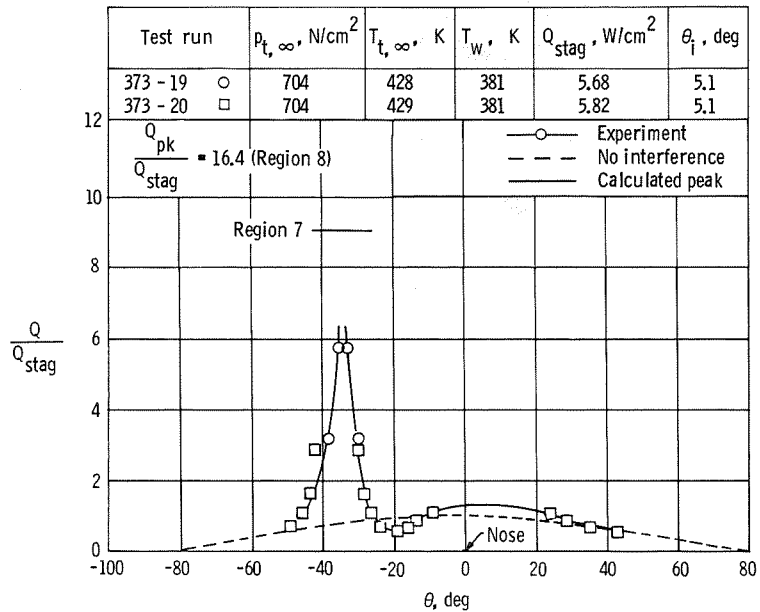
(c) Heat-transfer distribution.

Figure 24.- Type IV interference on a 0.025-m-diameter hemisphere at Mach 20.2 in helium. $\theta_i \approx 5^O$; $N_{Re,\infty}/m \approx 9.9 \times 10^6$; $\gamma = 1.67$.
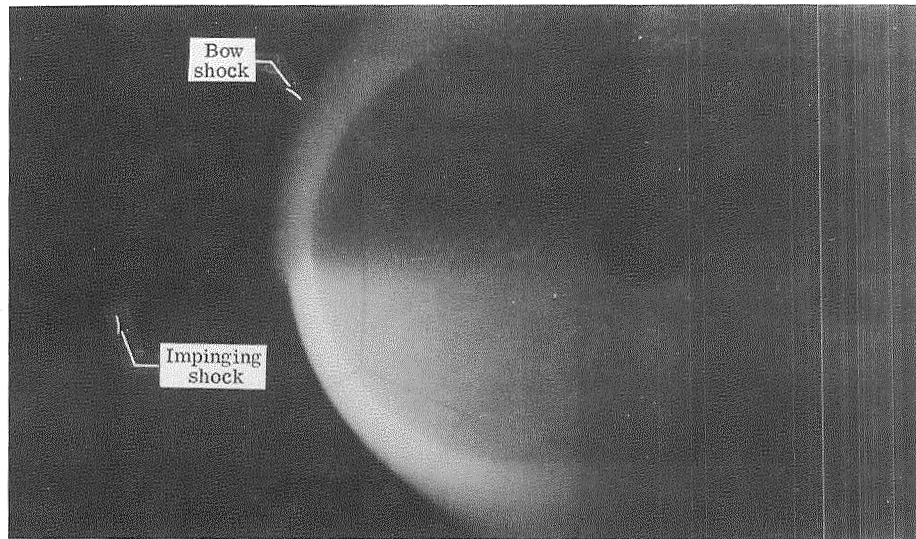
L-73-245

(a) Electron beam photograph.
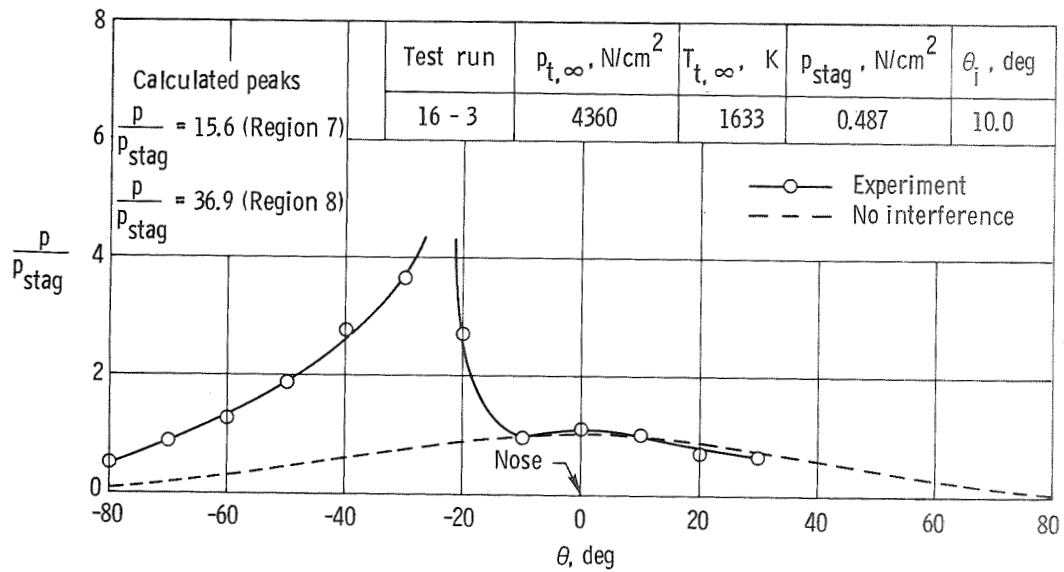
(b) Pressure distribution.

	Experiment	Calculated (laminar)
$\dfrac{Q_{pk}}{Q_{stag}}$	6.42	21.5 (Region 7) 62.5 (Region 8)

(c) Peak heat transfer (Run 16-20).

Figure 25.- Type IV interference on a 0.025-m-diameter hemisphere at Mach 19.8 in nitrogen. $\theta_i = 10^O$; $N_{Re,\infty}/m \approx 2.9 \times 10^6$; $\gamma = 1.4$.
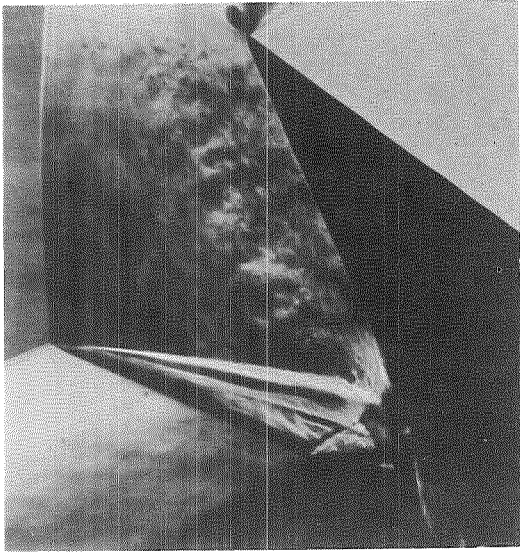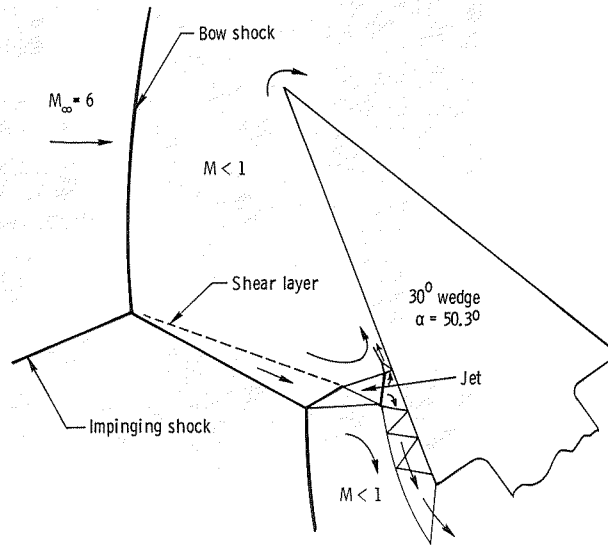
(a) Schlieren photograph.

(b) Sketch of shock pattern.

(c) Pressure distribution.

Test run	$p_{t,\infty}$, N/cm^2	$T_{t,\infty}$, K	p_{wedge}, N/cm^2	θ_i, deg	θ_b, deg
6358 - 28	292	492	8.73	15.0	-65.3

(d) Heat-transfer distribution.

Test run	$p_{t,\infty}$, N/cm^2	$T_{t,\infty}$, K	T_w, K	Q_{wedge}, W/cm^2	$\theta_i = 14.8^0$
6363-33 $\bigcirc$	292	484	436	1.28	$\theta_b = -65.0^0$
6363-34 $\square$	292	484	450	0.92	
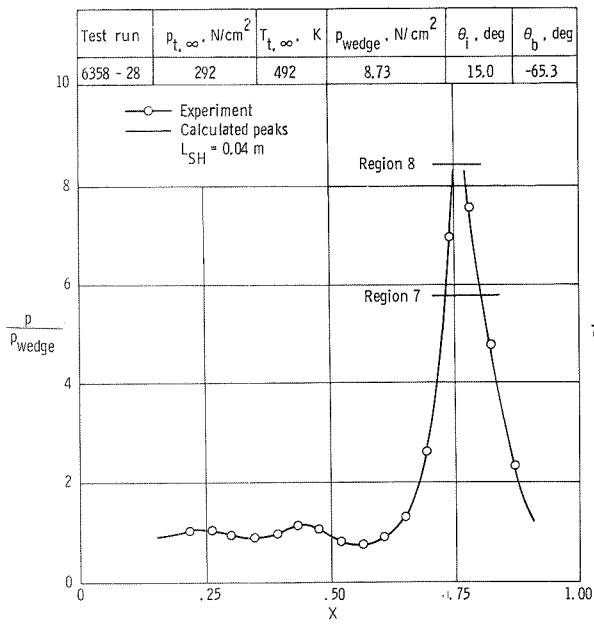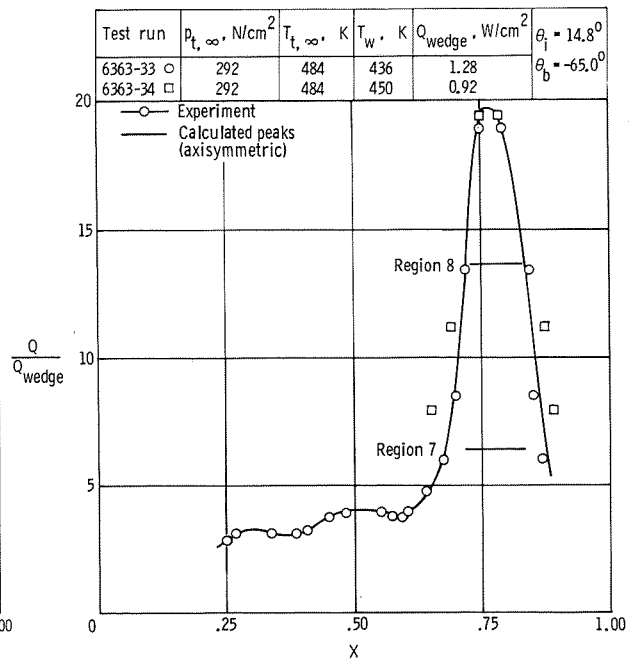
Figure 26.- Type IV interference on a 30° wedge at Mach 6.00 in air.
$\theta_i \approx 65^O$; $N_{Re,\infty}/m \approx 26.2 \times 10^6$; $\gamma = 1.4$.
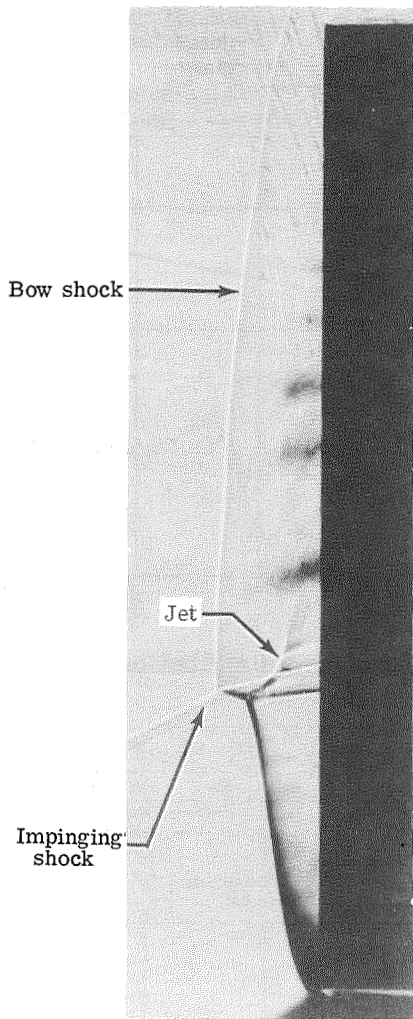
Bow shock

Jet

Impinging
shock

L-73-247

(a) Schlieren photograph.

Test run	$p_{t,\infty}$, N/cm^2	$T_{t,\infty}$, K	p_{cyl}, N/cm^2	$\theta_i = 19.9^0$
6358-12a	290	488	8.69	$\lambda = 0^0$

—○— Experiment
Calculated stagnation-line
values on infinite cylinder
— — — No interference
——— With interference

$\frac{p}{p_{cyl}}$

X

(b) Pressure distribution.

Test run	$p_{t,\infty}$, N/cm^2	$T_{t,\infty}$, K	T_w, K	Q_{cyl}, W/cm^2	$\theta_i = 19.9^0$
6363-19 ○	292	489	422	4.39	$\lambda = 0^0$

—○— Experiment
— — — Calculated, infinite
cylinder, laminar

$\frac{Q}{Q_{cyl}}$

X
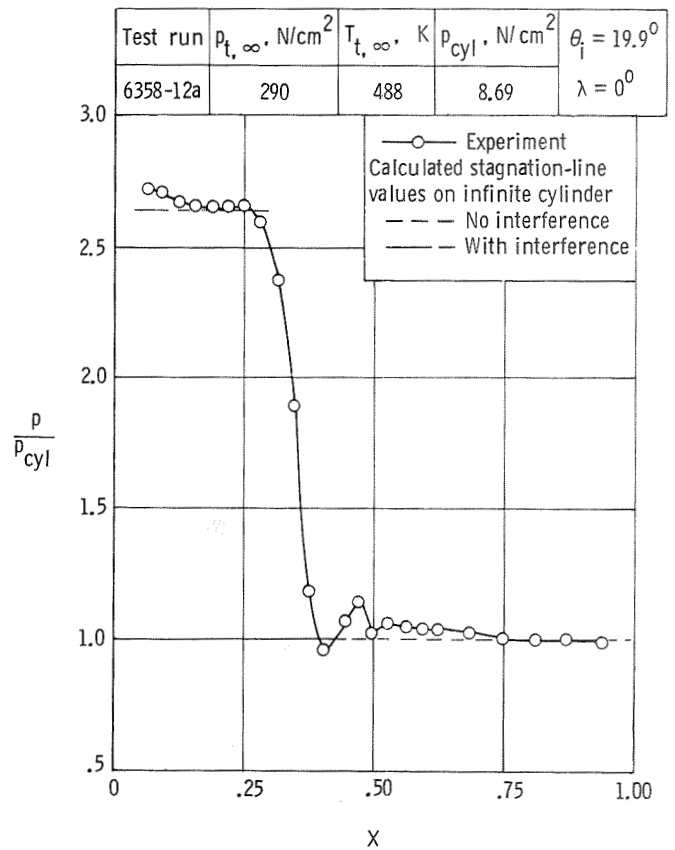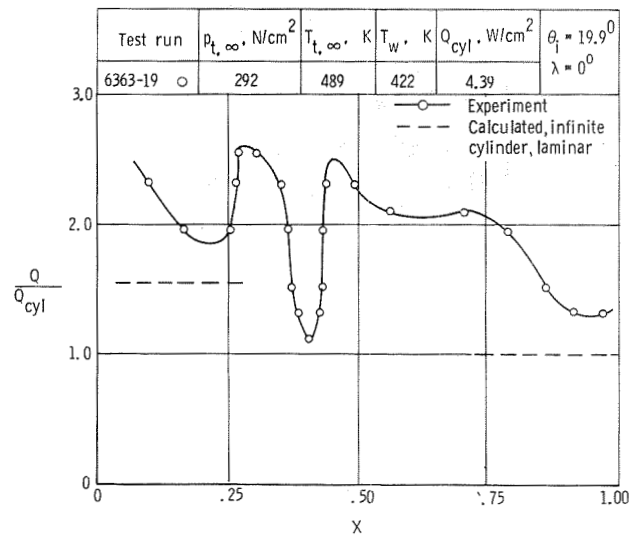
(c) Heat-transfer distribution.

Figure 27.- Type IVa interference on a fin at Mach 6.00 in air. $\theta_i = 19.9^0$;
$N_{Re,\infty}/m \approx 25.8 \times 10^6$; $\gamma = 1.4$.

L-73-248

(a) Schlieren photograph.

Test run	$p_{t, \infty}$, N/cm^2	$T_{t, \infty}$, K	p_{cyl}, N/cm^2	$\theta_i = 19.9^0$
6358-7a	293	473	7.17	$\lambda = 24.8^0$

Calculated peak, $p/p_{cyl} = 4.6$
$\theta_6 = 58^0$, $\beta_3 = 69^0$

Experiment
Calculated stagnation-line values on swept infinite cylinder
— — — No interference
—— With interference

(b) Pressure distribution.

Test run	$p_{t, \infty}$, N/cm^2	$T_{t, \infty}$, K	T_w, K	Q_{cyl}, W/cm^2	$\theta_i = 19.8^0$
6363-13	291	488	436	3.10	$\lambda = 24.9^0$

Experiment
Calculated, infinite cylinder, laminar
$\theta_6 = 58^0$
$\beta_3 = 69^0$

Calculated peak turbulent

(c) Heat-transfer distribution.

Figure 28.- Type V interference on a fin at Mach 6.00 in air. $\theta_i \approx 20^0$; $N_{Re,\infty}/m \approx 25.9 \times 10^6$; $\gamma = 1.4$.

L-73-249

(a) Schlieren photograph.

Test run	$p_{t,\infty}$, N/cm^2	$T_{t,\infty}$, K	p_{wedge}, N/cm^2	θ_i, deg	θ_b, deg
6358 - 38	296	492	6.93	5.1	39.6

—○— Experiment
- - - No interference
—— Calculated reduction

(b) Pressure distribution.

Test run		$p_{t,\infty}$, N/cm^2	$T_{t,\infty}$, K	T_w, K	Q_{wedge}, W/cm^2	$\theta_i = 5.0^0$
6363-63	○	290	488	367	10.44	$\theta_b = 40.5^0$
6363-64	□	290	488	422	5.67	

—○— Experiment

Calculated decrease
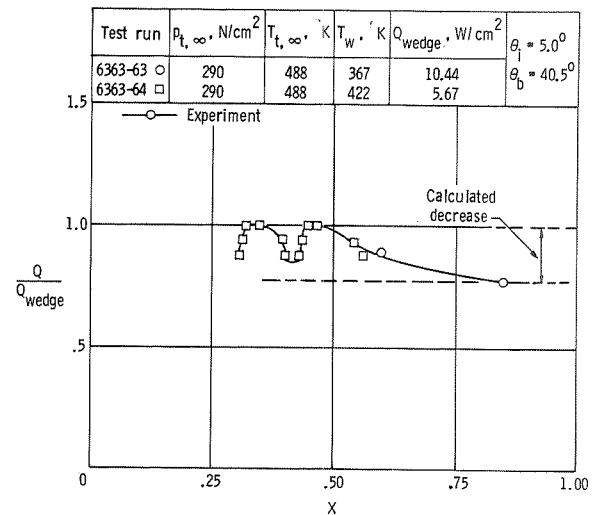
(c) Heat-transfer distribution.

Figure 29.- Type VI interference on a 30^0 wedge at Mach 6.00 in air. $\theta_i = 5^0$; $N_{Re,\infty}/m \approx 25.7 \times 10^6$; $\gamma = 1.4$.
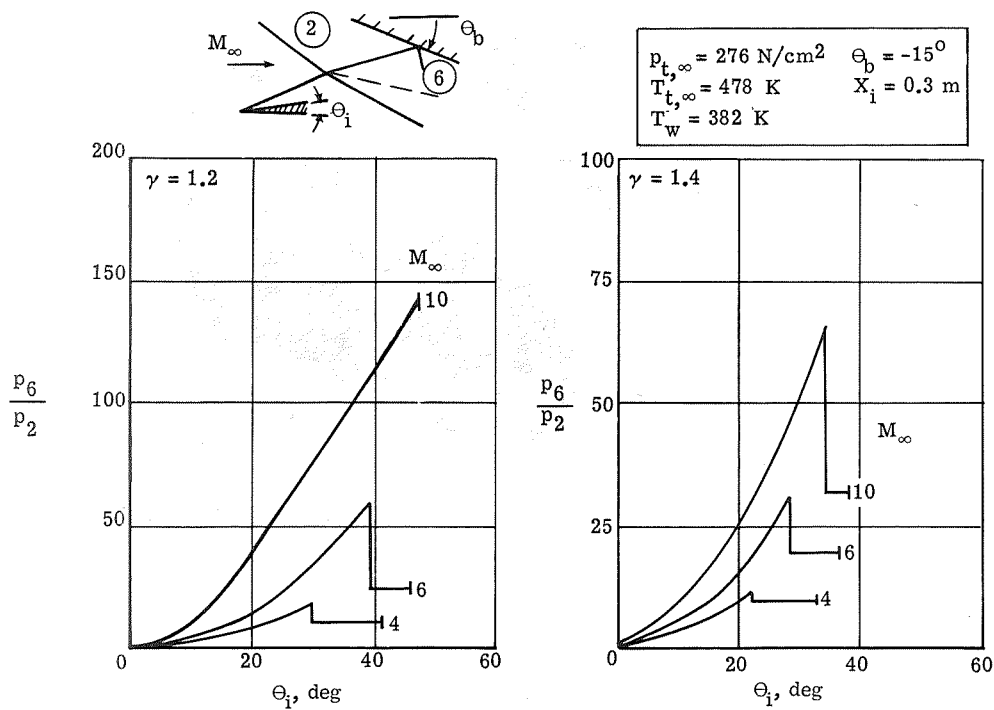
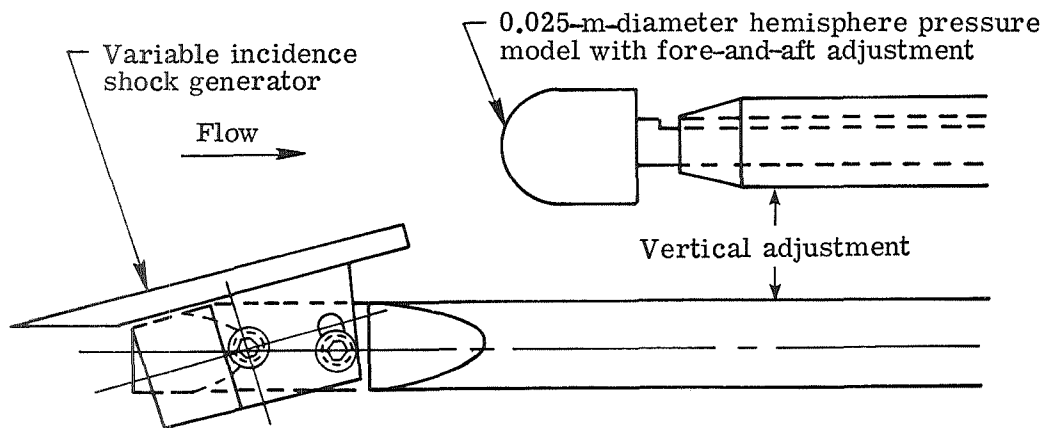(a) Pressure amplification.
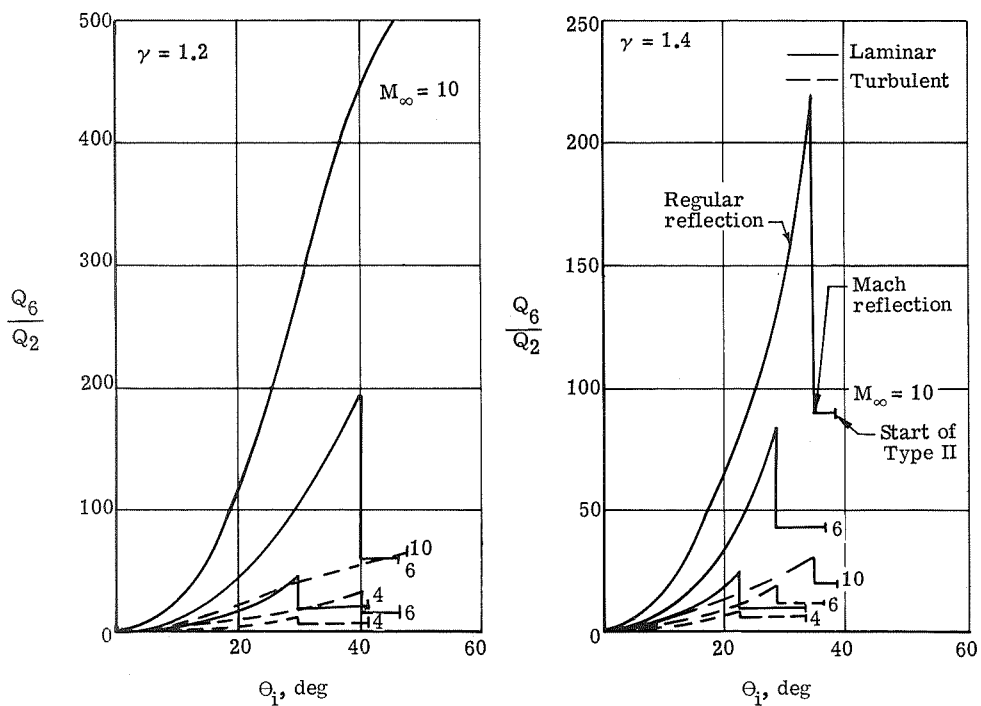
(b) Heat-transfer amplification.

Figure 30.- Pressure and heat-transfer amplification as a function of shock generator angle for type I interference on a wedge at various values of γ and free-stream Mach numbers.
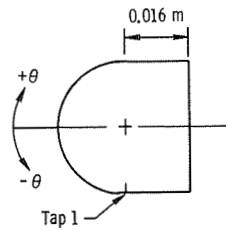
$M_\infty = 10$ $\gamma = 1.4$
$p_{t,\infty} = 276 \ N/cm^2$ $\Theta_i = 15^\circ$
$T_{t,\infty} = 478 \ K$ $X_i = 0.3 \ m$
$T_w = 382 \ K$
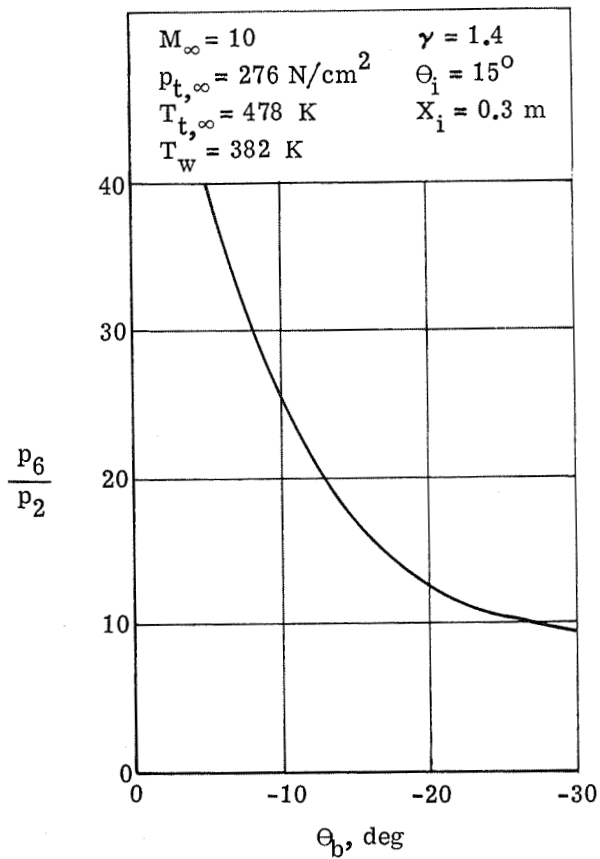
(a) Pressure amplification.
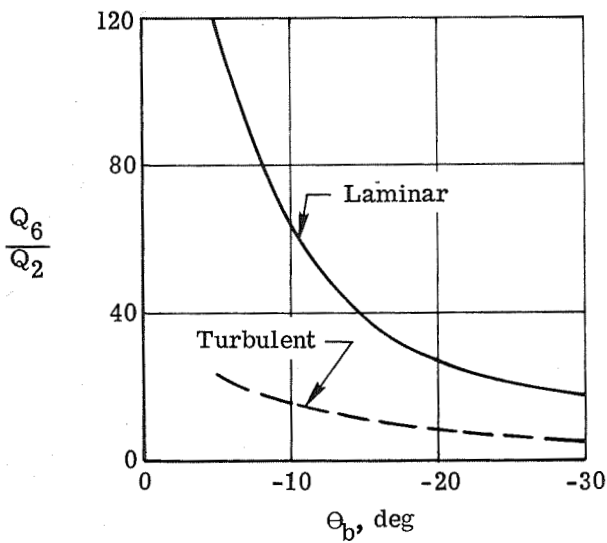
(b) Heat-transfer amplification.

Figure 31.- Pressure and heat-transfer amplification as a function of body angle for type I interference (with regular shock reflection) on a wedge.
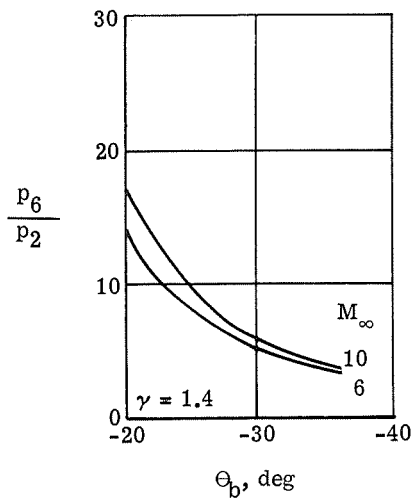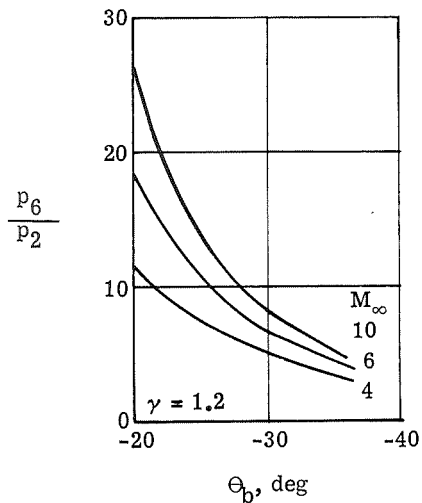
(a) Pressure amplification.
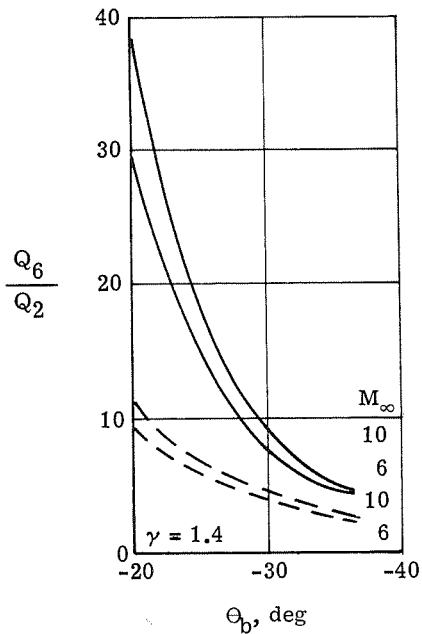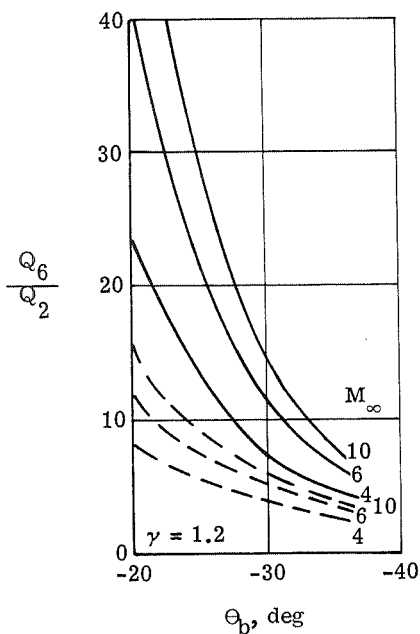
(b) Heat-transfer amplification.

Figure 32.- Pressure and heat-transfer amplification as a function of body angle for type II interference on a wedge at various values of γ and free-stream Mach number.

86

(a) Pressure amplification.

(b) Heat-transfer amplification.
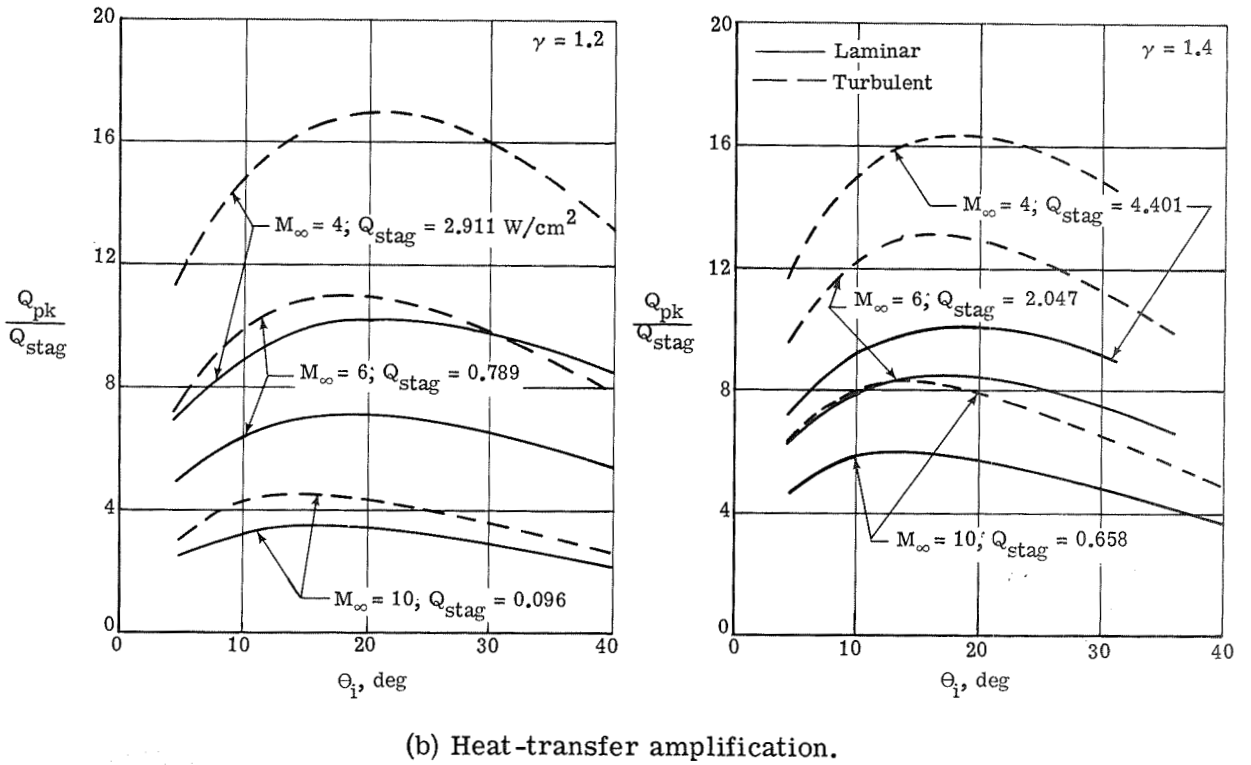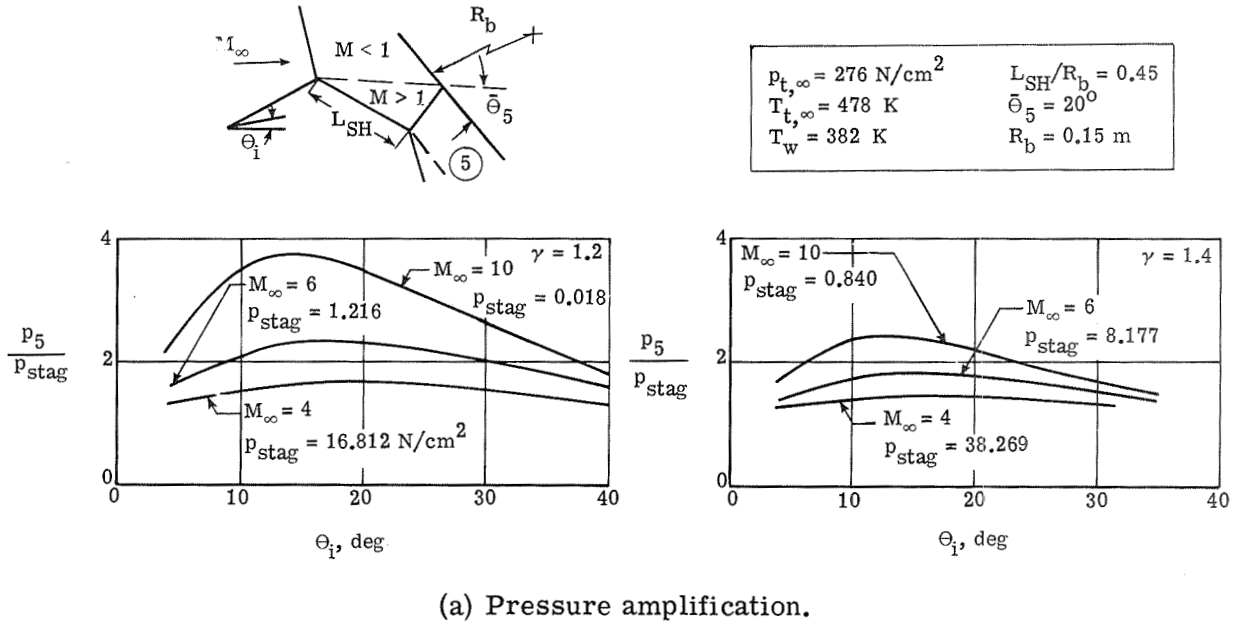
Figure 33.- Pressure and heat-transfer amplification on a 0.3-m-diameter sphere as a function of shock generator angle for type III interference for various values of γ and free-stream Mach number.
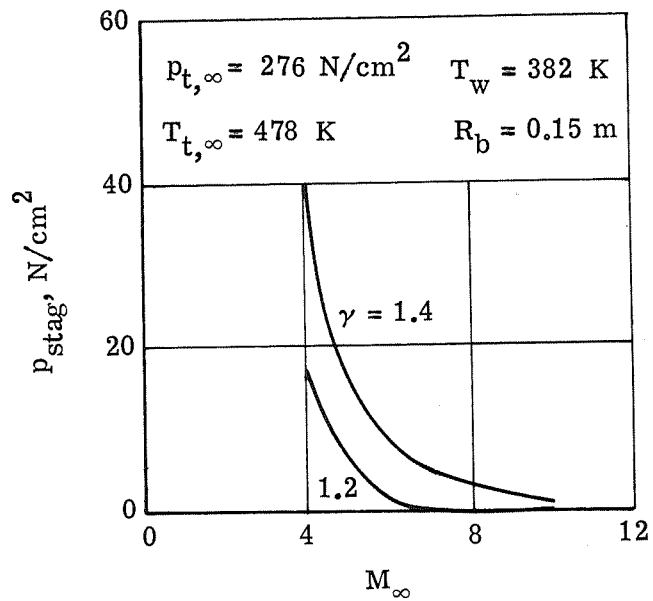
(a) Stagnation pressure.
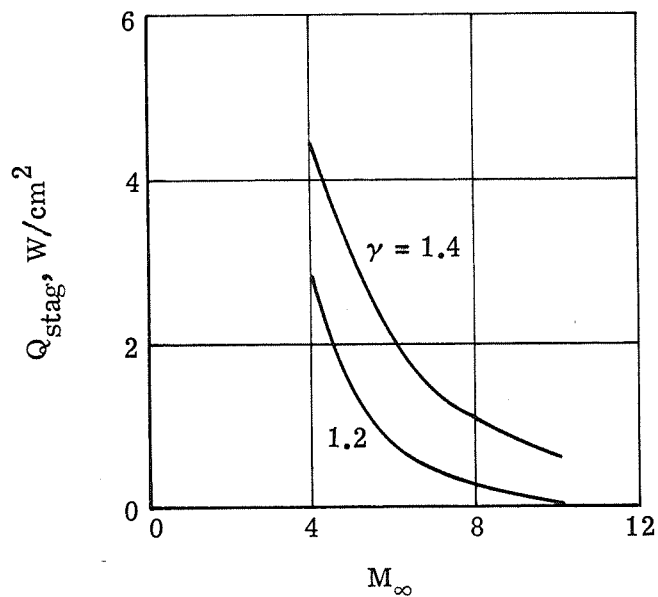
(b) Stagnation heat transfer.

Figure 34.- Variation of stagnation pressure and heat transfer with free-stream Mach number on a 0.3-m-diameter sphere for various specific heat ratios.
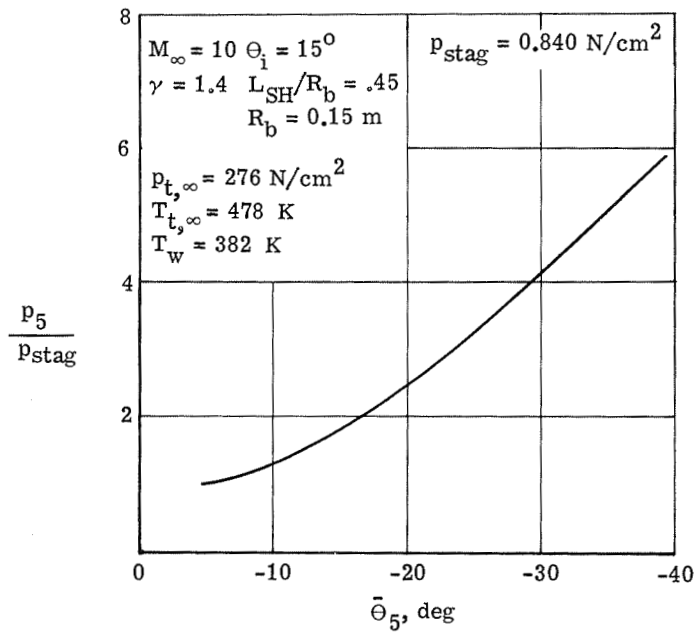
(a) Pressure amplification.
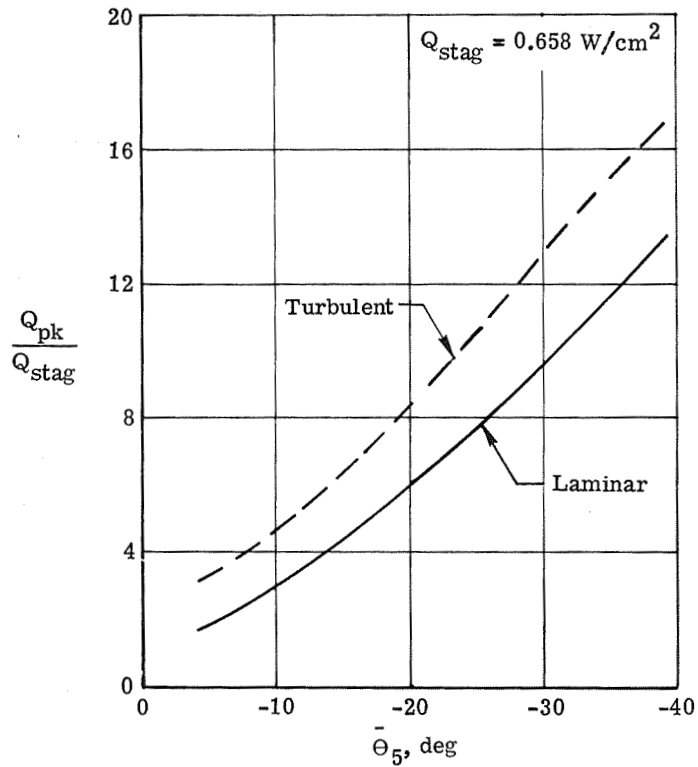
(b) Heat-transfer amplification.

Figure 35.- Pressure and heat-transfer amplification on a 0.3-m-diameter sphere as a function of shear layer angle at attachment for type III interference.
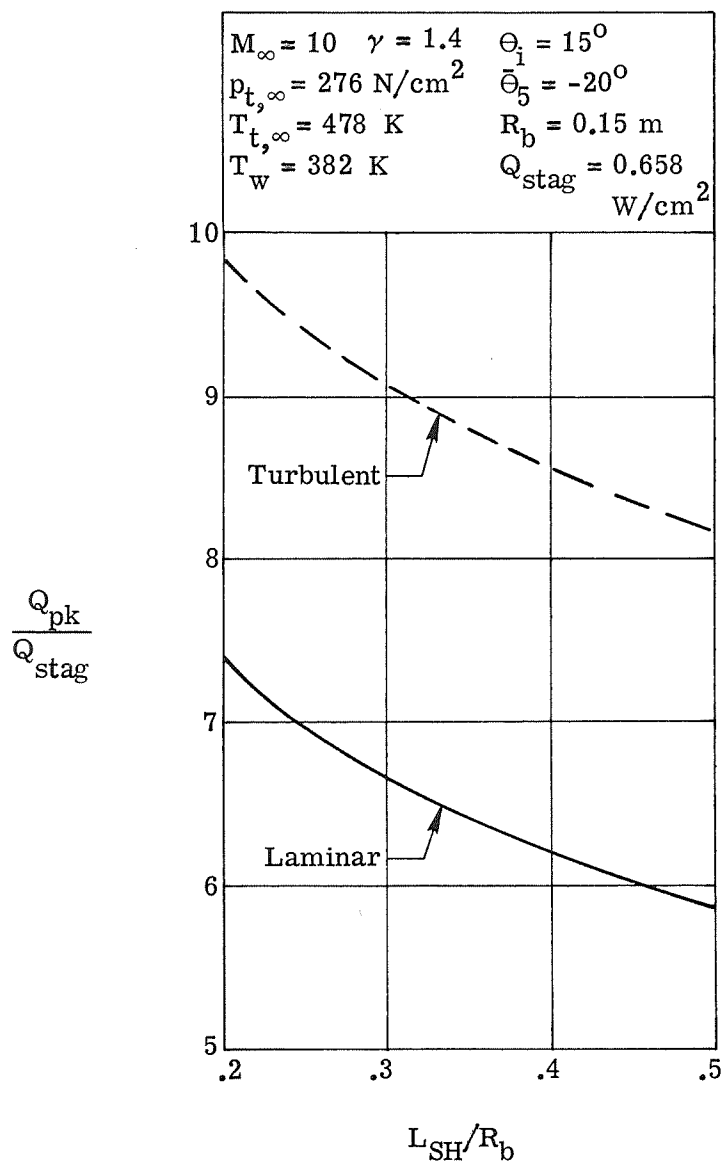
Figure 36.- Heat-transfer amplification as a function of shock displacement length (or shear layer thickness) on a 0.3-m-diameter sphere for type III interference.
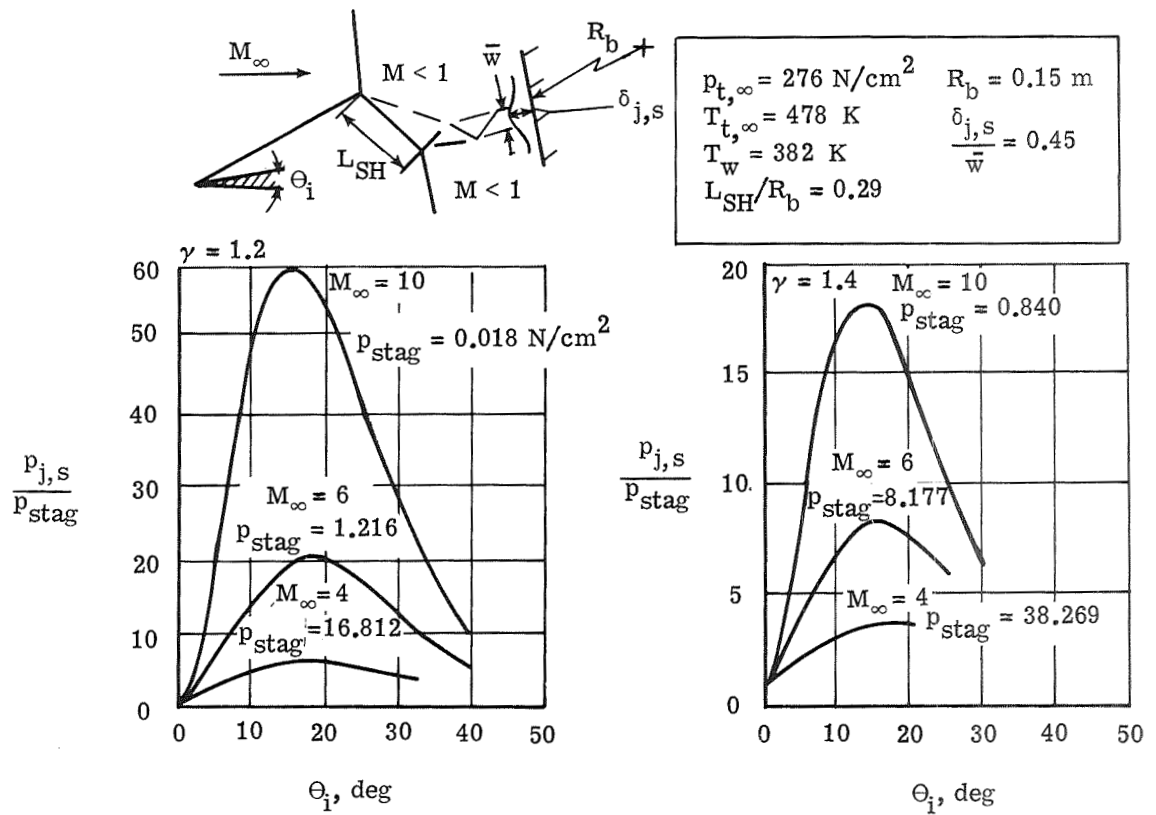
(a) Pressure amplification.
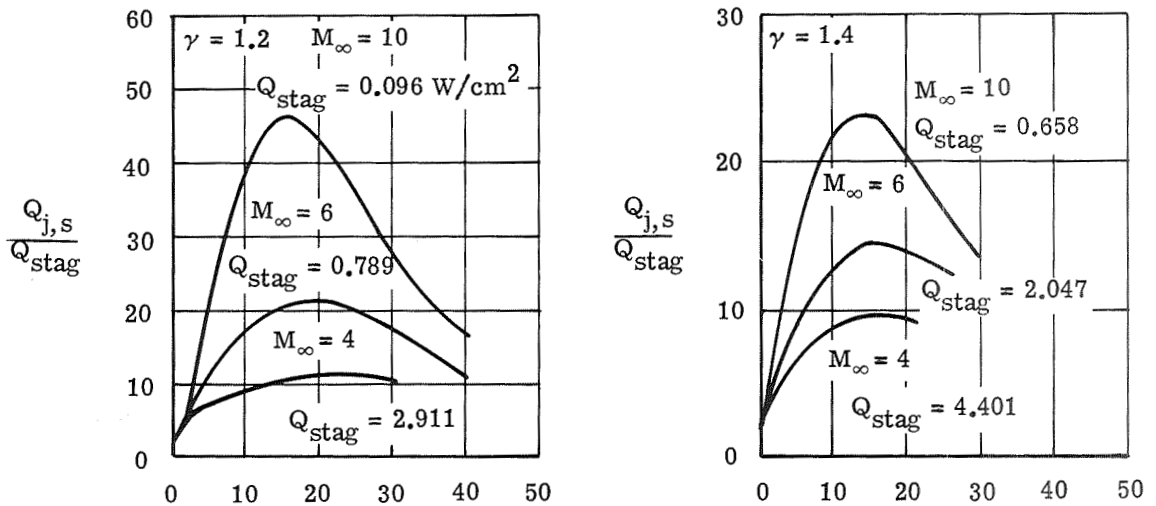
(b) Laminar jet heat-transfer amplification.

Figure 37.- Variation of pressure and heat-transfer amplification with shock generator angle for type IV interference (jet bow shock in region 8) for various values of γ and free-stream Mach number.
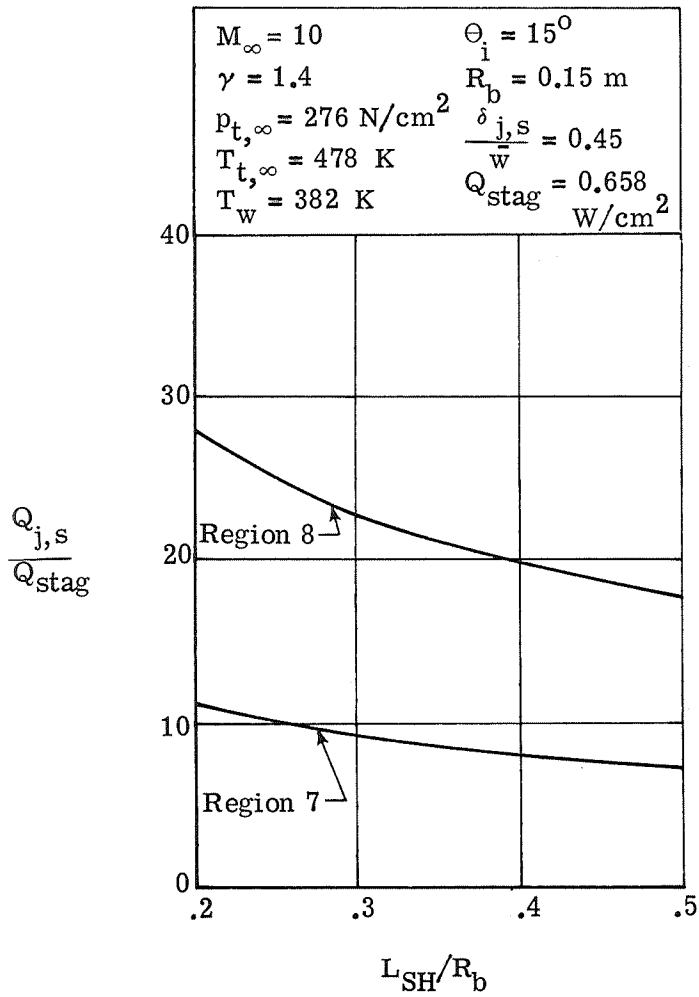
Figure 38.- Laminar jet stagnation heating as a function of shock displacement length (or jet scale length) on a 0.3-m-diameter sphere for type IV interference.

(a) Pressure amplification.

(b) Heat-transfer amplification.

Figure 39.- Pressure and heat-transfer amplification as a function of shock generator angle for type V interference on a wedge at various values of γ and free-stream Mach number.
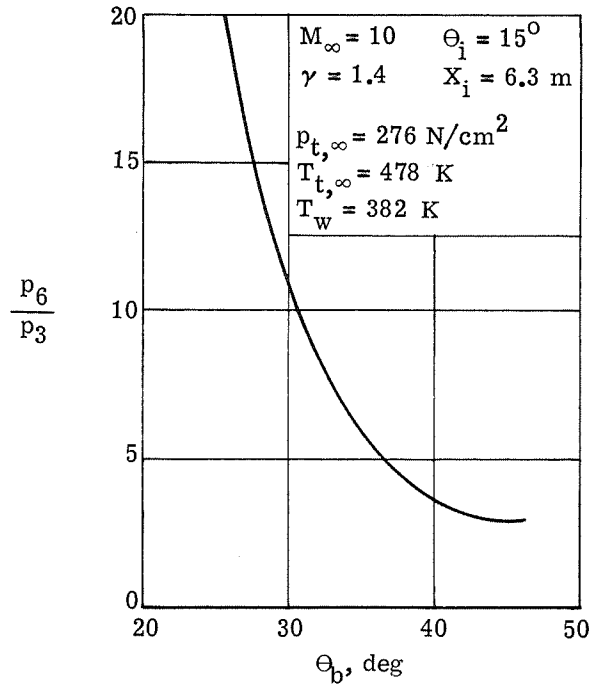
(a) Pressure amplification.
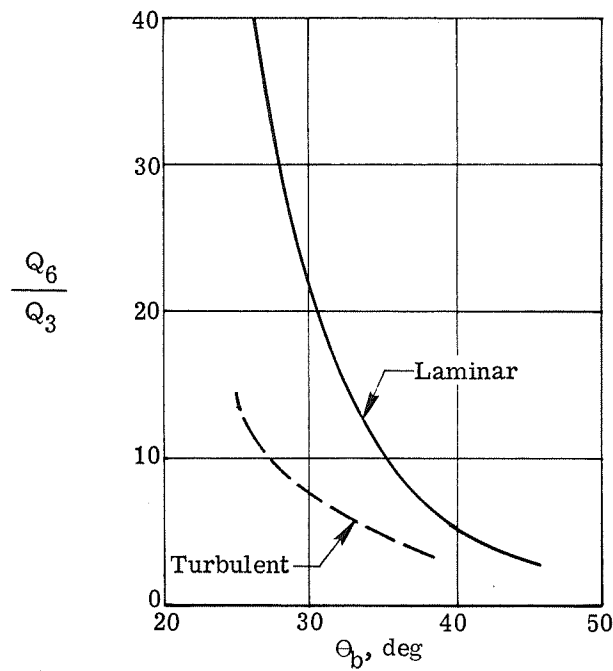
(b) Heat-transfer amplification.

Figure 40.- Pressure and heat-transfer amplification as a function of body angle for type V interference on a wedge.
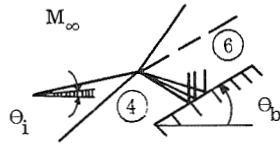
$$p_{t,\infty} = 276 \text{ N/cm}^2 \quad X_i = 0.3 \text{ m}$$
$$T_{t,\infty} = 478 \text{ K}$$
$$T_w = 382 \text{ K}$$
$$\Theta_b = 20^\circ$$
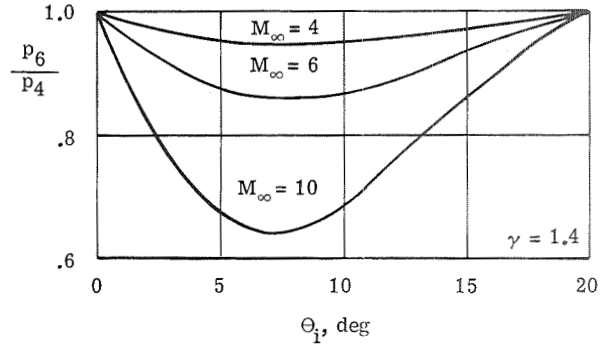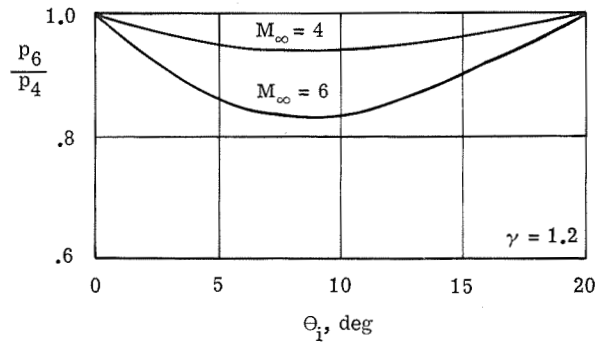
(a) Pressure reduction.
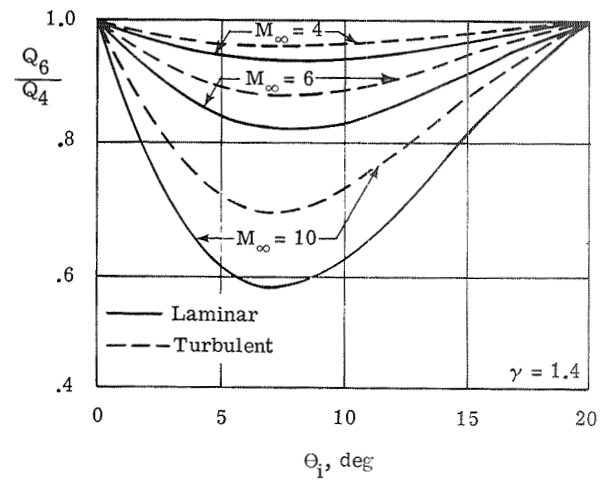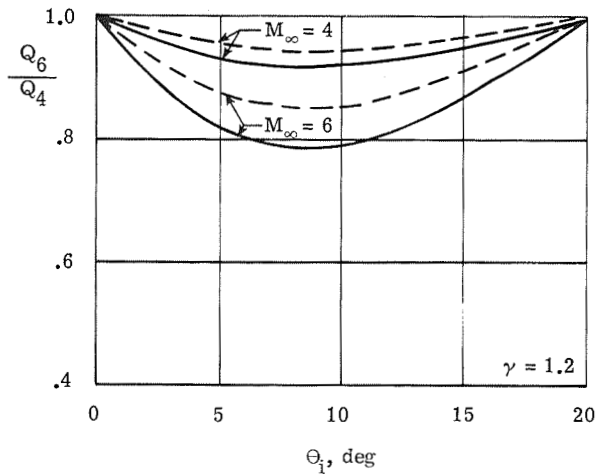
(b) Heat-transfer reduction.

Figure 41.- Pressure and heat-transfer reduction as a function of shock generator angle for type VI interference on a wedge at various values of γ and free-stream Mach number.

Interchangeable pressure
or heat-transfer
model with fore-and-aft
adjustment

Flow ⟶

Variable incidence
shock generator

Model support
with vertical
adjustment
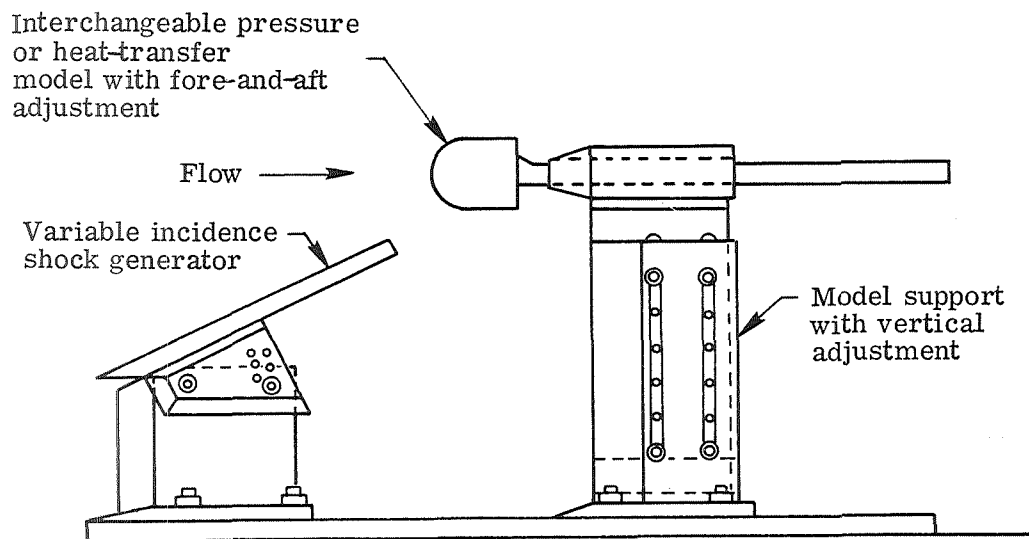
(a) Mach 6.00 air; Mach 20 helium; and Mach 19 nitrogen tests.

Variable incidence
shock generator

Flow ⟶

0.025-m-diameter hemisphere pressure
model with fore-and-aft adjustment

Vertical adjustment

(b) Mach 8.9 CF_4 test.

Figure 42.- Sketches of model test assembly.
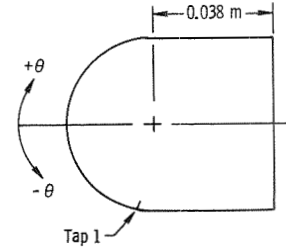
(a) 0.025-m-diameter hemisphere.

(b) 0.051-m-diameter hemisphere.

(c) 30° wedge.
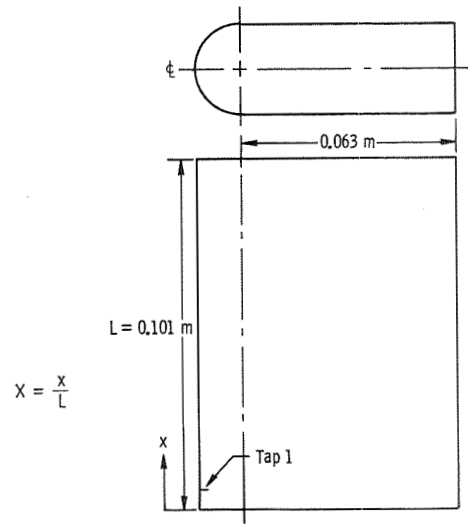
(d) 0.025-m-diameter cylindrical leading-edge fin model.

Figure 43.- Sketch of pressure models showing center-line tap locations.
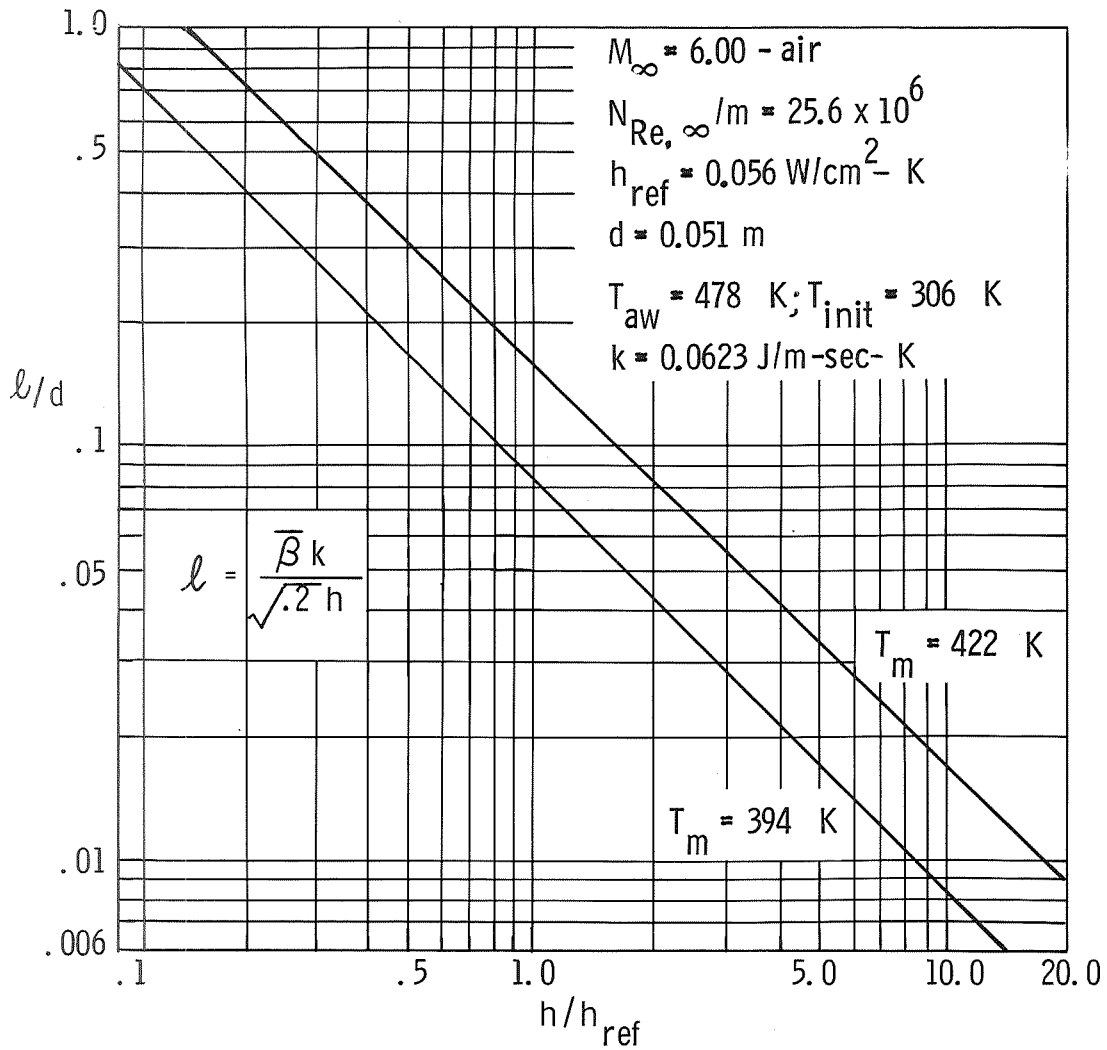
Figure 44.- Minimum distance from peak heating location for which semi-infinite slab solution is a good approximation to the solution of the general heat conduction equation.
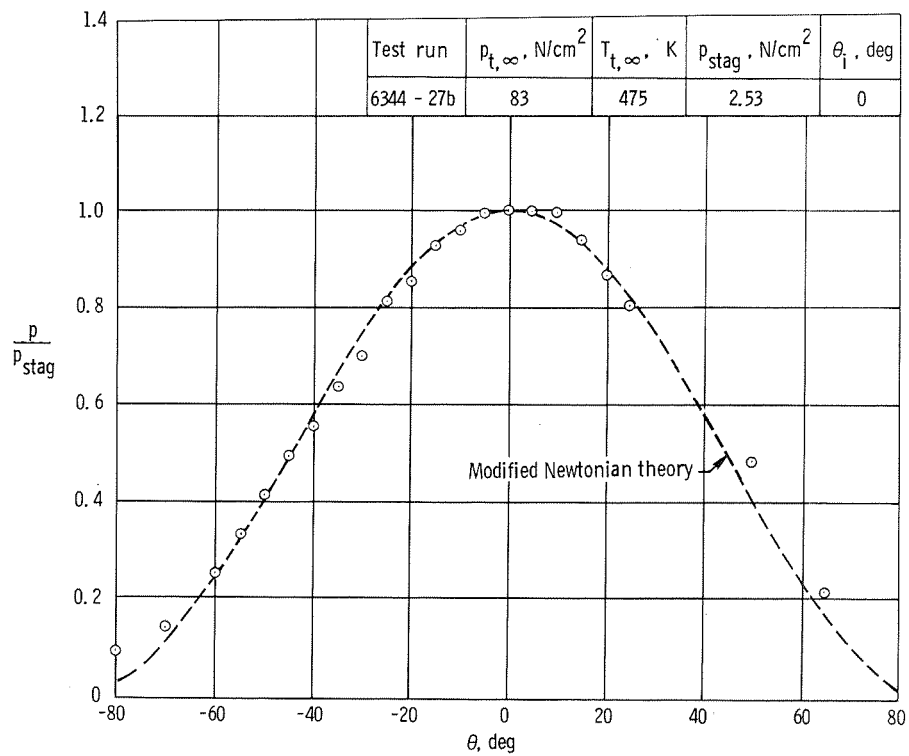
(a) Pressure distribution.
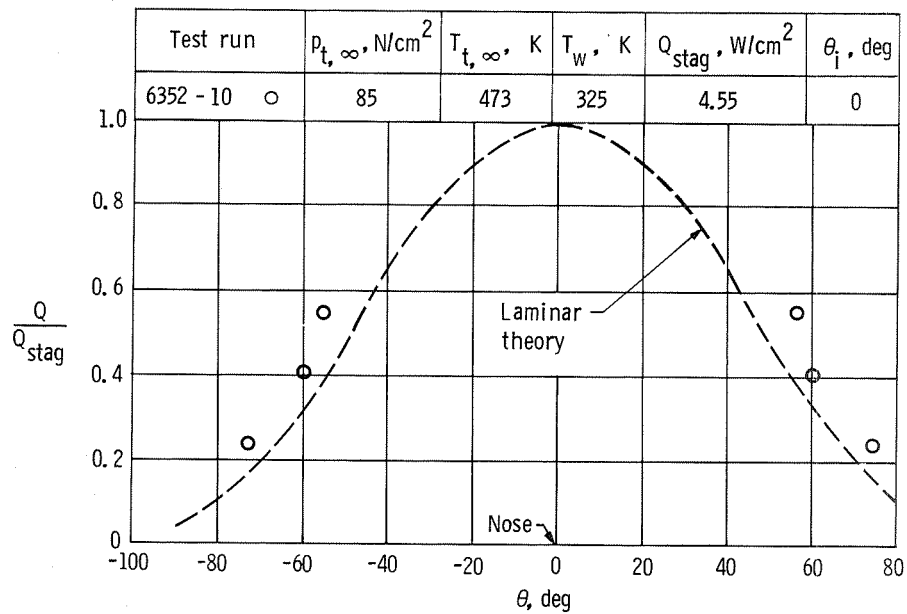
(b) Heat-transfer distribution.

Figure 45.- Pressure and heat-transfer distribution on a 0.051-m-diameter hemisphere at Mach 5.94 in air. $\theta_i = 0^O$; $N_{Re,\infty}/m \approx 8.1 \times 10^6$; $\gamma = 1.4$.
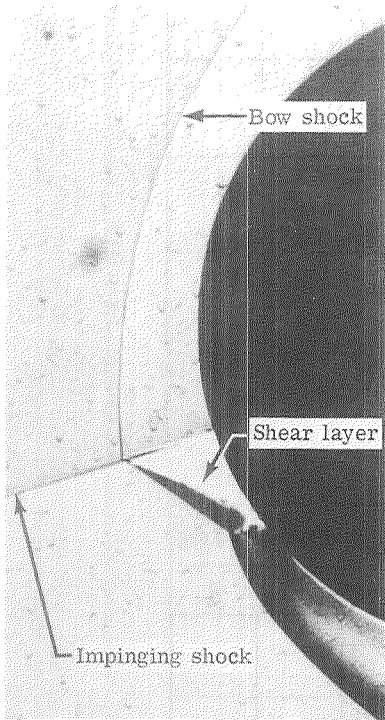
L-73-250

(a) Schlieren photograph.

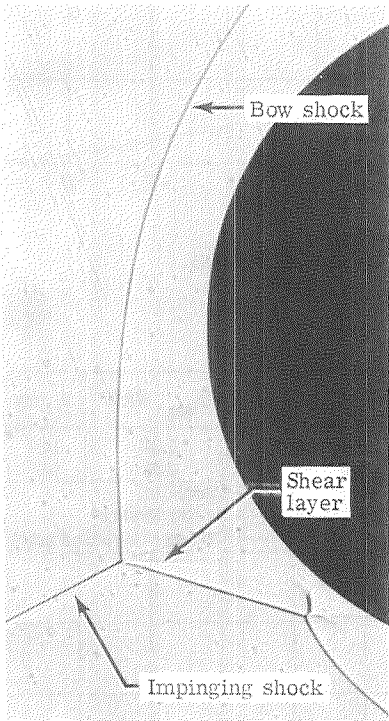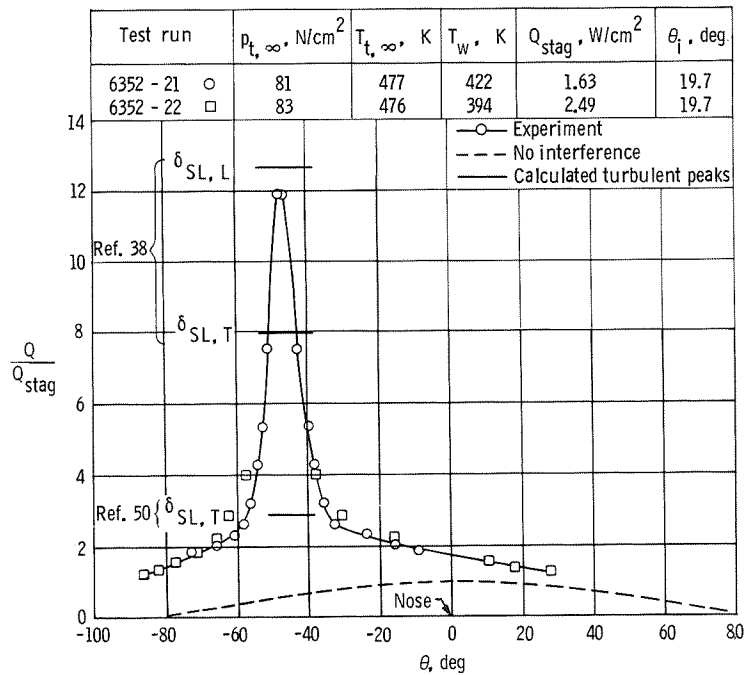| Test run	$p_{t,\infty}$, N/cm^2	$T_{t,\infty}$, K	p_{stag}, N/cm^2	θ_i, deg	$\bar{\theta}_5$, deg
6344 - 13b	85	468	2.61	9.8	32.0

—○— Experiment
– – – No interference
——— Calculated peak

(b) Pressure distribution.

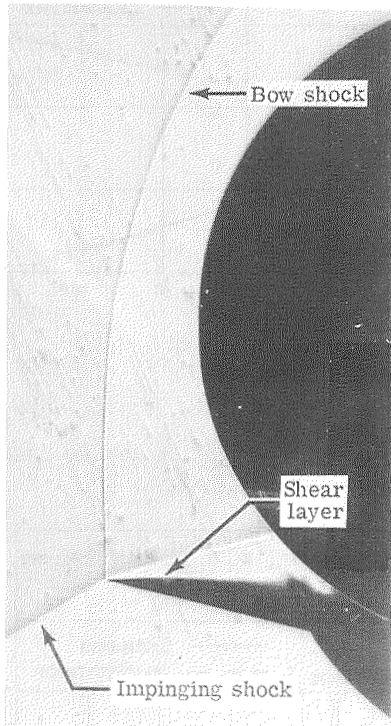| Test run		$p_{t,\infty}$, N/cm^2	$T_{t,\infty}$, K	T_w, K	Q_{stag}, W/cm^2	θ_i, deg
6352 - 30	○	81	474	436	1.15	9.9
6352 - 16	□	83	474	422	1.58	9.9
6352 - 17	◇	82	472	394	2.36	9.9

—○— Experiment
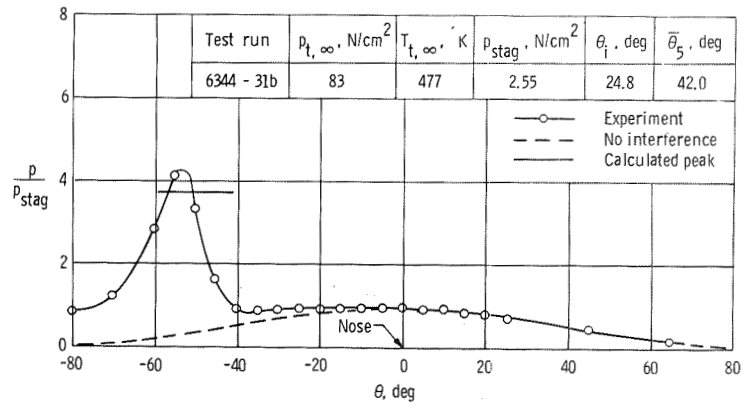– – – No interference
——— Calculated turbulent peaks
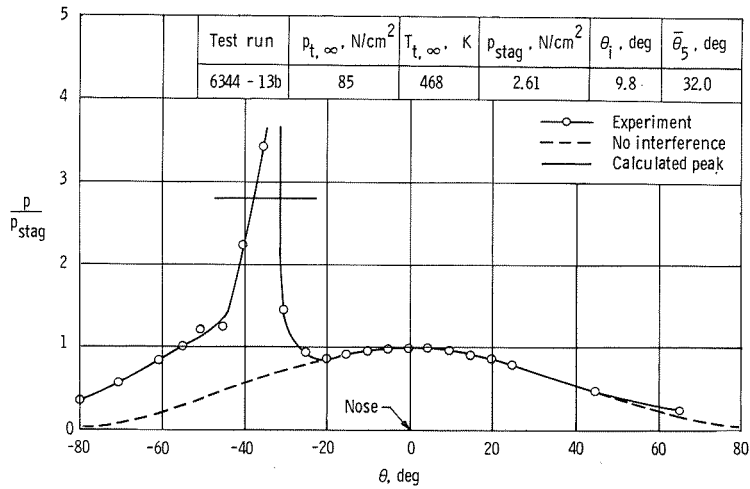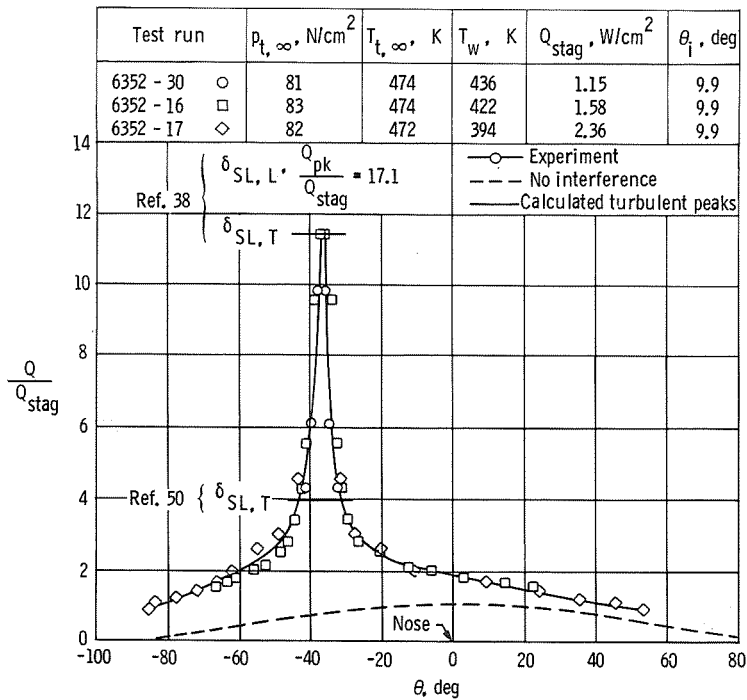
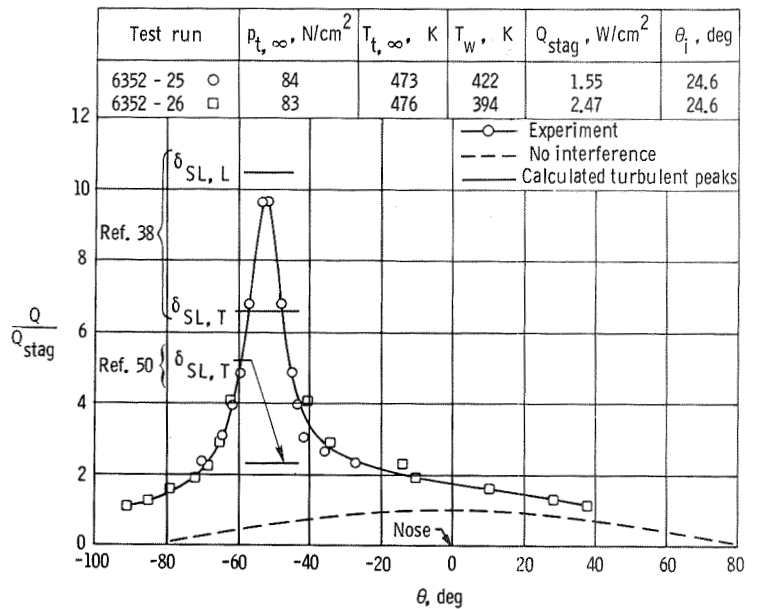(c) Heat-transfer distribution.

Figure 46.- Type III interference on a 0.051-m-diameter hemisphere at Mach 5.94 in air. $\theta_i \approx 10^{\circ}$; $N_{Re,\infty}/m \approx 7.7 \times 10^6$; $\gamma = 1.4$.
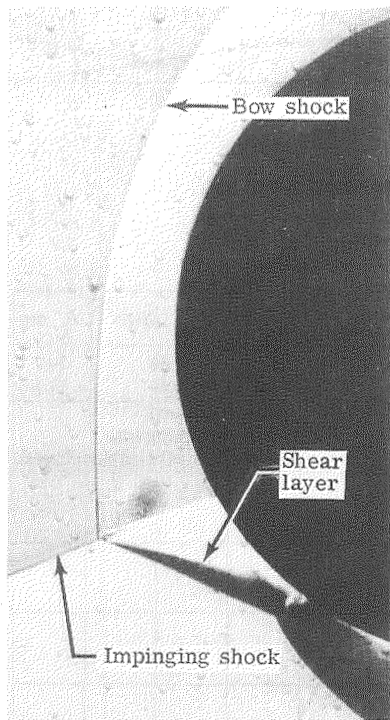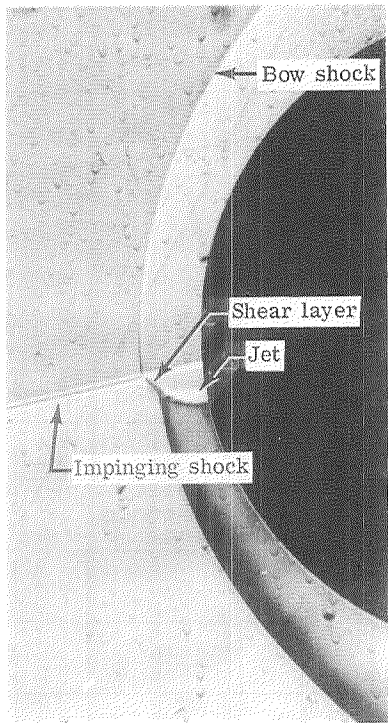
(a) Schlieren photograph.

L-73-251

Test run	$p_{t,\infty}$, N/cm^2	$T_{t,\infty}$, K	p_{stag}, N/cm^2	θ_i, deg	$\overline{\theta}_5$, deg
6344 – 7b	82	479	2.58	14.8	27.0

—o— Experiment
- - - No interference
—— Calculated peak

(b) Pressure distribution.

Test run		$p_{t,\infty}$, N/cm^2	$T_{t,\infty}$, K	T_w, K	Q_{stag}, W/cm^2	θ_i, deg
6352 – 12	o	84	476	436	1.24	14.8
6352 – 13	□	85	474	394	2.46	14.8

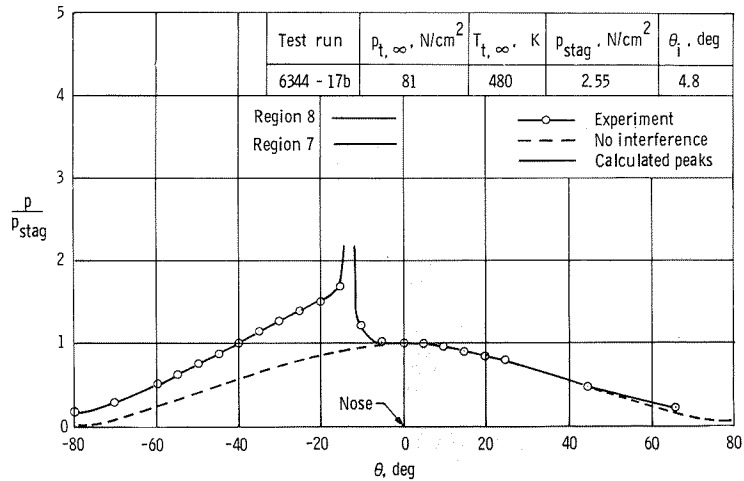—o— Experiment
- - - No interference
—— Calculated turbulent peaks
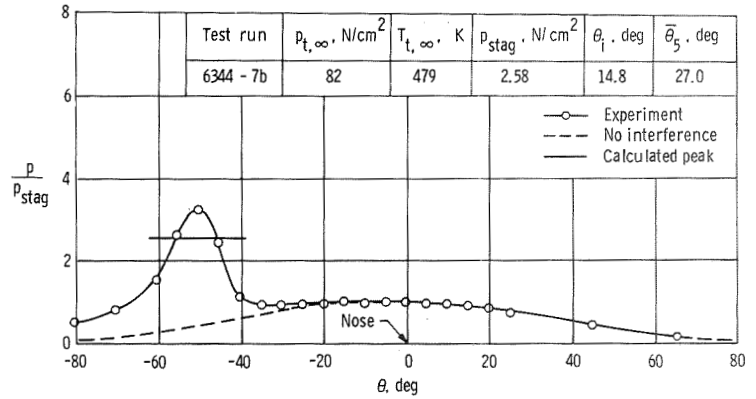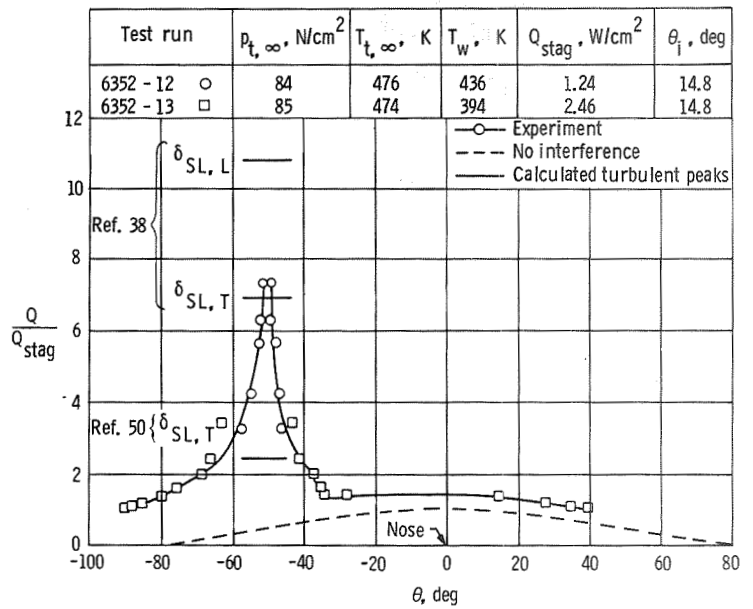
(c) Heat-transfer distribution.

Figure 47.- Type III interference on a 0.051-m-diameter hemisphere at Mach 5.94 in air. $\theta_i = 14.8^\circ$; $N_{Re,\infty}/m \approx 7.9 \times 10^6$; $\gamma = 1.4$.

(a) Schlieren photograph.

L-73-252

(b) Pressure distribution.

Test run	$p_{t,\infty}$, N/cm²	$T_{t,\infty}$, K	p_{stag}, N/cm²	θ_i, deg	$\bar{\theta}_5$, deg
6344 - 26b	85	475	2.61	19.8	39.0

(c) Heat-transfer distribution.

Test run		$p_{t,\infty}$, N/cm²	$T_{t,\infty}$, K	T_w, K	Q_{stag}, W/cm²	θ_i, deg.
6352 - 21	O	81	477	422	1.63	19.7
6352 - 22	□	83	476	394	2.49	19.7
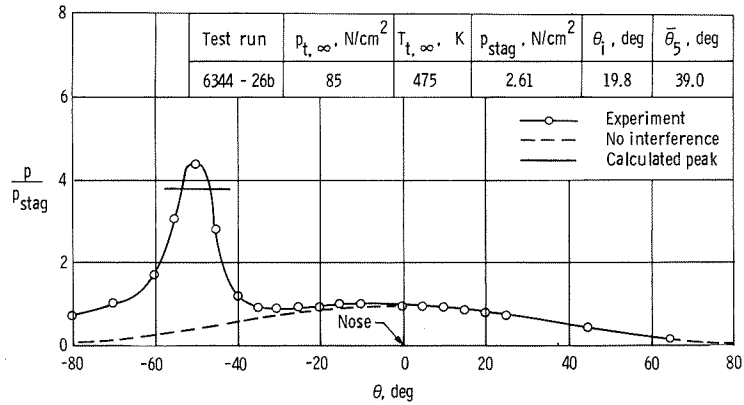
Figure 48.- Type III interference on a 0.051-m-diameter hemisphere at Mach 5.94 in air. $\theta_i \approx 20^\circ$; $N_{Re,\infty}/m \approx 7.6 \times 10^6$; $\gamma = 1.4$.
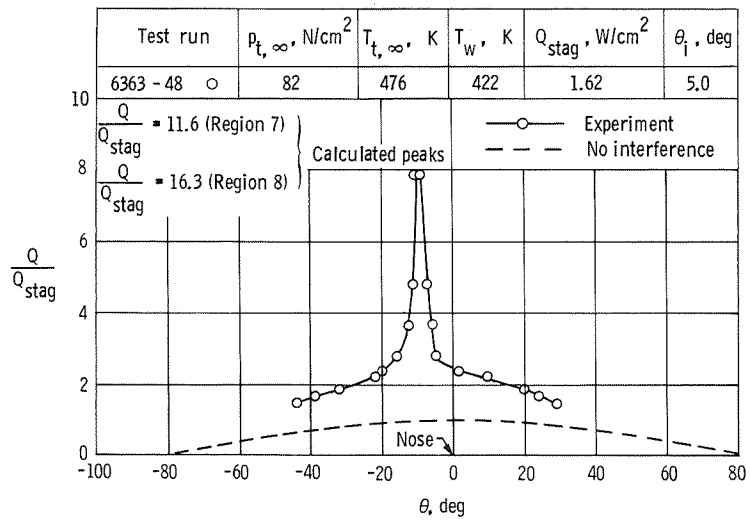
(a) Schlieren photograph.

L-73-253
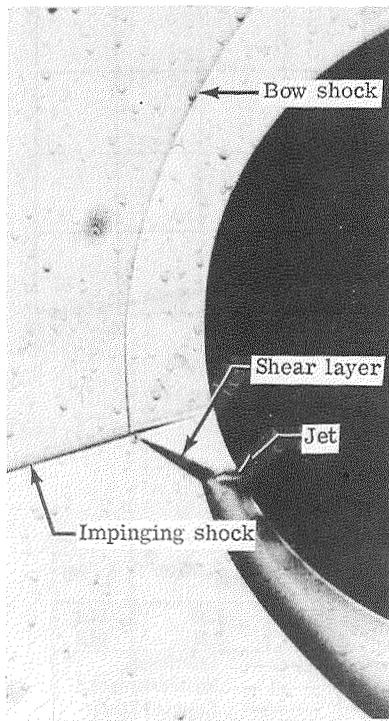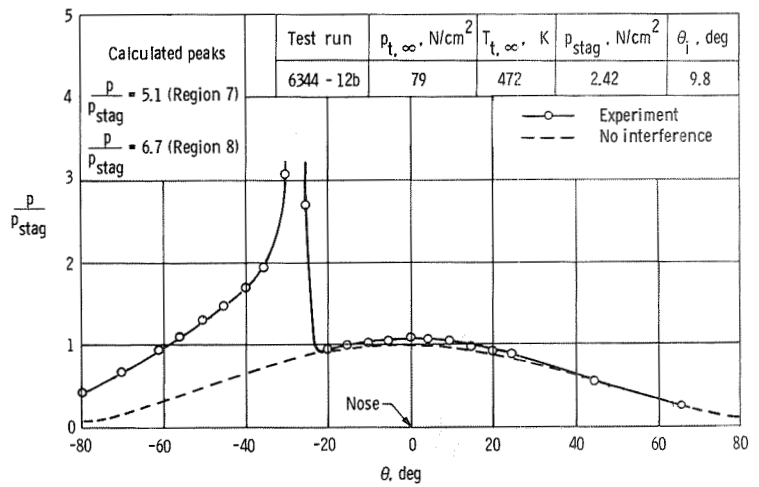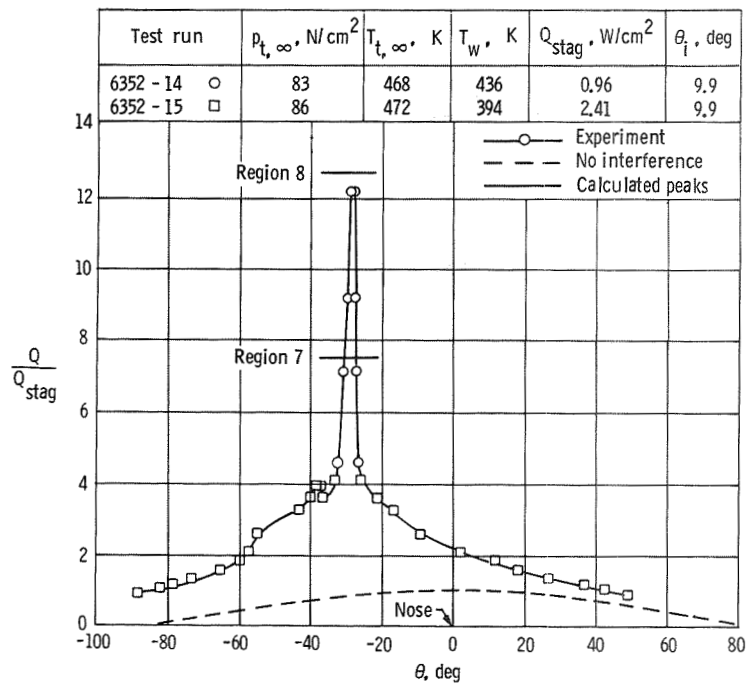

Test run	$p_{t,\infty}$, N/cm²	$T_{t,\infty}$, K	p_{stag}, N/cm²	θ_i, deg	$\bar{\theta}_s$, deg
6344 - 31b	83	477	2.55	24.8	42.0

Experiment
No interference
Calculated peak

(b) Pressure distribution.

Test run	$p_{t,\infty}$, N/cm²	$T_{t,\infty}$, K	T_w, K	Q_{stag}, W/cm²	θ_i, deg
6352 - 25 ○	84	473	422	1.55	24.6
6352 - 26 □	83	476	394	2.47	24.6

Experiment
No interference
Calculated turbulent peaks

(c) Heat-transfer distribution.

Figure 49.- Type III interference on a 0.051-m-diameter hemisphere at Mach 5.94 in air. $\theta_i \approx 25°$; $N_{Re,\infty}/m \approx 7.8 \times 10^6$; $\gamma = 1.4$.

(a) Schlieren photograph.

L-73-254

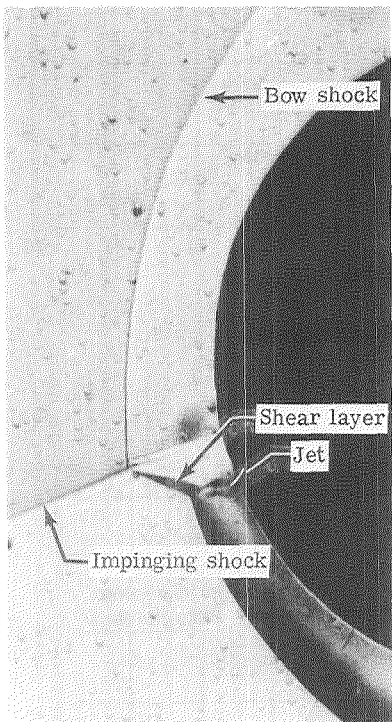
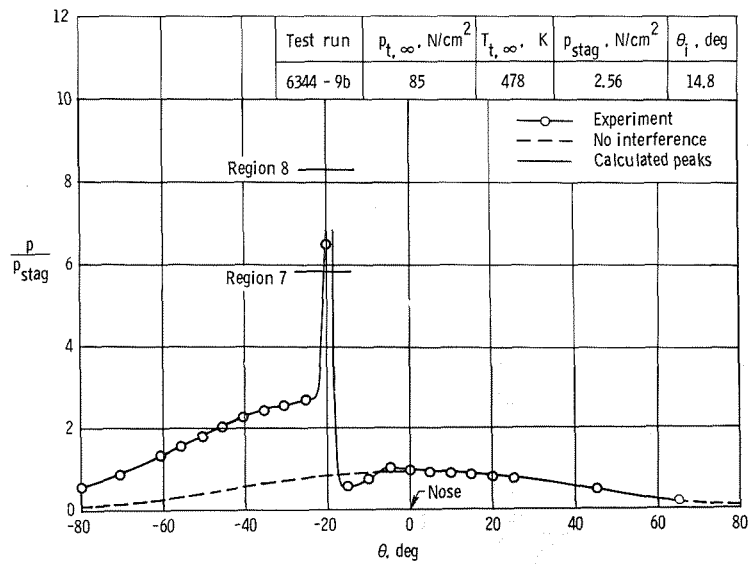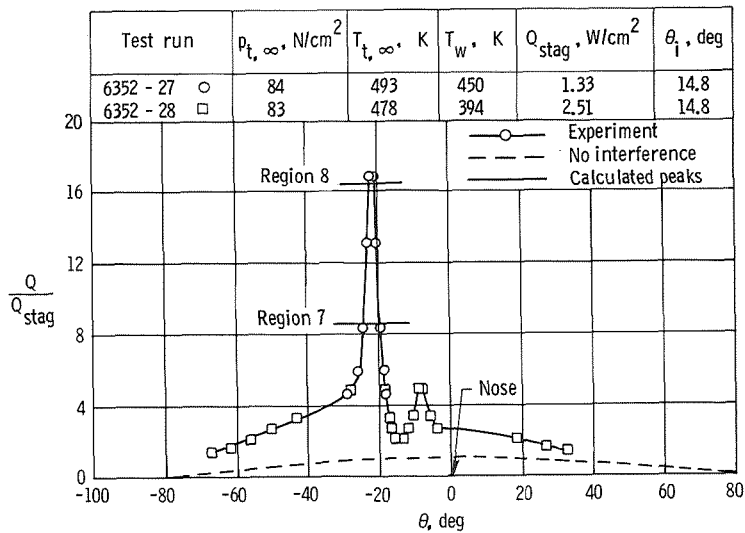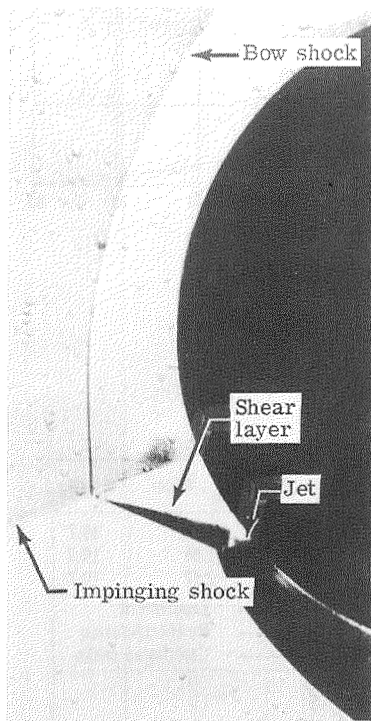(b) Pressure distribution.

(c) Heat-transfer distribution.

Figure 50.- Type IV interference on a 0.051-m-diameter hemisphere at Mach 5.94 in air. $\theta_i \approx 5.0^{\circ}$; $N_{Re,\infty}/m \approx 7.6 \times 10^6$; $\gamma = 1.4$.

L-73-255

(a) Schlieren photograph.

Bow shock

Shear layer

Jet

Impinging shock

Calculated peaks

$\dfrac{p}{p_{stag}} = 5.1$ (Region 7)

$\dfrac{p}{p_{stag}} = 6.7$ (Region 8)

Test run	$p_{t,\infty}$, N/cm^2	$T_{t,\infty}$, K	p_{stag}, N/cm^2	θ_i, deg
6344 - 12b	79	472	2.42	9.8

— o — Experiment
- - - No interference

Nose

$\dfrac{p}{p_{stag}}$

θ, deg

(b) Pressure distribution.

Test run		$p_{t,\infty}$, N/cm^2	$T_{t,\infty}$, K	T_w, K	Q_{stag}, W/cm^2	θ_i, deg
6352 - 14	o	83	468	436	0.96	9.9
6352 - 15	□	86	472	394	2.41	9.9

— o — Experiment
- - - No interference
——— Calculated peaks

Region 8
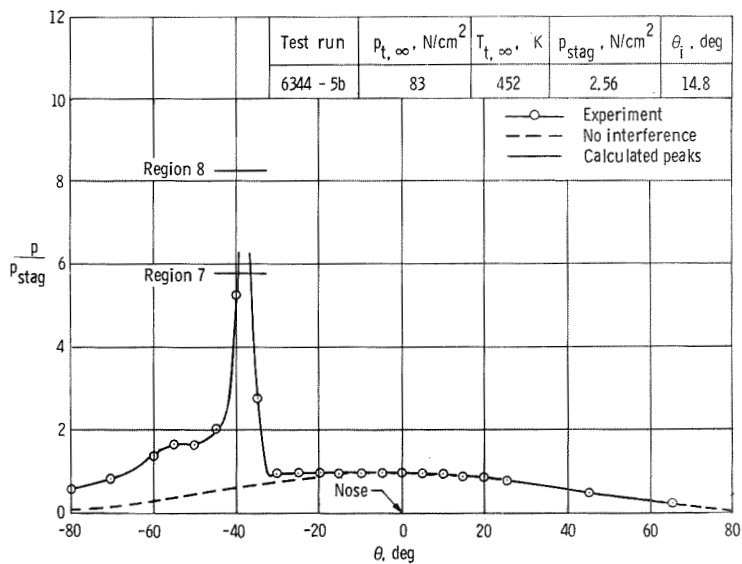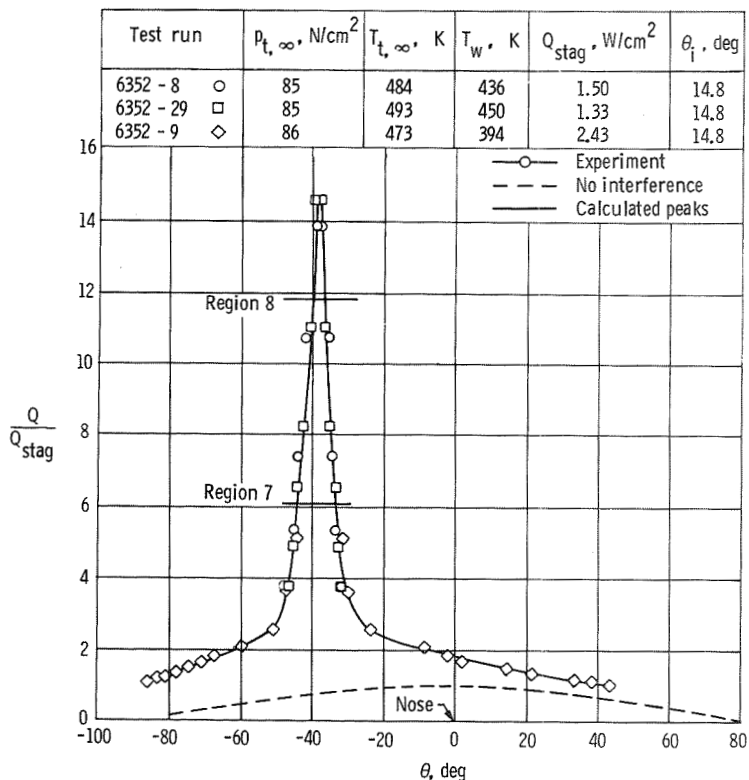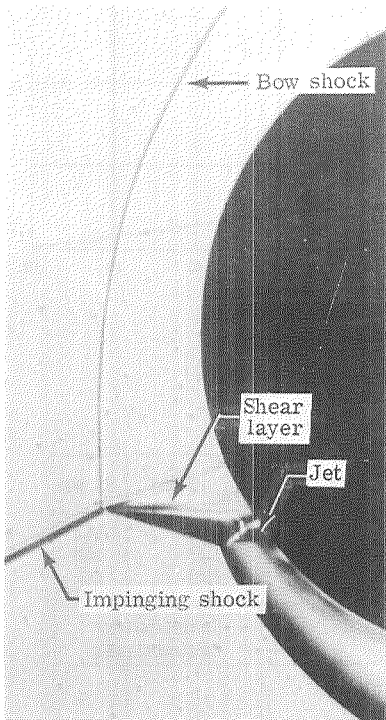
Region 7

Nose

$\dfrac{Q}{Q_{stag}}$

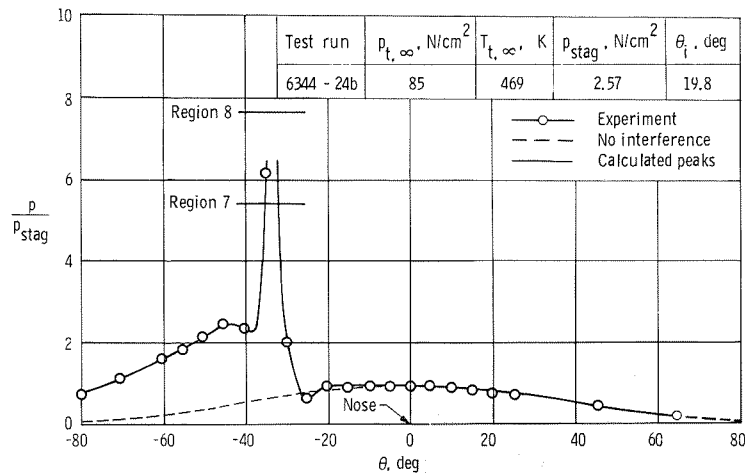θ, deg

(c) Heat-transfer distribution.

Figure 51.- Type IV interference on a 0.051-m-diameter hemisphere at Mach 5.94 in air.
$\theta_i \approx 9.8^o$; $N_{Re,\infty}/m \approx 8.0 \times 10^6$; $\gamma = 1.4$.

Test run	$P_{t,\infty}$, N/cm²	$T_{t,\infty}$, K	P_{stag}, N/cm²	θ_i, deg
6344 – 9b	85	478	2.56	14.8

Experiment
No interference
Calculated peaks

Region 8

Region 7

Nose

θ, deg

(b) Pressure distribution.

(a) Schlieren photograph.

L-73-256

Bow shock
Shear layer
Jet
Impinging shock

Test run		$P_{t,\infty}$, N/cm²	$T_{t,\infty}$, K	T_w, K	Q_{stag}, W/cm²	θ_i, deg
6352 – 27	○	84	493	450	1.33	14.8
6352 – 28	□	83	478	394	2.51	14.8

Experiment
No interference
Calculated peaks

Region 8

Region 7

Nose

θ, deg

(c) Heat-transfer distribution.

Figure 52.- Type IV interference on a 0.051-m-diameter hemisphere at Mach 5.94 in air.
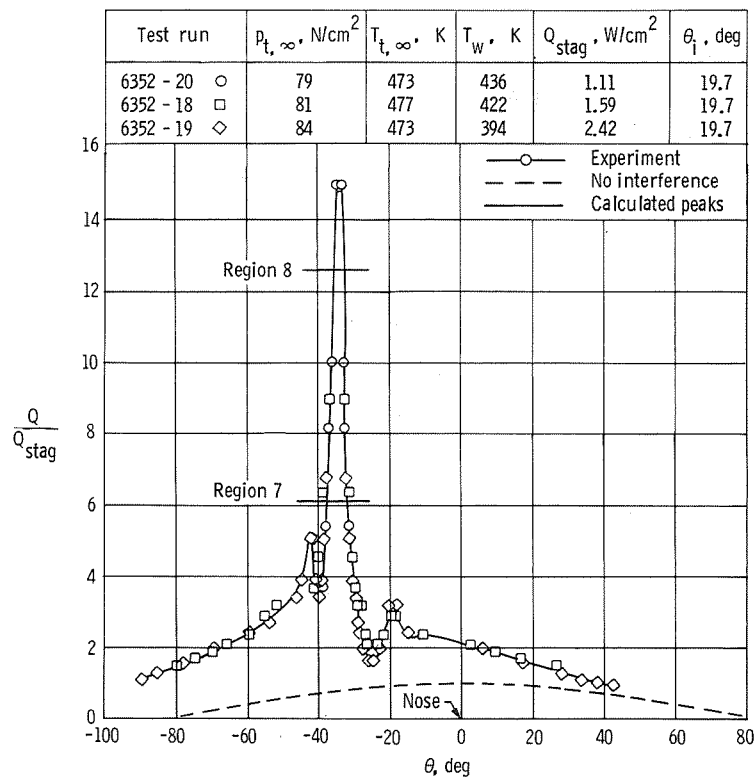$\theta_i = 14.8°$; $N_{Re,\infty}/m \approx 7.5 \times 10^6$; $\gamma = 1.4$.
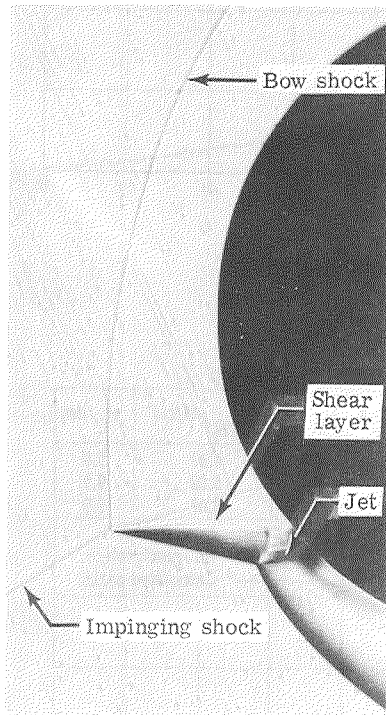
L-73-257

(a) Schlieren photograph.

Test run	$p_{t,\infty}$, N/cm^2	$T_{t,\infty}$, K	p_{stag}, N/cm^2	θ_i, deg
6344 – 5b	83	452	2.56	14.8

Region 8

Region 7

Nose

(b) Pressure distribution.

Test run		$p_{t,\infty}$, N/cm^2	$T_{t,\infty}$, K	T_w, K	Q_{stag}, W/cm^2	θ_i, deg
6352 – 8	O	85	484	436	1.50	14.8
6352 – 29	□	85	493	450	1.33	14.8
6352 – 9	◇	86	473	394	2.43	14.8

Region 8

Region 7

Nose

(c) Heat-transfer distribution.

Figure 53.- Type IV interference on a 0.051-m-diameter hemisphere at Mach 5.94 in air.
$\theta_i = 14.8^O$; $N_{Re,\infty}/m \approx 7.7 \times 10^6$; $\gamma = 1.4$.

L-73-258

(a) Schlieren photograph.

(b) Pressure distribution.

Test run	$p_{t,\infty}$, N/cm^2	$T_{t,\infty}$, K	p_{stag}, N/cm^2	θ_i, deg
6344 - 24b	85	469	2.57	19.8

| Test run		$p_{t,\infty}$, N/cm^2	$T_{t,\infty}$, K	T_w, K	Q_{stag}, W/cm^2	θ_i, deg
6352 - 20	○	79	473	436	1.11	19.7
6352 - 18	□	81	477	422	1.59	19.7
6352 - 19	◇	84	473	394	2.42	19.7

(c) Heat-transfer distribution.

Figure 54.- Type IV interference on a 0.051-m-diameter hemisphere at Mach 5.94 in air. $\theta_i \approx 20^\circ$; $N_{Re,\infty}/m \approx 7.6 \times 10^6$; $\gamma = 1.4$.
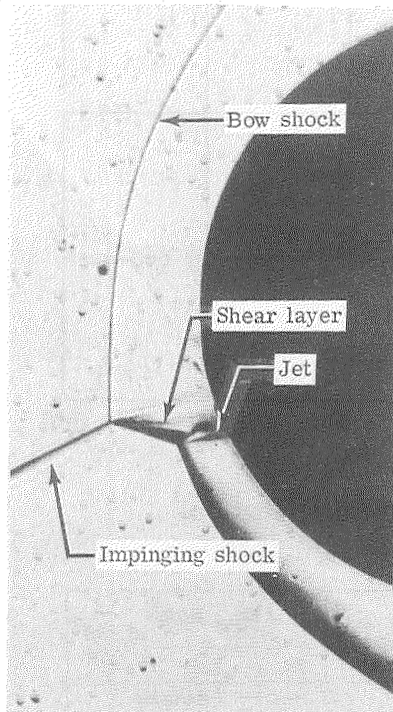
L-73-259

(a) Schlieren photograph.
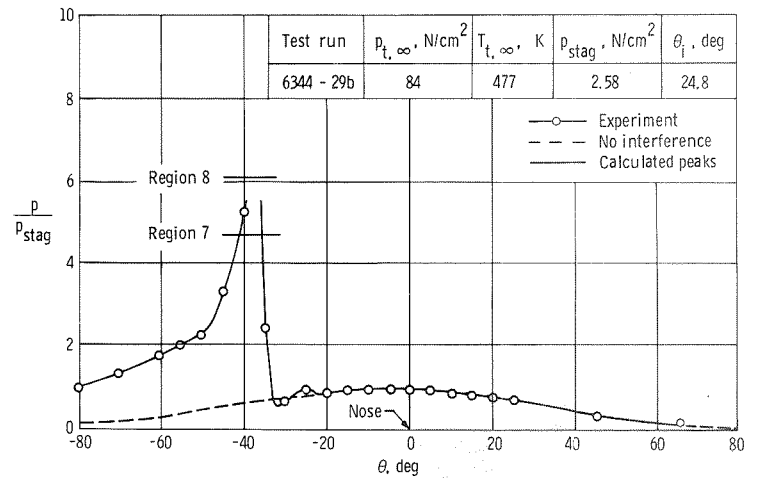
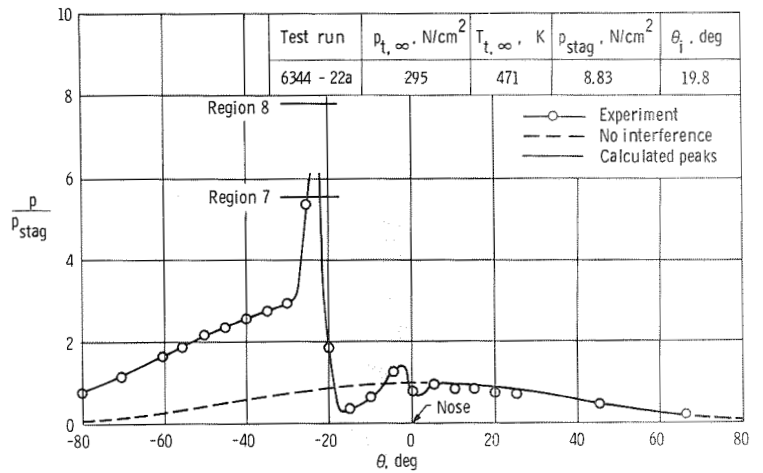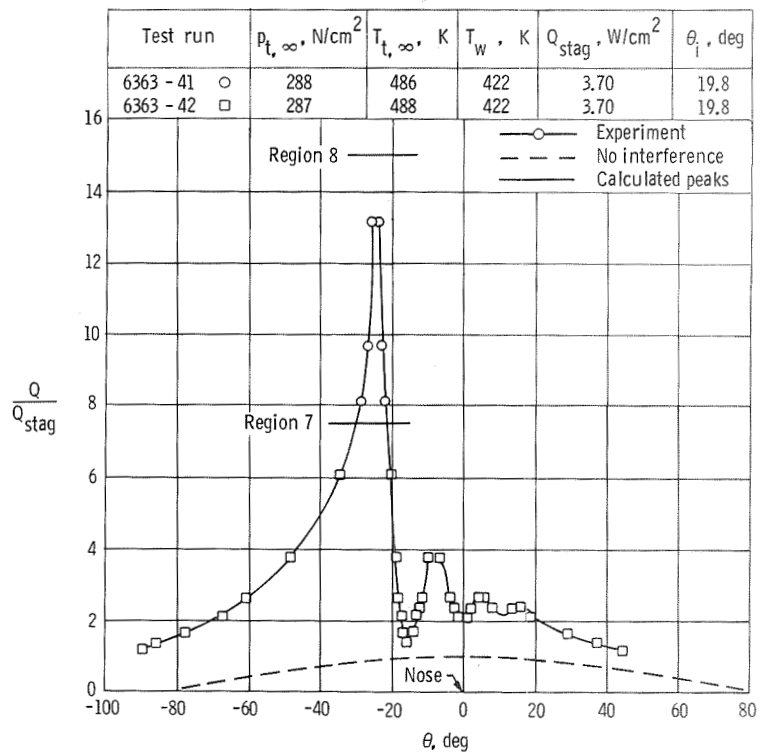(b) Pressure distribution.
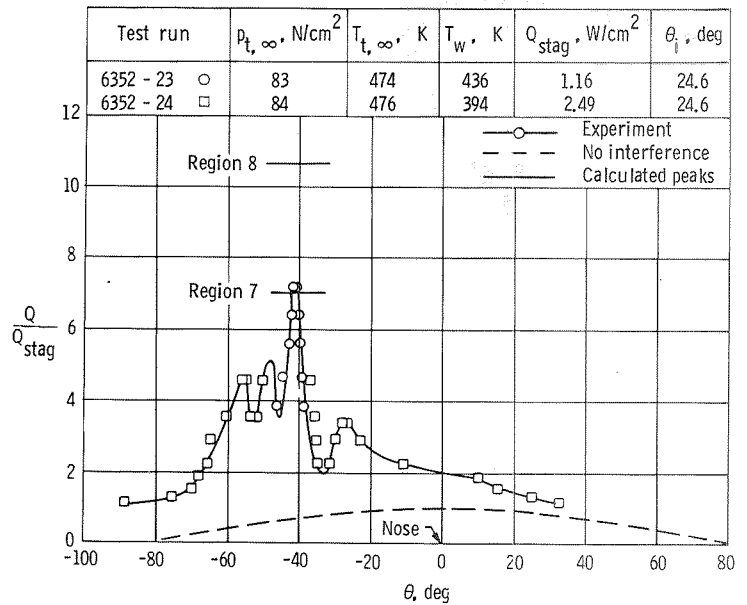
(c) Heat-transfer distribution.

Figure 55.- Type IV interference on a 0.051-m-diameter hemisphere at Mach 5.94 in air. $\theta_i \approx 25^\circ$; $N_{Re,\infty}/m \approx 7.8 \times 10^6$; $\gamma = 1.4$.
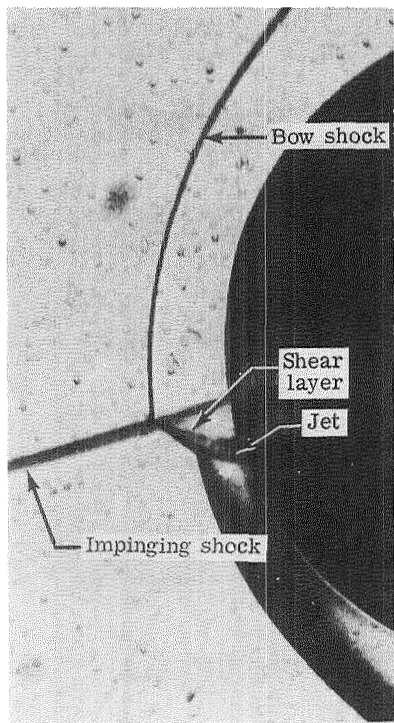
109

(b) Pressure distribution.
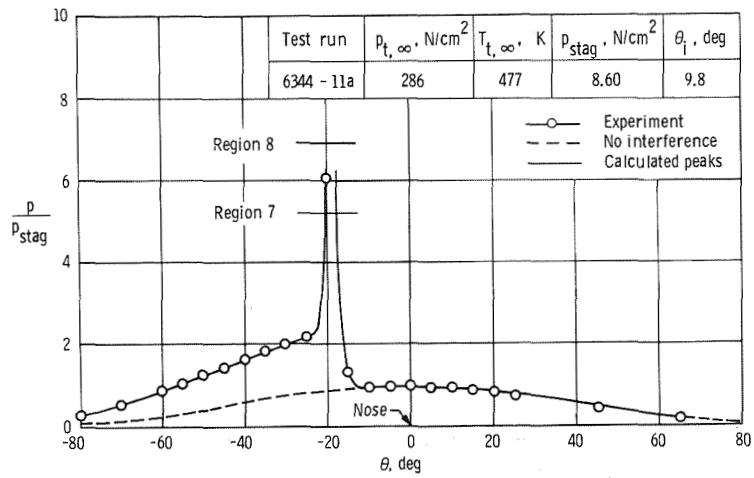
L-73-260
(a) Schlieren photograph.
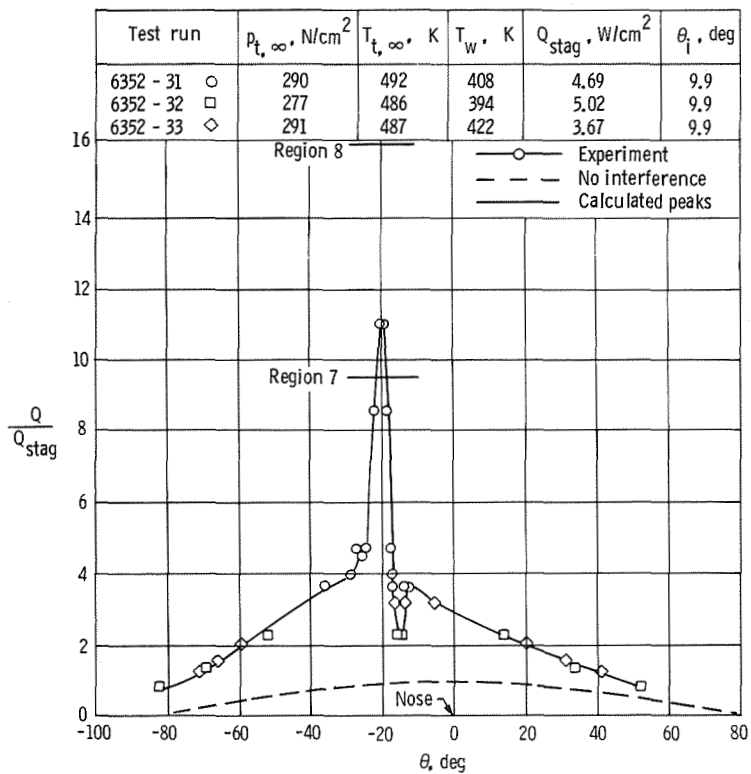
(c) Heat-transfer distribution.

Figure 56.- Type IV interference on a 0.051-m-diameter hemisphere at Mach 6.00 in air. $\theta_i = 9.8°$; $N_{Re,\infty}/m \approx 25.0 \times 10^6$; $\gamma = 1.4$.
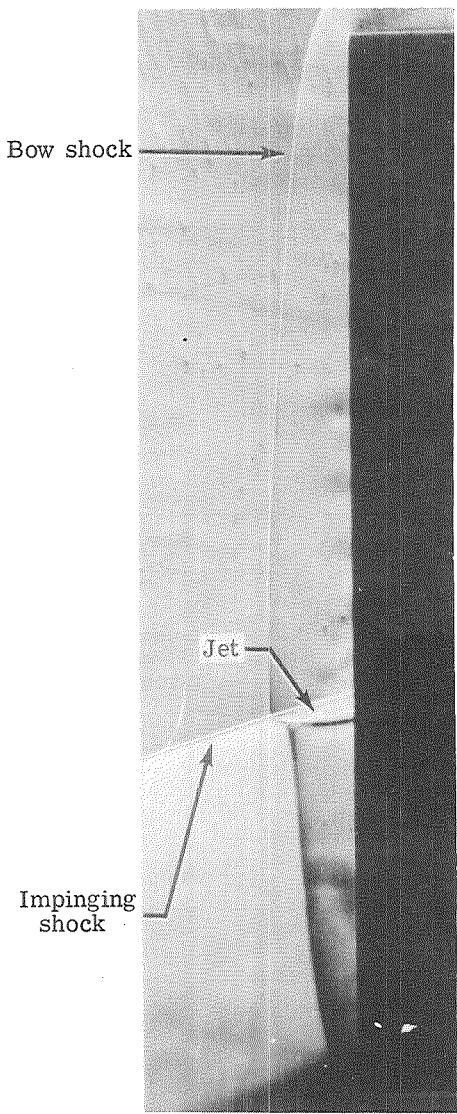
L-73-261

(a) Schlieren photograph.

Test run	$p_{t,\infty}$, N/cm^2	$T_{t,\infty}$, K	p_{stag}, N/cm^2	θ_i, deg
6344 - 22a	295	471	8.83	19.8

(b) Pressure distribution.

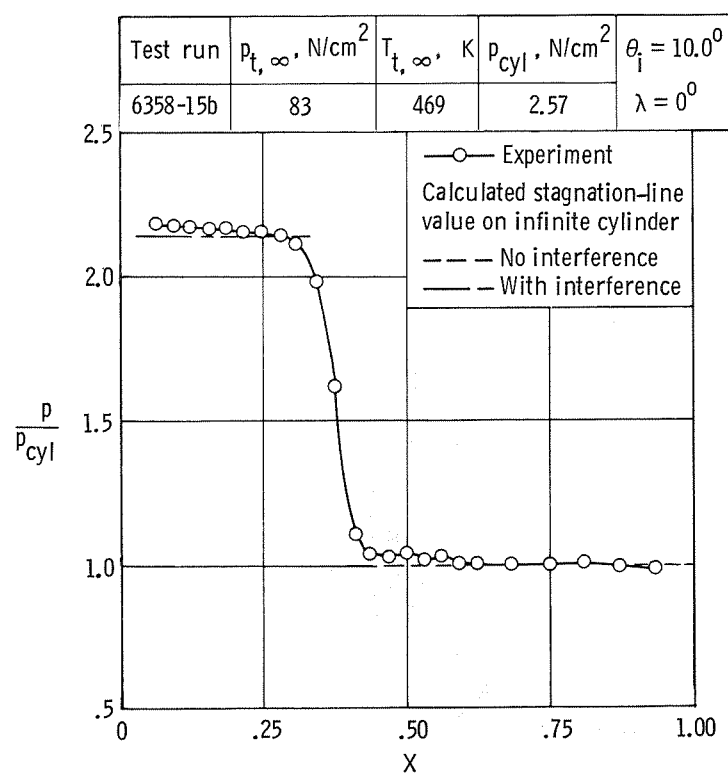| Test run		$p_{t,\infty}$, N/cm^2	$T_{t,\infty}$, K	T_w, K	Q_{stag}, W/cm^2	θ_i, deg
6363 - 41	O	288	486	422	3.70	19.8
6363 - 42	□	287	488	422	3.70	19.8

(c) Heat-transfer distribution.

Figure 57.- Type III interference on a 0.051-m-diameter hemisphere at Mach 6.00 in air. $\theta_i = 19.8^O$; $N_{Re,\infty}/m \approx 25.6 \times 10^6$; $\gamma = 1.4$.
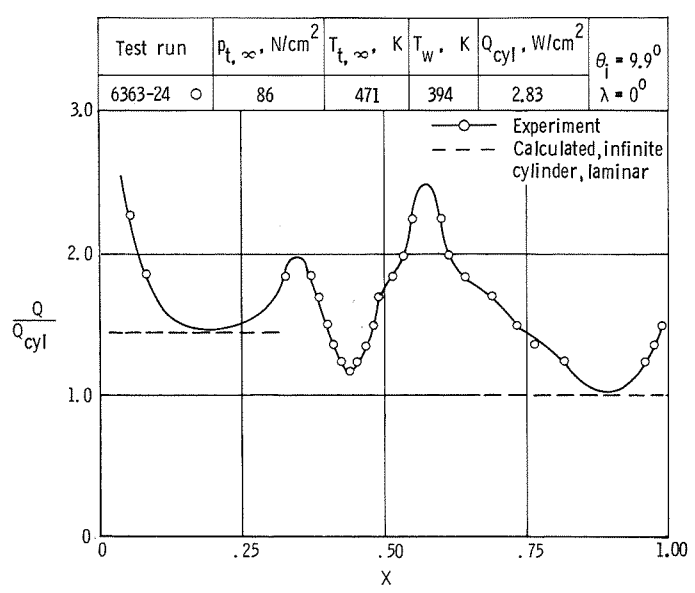
Bow shock

Jet

Impinging
shock

L-73-262

(a) Schlieren photograph.

Test run	$p_{t,\infty}$, N/cm^2	$T_{t,\infty}$, K	p_{cyl}, N/cm^2	$\theta_i = 10.0^0$
6358-15b	83	469	2.57	$\lambda = 0^0$

Experiment

Calculated stagnation-line
value on infinite cylinder

— — — No interference

———— With interference

(b) Pressure distribution.

Test run	$p_{t,\infty}$, N/cm^2	$T_{t,\infty}$, K	T_w, K	Q_{cyl}, W/cm^2	$\theta_i = 9.9^0$
6363-24 ○	86	471	394	2.83	$\lambda = 0^0$

Experiment

Calculated, infinite
cylinder, laminar
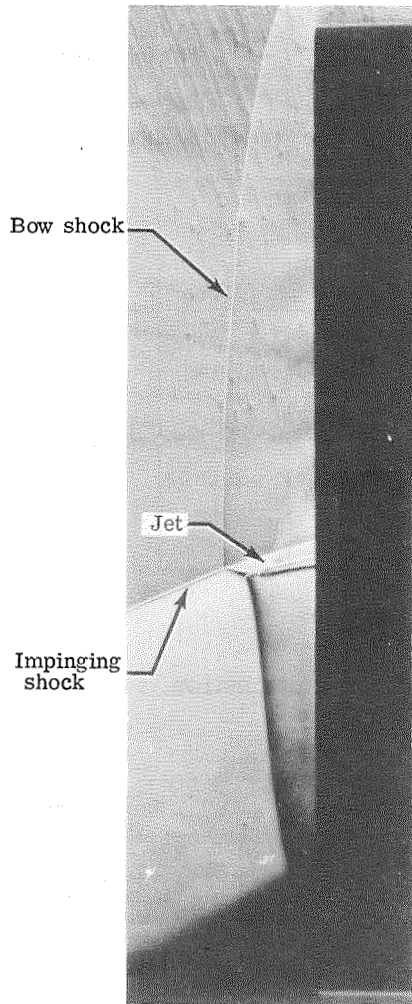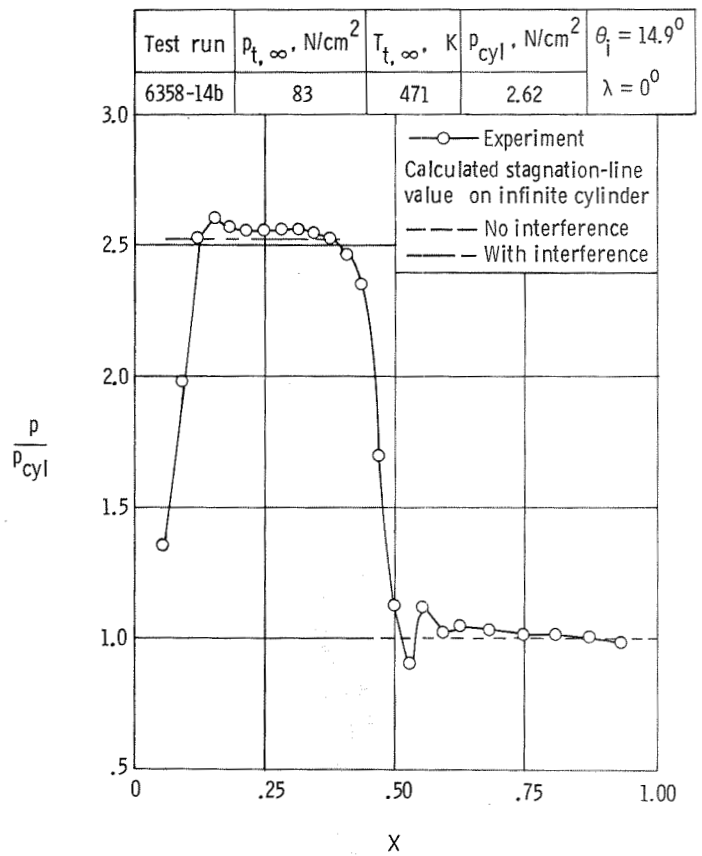
(c) Heat-transfer distribution.

Figure 58.- Type IVa interference on a fin at Mach 5.94 in air. $\theta_i \approx 10^0$;
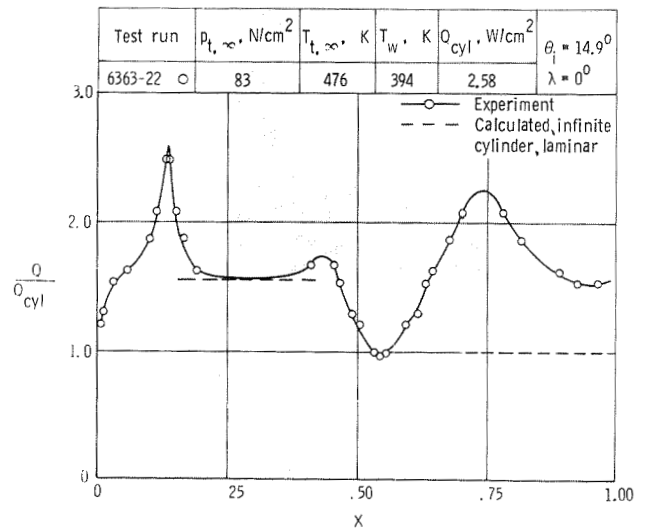$N_{Re,\infty}/m \approx 8.1 \times 10^6$; $\gamma = 1.4$.

L-73-263

(a) Schlieren photograph.

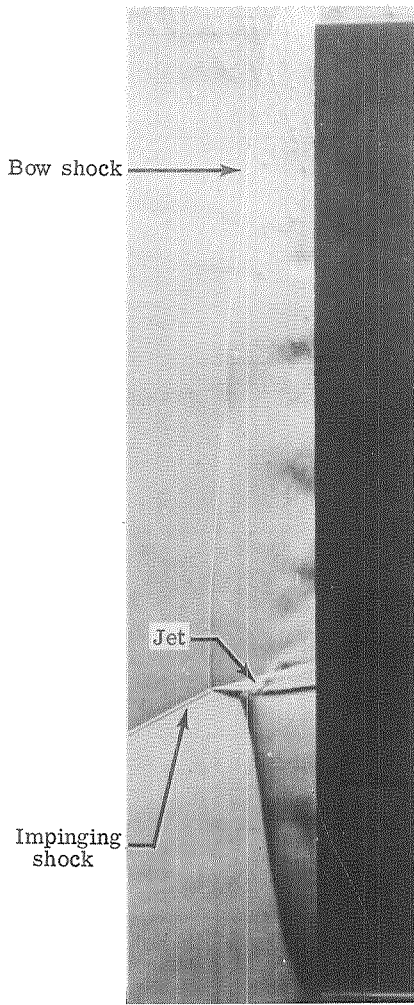| Test run	$p_{t,\infty}$, N/cm^2	$T_{t,\infty}$, K	p_{cyl}, N/cm^2	$\theta_i = 14.9^0$
6358-14b	83	471	2.62	$\lambda = 0^0$

(b) Pressure distribution.

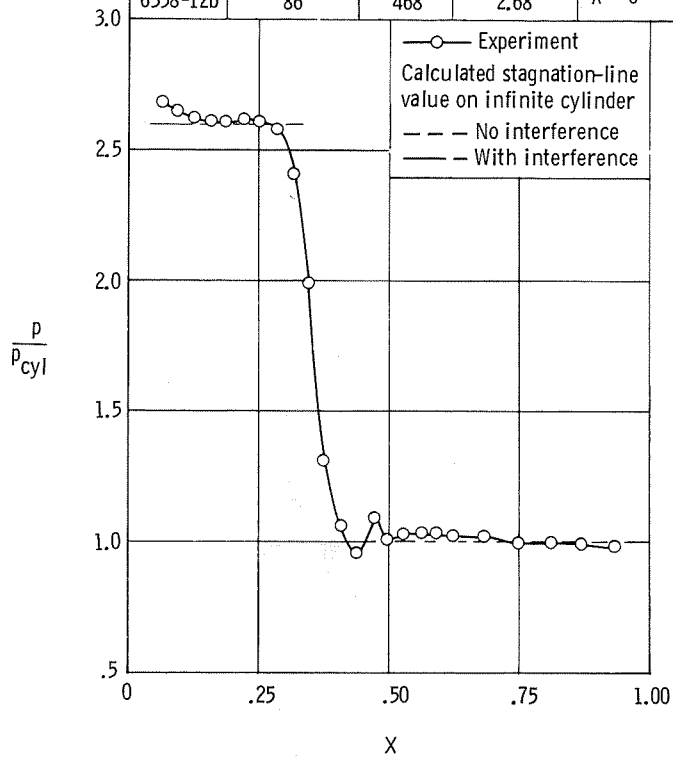| Test run	$p_{t,\infty}$, N/cm^2	$T_{t,\infty}$, K	T_w, K	Q_{cyl}, W/cm^2	$\theta_i = 14.9^0$
6363-22	83	476	394	2.58	$\lambda = 0^0$

(c) Heat-transfer distribution.

Figure 59.- Type IVa interference on a fin at Mach 5.94 in air. $\theta_i = 14.9^0$; $N_{Re,\infty}/m \approx 7.7 \times 10^6$; $\gamma = 1.4$.

113

Bow shock →
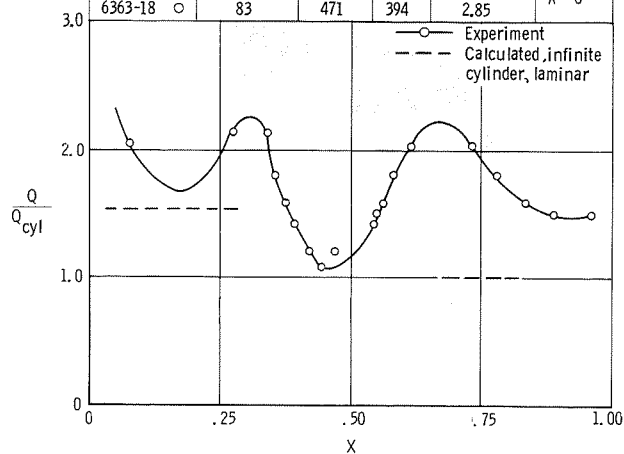
Jet →

Impinging shock →

L-73-264

(a) Schlieren photograph.

Test run	$p_{t,\infty}$, N/cm^2	$T_{t,\infty}$, K	p_{cyl}, N/cm^2	$\theta_i = 19.9^0$
6358-12b	86	468	2.68	$\lambda = 0^0$

—o— Experiment

Calculated stagnation-line value on infinite cylinder

— — — No interference

——— With interference

(b) Pressure distribution.

Test run	$p_{t,\infty}$, N/cm^2	$T_{t,\infty}$, K	T_w, K	Q_{cyl}, W/cm^2	$\theta_i = 19.9^0$
6363-18 o	83	471	394	2.85	$\lambda = 0^0$

—o— Experiment

— — — Calculated, infinite cylinder, laminar
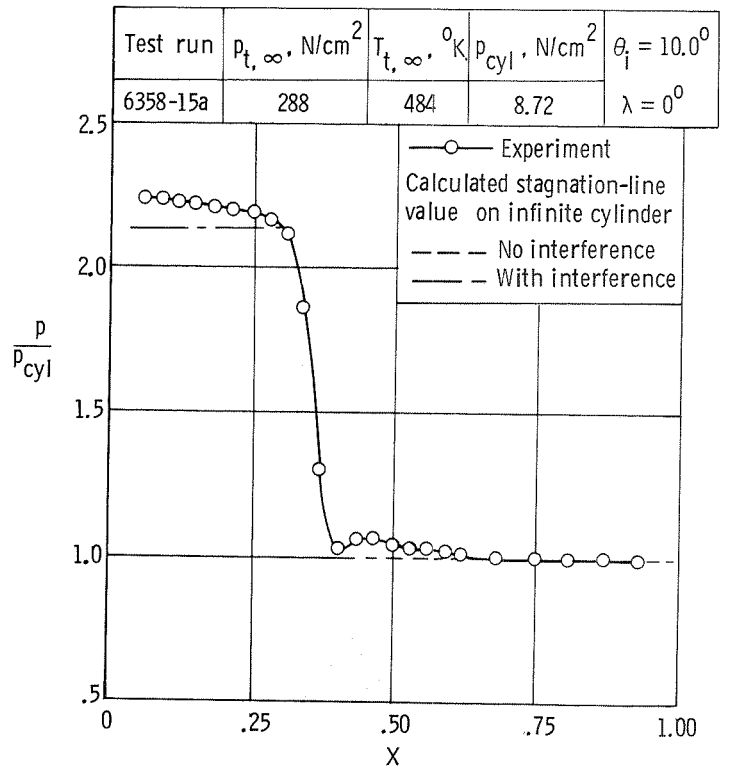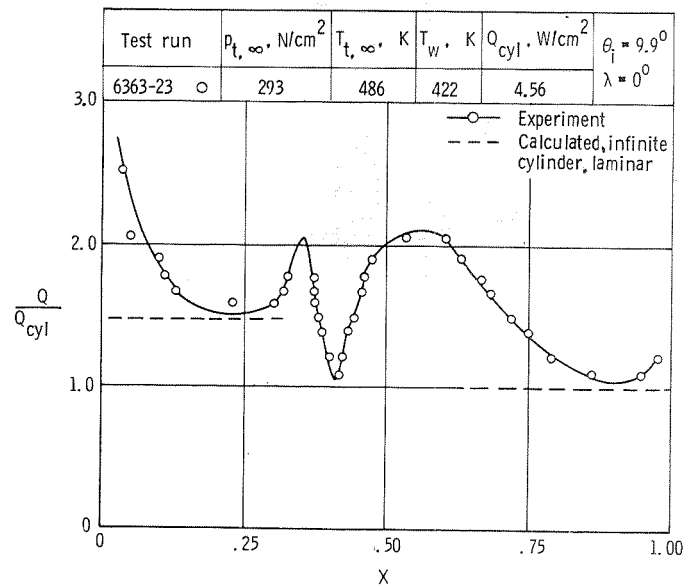
(c) Heat-transfer distribution.

Figure 60.- Type IVa interference on a fin at Mach 5.94 in air. $\theta_i = 19.9^0$; $N_{Re,\infty}/m \approx 7.9 \times 10^6$; $\gamma = 1.4$.
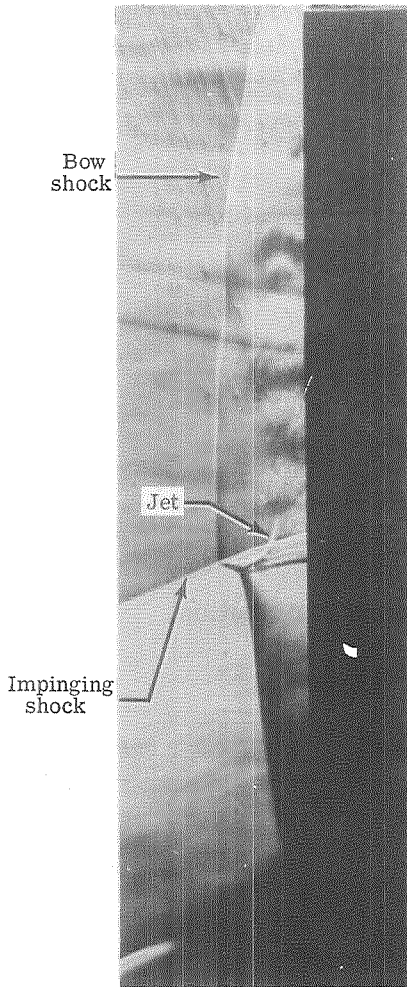
114

(a) Schlieren photograph.

L-73-265

Test run	$p_{t,\infty}$, N/cm^2	$T_{t,\infty}$, $^\circ$K	p_{cyl}, N/cm^2	$\theta_i = 10.0^0$
6358-15a	288	484	8.72	$\lambda = 0^0$

(b) Pressure distribution.

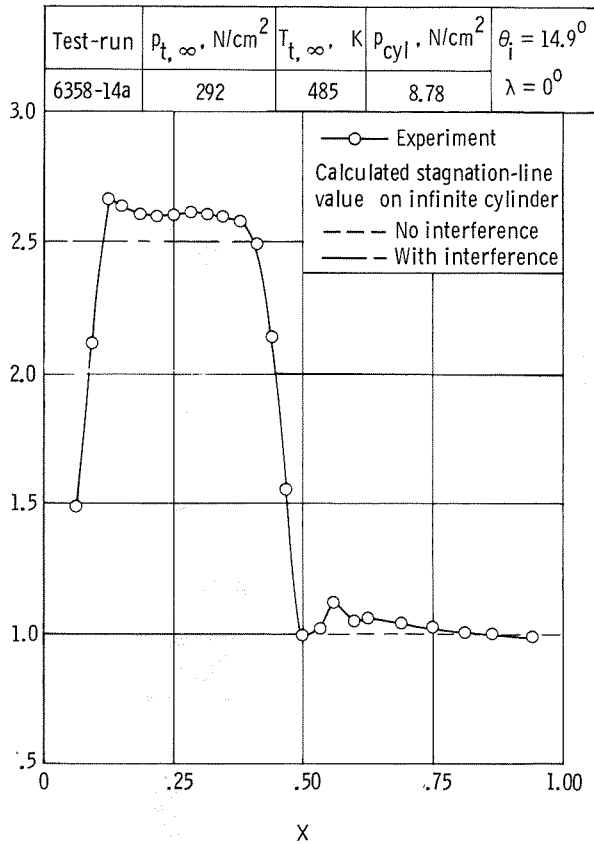| Test run	$p_{t,\infty}$, N/cm^2	$T_{t,\infty}$, K	T_w, K	Q_{cyl}, W/cm^2	$\theta_i = 9.9^0$
6363-23 ○	293	486	422	4.56	$\lambda = 0^0$
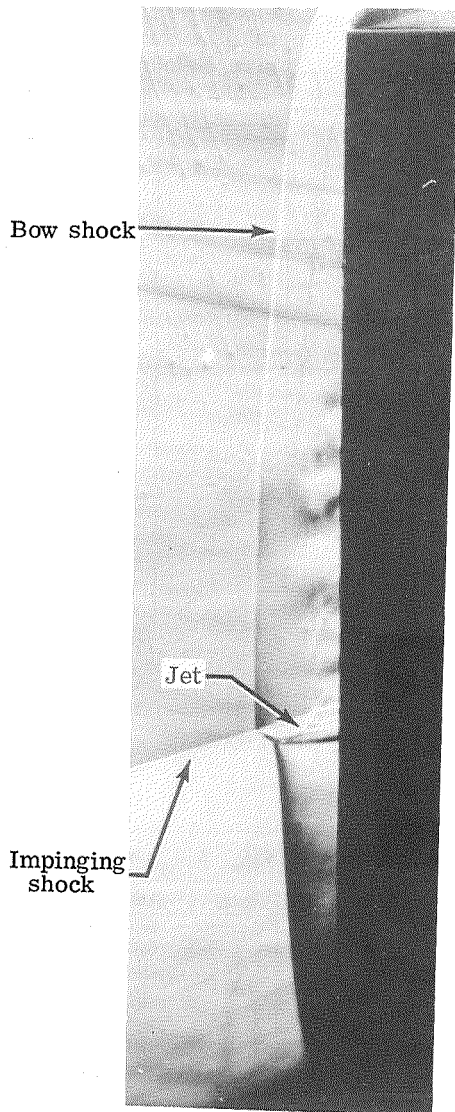
(c) Heat-transfer distribution.

Figure 61.- Type IVa interference on a fin at Mach 6.00 in air. $\theta_i \approx 10^0$; $N_{Re,\infty}/m \approx 26.2 \times 10^6$; $\gamma = 1.4$.

Bow shock

Jet

Impinging shock

L-73-266

(a) Schlieren photograph.

Test-run	$p_{t,\infty}$, N/cm^2	$T_{t,\infty}$, K	p_{cyl}, N/cm^2	$\theta_i = 14.9^0$
6358-14a	292	485	8.78	$\lambda = 0^0$

Experiment ⊶⊙⊸

Calculated stagnation-line value on infinite cylinder

— — No interference

—— With interference

$\dfrac{p}{p_{cyl}}$

X

(b) Pressure distribution.

Test run	$p_{t,\infty}$, N/cm^2	$T_{t,\infty}$, K	T_w, K	Q_{cyl}, W/cm^2	$\theta_i = 14.9^0$
6363-20 ○	289	491	422	4.87	$\lambda = 0^0$

Experiment ⊶⊙⊸

Calculated, infinite cylinder, laminar

$\dfrac{Q}{Q_{cyl}}$

X

(c) Heat-transfer distribution.

Figure 62.- Type IVa interference on a fin at Mach 6.00 in air. $\theta_i = 14.9^0$; $N_{Re,\infty}/m \approx 25.4 \times 10^6$; $\gamma = 1.4$.
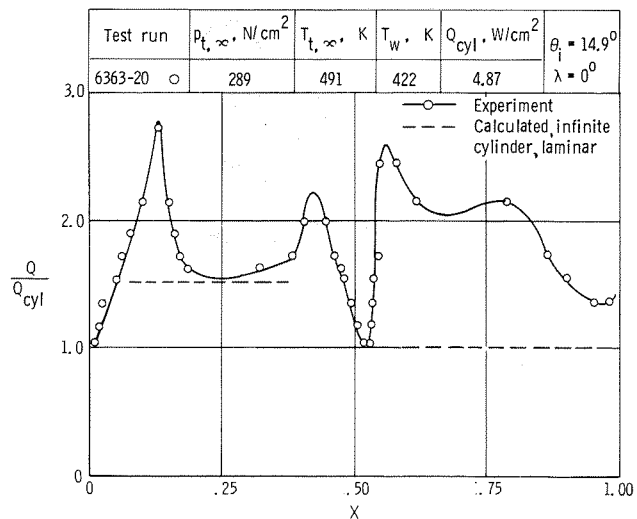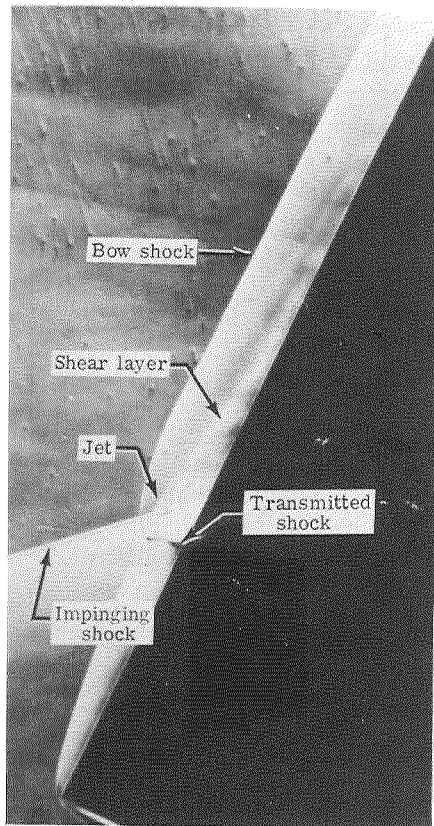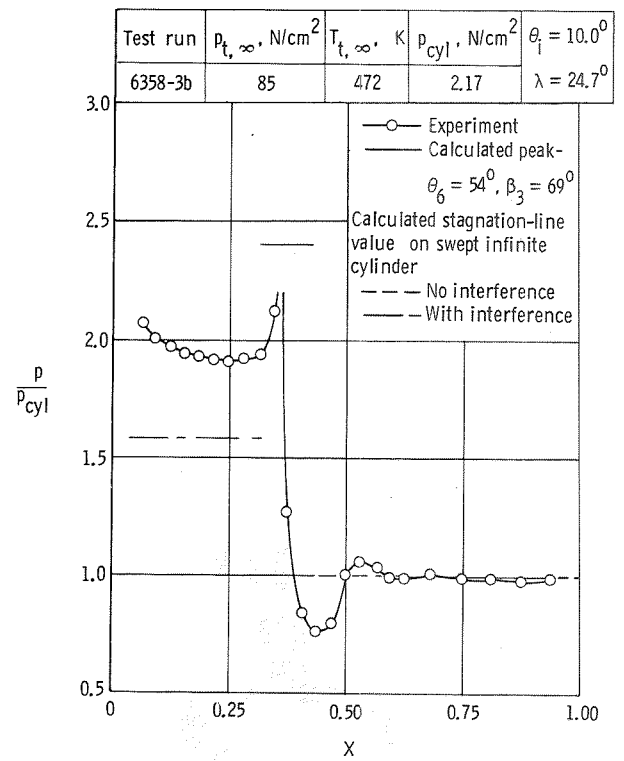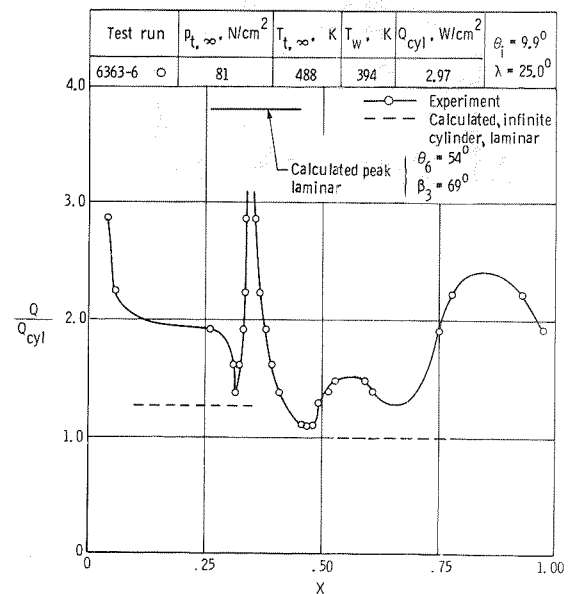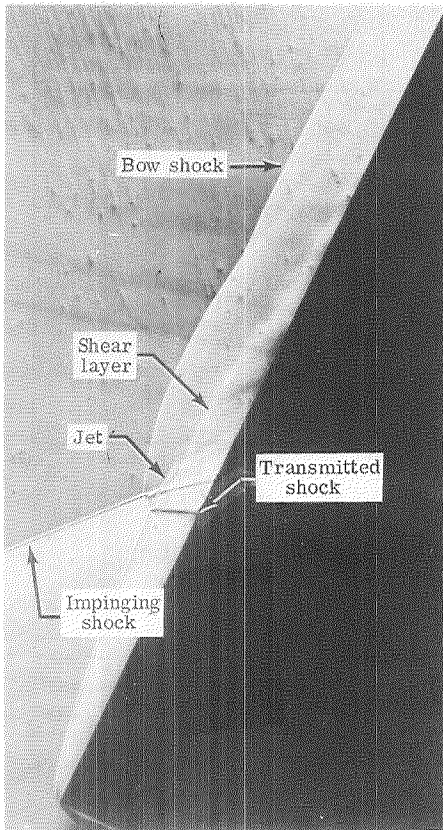
L-73-267

(a) Schlieren photograph.

Test run	$p_{t,\infty}$, N/cm^2	$T_{t,\infty}$, K	p_{cyl}, N/cm^2	$\theta_i = 10.0^0$
6358-3b	85	472	2.17	$\lambda = 24.7^0$

Experiment
Calculated peak-
$\theta_6 = 54^0$, $\beta_3 = 69^0$
Calculated stagnation-line value on swept infinite cylinder
— — No interference
— — With interference

(b) Pressure distribution.

Test run	$p_{t,\infty}$, N/cm^2	$T_{t,\infty}$, K	T_w, K	Q_{cyl}, W/cm^2	$\theta_i = 9.9^0$
6363-6 $\circ$	81	488	394	2.97	$\lambda = 25.0^0$

Experiment
Calculated, infinite cylinder, laminar
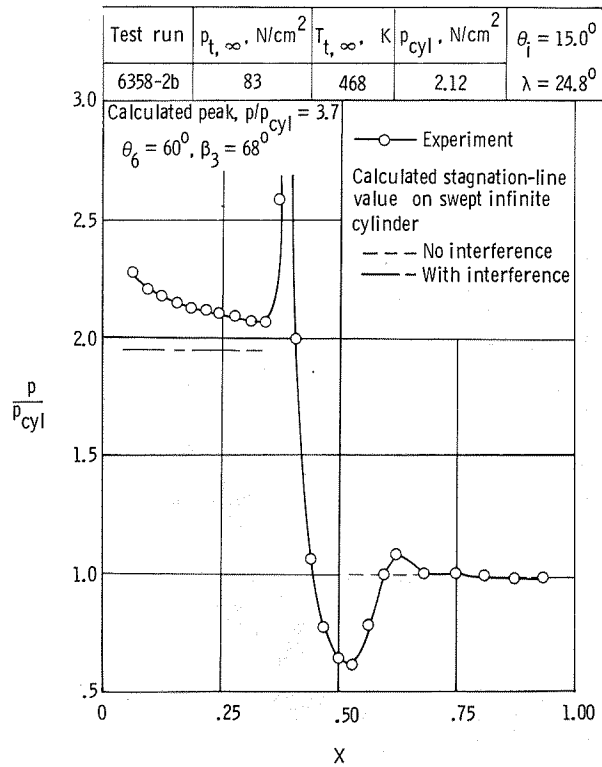Calculated peak laminar
$\theta_6 = 54^0$
$\beta_3 = 69^0$

(c) Heat-transfer distribution.

Figure 63.- Type V interference on a fin at Mach 5.94 in air. $\theta_i \approx 10^0$; $N_{Re,\infty}/m \approx 7.2 \times 10^6$; $\gamma = 1.4$.
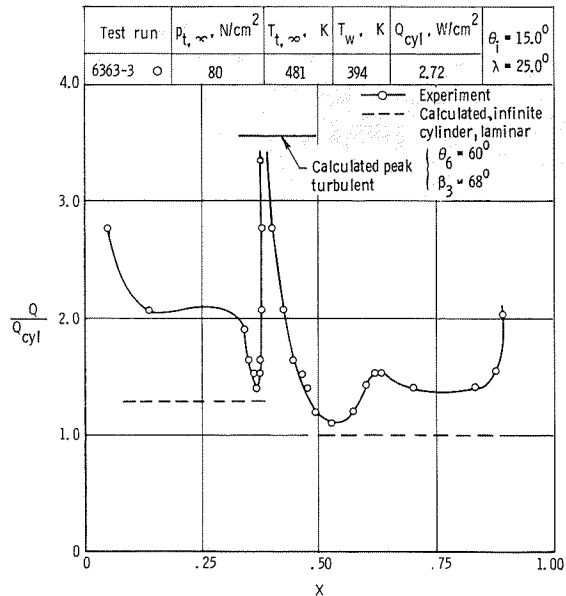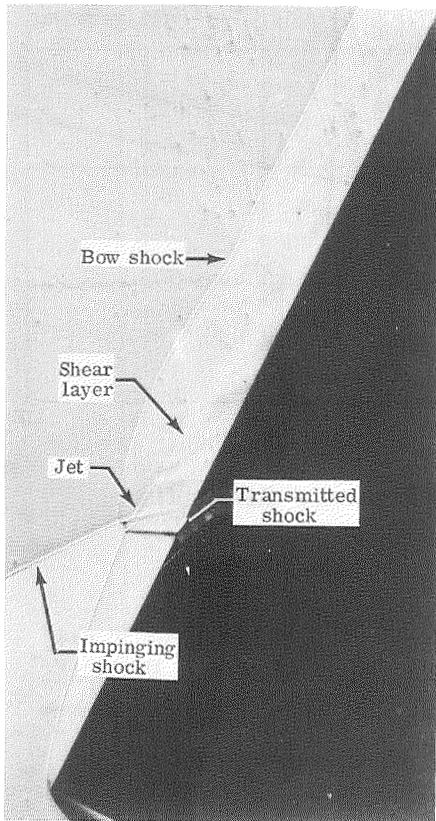
117

L-73-268

(a) Schlieren photograph.

Test run	$p_{t,\infty}$, N/cm^2	$T_{t,\infty}$, K	p_{cyl}, N/cm^2	$\theta_i = 15.0^0$
6358-2b	83	468	2.12	$\lambda = 24.8^0$

Calculated peak, $p/p_{cyl} = 3.7$
$\theta_6 = 60^0$, $\beta_3 = 68^0$

— Experiment

Calculated stagnation-line value on swept infinite cylinder
— — — No interference
—— With interference

(b) Pressure distribution.

Test run	$p_{t,\infty}$, N/cm^2	$T_{t,\infty}$, K	T_w, K	Q_{cyl}, W/cm^2	$\theta_i = 15.0^0$
6363-3 ○	80	481	394	2.72	$\lambda = 25.0^0$

— Experiment
— — — Calculated, infinite cylinder, laminar $\{\theta_6 = 60^0 \atop \beta_3 = 68^0$

Calculated peak turbulent

(c) Heat-transfer distribution.
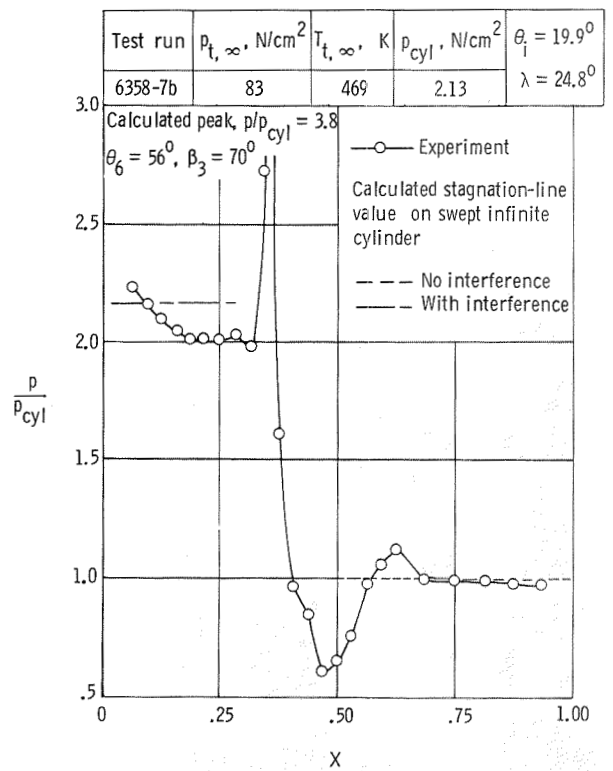
Figure 64.- Type V interference on a fin at Mach 5.94 in air. $\theta_i = 15^0$;
$N_{Re,\infty}/m \approx 7.3 \times 10^6$; $\gamma = -1.4$.

118

L-73-269

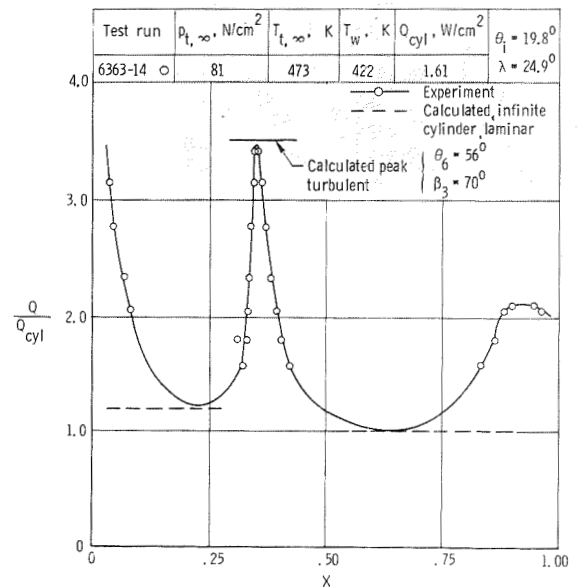(a) Schlieren photograph.

Test run	$p_{t,\infty}$, N/cm^2	$T_{t,\infty}$, K	p_{cyl}, N/cm^2	$\theta_i = 19.9^0$
6358-7b	83	469	2.13	$\lambda = 24.8^0$

Calculated peak, p/p_{cyl} = 3.8
$\theta_6 = 56^0$, $\beta_3 = 70^0$

—○— Experiment

Calculated stagnation-line value on swept infinite cylinder

— — — No interference
— — With interference

(b) Pressure distribution.

Test run	$p_{t,\infty}$, N/cm^2	$T_{t,\infty}$, K	T_w, K	Q_{cyl}, W/cm^2	$\theta_i = 19.8^0$
6363-14 ○	81	473	422	1.61	$\lambda = 24.9^0$

—○— Experiment
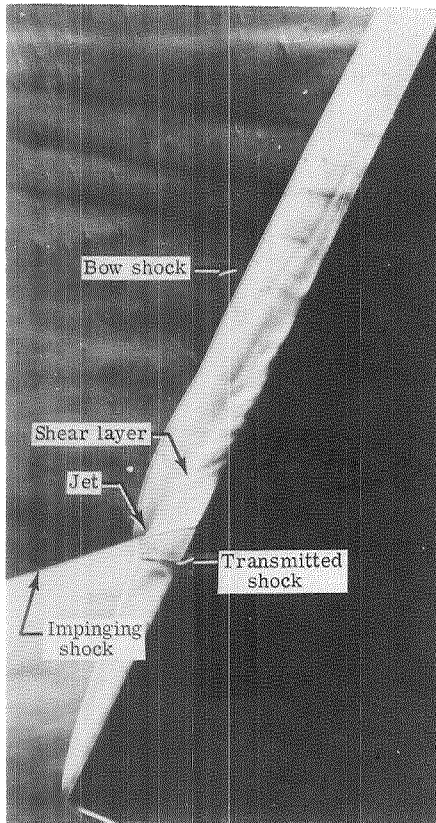— — Calculated, infinite cylinder, laminar

$\theta_6 = 56^0$
$\beta_3 = 70^0$

Calculated peak turbulent
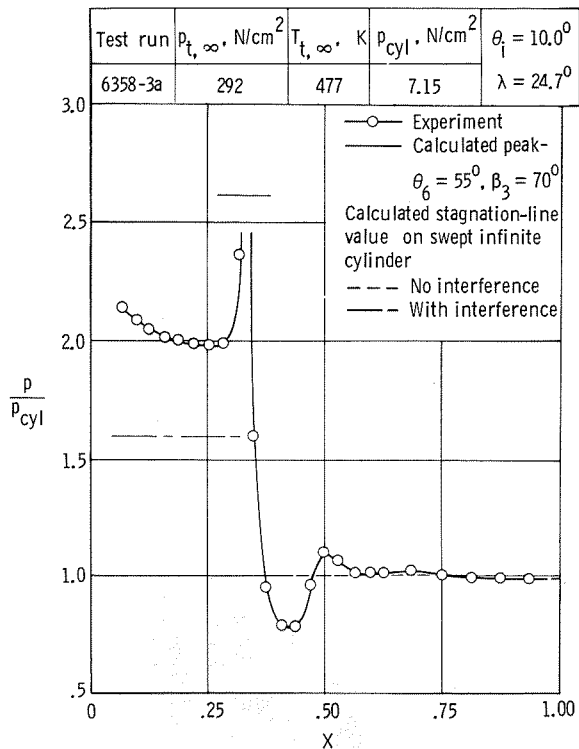
(c) Heat-transfer distribution.

Figure 65.- Type V interference on a fin at Mach 5.94 in air. $\theta_i \approx 20^0$;
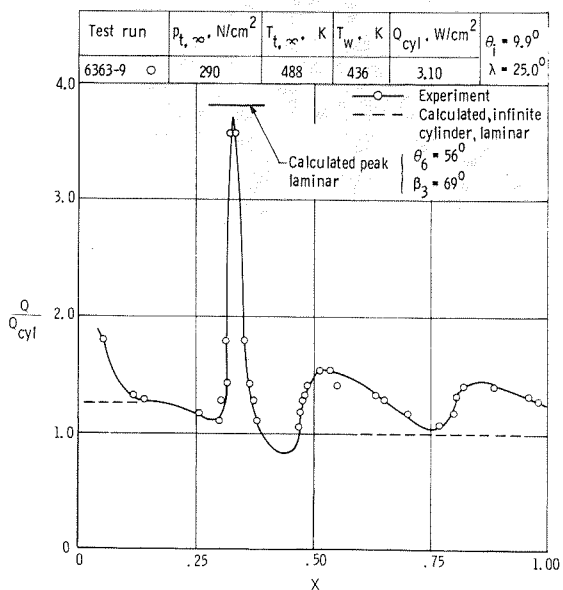$N_{Re,\infty}/m \approx 7.6 \times 10^6$; $\gamma = 1.4$.

119

L-73-270

(a) Schlieren photograph.

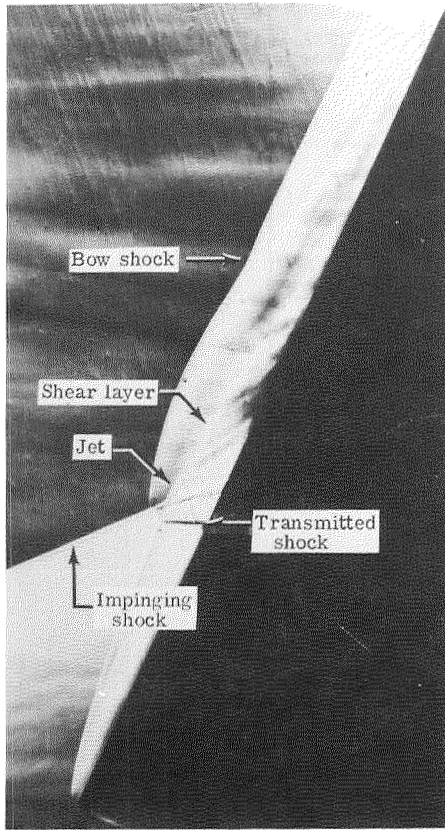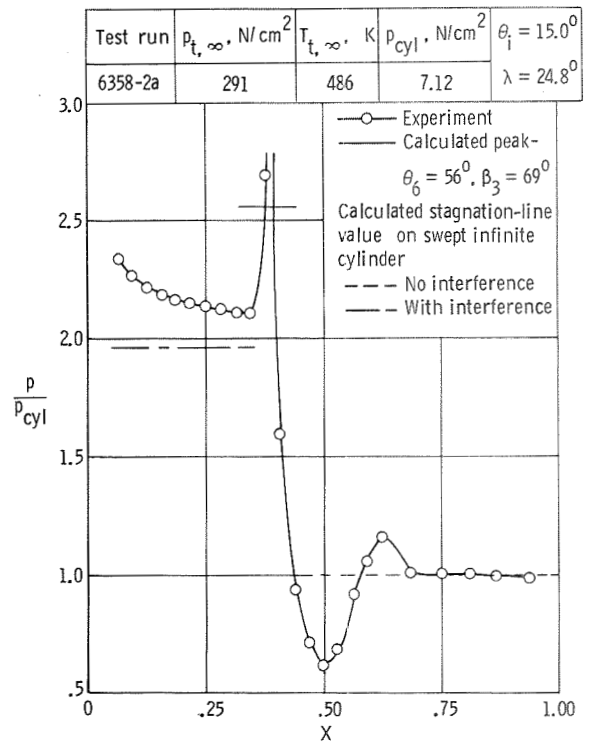| Test run	$p_{t,\infty}$, N/cm^2	$T_{t,\infty}$, K	p_{cyl}, N/cm^2	$\theta_i = 10.0^0$
6358-3a	292	477	7.15	$\lambda = 24.7^0$

- —○— Experiment
- —— Calculated peak-
- $\theta_6 = 55^0$, $\beta_3 = 70^0$
- Calculated stagnation-line value on swept infinite cylinder
- — — — No interference
- — · — With interference

(b) Pressure distribution.

Test run		$p_{t,\infty}$, N/cm^2	$T_{t,\infty}$, K	T_w, K	Q_{cyl}, W/cm^2	$\theta_i = 9.9^0$
6363-9	○	290	488	436	3.10	$\lambda = 25.0^0$

- —○— Experiment
- — — — Calculated, infinite cylinder, laminar
- Calculated peak laminar $\theta_6 = 56^0$ $\beta_3 = 69^0$
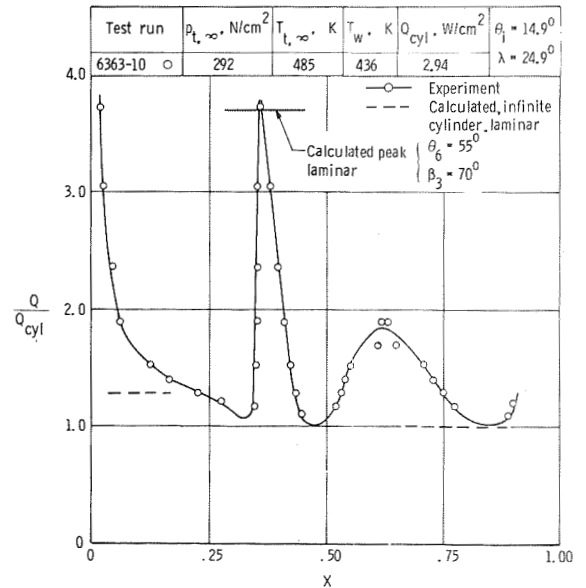
(c) Heat-transfer distribution.

Figure 66.- Type V interference on a fin at Mach 6.00 in air. $\theta_i \approx 10^0$; $N_{Re,\infty}/m \approx 25.7 \times 10^6$; $\gamma = 1.4$.
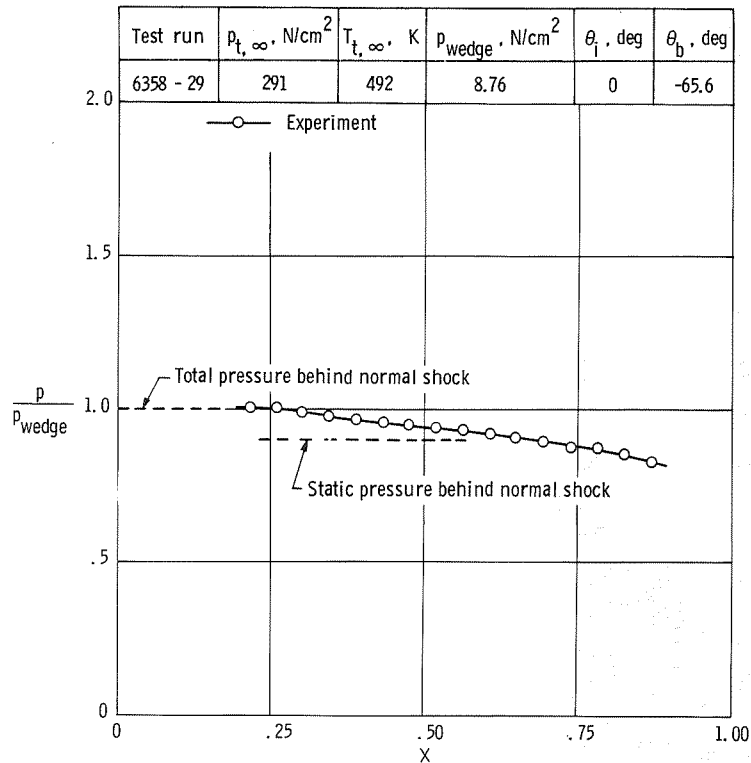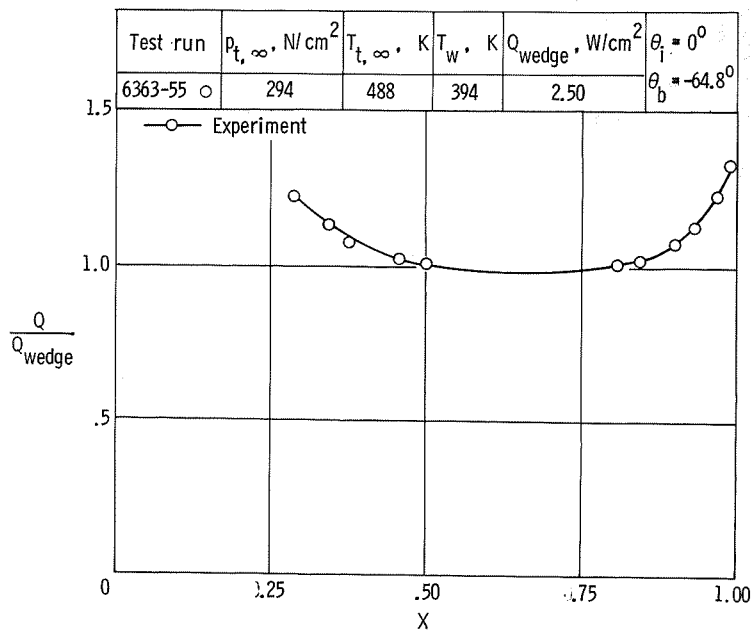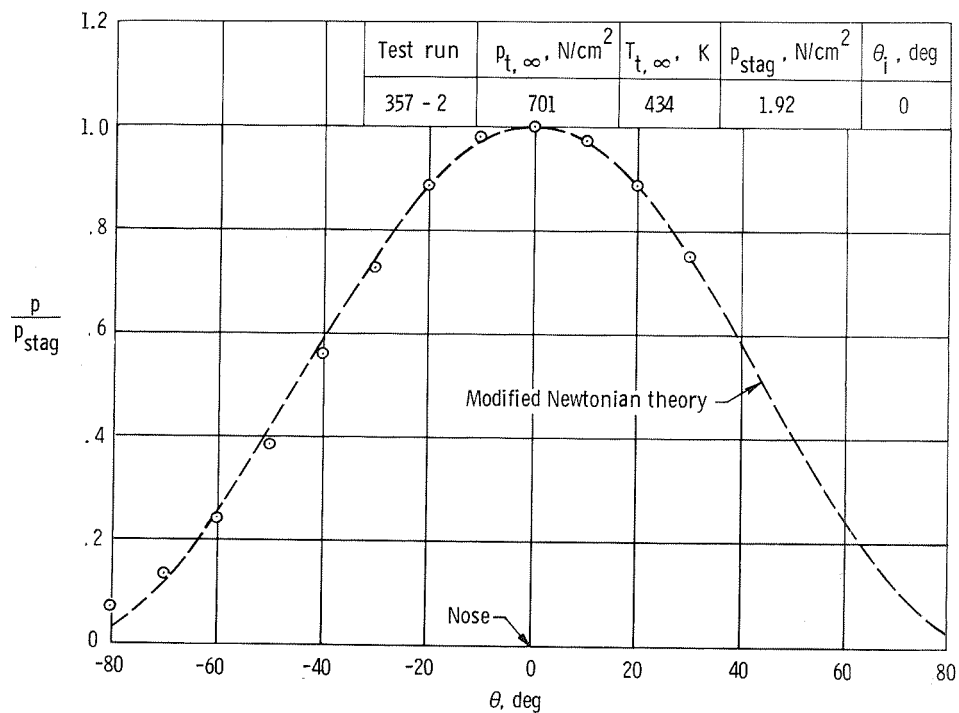
L-73-271

(a) Schlieren photograph.

Labels in photograph: Bow shock, Shear layer, Jet, Transmitted shock, Impinging shock

Test run	$p_{t,\infty}$, N/cm^2	$T_{t,\infty}$, K	p_{cyl}, N/cm^2	$\theta_i = 15.0^0$
6358-2a	291	486	7.12	$\lambda = 24.8^0$

Experiment
Calculated peak–
$\theta_6 = 56^0$, $\beta_3 = 69^0$
Calculated stagnation-line value on swept infinite cylinder
— — — No interference
— · — With interference

(b) Pressure distribution.

Test run	$p_{t,\infty}$, N/cm^2	$T_{t,\infty}$, K	T_w, K	Q_{cyl}, W/cm^2	$\theta_i = 14.9^0$
6363-10	292	485	436	2.94	$\lambda = 24.9^0$

Experiment
Calculated, infinite cylinder, laminar
Calculated peak laminar $\theta_6 = 55^0$ $\beta_3 = 70^0$

(c) Heat-transfer distribution.

Figure 67.- Type V interference on a fin at Mach 6.00 in air. $\theta_i \approx 15^0$; $N_{Re,\infty}/m \approx 26.2 \times 10^6$; $\gamma = 1.4$.

121

Test run	$p_{t,\infty}$, N/cm^2	$T_{t,\infty}$, K	p_{wedge}, N/cm^2	θ_i, deg	θ_b, deg
6358 - 29	291	492	8.76	0	-65.6

(a) Pressure distribution.

Test run	$p_{t,\infty}$, N/cm^2	$T_{t,\infty}$, K	T_w, K	Q_{wedge}, W/cm^2	$\theta_i = 0^0$
6363-55 ○	294	488	394	2.50	$\theta_b = -64.8^0$

(b) Heat-transfer distribution.

Figure 68.- Pressure and heat-transfer distribution on a 30^0 wedge at Mach 6.00 in air. $\theta_i = 0^0$; $N_{Re,\infty}/m \approx 26.1 \times 10^6$; $\gamma = 1.4$.

(a) Pressure distribution.
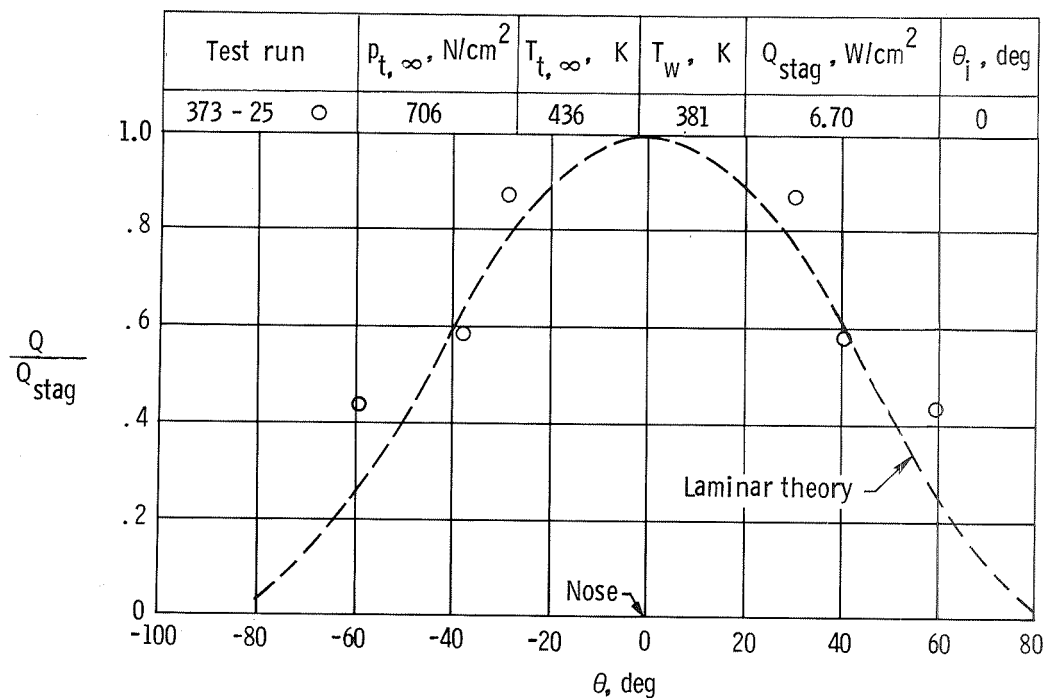
(b) Heat-transfer distribution.

Figure 69.- Pressure and heat-transfer distribution on a 0.025-m-diameter hemisphere at Mach 20.2 in helium. $\theta_i = 0°$; $N_{Re,\infty}/m \approx 9.6 \times 10^6$; $\gamma = 1.67$.
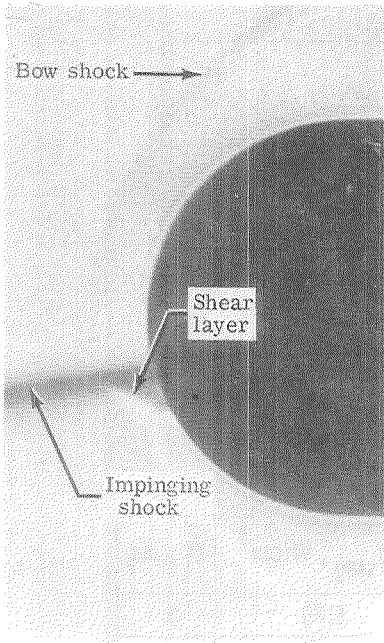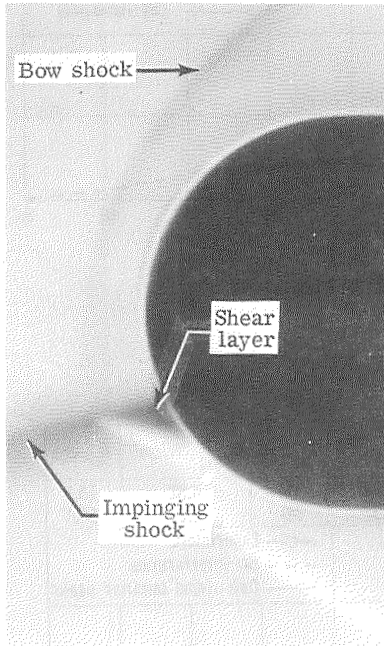
L-73-272
(a) Schlieren photograph.

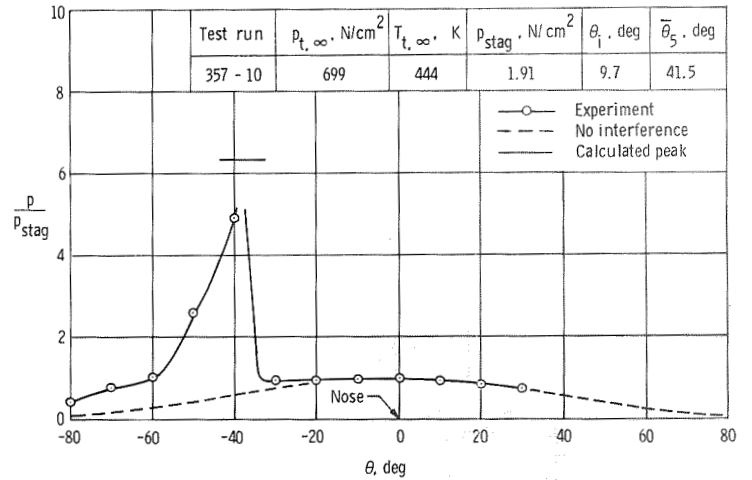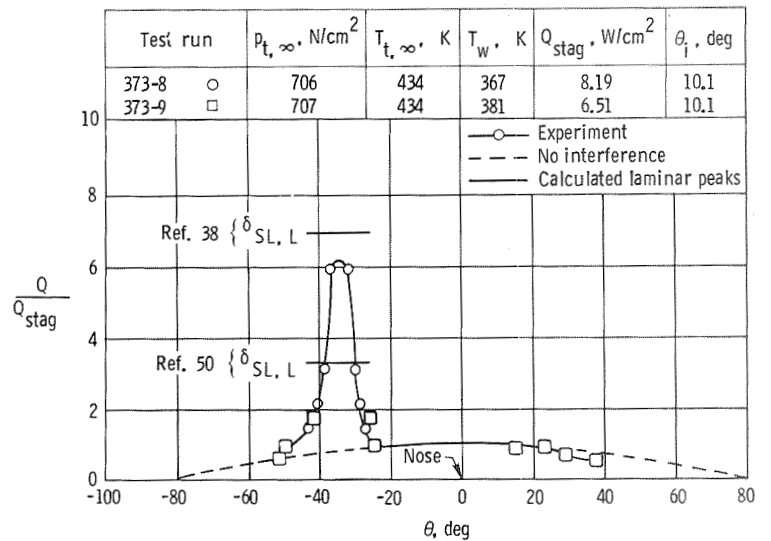| Test run	$p_{t,\infty}$, N/cm^2	$T_{t,\infty}$, K	p_{stag}, N/cm^2	θ_i, deg	$\bar{\theta}_5$, deg
357-14	698	443	1.91	4.5	35.0

Experiment
No interference
Calculated peak

(b) Pressure distribution.

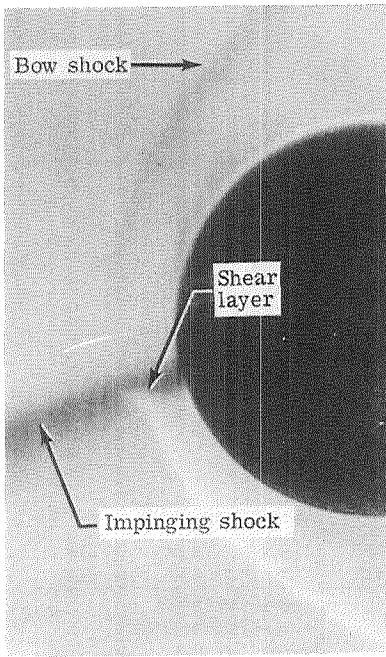| Test run		$p_{t,\infty}$, N/cm^2	$T_{t,\infty}$, K	T_w, K	Q_{stag}, W/cm^2	θ_i, deg
373 - 22	○	705	438	367	8.60	5.1
373 - 23	□	707	434	367	8.21	5.1
373 - 24	◇	703	429	381	5.81	5.1

Experiment
No interference
Calculated laminar peaks
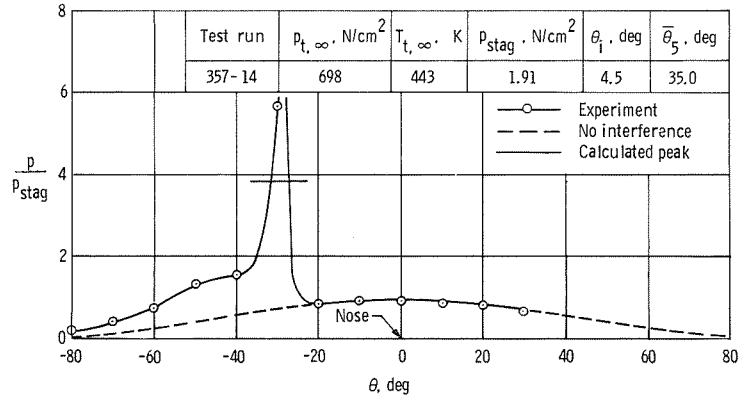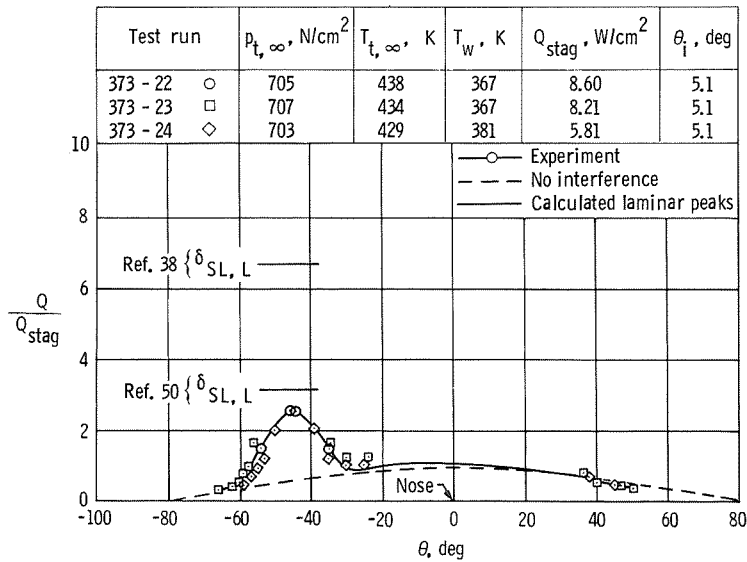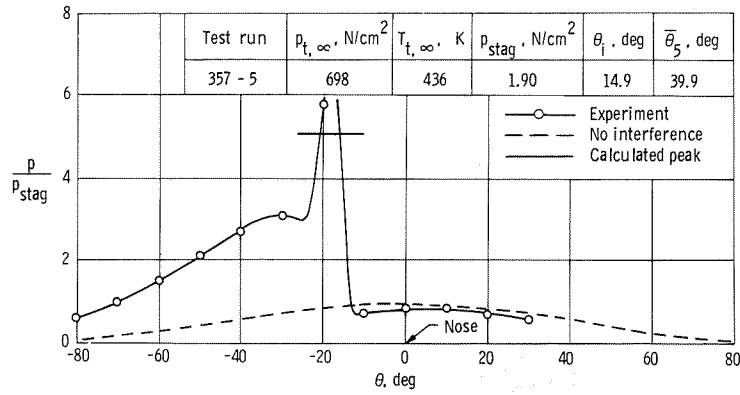
(c) Heat-transfer distribution.
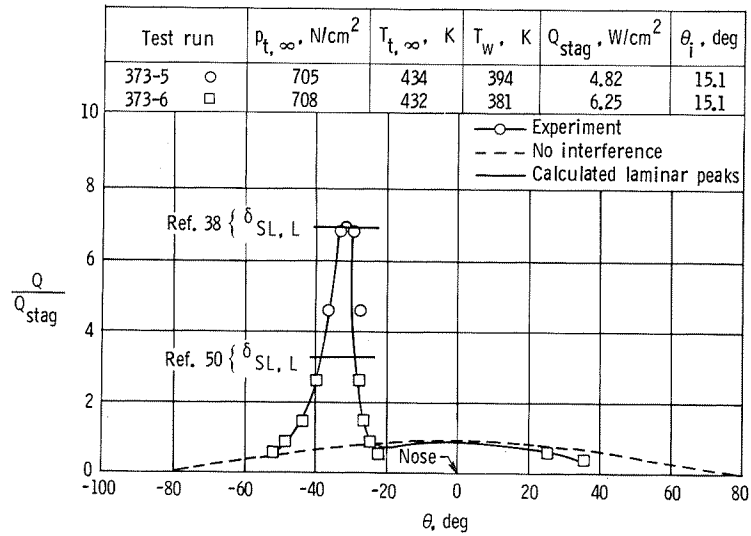
Figure 70.- Type III interference on a 0.025-m-diameter hemisphere at Mach 20.2 in helium. $\theta_i \approx 5°$; $N_{Re,\infty}/m \approx 9.7 \times 10^6$; $\gamma = 1.67$.

Bow shock

Shear layer

Impinging shock

L-73-273

(a) Schlieren photograph.

Test run	$p_{t,\infty}$, N/cm^2	$T_{t,\infty}$, K	p_{stag}, N/cm^2	θ_i, deg	$\bar{\theta}_5$, deg
357 - 10	699	444	1.91	9.7	41.5

Experiment
No interference
Calculated peak

$\dfrac{p}{p_{stag}}$

Nose

θ, deg

(b) Pressure distribution.

Test run		$p_{t,\infty}$, N/cm^2	$T_{t,\infty}$, K	T_w, K	Q_{stag}, W/cm^2	θ_i, deg
373-8	○	706	434	367	8.19	10.1
373-9	□	707	434	381	6.51	10.1

Experiment
No interference
Calculated laminar peaks

Ref. 38 $\{\delta_{SL,L}$

Ref. 50 $\{\delta_{SL,L}$

$\dfrac{Q}{Q_{stag}}$

Nose

θ, deg

(c) Heat-transfer distribution.

Figure 71.- Type III interference on a 0.025-m-diameter hemisphere at Mach 20.2 in helium. $\theta_i \approx 10^\circ$; $N_{Re,\infty}/m \approx 9.7 \times 10^6$; $\gamma = 1.67$.
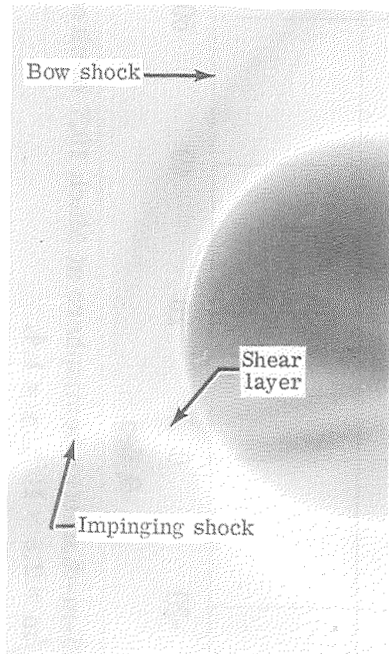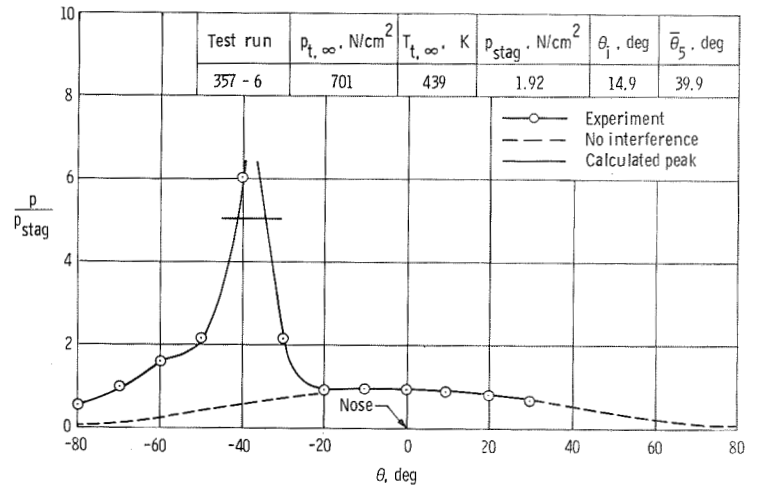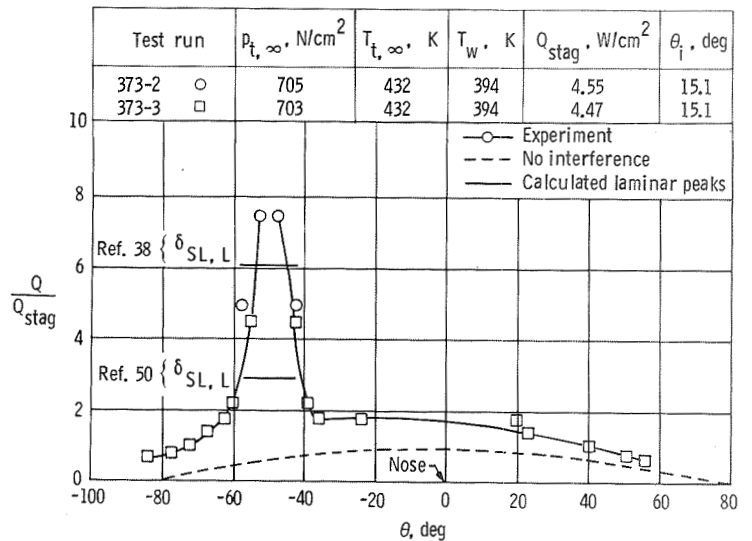
125

(a) Schlieren photograph.

L-73-274

Test run	$p_{t,\infty}$, N/cm^2	$T_{t,\infty}$, K	p_{stag}, N/cm^2	θ_i, deg	$\bar{\theta}_5$, deg
357 - 5	698	436	1.90	14.9	39.9

Experiment
No interference
Calculated peak

(b) Pressure distribution.

Test run		$p_{t,\infty}$, N/cm^2	$T_{t,\infty}$, K	T_w, K	Q_{stag}, W/cm^2	θ_i, deg
373-5	○	705	434	394	4.82	15.1
373-6	□	708	432	381	6.25	15.1

Experiment
No interference
Calculated laminar peaks

(c) Heat-transfer distribution.

Figure 72.- Type III interference on a 0.025-m-diameter hemisphere at Mach 20.2 in helium. $\theta_i \approx 15^O$; $N_{Re,\infty}/m \approx 9.8 \times 10^6$; $\gamma = 1.67$.
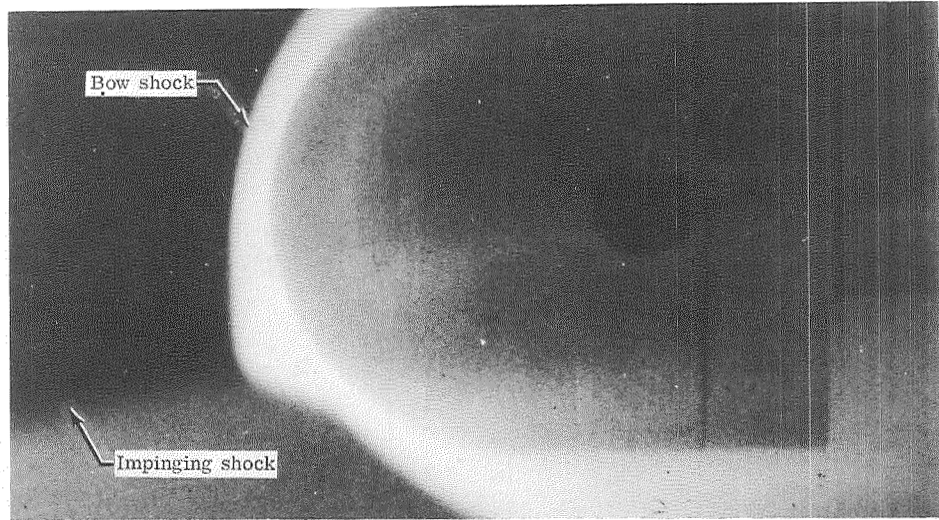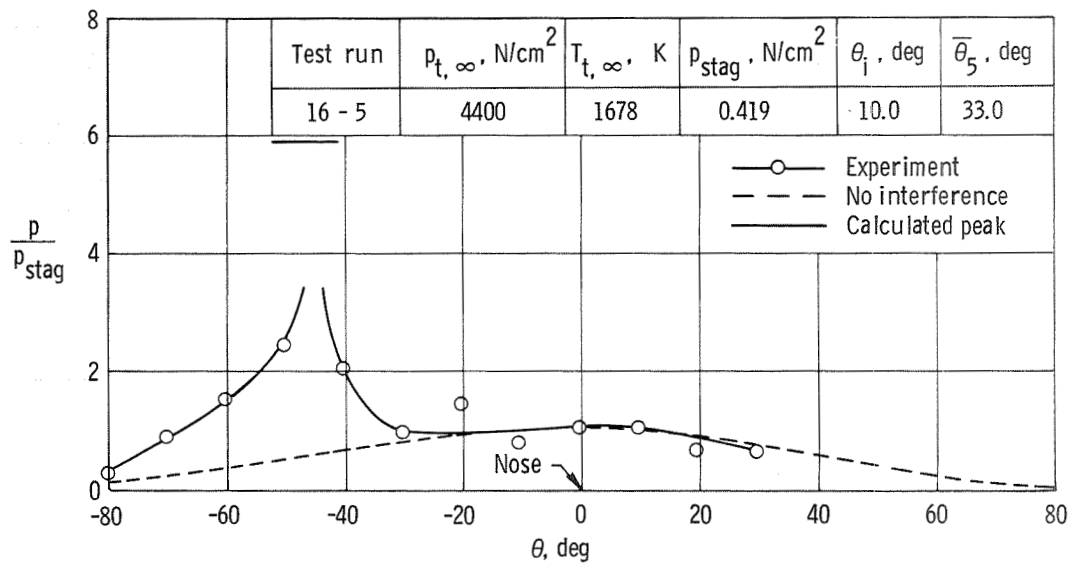
Bow shock

Shear layer

Impinging shock

L-73-275

(a) Schlieren photograph.

Test run	$p_{t,\infty}$, N/cm^2	$T_{t,\infty}$, K	p_{stag}, N/cm^2	θ_i, deg	$\bar{\theta}_5$, deg
357 - 6	701	439	1.92	14.9	39.9

Experiment
No interference
Calculated peak

$\frac{p}{p_{stag}}$

Nose

θ, deg

(b) Pressure distribution.

Test run		$p_{t,\infty}$, N/cm^2	$T_{t,\infty}$, K	T_w, K	Q_{stag}, W/cm^2	θ_i, deg
373-2	○	705	432	394	4.55	15.1
373-3	□	703	432	394	4.47	15.1

Experiment
No interference
Calculated laminar peaks

Ref. 38 $\{ \delta_{SL,L}$

Ref. 50 $\{ \delta_{SL,L}$

$\frac{Q}{Q_{stag}}$

Nose

θ, deg

(c) Heat-transfer distribution.

Figure 73.- Type III interference on a 0.025-m-diameter hemisphere at Mach 20.2 in helium. $\theta_i \approx 15°$; $N_{Re,\infty}/m \approx 9.8 \times 10^6$; $\gamma = 1.67$.
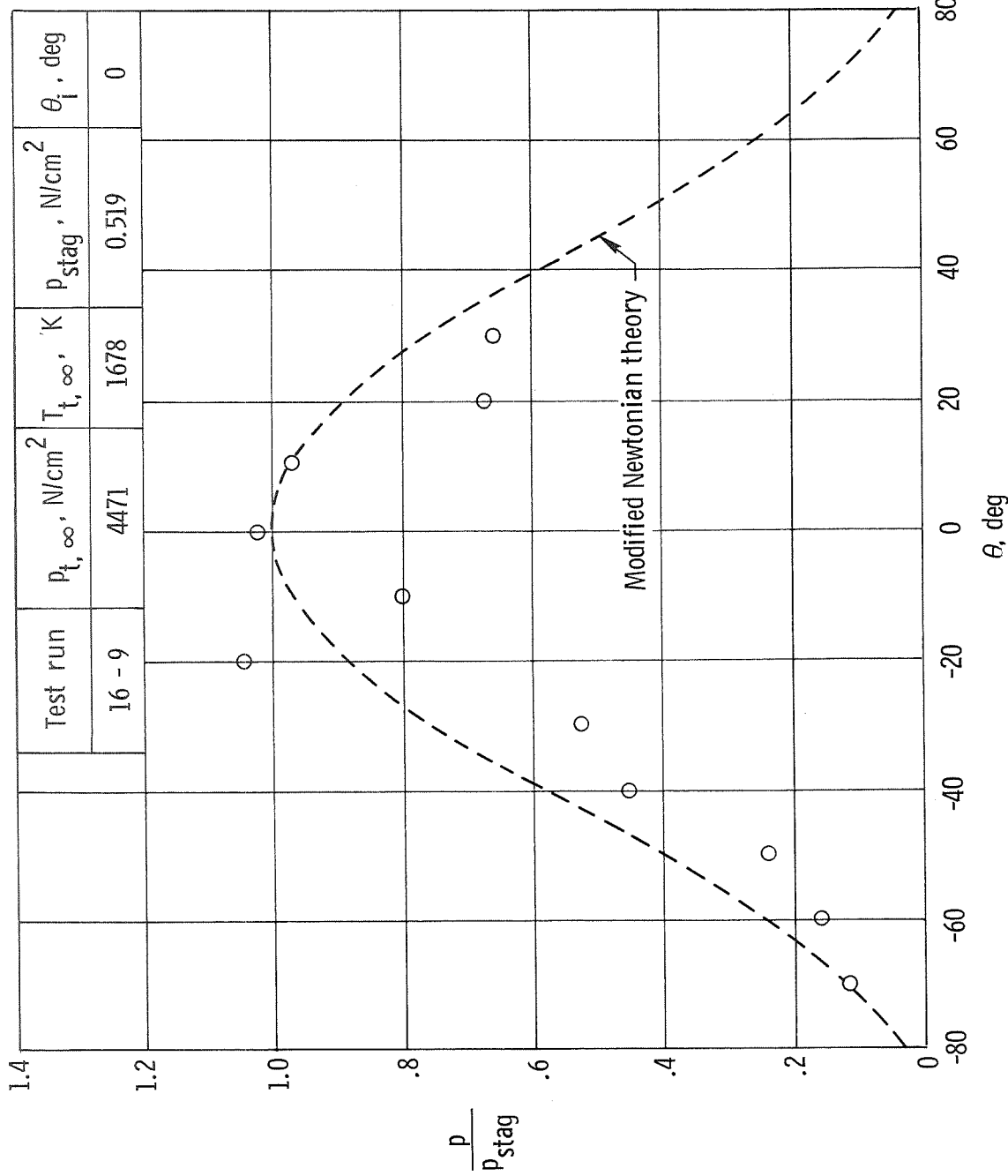
Figure 74.- Pressure distribution on a 0.025-m-diameter hemisphere at Mach 19.7 in nitrogen. $\theta_i = 0°$; $N_{Re,\infty}/m \approx 2.8 \times 10^6$; $\gamma = 1.4$.

The chart contains a table with the following data:

Test run	$p_{t,\infty}$, N/cm^2	$T_{t,\infty}$, °K	p_{stag}, N/cm^2	θ_i, deg
16 - 9	4471	1678	0.519	0

The plot shows $\frac{p}{p_{stag}}$ versus θ, deg, with a curve labeled "Modified Newtonian theory".

(a) Electron beam photograph.

L-73-276

Test run	$p_{t,\infty}$, N/cm^2	$T_{t,\infty}$, K	p_{stag}, N/cm^2	θ_i, deg	$\overline{\theta}_5$, deg
16 - 5	4400	1678	0.419	10.0	33.0

(b) Pressure distribution.

	Experiment	Calculated (laminar)
$\dfrac{Q_{pk}}{Q_{stag}}$	2.42	4.3 (Ref. 50) 10.0 (Ref. 38)

(c) Peak heat transfer (Run 16-19).

Figure 75.- Type III interference on a 0.025-m-diameter hemisphere at Mach 20.6 in nitrogen. $\theta_i = 10°$; $N_{Re,\infty}/m \approx 2.8 \times 10^6$; $\gamma = 1.4$.
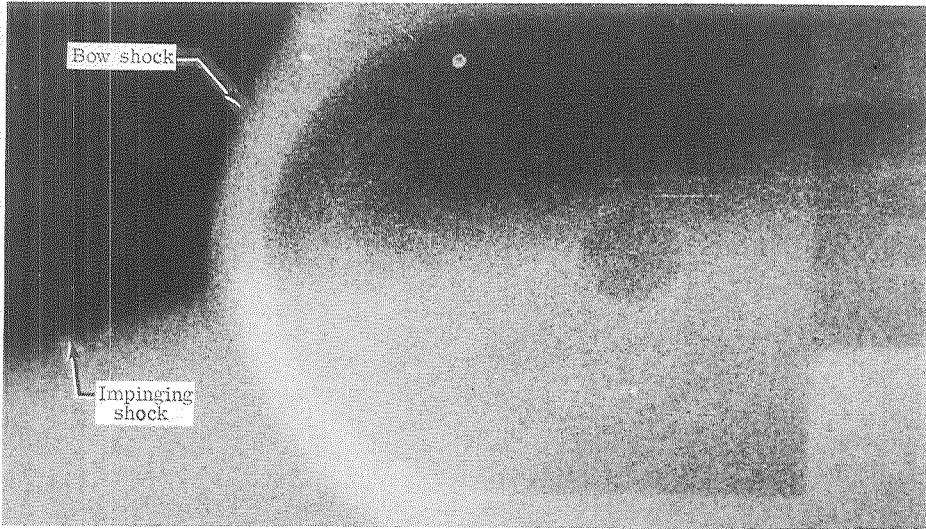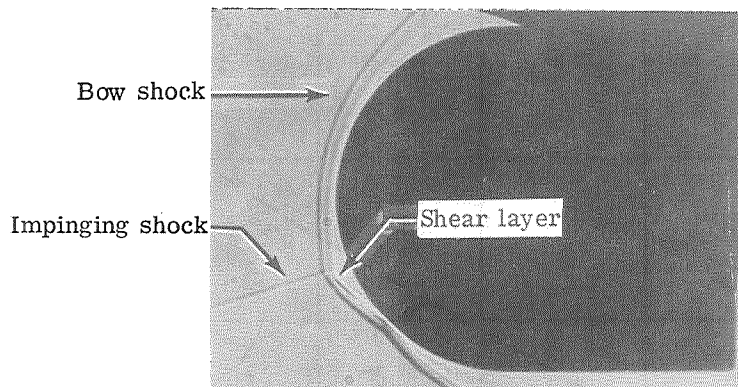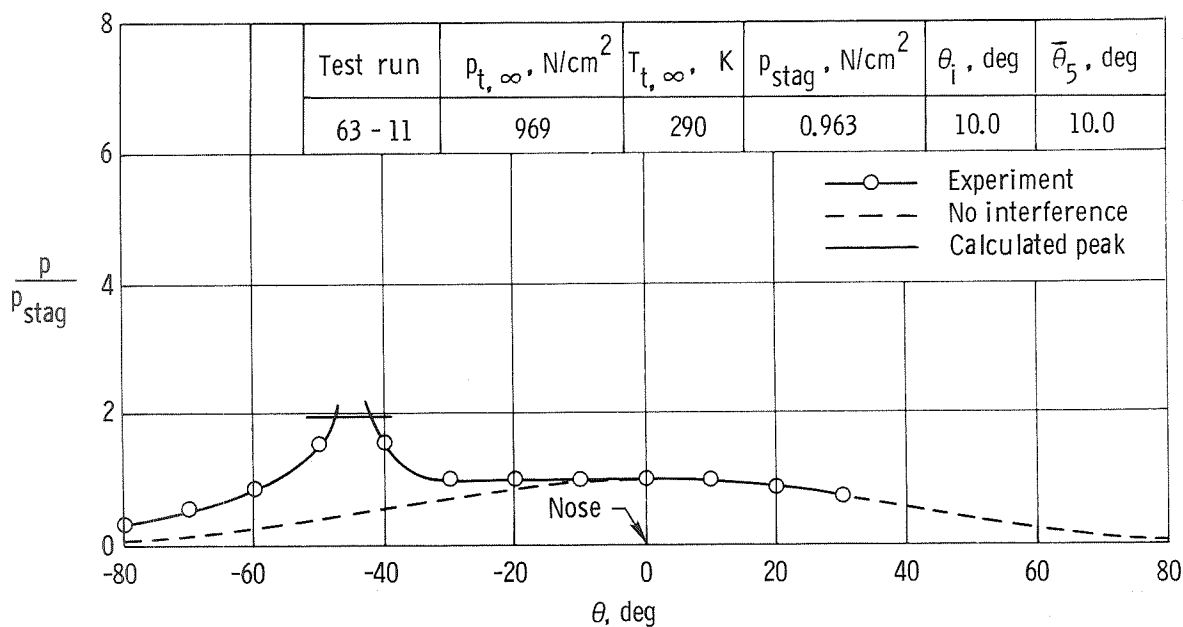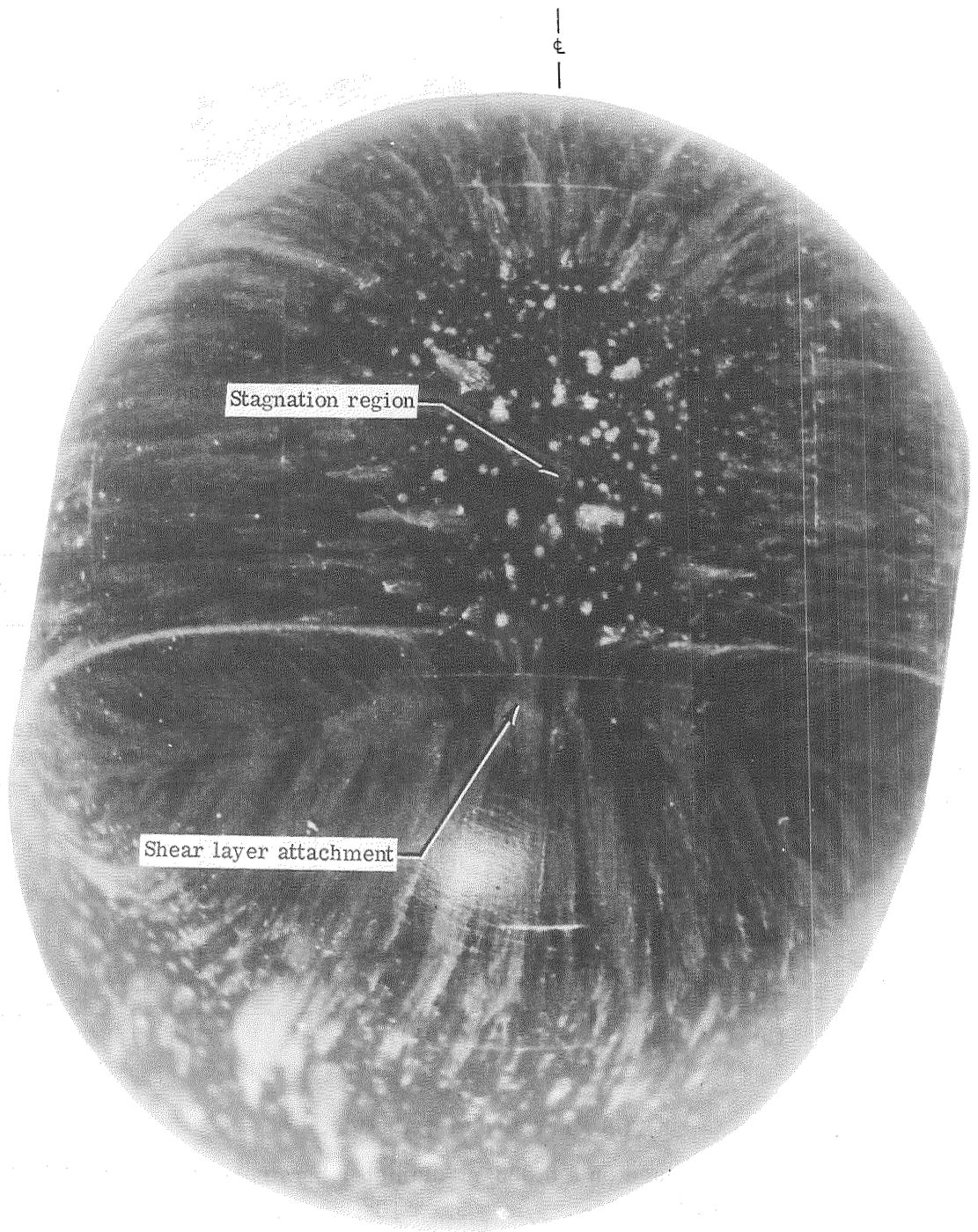
L-73-277

(a) Electron beam photograph.
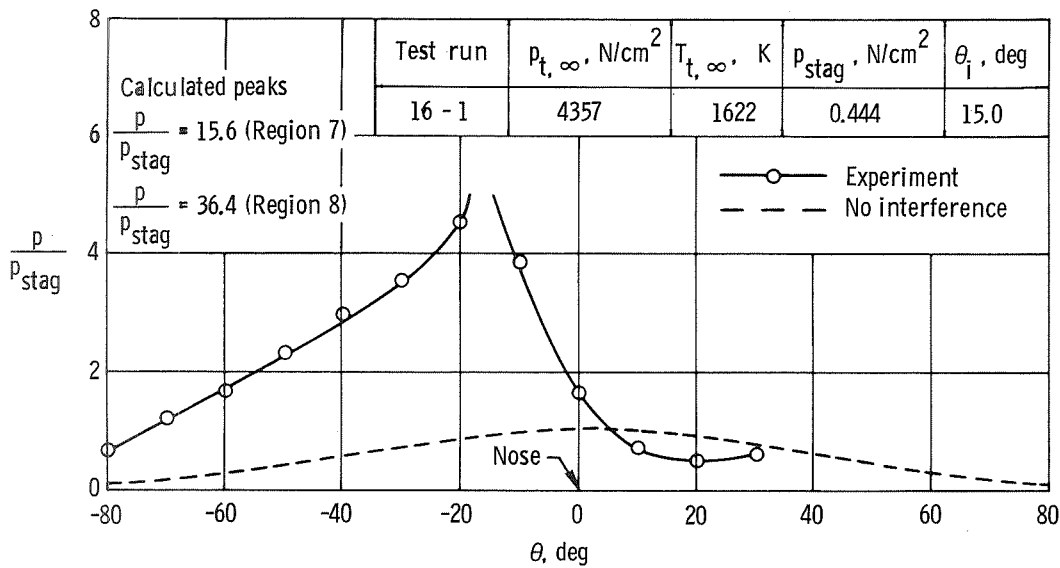
(b) Pressure distribution.

	Experiment	Calculated (laminar)
$\dfrac{Q_{pk}}{Q_{stag}}$	5.51	13.4 (Region 7) 49.5 (Region 8)

(c) Peak heat transfer (Run 16-14).

Figure 76.- Type IV interference on a 0.025-m-diameter hemisphere at Mach 20.2 in nitrogen. $\theta_i = 15°$; $N_{Re,\infty}/m \approx 3.0 \times 10^6$; $\gamma = 1.4$.
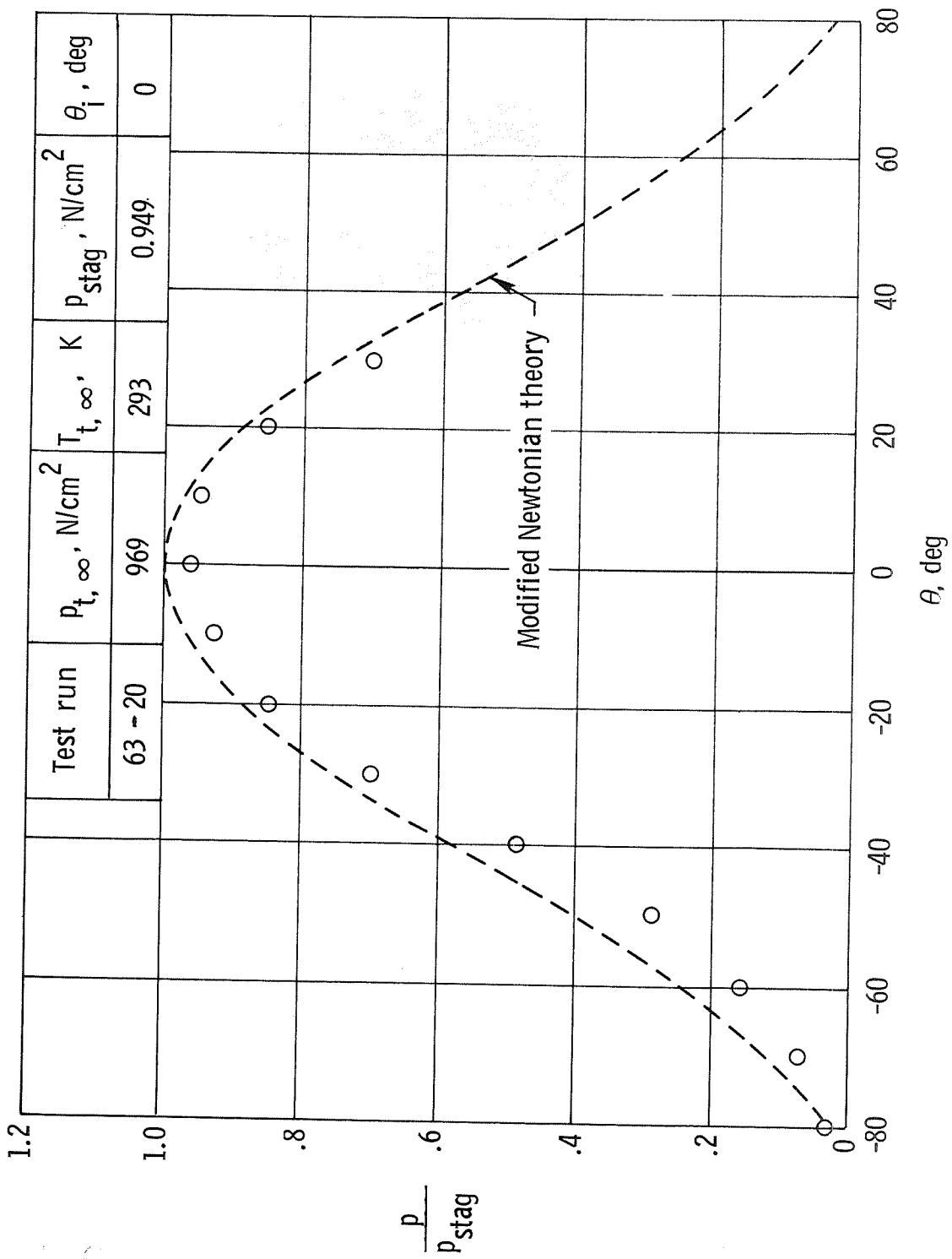
Figure 77.- Pressure distribution on a 0.025-m-diameter hemisphere at Mach 8.9 in CF4. $\theta_i = 0^o$; $N_{Re,\infty}/m \approx 5.6 \times 10^6$; $\gamma = 1.27$.

131

L-73-278

(a) Shadowgraph.

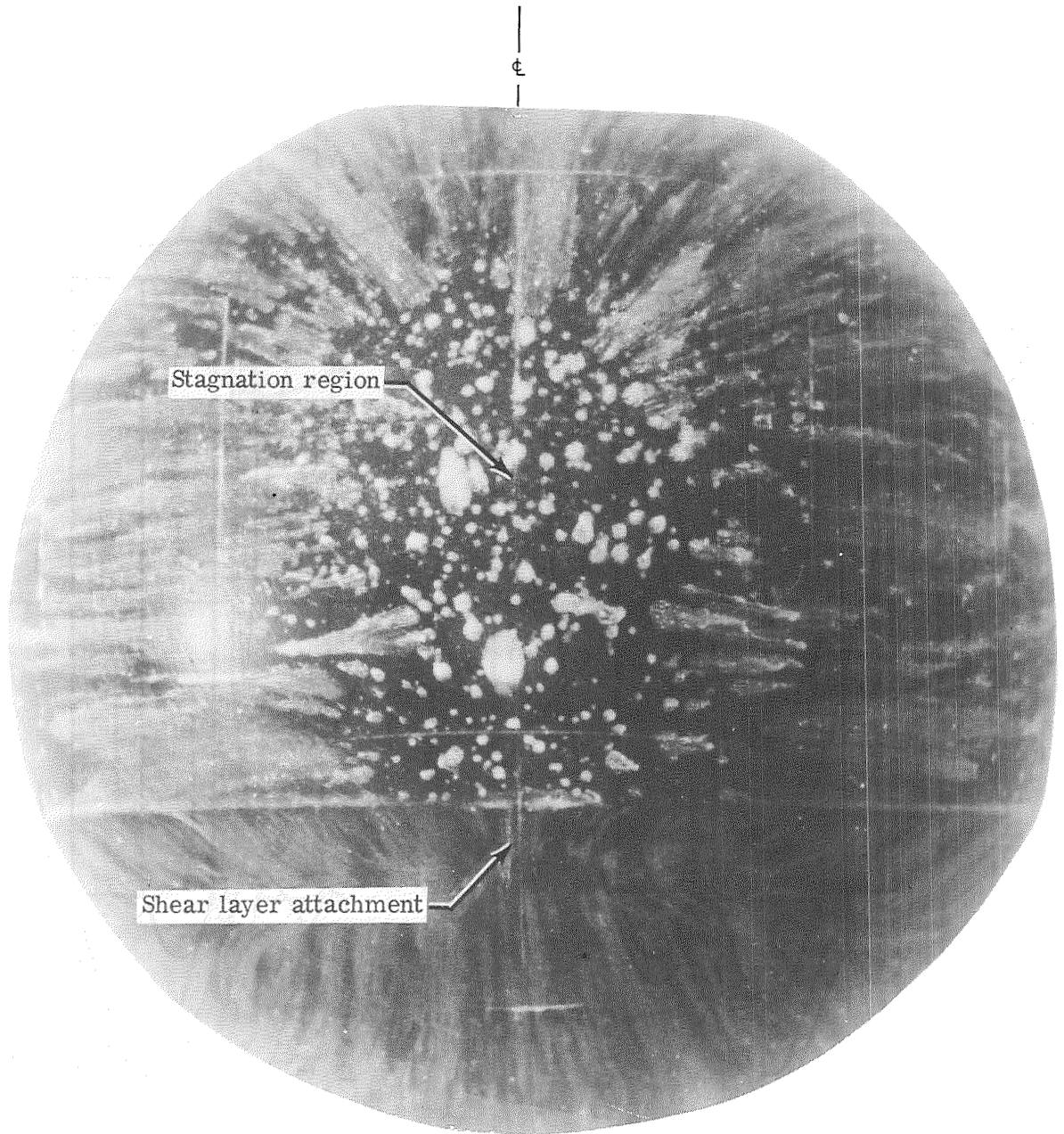| Test run	$p_{t,\infty}$, N/cm^2	$T_{t,\infty}$, K	p_{stag}, N/cm^2	θ_i, deg	$\bar{\theta}_5$, deg
63 - 11	969	290	0.963	10.0	10.0

(b) Pressure distribution.

Figure 78.- Type III interference on a 0.025-m-diameter hemisphere at Mach 8.90 in CF$_4$.
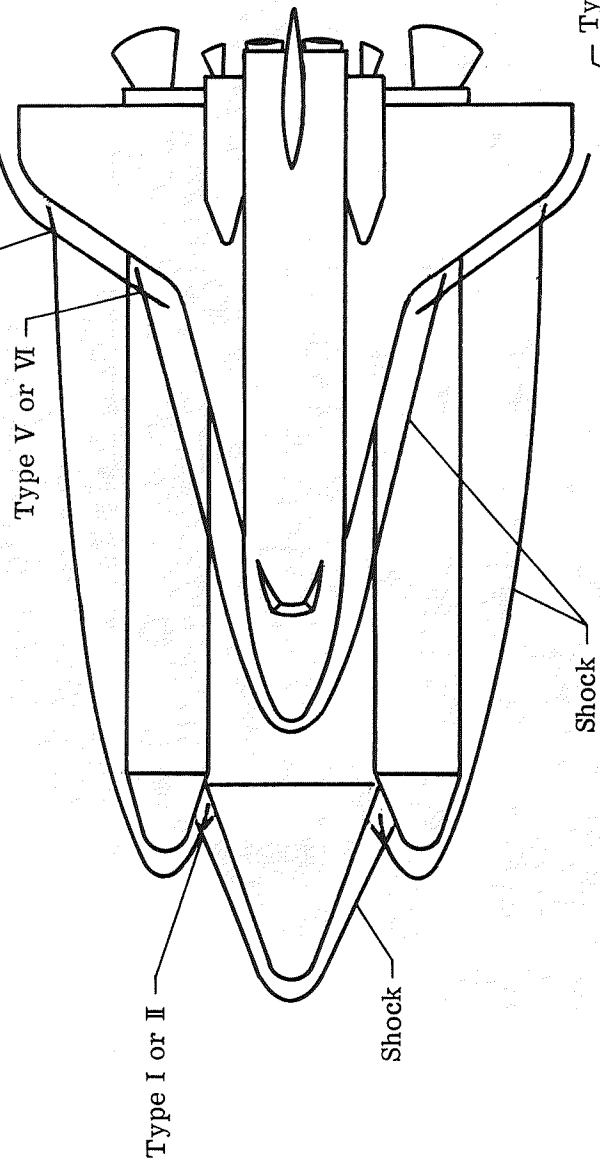$\theta_i = 10^O$; $N_{Re,\infty}/m \approx 5.6 \times 10^6$; $\gamma = 1.27$.

132

Stagnation region

Shear layer attachment

L-73-279

(c) Oil flow distribution.

Figure 78.- Concluded.

(a) Shadowgraph.

Test run	$p_{t,\infty}$, N/cm^2	$T_{t,\infty}$, K	p_{stag}, N/cm^2	θ_i, deg	$\overline{\theta}_5$, deg
63 – 8	965	292	0.948	14.9	15.0
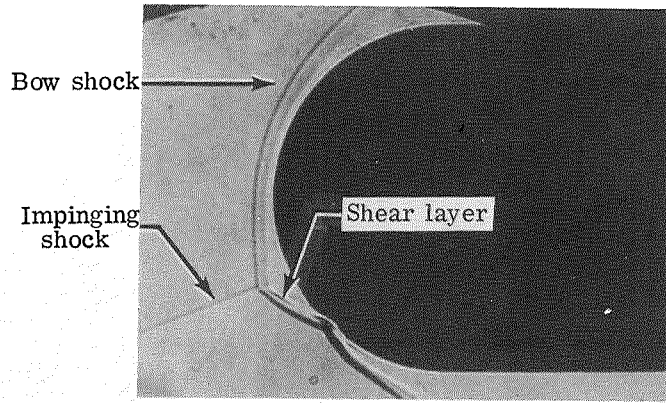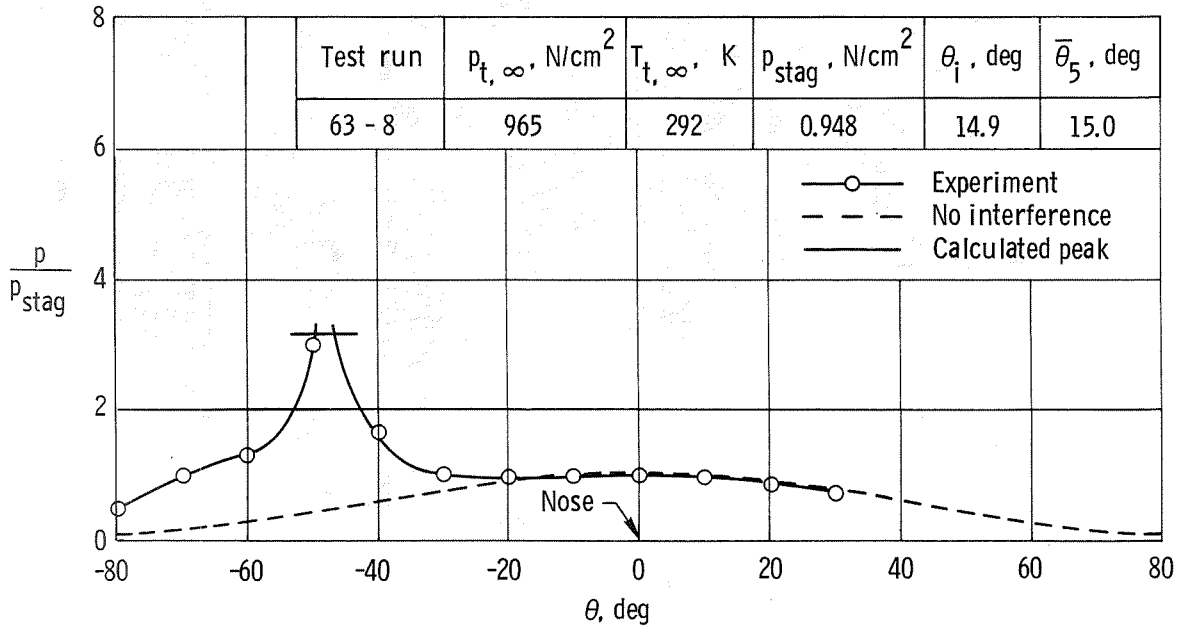
(b) Pressure distribution.

Figure 79.- Type III interference on a 0.025-m-diameter hemisphere at Mach 8.90 in CF_4. $\theta_i = 15^O$; $N_{Re,\infty}/m \approx 5.6 \times 10^6$; $\gamma = 1.27$.
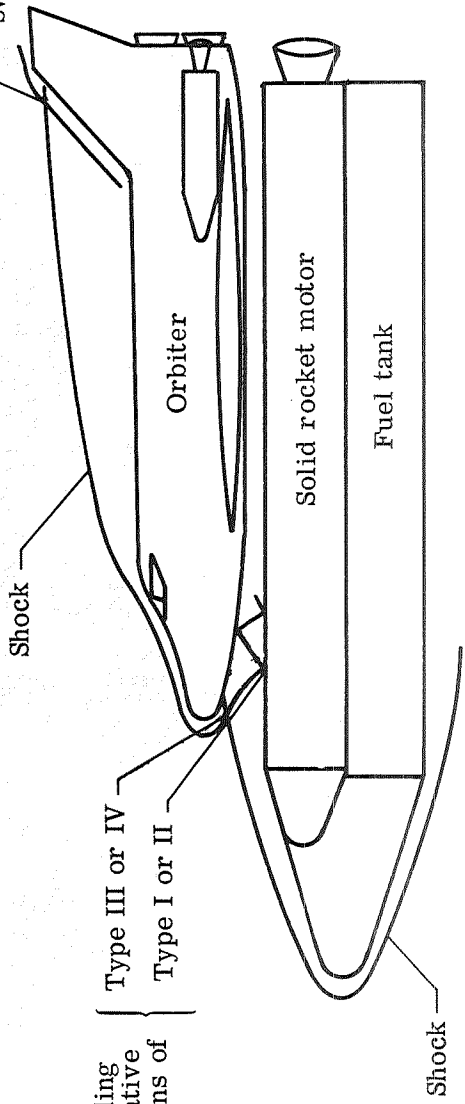
¢

Stagnation region

Shear layer attachment

L-73-281

(c) Oil flow distribution.

Figure 79.- Concluded.

Figure 80.- Locations of types of interference heating on mated configuration at $M_\infty \approx 20$.

Type IV, V or VI depending on sweep

Type IV, V or VI depending on sweep

Type V or VI

Type I or II

Shock

Shock

Shock

Shock

Orbiter

Solid rocket motor

Fuel tank

Depending on relative positions of bodies

Type III or IV

Type I or II
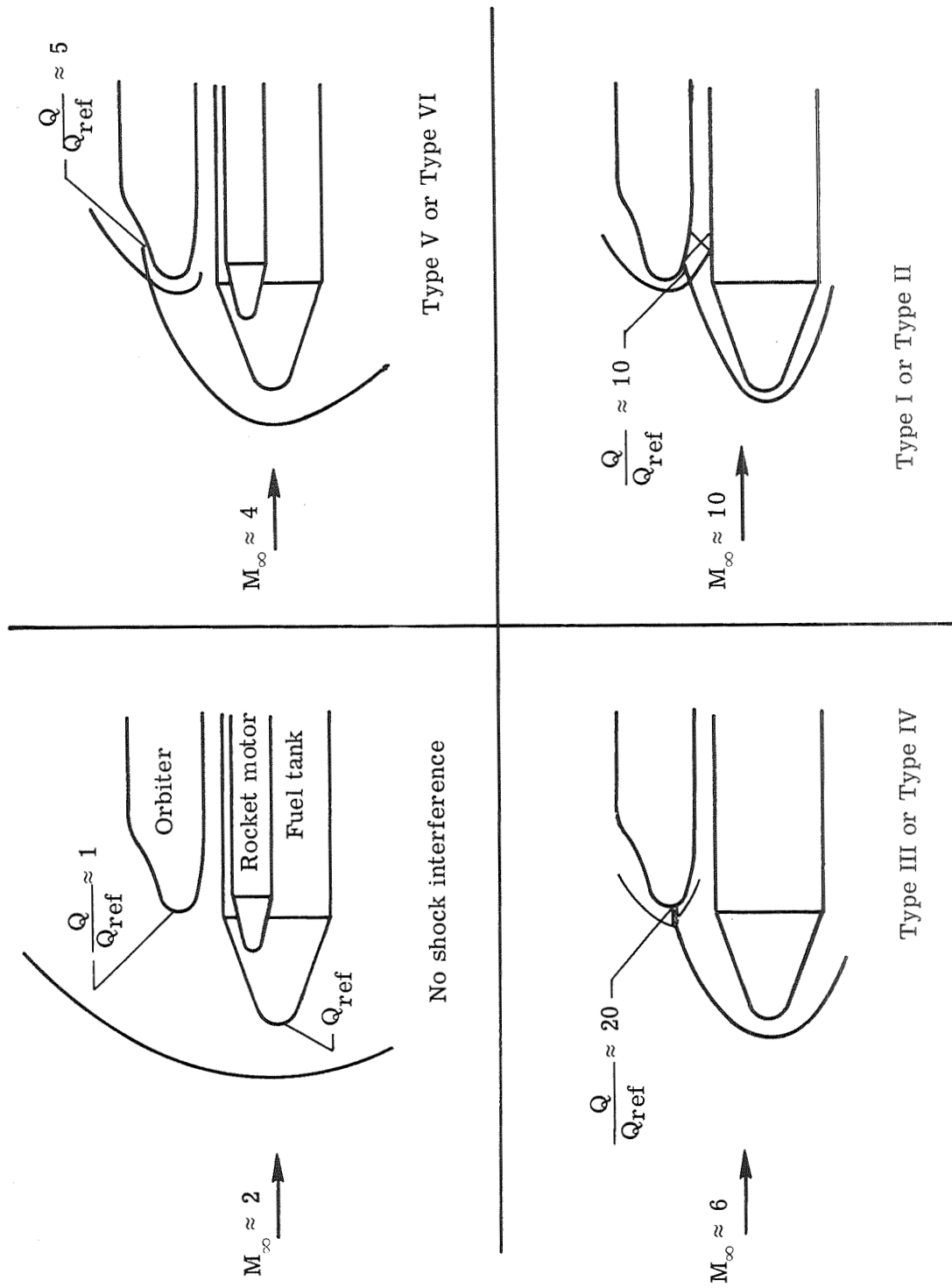
Figure 81.- Shock interference heating during ascent of a mated shuttle configuration.

"The aeronautical and space activities of the United States shall be conducted so as to contribute . . . to the expansion of human knowledge of phenomena in the atmosphere and space. The Administration shall provide for the widest practicable and appropriate dissemination of information concerning its activities and the results thereof."
—NATIONAL AERONAUTICS AND SPACE ACT OF 1958

NASA SCIENTIFIC AND TECHNICAL PUBLICATIONS

TECHNICAL REPORTS: Scientific and technical information considered important, complete, and a lasting contribution to existing knowledge.

TECHNICAL NOTES: Information less broad in scope but nevertheless of importance as a contribution to existing knowledge.

TECHNICAL MEMORANDUMS: Information receiving limited distribution because of preliminary data, security classification, or other reasons. Also includes conference proceedings with either limited or unlimited distribution.

CONTRACTOR REPORTS: Scientific and technical information generated under a NASA contract or grant and considered an important contribution to existing knowledge.

TECHNICAL TRANSLATIONS: Information published in a foreign language considered to merit NASA distribution in English.

SPECIAL PUBLICATIONS: Information derived from or of value to NASA activities. Publications include final reports of major projects, monographs, data compilations, handbooks, sourcebooks, and special bibliographies.

TECHNOLOGY UTILIZATION PUBLICATIONS: Information on technology used by NASA that may be of particular interest in commercial and other non-aerospace applications. Publications include Tech Briefs, Technology Utilization Reports and Technology Surveys.

Details on the availability of these publications may be obtained from:

SCIENTIFIC AND TECHNICAL INFORMATION OFFICE

NATIONAL AERONAUTICS AND SPACE ADMINISTRATION
Washington, D.C. 20546